# Hyperredundant Dynamic Robotic Tails for Stabilizing and Maneuvering Control of Legged Robots

William S. Rone, Jr.

Dissertation submitted to the Faculty of the
Virginia Polytechnic Institute and State University
in partial fulfillment of the requirements for the degree of

Doctor of Philosophy
in
Mechanical Engineering

Pinhas Ben-Tzvi, Chair
Rolf Mueller
Corina Sandu
Daniel J. Stilwell
Alfred L. Wicks

December 13, 2017
Blacksburg, Virginia

Keywords: Robotics, Hyperredundant Robots, Legged Robots, Dynamics, Control

# Hyperredundant Dynamic Robotic Tails for Stabilizing and Maneuvering Control of Legged Robots

William S. Rone, Jr.

(ABSTRACT)

High-performing legged robots require complex spatial leg designs and controllers to simultaneously implement propulsion, maneuvering and stabilization behaviors. Looking to nature, tails assist a variety of animals with these functionalities separate from the animals' legs. However, prior research into robotic tails primarily focuses on single-mass pendulums driven in a single plane of motion and designed to perform a specific task. In order to justify including a robotic tail on-board a legged robot, the tail should be capable of performing multiple functionalities in the robot's yaw, pitch and roll directions. The aim of this research is to study bioinspired articulated spatial robotic tails capable of implementing maneuvering and stabilization behaviors in quadrupedal and bipedal legged robots. To this end, two novel serpentine tails designs are presented and integrated into prototypes to test their maneuvering and stabilizing capabilities. Dynamic models for these two tail designs are formulated, along with the dynamic model of a previously considered continuum robot, to predict the tails' motion and the loading they will apply on their legged robots. To implement the desired behaviors, outer- and inner-loop controllers are formulated for the serpentine tails: the outer-loop controllers generate the desired tail trajectory to maneuver or stabilize the legged robot, and the inner-loop controllers calculate control inputs for the tail that implement the desired tail trajectory using feedback linearization. Maneuvering and stabilizing case studies are generated to demonstrate the tails' ability to: (1) generate yaw angle turning in both a quadruped and a biped, (2) improve the quadruped's ability to reject an externally applied

roll moment disturbance that would otherwise destabilize it, and (3) counteract the biped's roll angle instability when it lifts one of its legs (for example, during its gait cycle). Tail simulations and experimental results are used to implement these case studies in conjunction with multi-body dynamic simulations of the quadrupedal and bipedal legged platforms. Results successfully demonstrate the tails' ability to maneuver and stabilize legged robots, and provide a firm foundation for future work implementing a tailed-legged robot.

# Hyperredundant Dynamic Robotic Tails for Stabilizing and Maneuvering Control of Legged Robots

William S. Rone, Jr.

(GENERAL AUDIENCE ABSTRACT)

Looking to nature, animals utilize their tails to provide a variety of functions, including maneuvering (changing direction) and stabilization (not falling). However, research to implement tail-like structures that mimic these behaviors on-board legged robots has been limited. Furthermore, prior research into robotic tails has focused on single-link, pendulum-like structures that move in one (more common) or two (less common) directions. This research studies articulated tail structures, inspired by the way biological tails continuously bend along their length, to implement maneuvering and stabilizing behaviors in quadrupedal (four-legged) and bipedal (two-legged) robots. Two new serpentine tail designs are presented (serpentine robots are defined by numerous similar rigid links connected together), along with dynamic models that predict how the tails move and the loading that they apply to their legged robots. An additional dynamic model for a continuum robot is also presented (continuum robots are defined by their continuous, deformable structure). Controllers that plan and implement the maneuvering and stabilizing behaviors in the quadruped and biped are generated, and case studies are presented demonstrating the tails' ability to (1) turn the quadruped and biped, (2) improve the quadruped's ability to prevent tipping due to an external roll disturbance, and (3) prevent the biped from tipping when lifting one of its legs (for example, to step forward). Results are generated using both tail simulations and prototypes of the two tail designs under consideration. These results are used in conjunction with simulations of the quadrupedal and bipedal robots to implement the case studies.

*In memory of my aunt Judy Armstrong, my grandmother Ann Rone, my teacher Linda Knowles and my neighbor Norma Murray.*

# Acknowledgments

There is only one person who I could even consider acknowledging first, and that person is my adviser, Dr. Pinhas Ben-Tzvi. Over our past 9 years together, you have guided me through good times and bad and have helped me through more than an adviser should have to. That this dissertation is finished is due primarily to the ways you have pushed and challenged me, and while I didn't thank you at the time, I thank you here. To my colleagues Wael and Anil: without your support, I would likely still be toying with ADAMS simulations or soldering components to PCBs, dreaming of the day I would finish my dissertation. I have learned much from each of you and could not have selected a better pair of people to transfer with from GW to Tech. To my committee, Drs. Mueller, Sandu, Stilwell and Wicks: thank you for your guidance during my preliminary defense, and your attentive questioning during my dissertation defense—my work is stronger because of your input. And special thanks to Dr. Abaid for her willingness to "pinch hit" in my defenses.

To my teachers: thank you for your guidance and support throughout my life. First and foremost, my deepest love for the late Ms. Linda Knowles, Calculus Queen and a woman whose clear vision and persistence rightly guided me to engineering. To my science teachers and Science Olympiad coaches, including Ms. Parker, Ms. Cathey, Ms. Skinner, Ms. Cundiff, Ms. Bordelon and Dr. Yelverton: thank you for the efforts each of you made to offer opportunities outside of the classroom for my classmates and myself to explore our

interests, travel the country and compete. And to Ms. Morres, Ms. Duffy, Ms. McDonald, Doc Chapin, Ms. Hardee and Ms. Walker, thank each of you for the impact you had on me in my teenage years.

Outside of academia, my faith has been an immense support over the three-and-a-half years, manifested primarily through those people God has set in my path. To Jill: I am so thankful for you not just as my co-teacher, but also my friend. I have learned so much from you, both inside and outside of the classroom, and will forever appreciate your eagerness to include me in your holiday celebrations and help me celebrate my milestones. And to Denis, Simonne, Chloe and Sharon, thank you for always making me feel so welcome for these celebrations. To Bob, Glenda, Sue, Deacon Mike and my Holy Family small group: thank you for your love and support over the past two and a half years. To my priests: Frs. Greg, Adam, Remi and John, thank you for your service, your teaching and the Newman/parish environments you fostered. To Julie, Sam and Anthony: thank you for fostering my curiosity about Catholicism into a deeper love for Christ and new love for the Church, the sacraments and Mary. And, finally, although I now find myself a confirmed Catholic, I cannot set aside the profound impact my high school Sunday school teachers Susan and Coach McAuley had on me and my faith life. Whenever I teach my high school religious education students, I constantly guide myself by trying to imagining what you would have said or done.

After a year of graduate work, joining the Labyrinth community was everything I didn't know I needed in my life. I will forever be indebted to Kathleen for the store she created and the numerous lifelong friends I have made hanging around her store, herself included. Chris and Joe: I still remember my excitement when you first invited me to Mr. Henry's after FNM, and I treasure the countless hours we spent there and elsewhere not just as a group of people who share a hobby, but as friends. Hannah and Andrew: my affection for you dramatically exceeds what is reasonable for the length of time we have been friends, and I hope to one day reciprocate the infinite hospitality you have shown me on my visits back

to DC. And to Judy, Connor, Eli, Scott, Ben, Christian, Jim, Jon-Carlo, Elliott, James, Mark, Charles and Alex: thank you for your friendship and the nigh countless games played between us.

Among the reasons I didn't plan to leave GW or DC for my graduate work is the corps of friends I had there. Nicole: although every time I see you it feels like no time has passed, one thing I look forward to is having less time between those visits. You were the first friend I made at GW, and your passion has always been an inspiration. Mike: you've come a long way from that freshman I all-but-scolded in our first Senate-elect meeting. I greatly enjoyed our friendship during my latter years at GW and will miss seeing you when I visit DC. I guess I'm going to have to come see that other Washington you're always going on about. To Gina and John: thank you both for your support and advice throughout my many years at GW. Anyone would be lucky to have a single advocate as fierce as you: I was blessed with two. To Julie and Jamie: I figured I'd make friends in the SA, but I hit the jackpot with you two. From our countless hours watching Glee together to countless meals at Founding Farmers and KBC (RIP), spending time with you two was always a highlight of my week, even more so since I've moved. And while new friend are obviously great, there is nothing quite like old friends. I am so happy for my years in DC with Emily and Nancy, and look forward to new memories in the new locales they now call home.

To my godparents, Rachel and Stephen: your example lit the path that lead me to the Church. That alone is worth more than I could ever repay. Add to that the countless nights you have welcomed me into your home and our numerous unconventional holiday celebrations, and you have a pair of the most special people in my life. And to their children, AT, LG, JE, HW and JF: thank you for simply being the wonderful children you are.

Stephanie and Andy: I often feel thankful for the fact that I have two sisters and two brothers-in-law: one pair several years older than me, and one pair my own age. I can't fathom what high school, undergrad or grad school would have been like without you. I

know for certain I would not be the person I am today without both of you in my life. And to your family, particularly Cindy, Mike, Ray, Val, Kristy, Dale, Lauren and Jantzen: thank you for the countless times you have welcomed me into your homes and made me feel part of your family.

The most marvelous thing about growing older is that differences in ages mean less and less with each passing year. Of the many things that have changed as I've pursued this degree, one which I am happiest about has been drawing closer with my sister Carre and brother-in-law Nelson. Of the many things I want to do now that I've finished this degree, the top of the list is spending more time with you, not simply because we are related, but because we are friends.

And, finally, Mom and Dad. I could match this dissertation word-for-word with lists of reasons why you're amazing and how you've supported me and what you mean to me. But words cannot truly express the love I feel for two of the most singular people I know. Everything good that I am and anything good that I do is because of your love, influence and example.

This material is based upon work supported by the National Science Foundation under Grant No. 1557312.

# Contents

# List of Figures

# List of Tables

# Chapter 1

# Introduction

## 1.1 Background

The dominant approach for legged locomotion is to propel, maneuver and stabilize the robot using its legs during locomotion. In bipedal robots, this stems from the field's primary focus on mimicking humanoid locomotion. In quadrupedal robots, this necessitates four spatial legs with a minimum of 3 active degrees-of-freedom (DOF), resulting in systems with at least 12 DOF. These DOFs must be controlled by sophisticated algorithms that simultaneously produce propulsion and maneuvering while maintaining stability. Furthermore, loss of ground contact severely impairs the robot's ability to perform these tasks, as the ground contact loading at the feet is the legged robot's implicit control input (based on the legs' motion).

However, looking to legged animals, tails are commonly observed to perform one or more functions that assist in locomotion ranging from propulsion [54, 59, 77, 78] to maneuvering [22, 36, 58, 89] to stabilization [3, 5, 46, 54, 87, 93].

Although these biological tails vary dramatically in terms of scale and function, a common feature is their articulated structure. However, existing research in the field of robotic tails is dominated by the implementation of one- and two-DOF pendulum-like tails consisting of a single mass [74]. This dissertation aims to study ways in which articulated robotic structures can be applied as robotic tails to aid the maneuvering and stabilization of legged robots.

## 1.2 Contributions

In this dissertation, the fields of robotic tails and hyperrredundant robotics intersect to consider the use of bioinspired, articulated robotic tails to maneuver and stabilize quadrupedal and bipedal legged robots. This dissertation presents work that provides the following contributions to these fields:

1. Design: Two novel serpentine robotic tails of differing topology, degree of actuation and redundancy resolution are conceptualized, designed and implemented as prototypes.

    - The Roll-Revolute-Revolute Robotic Tail (R3RT) consists of a fully actuated chain of rigid links connected by parallel revolute joints with rigid gears distributing loading within each actuated segment.
    - The Universal-Spatial Robotic Tail (USRT) consists of an underactuated chain of rigid links connected by universal joints with elastic springs distributing loading within each actuated segment.

2. Dynamics: Dynamic models are generated for both serpentine and continuum structures and are cross-validated using alternative means of simulation and experimental results.

- Novel dynamic models for the R3RT and USRT are formulated, and simulation results from these models are compared to experimentally measured joint and loading trajectories.
- Novel dynamic models for cable- and rod-driven continuum robots are derived that bridge the gap between existing segment-based lumped parameter models and continuous distributed parameter models
- Cross validation of the continuum robot dynamics models is performed using finite element analysis and experimental results

3. Controls: Outer- and inner-loop controllers are formulated, simulated and experimentally implemented to implement maneuvering and stabilization behaviors using the R3RT and USRT.
   - An outer-loop controller is designed for using the two novel serpentine tails for yaw-angle maneuvering of bipedal and quadrupedal robots.
   - An outer-loop controller is designed for tail-based disturbance rejection for a quadrupedal robot.
   - An outer-loop controller is designed for tail-based active balancing for a bipedal robot.
   - Inner-loop controllers are formulated to generate the tails' desired motion and maintain minimum cable tensions in the USRT during motion.
   - Case study simulations are generated to demonstrate the tails' ability to maneuver and stabilize simulated quadrupedal and bipedal robots.
4. Hardware-in-the-Loop Simulations: Experimentally measured tail loading is used in conjunction with the quadrupedal and bipedal robot simulations to formulate hardware-in-the-loop analyses to further demonstrate the tails' capabilities.

## 1.3 Dissertation Structure

The dissertation is organized as follows:

**Chapter 1**: Introduces the topic and outlines the main contributions of the dissertation.

**Chapter 2**: Reviews prior research associated with the two primary fields covering this dissertation: robotic tails and hyperredundant robots.

**Chapter 3**: Discusses the factors that motivated the evolution of the tail designs and discusses the research hypothesis.

**Chapter 4**: Presents the dynamic modeling for cable-driven and rod-driven continuum robots initially planned to implement the articulated tails, along with associated simulation and experimental results.

**Chapter 5**: Presents the two serpentine tail designs, including the design concepts, mechanical designs, electrical designs and prototype implementation.

**Chapter 6**: Presents the dynamic modeling for the two serpentine tail designs, including definitions of the equations of motion, kinematic models, loading models and tail base loading calculations. Simulation results are provided along with experimental validation.

**Chapter 7**: Presents the sensing and state estimation considerations for the two tails, the outer-loop controller designs for maneuvering and stabilizing a quadruped and a biped, and the inner-loop controller designs for implementing the desired tail trajectories on the two tails.

**Chapter 8**: Presents case studies for maneuvering and stabilizing simulations of quadrupedal and bipedal robots using both simulated and experimentally measured tail loading.

**Chapter 9**: Concludes the dissertation with a summary and a discussion about potential

future work.

## 1.4 Selected Publications

**Disclosure**: This dissertation uses content directly adapted from the following journal publications:

1. **W. S. Rone**, W. Saab, P. Ben-Tzvi, "Maneuvering and Stabilization Control of a Bipedal Robot with a Universal-Spatial Robotic Tail", *Bioinspiration and Biomimetics*, *ASME Journal of Dynamic Systems, Measurement and Control*, Under Review, August 2017.

2. **W. S. Rone**, W. Saab, A. Kumar, P. Ben-Tzvi, "Controller Design, Analysis and Experimental Validation of a Robotic Serpentine Tail to Maneuver and Stabilize a Quadrupedal Robot", *ASME Journal of Dynamic Systems, Measurement and Control*, Under Review, November 2017.

3. **W. S. Rone**, W. Saab, P. Ben-Tzvi, "Design, Modeling and Integration of a Flexible Universal Spatial Robotic Tail", *ASME Journal of Mechanisms and Robotics*, vol. 10, no. 4, pp 041001: 1-14, August 2018.

4. W. Saab, **W. S. Rone**, A. Kumar, P. Ben-Tzvi, "Design and Integration of a Novel Spatial Articulated Robotic Tail", *IEEE/ASME Transactions on Mechatronics*, Under Review, August 2018.

5. W. Saab, **W. S. Rone**, P. Ben-Tzvi, "Robotic Modular Leg: Design, Analysis and Experimentation", *ASME Journal of Mechanisms and Robotics*, vol. 9, no. 2, pp. 024501: 1-6, April 2017.

6. **W. S. Rone**, P. Ben-Tzvi, "Mechanics Modeling of Multi-Segment Rod-Driven Continuum Robots", *ASME Journal of Mechanisms and Robotics*, vol. 6, no. 4, pp. 041006: 1-12, November 2014.

7. **W. S. Rone**, P. Ben-Tzvi, "Continuum Robot Dynamics Utilizing the Principle of Virtual Power", *IEEE Transactions on Robotics*, vol. 30, no. 1, pp. 275-287, February 2014.

Additional papers related to the topic of this dissertation but not directly adapted into chapters, sections or subsections of this dissertation include the journal publications [69, 74, 75] and the conference publications [65, 66, 67, 68, 70, 71].

# Chapter 2

# Literature Review

This chapter provides an overview of prior research associated with the two fields most closely related to the focus of this dissertation: robotic tails (section 2.1) and hyperredundant robots (section 2.2).

## 2.1 Robotic Tails

Similar to their biological counterparts, robotic tails can be classified by the functionality they provide, including propulsion, maneuvering and stabilization. In relation to propulsion, the most common use of a robotic tail is in aquatic applications for generating hydrodynamic thrust similar to a fish [40, 81] or tadpole [37]. For terrestrial locomotion, tails have been used to dynamically actuate legged locomotion [4], rapidly accelerate and decelerate a wheeled robot [57] and climb vertical surfaces [60].

In relation to stabilization, tail-like pendulums have been used to compensate for the undesired motion generated by a robot's hopping motion [29, 45, 94] and adjust a quadruped's

COM while moving [52].

In relation to maneuvering, prior work has focused on implementing two functionalities: yaw-angle steering for legged [11, 39] and wheeled [56] robots, and pitch-angle reorientation while falling to land parallel to the ground [13, 33].

In addition to these tails designed to demonstrate a single functionality, multi-functionality tails have also been presented. Chang-Siu et al. [12] present a tail that provides maneuvering capabilities to re-orient the robot while airborne and stabilizing capabilities to reject the pitch disturbance due to an obstacle. Ikeda and Toyama [31] present a system that uses its tail's pitching motion to propel a quasi-passive biped and its rolling motion to steer. Briggs et al. [9] present a tail used to generate attitude maneuvers in an airborne quadruped and to reject external disturbances acting on a quadruped.

Beyond their functionalities, existing robotic tails can also be classified by the DOF(s) in which they operate. The majority of prior research focuses on single-mass, pendulum-like tails operating in a single plane of motion. Tails rotating about the pitch axis have been shown in the literature to be the most versatile, demonstrating propulsion [57], stabilization [29, 45, 94] and maneuvering [33] capabilities. Tails rotating about the yaw axis have primarily been utilized for propulsion [4, 37, 40, 60, 81], but have also demonstrated the ability to impact the legged robot's yaw angle maneuvering [11, 39]. Tails rotating about the roll axis are the most limited of the single-DOF robotic tails, providing yaw-angle maneuvering on a wheeled robot [56].

Research into multi-DOF, single-mass tails is more limited, but more promising in the array of functionalities they can provide. These tails are classified by the reported or apparent nominal configurations of the tails; however, as an example, a yaw-pitch joint becomes a yaw-roll joint after rotating the yaw joint by 90°. Chang-Siu et al. [13] studied a two-DOF tail

comprised of a pitch-yaw joint pair used to adjust the robot's yaw, pitch and roll orientations as the robot falls. Mutka et al. [52] studied a two-DOF tail comprised of a yaw-pitch joint pair used to adjust the robot's COM position in the transverse plane during locomotion to assist in stabilizing the robot. Ikeda and Toyama [31] studied a two-DOF tail comprised of a pitch-roll joint pair used to propel a passive biped with its pitching motion and steer the passive biped with its rolling motion. Briggs et al. [9] studied a two-DOF tail comprised of a roll-pitch joint pair used to generate aerial maneuvers in its quadruped and stabilize its quadruped by rejecting external disturbances.

## 2.2 Hyperredundant Robots

In nature, a wide variety of biological structures (such as tails, tentacles, snakes' bodies and elephants' trunks) have morphologies which can be considered as hyperredundant, which are characterized by having numerous redundant DOFs. Robotic systems that tend to mimic these types of articulated structures are called hyperredundant, and may be categorized as continuum or serpentine [64]. Continuum robots are defined by their theoretically infinite DOFs and are capable of bending cotinuously along their length. Serpentine robots are composed of a serial chain of numerous, similar (often identical) rigid links capable of forming discretized curvatures.

The similarity of this type of robotic structure to biological tails motivated its consideration in this research. Prior research related to the topics addressed in this dissertation may considered in three categories: continuum robot designs and modeling (section 2.2.1), serpentine robot designs and modeling (section 2.2.2) and hyperredundant manipulator control (section 2.2.3).

### 2.2.1 Continuum Robot Designs and Modeling

#### Continuum Robot Designs

Continuum robot designs may be classified by the form of their elastic structure. Solid core structures are defined by a solid, elastic backbone that extends the length of the robot. A common structure for which many researchers have analyzed the mechanics are cable-driven spring-steel core robots with disks rigidly mounted to the core [43]. Alternatively, serial chains of coil springs have been used to implement continuum robots designed to be vertically hung [17, 61]. Solid core structure with non-metallic cores have also been demonstrated, including a design in which plastic interlocking fibers are used as both the structure and actuation mechanism for the robot [51], along with a silicone octopus-tentacle-like robot designed for use underwater [62].

Fluid core structures use a flexible solid structure containing pressurized air to provide structural support for the continuum robot. The most common approach is the use of a single pneumatic tube with cables routed along the structure to deform the variable-stiffness pneumatic tube to the desired configuration [1, 32, 49]. Alternatively, the continuum robot's segments can be comprised of sets of three pneumatic muscles or bellows capable of extending and retracting based on their pressurization [21, 50]. By adjusting the relative pressurization of the three actuators, the shape of the robot can be controlled. Finally, a elastomeric structure with embedded microchannels for fluid pressurization has also been demonstrated on the meso-scale [47].

Precurved tube robots consist of a set of hyperelastic tubes of increasing inner and outer diameter, capable of nesting within one another [18, 73]. The relative extension and rotation of the tubes with respect to one anther changes the configuration of the robot.

For this work, precurved tube robots were set aside due to the need for highly dynamic motions of the robot, which are limited by the high level of contact friction between the constituent parts. Likewise, fluid core structures provide severe limitations with respect to their implementation in field robots. Whether the core is filled with liquid or gas, in addition to any actuators driving the structure's motion, pumps, regulators and other equipment are needed to maintain the core's pressurization. Therefore, a solid core structure was initially considered to implement the robotic tail.

In addition to the cable-driven actuation described in [43] and further considered in [26, 35, 72] for spring-steel solid core robots, rod-driven actuation has also been demonstrated [80, 91]. As a result, the relative merits of both forms of actuation were considered when analyzing the continuum robot's suitability as a robotic tail.

### Continuum Robot Modeling

Previous efforts to model continuum robot motion may be categorized into two approaches: low-fidelity lumped parameter models and high-fidelity distributed parameter models. The low-fidelity lumped parameter models assume that each actuated segment of the robot may be characterized by a single circular arc, whereas the high-fidelity distributed model represents the continuum robot with a spatial parameterized curve or a 3-D volume. Purely kinematic models have been derived for the lumped parameter models, static models have been derived for the distributed parameter models, and dynamic models have been derived for both.

The previously studied lumped-parameter models are characterized as low fidelity because they ignore the curvature variations along their actuated segments due to loading such as gravity, friction, or contact forces. Webster III and Jones [88] provide a detailed review

of constant-curvature kinematic methods for continuum robots that feature direct analytical calculation of continuum segment shape using actuation inputs for different actuation structures (e.g., cable or rod displacement, pneumatic bellow pressure). Prior research has also studied lumped parameter dynamic models. Tatlicioglu et al. [82] and Godage et al. [25] adapted the Euler-Lagrange equations by formulating a Lagrangian from the kinetic energy (due to continuum robot motion), potential energy (due to elasticity and gravity), and actuation effects for pneumatic [82] and hydraulic [25] continuum robots. When only considering elasticity and actuation and with special design considerations for the arm itself (e.g., optimal spacing between disks), this lumped-paramter approach is a valid assumption. However, in the presence of gravity, inertia and other external forces, the accuracy is reduced [34].

The previously studied distributed parameter models are characterized as high fidelity because they allow for an arbitrary shape of the continuum robot in response to the applied loading. Time-invariant static formulations have been studied extensively using a variety of analytical methods, including Cosserat rod theory [34, 62] and local minimization of an energy function [73]. In addition, dynamic models have been studied to also account for inertia. Rucker and Webster III [72] and Lang et al. [41] formulated dynamic Cosserat rod models, resulting in a set of coupled partial differential equations (PDEs) defining the dynamics. Gravagne et al. [26] utilized Hamilton's principle to formulate the dynamics as a set of PDEs for a cable-driven robot. Although these models are capable of capturing variations in curvature within a given segment, they lack a finite joint space intrinsically defined by the structure of the robot; instead, for numerical solutions of the dynamic PDEs, a mesh is used to sufficiently discretize the tail structure to capture the mass variations along its length.

The separation between these two approaches—low-fidelity lumped-parameter models versus high-fidelity distributed parameter models—motivated the high-fidelity, lumped parameter

continuum robot modeling approach in Chapter 4. Prior work in this area had been limited: Xu and Simaan [92] used a subsegment-based analysis for rod-driven continuum robot statics using constrained minimization. Jung et al. [35] utilized a lumped mass model for each disk and Newton's second law to formulate the dynamic equations of motion for a cable-driven continuum robot. Giri and Walker [24] utilized a similar mass-spring-damper model to simulate a pneumatic-muscle based continuum robot using Lagrangian mechanics.

### 2.2.2 Serpentine Robot Designs and Modeling

#### Serpentine Robot Designs

The field of serpentine robotics is dominated by system designs to implement snake-like locomotion [7, 48, 55, 90]. As a result, in comparison to the breadth of continuum manipulators, the range of hyperredundant serpentine manipulators is more limited.

One set of serpentine robotic manipulators is comprised of robots designed to be hung vertically [6, 19, 28]. Although suitable for pick-and-place operations, their mass is such that they would exhibit significant sag is operated in a cantilevered mode. Another set of serpentine robotic manipulators are long, slender structures designed primarily for decommissioning work inside nuclear reactors [30, 53]. Kim et al. [38] demonstrates a serpentine manipulator lacking conventional joints; instead, cabling is used to reconfigure a serial chain of links rotating with respect to one another on cylindrical surfaces.

Overall, the limited variety of serpentine tail designs motivates the study of new designs. However, these new designs are built on lessons demonstrated by these serpentine structures and their prior implementation.

#### Serpentine Robot Modeling

Likewise, much of the existing literature related to serpentine robot dynamics focuses on the modeling of snake-like locomotion, not manipulation. Furthermore, since serpentine robots are simply conventional robots with more links, conventional approaches for modeling the kinematics and dynamics of the structures may also be applied.

Chirikjian and Burdick [15] analyze a method for approximating the kinematics of a serpentine robot using Bessel functions and shaping the robot to the desired configuration represented by the continuous curve. Chirikjian [14] approximates the dynamics of a serpentine manipulator by representing it as a continuum body and analyzing the dynamics utilizing continuum mechanics conservation equations. Gallardo-Alvarado and Rico-Martínez [23] utilize screw theory to represent the kinematics of a serpentine robot comprised of a serial chain of parallel mechanisms. Hannan and Walker [28] formulate the velocity kinematics of their elephant trunk manipulator and utilizes these formulations to guide control synthesis. Lau et al. [42] formulates the inverse dynamics of a cable-driven serpentine manipulator.

### 2.2.3 Hyperredundant Manipulator Control

Similar to the fields of serpentine robot design and modeling, prior research focused on controllers for serpentine manipulators is limited compared to those focused on ground-supported snake-like robots and controllers designed to implement locomotion patterns. Furthermore, much of the prior work associated with continuum robot control focuses on cantilevered structures operating as manipulators. Therefore, despite this dissertation's control analysis focusing on serpentine robot control, this section considers the control of hyperredundant manipulators in general.

Hyperredundant robot controllers are primarily differentiated by whether or not they utilize

a model of the robot in the control formulation. Prior work into controllers that do not use a system model include PID-based approaches and neural-network based approaches. Examples of PID-based controllers include individual joint controllers [25] and a PD-controller acting based on segment curvatures [28]. Neural-network-based controllers utilize online tuning of the neural network during use of the robot, as either a standalone controller [44] or as a feedforward contribution to a controller that also employs a model-free nonlinear feedback loop [8]. This approach is particularly beneficial for continuum-type robots for which the robot's continuous deformation makes state modeling challenging.

Model-based approaches augment aspects of the model-free approaches (specifically, PID-based control terms) with additional considerations for the modeled kinematics and/or dynamics of the robot. Prior work has utilized the robots' Jacobians to map task-space sensor data into the joint-space in real time [2, 10, 16], dynamics-based controllers for vibration damping [26], and feedback-linearization-based impedance control [83].

# Chapter 3

# Problem Statement and Proposed Solution

The state of research into robotic tails as discussed in Chapter 2 demonstrated clear shortcomings in relation to implementing bioinspired articulated robots as robotic tails. This chapter defines the factors motivating this research (section 3.1), along with the research hypothesis addressed in this dissertation (section 3.2).

## 3.1 Research Motivation

In general, the key motivating factor for including a robotic tail (either pendulum or articulated) on-board a legged robot is the tail's ability to generate loading independent of the ground contact. During a gait cycle, the nature of contact between the robot and ground changes constantly, either by design, during to the planned gait cycle, or unexpectedly, due to irregular terrain or external disturbance. The legs require ground contact in order to generate the external loading needed to maneuver or stabilize the robot; tails are capable of

generating their loading regardless of ground contact.

An additional motivating factor for including a robotic tail is its ability to offset some of the required control functionalities in terms of maneuvering and stabilization from the legs to the tail. This could allow reduced complexity leg designs to meet or exceed the performance of their more complex counterparts. In particular, the ability to use planar leg mechanisms in high performance quadrupeds or bipeds is particularly appealing.

Beyond these general motivating factors for the inclusion of any type of tail, the motivating factors which led to the articulated serpentine tail designs presented in chapter 5 via the continuum robot designs considered in chapter 4 are also presented. Although an subset of several of these motivating factors initially led to the consideration of continuum robots as robotic tails, the experience analyzing the continuum robot designs and dynamics further refined and enhanced those factors, resulting in these here outlined.

The most fundamental requirement of the robotic tail is that it be multi-purpose. In order to justify the inclusion of such a structure on-board a mobile robot eventually envisioned for field deployment, a tail must be able to assist in multiple functionalities relating to maneuvering and stabilization. To best enable this, the tail should be capable of spatial motion, which will allow for loading to be generated to affect the pitch, yaw and roll dynamics of the legged robot.

Furthermore, the tail should be capable of generating significant dynamic loading during operation. Many of the hyperredundant robotic designs discussed in section 2.2 cannot achieve the high speed motions that will be necessary to generate sufficient inertial loading to aid in maneuvering or stabilization.

A robotic tail must also effectively cantilever when attached to a legged robot. A key shortcoming of continuum robots is the high stiffness required in the structure to resist

excessive sag when cantilevered. Existing macro-scale continuum robots use pneumatics or coil springs to form their structures, but pneumatics do not lend themselves to controlled highly dynamic motion, and coil spring structures have only been demonstrated in vertical hanging orientations. Furthermore, the uniform stiffness along existing solid-core continuum robots does not facilitate asymmetric elastic loading in the tail's vertical direction, in which gravity acts, and in the tail's horizontal direction, in which it does not. This motivating factor, along with the challenges of effectively sensing the continuum robot's shape, was a key reason for the shift from continuum robotic tails to serpentine robotic tails.

Minimizing the number of actuators along the tail is another key factor. Instead of individually actuating each joint along the tail, different forms of coupling should be used to resolve redundancy. For example, rigid kinematic coupling (such as gears) could be used to ensure fixed relationship between link rotations, or elastic mechanical coupling (such as springs) could be used to help distribute actuation along the tail. Depending on the nature of the coupling used, this minimum number may differ, but excess actuation should be avoided.

Finally, the robotic tail should be capable of forming multiple curvatures along its length, actuated at least quasi-independently, with actuation localized at the base. Single-segment robots are more limited in their COM workspace than multi-segment robots, and greater flexibility in moving the COM provides greater functionality. Localizing actuation at the base will allow for greater control over the tail dynamics by reducing the need to incorporate bulky actuators along the structure.

## 3.2 Research Hypothesis

The hypothesis driving this research is that articulated robotic tails can be used to effectively assist in the maneuvering and stabilization of legged robots. To test this hypothesis,

case studies are performed (chapter 8) to analyze the performance of controllers (chapter 7) designed to implement desired maneuvering and stabilization behaviors on two novel serpentine tail designs (chapter 5). In support of this analysis, dynamic models of the serpentine tail designs are formulated (chapter 6), along with dynamic models for the continuum robot designs initially envisioned for implementing the robotic tails (chapter 4).

# Chapter 4

# Continuum Robot Dynamics

Initially, continuum robotic structures were considered to implement the robotic tails. However, existing modeling approaches for continuum robot dynamics were either too low-fidelity to capture the continuous deformation along the robot or implemented using computationally inefficient distributed parameters, as highlighted in section 2.2.1. Therefore, as an initial step toward continuum tails, a novel method was studied to formulate the dynamic equations of motion for both cable-driven and rod-driven elastic core continuum robots in a manner capable of capturing curvature variations along the robot and defined by a finite set of state coordinates.

This chapter is organized as follows: Section 4.1 discusses the discretization of the continuum robot used to formulate the finite-state tail model capable of capturing the tail's continuous curvature deformation. Section 4.2 presents the cable-driven and rod-driven continuum robot designs that are modeled in this chapter. Section 4.3 formulates the continuum robot's equations of motion using the method of virtual power. Section 4.4 models the kinematics of the continuum robot, including generalized formulations for the disk orientations, linear positions and angular velocities and actuation-specific formulations for cable- and rod-driven

considerations. Section 4.5 calculates the loading effects contributing to the continuum robot dynamics, including inertia, gravity, coupling and actuation. Section 4.6 simulates cable-driven and rod-driven continuum tails and validates aspects of these simulations using experimental results and finite element analysis.

## 4.1 Continuum Robot Discretization and Modeling

Modeling continuum robot mechanics poses several challenges in comparison to conventional robots with discrete joints [84], including: (1) Joint Space Definition: there is no intrinsic discrete set of variables that composes the joint space—the arm's continuous nature leads to theoretically infinite degrees of freedom; (2) Importance of Elasticity: unlike many conventional robots in which it is considered as secondary effect, elasticity plays a key role in determining the continuum robot's shape; and (3) Actuation Localization: continuum robots typically localize actuation at the base of arm and transmit the actuation along the structure, and this actuation transmission to a distant segment will also load intermediate segments through which it is routed.

In this chapter, a novel high-fidelity, lumped parameter model for discretizing a continuum robot to formulate the continuum robot dynamics using the principle of virtual power is presented. Instead of modeling a continuum robot segment as a single circular arc, a serial chain of subsegment circular arcs defines the segment shape. A subsegment is defined as the length of continuum core separating two disks. This methodology provides a systematic way of discretizing the continuum robot into a set of state coordinates and is capable of incorporating actuation, friction, elastic, and gravitational loading effects. Xu and Simaan [92] previously used subsegment-based analysis for the statics of a rod-driven continuum robot. However, the governing equations needed to be solved using an optimization solver

and were not formulated in the standard dynamic form of coupled ordinary differential equations.

The primary benefit of the proposed high-fidelity lumped parameter subsegment model is the balance it achieves between previous low-fidelity lumped parameter and high-fidelity distributed parameter models. Like the lumped parameter models, the continuum robot shape is defined by a finite set of variables, instead of a parameterized spatial curve like the distributed parameter model. However, the proposed model can also capture variation in curvature along the robot's length, unlike previous lumped parameter models. In addition, unlike the distributed parameter models, the dynamic equations of motion using the subsegment modeling approach results in a set of coupled ordinary differential equations in time, instead of coupled partial differential equations in time and one-dimensional space. In addition, there are also benefits to the modeling approach that stem from the use of the method of virtual power. Unlike the Newton-Euler method, explicit internal force calculations are not needed at each disk, improving computational efficiency, and unlike the Euler-Lagrange method, direct numerical calculation of the loading effects present in the tail can be used, instead of requiring differentiable energy functions for each type of loading.

## 4.2 Continuum Robot Designs

Figure 4.1 illustrates the design schematics of the single-segment cable-driven continuum robot and multi-segment rod-driven continuum robots considered in this analysis. In terms of structure, a spring steel elastic core acts as the robot's backbone, along which are rigidly mounted eight disks. The cable-driven robot in Fig. 4.1a has three cables spaced at 120° intervals that route through holes at a fixed distance from the disk centers. These cables all terminate/tie off at disk 8, resulting in a single-segment structure. The rod-driven robot in

Fig. 4.1b has six rods spaced at 60° intervals at similar fixed distances from the disk centers. A two-segment continuum robot is created by rigidly attaching three of the rods to disk 4 and the other three rods to disk 8.

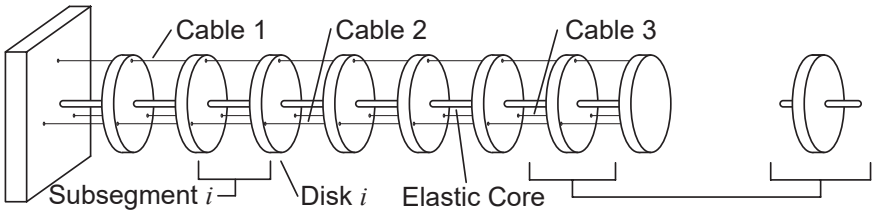


(a) Cable-driven continuum robotic structure

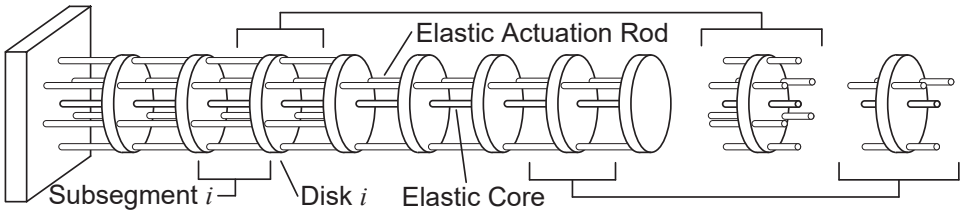


(b) Rod-driven continuum robotic structure

Figure 4.1: Continuum robotic structures under consideration with rigid-body discretizations illustrated.

These continuum robot structures lead to a natural choice for the robot's discretization into subsegments, for which each disk is modeled as a rigid body. The mass and inertia of each rigid body are determined by the mass and inertia of the disk, the elastic core surrounding the disk, and the actuation rods surrounding the disk, which is illustrated in Fig. 4.1 for the both actuation structures. The kinematic model assumes circular subsegment arcs separate each rigid body, and each subsegment's elastic and damping effects apply moments to the subsegment's two adjacent disks. Compressive and shear loads are neglected due to the relative incompressibility of the elastic core compared with its bending and twist. Furthermore, torsion is neglected in the rod-driven design analysis due to the actuating rods added resistance to twist.

## 4.3 Continuum Robot Equations of Motion

The method of virtual power, also called Kane's method, uses variational calculus to calculate the dynamics of a system by minimizing the virtual power of the external forces and moments applied to the system [63]. It has been previously applied to both rigid-link [27, 95] and flexible [20] robotic systems. This scalar virtual power $P$ is found by adding the dot products of each rigid body $i$'s net moment $\mathbf{M}_{i,bdy}$ and force $\mathbf{F}_{i,bdy}$ with the associated rigid body $i$ angular velocity $\boldsymbol{\omega}_i$ and rigid body $i$ COM linear velocity $\mathbf{v}_i$, as shown in Eq. 4.1 for the 8 rigid-bodies comprising the modeled system. To take the variation of this equation, a set of state coordinates $\mathbf{q} \in \mathbb{R}^n$ and their derivatives $\dot{\mathbf{q}} \in \mathbb{R}^n$ are used to define the system's dynamic configuration, where $n$ is the number of state coordinates ($n = 24$ for the cable-driven structure, $n = 16$ for the rod-driven structure).

$$P = \sum_{i=1}^{8} (\mathbf{M}_{i,bdy} \cdot \boldsymbol{\omega}_i + \mathbf{F}_{i,bdy} \cdot \mathbf{v}_i) \tag{4.1}$$

The velocities $\boldsymbol{\omega}_i$ and $\mathbf{v}_i$ of each rigid body $i$ may be defined with respect to $\dot{\mathbf{q}}$ using the rigid body $i$ angular velocity Jacobian $\mathbf{J}_{\boldsymbol{\omega},i}$ and rigid body $i$ linear velocity Jacobian $\mathbf{J}_{\mathbf{p},i}$, as shown in Eq. 4.2. Using this velocity formulation, the virtual power variation $\Delta P$ may be found using Eq. 4.3. To minimize the virtual power, set $\Delta P = 0$. To enforce this condition for any arbitrary state velocity variation $\Delta\dot{\mathbf{q}}$, Eq. 4.4 is formulated for each column $\{1, \cdots, n\}$ of $\mathbf{J}_{\boldsymbol{\omega},i}$ and $\mathbf{J}_{\mathbf{p},i}$, which defines an equation of motion for each coordinate of $\mathbf{q}$.

$$\boldsymbol{\omega}_i = \mathbf{J}_{\boldsymbol{\omega},i}\dot{\mathbf{q}}, \quad \mathbf{v}_i = \mathbf{J}_{\mathbf{p},i}\dot{\mathbf{q}} \tag{4.2}$$

$$\Delta P = \left( \left[ \sum_{i=1}^{8} \left( \mathbf{M}_{i,bdy} \cdot \mathbf{J}_{\boldsymbol{\omega},i} + \mathbf{F}_{i,bdy} \cdot \mathbf{J}_{\mathbf{p},i} \right) \right] \Delta \dot{\mathbf{q}} \right) \tag{4.3}$$

$$\sum_{i=1}^{8} \left( \mathbf{M}_{i,bdy} \cdot \left( \mathbf{J}_{\boldsymbol{\omega},i} \right)_{\{1,\cdots,n\}} + \mathbf{F}_{i,bdy} \cdot \left( \mathbf{J}_{\mathbf{p},i} \right)_{\{1,\cdots,n\}} \right) = 0 \tag{4.4}$$

The net moments $\mathbf{M}_{i,bdy}$ and forces $\mathbf{F}_{i,bdy}$ are composed of two types of effects: inertial and active. Inertial effects are due to the rigid bodies' resistance to changes in acceleration. Active effects are due to both external loading (such as actuation, gravity, or contact forces) and internal coupling effects (such as elasticity and damping). Furthermore, $\mathbf{M}_{i,bdy}$ and $\mathbf{F}_{i,bdy}$ are based on loading applied at each rigid body's COM; if a force is applied on a rigid body at a point other than its COM, an equivalent force and moment at the center of mass is calculated.

## 4.4 Continuum Robot Kinematic Model

As discussed in section 4.3, a set of state coordinates and their velocities are needed to define the dynamic configuration of the system. Based on the subsegment discretization in section 4.2, either two or three scalar coordinates are used to describe the relative configuration for subsegment $i$ between disks $i-1$ and $i$, depending on the system's actuation transmission mechanism. For both cable-driven and rod-driven structures, two orthogonal subsegment curvatures $\beta_i$ and $\gamma_i$ are defined for the pitch ($\beta_i$) and yaw ($\gamma_i$) components of the net curvature, and for cable-driven structures, the subsegment roll twist angle $\epsilon_i$ is also defined (in the subsequent analysis, for rod-driven structures, $\epsilon_i \equiv 0$). These parameters are illustrated in Fig. 4.2a for subsegment $i$ between disks $i-1$ and $i$. These $n = 24$ (cable-driven) or $n = 16$ (rod-driven) coordinates are collected into the state vector $\mathbf{q}$, as shown in Eq. 4.5.

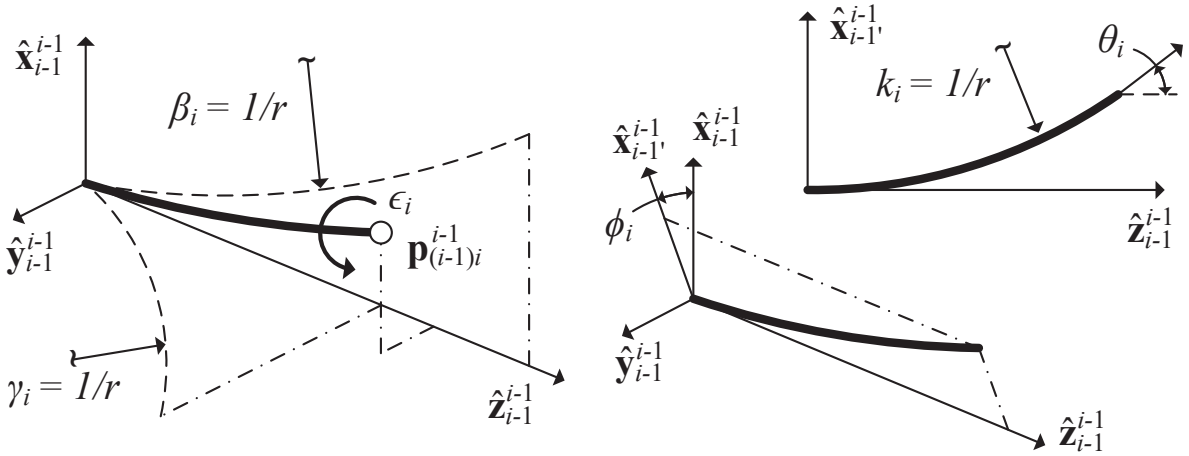


(a) Continuum robot state coordinates (b) Continuum robot additional coordinates

Figure 4.2: Continuum robotic coordinates.

$$\mathbf{q} = \begin{cases} [\beta_1, \ \gamma_1, \ \epsilon_1, \ \beta_2, \ \gamma_2, \ \epsilon_2, \ \cdots, \ \beta_n, \ \gamma_n, \ \epsilon_n]^T, & \text{Cable-Actuated} \\ [\beta_1, \ \gamma_1, \ \beta_2, \ \gamma_2, \ \cdots, \ \beta_n, \ \gamma_n]^T, & \text{Rod-Actuated} \end{cases} \tag{4.5}$$

To simplify the analysis, three intermediate variables are defined in Eq. 4.6: the subsegment curvature magnitude $k_i$; the bending plane angle $\phi_i$; and the subsegment bending angle $\theta_i$, where $L_0$ is the subsegment length. An illustration of these parameters is shown in Fig. 4.2b. Each disk has a local coordinate system coincident with its center of mass. For disk $i$, the disk-fixed coordinate system is $\hat{\mathbf{x}}_i$, $\hat{\mathbf{y}}_i$, $\hat{\mathbf{z}}_i$. The inertial base frame of the continuum robots is represented by $\hat{\mathbf{x}}_0$, $\hat{\mathbf{y}}_0$, $\hat{\mathbf{z}}_0$. A superscript other than $T$ denotes the frame in which a vector or matrix is defined; if a superscript is omitted, that vector or matrix is defined with respect to the inertial base frame.

$$k_i = \sqrt{\beta_i^2 + \gamma_i^2}, \quad \phi_i = \operatorname{atan2}(\gamma_i, \beta_i), \quad \theta_i = k_i L_0 \tag{4.6}$$

Based on geometric analysis [88], the position vector $\mathbf{p}_{(i-1)i}^{i-1}$ from the frame $i-1$ origin to

the disk $i$ COM is defined in Eq. 4.7. For this and other expressions, special consideration must be made for cases in which $k_i = 0$. Analytically, the expressions all become zero divided by zero. However, as the limit of $k_i$ approaches 0, the coordinates asymptotically approach $\mathbf{p}^{i-1}_{(i-1)i} = [0,\ 0,\ L_0]^T$ . In numerical solvers, this singularity (and others throughout the analysis) are avoided by substituting the asymptotic values when $k_i \approx 0$. In addition, based on this lumped parameter modeling approach, the torsion does not contribute to the subsegment's position vector. Instead, it is incorporated as a rotation between rigid bodies.

$$\mathbf{p}^{i-1}_{(i-1)i} = \left[\frac{\cos\phi_i\,(1-\cos\theta_i)}{k_i},\quad \frac{\sin\phi_i\,(1-\cos\theta_i)}{k_i},\quad \frac{\sin\theta_i}{k_i}\right]^T \tag{4.7}$$

Three sequential rotations are used to formulate the relative orientation $\mathbf{R}^{i-1}_{(i-1)i}$ between rigid bodies $i-1$ and $i$: (1) a rotation by $\phi_i$ about the z-axis, (2) followed by a rotation by $\theta_i$ about the y-axis, (3) followed by a rotation of $\epsilon_i - \phi_i$ about the z-axis, as defined in Eq. 4.8, where $\mathbf{R}_Z(\cdot)$ and $\mathbf{R}_Y(\cdot)$ represent rotation matrices for z-axis and y-axis rotations, respectively, of angle $(\cdot)$. The $-\phi_i$ term in the third rotation ensures the frame is not subjected to a "torsional" rotation along the subsegment due to the first rotation [88].

$$\mathbf{R}^{i-1}_{(i-1)i} = \mathbf{R}_Z(\phi_i)\,\mathbf{R}_Y(\theta_i)\,\mathbf{R}_Z(\epsilon_i - \phi_i) \tag{4.8}$$

The relative angular velocity $\boldsymbol{\omega}^{i-1}_{(i-1)i}$ between rigid bodies $i-1$ and $i$ is defined based on the motion of the z-axis unit vector $\hat{\mathbf{z}}^{i-1}_{(i-1)i}$ of the rotation matrix $\mathbf{R}^{i-1}_{(i-1)i}$, along with the subsegment $i$ twist velocity $\dot{\epsilon}_i$. The derivatives $\dot{\hat{\mathbf{z}}}^{i-1}_{(i-1)i}$ and $\dot{\epsilon}_i$ can be related to $\boldsymbol{\omega}^{i-1}_{(i-1)i}$ using Eqs. 4.9 and 4.10, and the definition of the vector triple product in Eq. 4.11 may be used in conjunction with these expressions to formulate $\boldsymbol{\omega}^{i-1}_{(i-1)i}$ in Eq. 4.12.

$$\dot{\hat{\mathbf{z}}}^{i-1}_{(i-1)i} = \boldsymbol{\omega}^{i-1}_{(i-1)i} \times \hat{\mathbf{z}}^{i-1}_{(i-1)i} \tag{4.9}$$

$$\dot{\epsilon}_i = \boldsymbol{\omega}^{i-1}_{(i-1)i} \cdot \hat{\mathbf{z}}^{i-1}_{(i-1)i} \tag{4.10}$$

$$\hat{\mathbf{z}}^{i-1}_{(i-1)i} \times \left(\boldsymbol{\omega}^{i-1}_{(i-1)i} \times \hat{\mathbf{z}}^{i-1}_{(i-1)i}\right) = \left(\hat{\mathbf{z}}^{i-1}_{(i-1)i} \cdot \hat{\mathbf{z}}^{i-1}_{(i-1)i}\right) \boldsymbol{\omega}^{i-1}_{(i-1)i} - \left(\hat{\mathbf{z}}^{i-1}_{(i-1)i} \cdot \boldsymbol{\omega}^{i-1}_{(i-1)i}\right) \hat{\mathbf{z}}^{i-1}_{(i-1)i} \tag{4.11}$$

$$\boldsymbol{\omega}^{i-1}_{(i-1)i} = \hat{\mathbf{z}}^{i-1}_{(i-1)i} \times \dot{\hat{\mathbf{z}}}^{i-1}_{(i-1)i} + \dot{\epsilon}_i \hat{\mathbf{z}}^{i-1}_{(i-1)i} \tag{4.12}$$

Rotation matrices $\mathbf{R}_i$ for each disk's orientation may be found recursively using Eq. 4.13, where $\mathbf{E}_3$ is the 3-by-3 identity matrix. With these, the disk $i$ center/COM position $\mathbf{p}_i$ and angular velocity $\boldsymbol{\omega}_i$ may be defined with respect to the inertial base frame in Eqs. 4.14 and 4.15.

$$\mathbf{R}_i = \begin{cases} \mathbf{E}_3, & i = 0, \\ \mathbf{R}_{i-1}\mathbf{R}^{i-1}_{(i-1)i}, & i > 0 \end{cases} \tag{4.13}$$

$$\mathbf{p}_i = \begin{cases} \mathbf{p}^{i-1}_{(i-1)i}, & i = 1 \\ \mathbf{p}_{i-1} + \mathbf{R}_{i-1}\mathbf{p}^{i-1}_{(i-1)i} & i > 1 \end{cases} \tag{4.14}$$

$$\boldsymbol{\omega}_i = \begin{cases} \boldsymbol{\omega}^{i-1}_{(i-1)i}, & i = 1 \\ \boldsymbol{\omega}_{i-1} + \mathbf{R}_{i-1}\boldsymbol{\omega}^{i-1}_{(i-1)i} & i > 1 \end{cases} \tag{4.15}$$

To aid in the formulation of the derivatives of Eqs. 4.14 and 4.15, Eq. 4.16 may be used to reformulate the derivative of a rotation matrix in terms of its angular velocity and the rotation matrix itself.

$$\dot{\mathbf{R}}_i = \boldsymbol{\omega}_i \times \mathbf{R}_i \tag{4.16}$$

In addition to these general kinematic analyses applicable to both cable-driven and rod-driven robots, actuation-specific kinematic analyses are needed to support the calculation of the external loading terms in section 4.5.

### 4.4.1 Cable-Specific Kinematic Calculations

For the single-segment, cable-driven continuum robot, Eq. 4.17 defines the disk-frame fixed positions $\mathbf{r}^i_{i,k,cbl}$ of the disk $i$ cable $k \in \{1,2,3\}$ routing holes, where $r_{hl}$ is the radial distance of the hole from the disk center and $\alpha_k$ is the angle from $\hat{\mathbf{x}}^i_i$ to $\mathbf{r}^i_{i,k,cbl}$ about $\hat{\mathbf{z}}^i_i$. With this, the position vector $\mathbf{p}_{(i-1)i,k,cbl}$ of the cable $k$ subsegment from disk $i-1$ to disk $i$ is defined.

$$\mathbf{r}^i_{i,k,cbl} = r_{hl} \begin{bmatrix} \cos\alpha_k \\ \sin\alpha_k \\ 0 \end{bmatrix}, \quad \alpha_k = 120^\circ\,(k-1) \tag{4.17}$$

$$\mathbf{p}_{(i-1)i,k,cbl} = \mathbf{R}_{i-1}\left(-\mathbf{r}^{i-1}_{i-1,k,cbl} + \mathbf{p}^{i-1}_{(i-1)i}\right) + \mathbf{R}_i \mathbf{r}^i_{i,k,cbl} \tag{4.18}$$

In addition to the cable positions, the sliding velocity between cable $k$ and its disk $i$ routing hole is also needed. In order to determine this, the rate of change of each cable's subsegment lengths will be calculated. For cable $k$ in subsegment $i$, $L_{i,k,cbl,ss}$ is the subsegment cable

length, defined in Eq. 4.19. Its derivative $\dot{L}_{i,k,cbl,ss}$, defined in Eq. 4.20, can be used to recursively calculate the cable's sliding velocity $\dot{d}_{i,k,cbl}$ with respect to disk $i$. Because each cable is tied to disk $i = 8$, by definition there is zero sliding velocity at this disk. For the disks $i < 8$, the sliding velocity is the sum of the disk $i+1$ cable $k$ sliding velocity $\dot{d}_{i+1,k,cbl}$ and the cable $k$ subsegment $i+1$ length rate of change $\dot{L}_{i+1,k,cbl,ss}$. These two definitions are shown recursively in Eq. 4.21.

$$L^2_{i,k,cbl,ss} = \mathbf{p}_{(i-1)i,k,cbl} \cdot \mathbf{p}_{(i-1)i,k,cbl} \tag{4.19}$$

$$\dot{L}_{i,k,cbl,ss} = \frac{\mathbf{p}_{(i-1)i,k,cbl} \cdot \dot{\mathbf{p}}_{(i-1)i,k,cbl}}{L_{i,k,cbl,ss}} \tag{4.20}$$

$$\dot{d}_{i,k,cbl} = \begin{cases} 0, & i = 8 \\ \dot{d}_{i+1,k,cbl} + \dot{L}_{i+1,k,cbl,ss}, & i < 8 \end{cases} \tag{4.21}$$

### 4.4.2 Rod-Specific Kinematic Calculations

For the two-segment, rod-driven continuum robot, Eq. 4.22 defines the disk-frame fixed positions $\mathbf{r}^i_{i,k,rod}$ of the rod $k \in \{1, \ldots, 6\}$ routing holes, where $r_{hl}$ is the distance from the disk center to the routing hole and $\alpha_k$ is the angle from $\hat{\mathbf{x}}^i_i$ to $\mathbf{r}^i_{i,k,rod}$ about $\hat{\mathbf{z}}^i_i$.

$$\mathbf{r}^i_{i,k,rod} = r_{hl} \begin{bmatrix} \cos\alpha_k \\ \sin\alpha_k \\ 0 \end{bmatrix}, \quad \alpha_k = \begin{cases} 120^\circ\,(k-1)\,, & k \in \{1,2,3\} \\ 120^\circ\,(k-4) + 60^\circ, & k \in \{4,5,6\} \end{cases} \tag{4.22}$$

Using these hole position vectors, a mathematical formulation for the rod $k$ subsegment $i$ curvature $k_{i,k}$ can be determined. Each subsegment's actuation rods (six in segment 1, three in segment 2) are assumed to bend as circular arcs in planes parallel to the core subsegment

bending plane defined by $\phi_i$. The curvature $k_{i,k}$ is calculated from $k_i$, $\phi_i$ and $\mathbf{r}^{i-1}_{i-1,k,rod}$ by assuming the actuation rods' circular arcs are concentric with the core's circular arc, since the subsegment $i$ core and rods are assumed to be orthogonal to the surfaces of subsegment's adjacent disks $i-1$ and $i$. The intersection of the two disk planes defines the locus of points on which the centers of these circular arcs lie. The rod curvatures are found by determining the radius of curvature offset $\delta_{i,k}$ of rod $k$ subsegment $i$ relative to the core's radius of curvature $1/k_i$ using Eq. 4.23. Figure 4.3 illustrates the hole position vectors and offsets for a three-rod subsegment, with hole positions defined by Eq. 4.22 for $k \in \{1,2,3\}$. This offset $\delta_{i,k}$ may then be added to the core's radius of curvature $1/k_i$ to determine the rod's radius of curvature $1/k_{i,k}$. This expression is solved for $k_{i,k}$ in Eq. 4.24

$$\delta_{i,k} = \begin{bmatrix} \cos\phi_i \\ \sin\phi_i \\ 0 \end{bmatrix} \cdot \mathbf{r}^{i-1}_{i-1,k,rod} \tag{4.23}$$

$$k_{i,k} = \frac{k_i}{1 - k_i\delta_{i,k}} \tag{4.24}$$

The unit vector $\hat{\mathbf{F}}_{i,k,rod,con}$ of the rod $k$ contact force acting on disk $i$ is calculated from the bending plane angle of subsegment $i+1$, defined in Eq. 4.25. The position vector $\mathbf{p}_{i,k,rod}$ from the rod $k$ base to its disk $i$ routing hole is defined using Eq. 4.26.

$$\hat{\mathbf{F}}_{i,k,rod,con} = \mathbf{R}_i \begin{bmatrix} \cos\phi_{i+1} \\ \sin\phi_{i+1} \\ 0 \end{bmatrix} \tag{4.25}$$

$$\mathbf{p}_{i,k,rod} = -\mathbf{r}_{0,k,rod} + \mathbf{p}_i + \mathbf{R}_i\mathbf{r}^i_{i,k,rod} \tag{4.26}$$

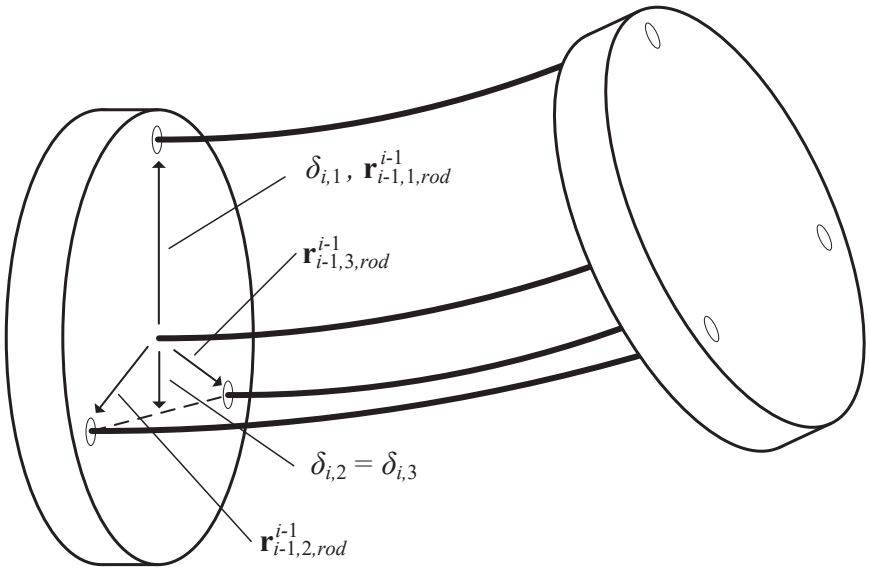


Figure 4.3: Curvature radius offsets when $\phi = 0$.

The sliding velocity $\dot{d}_{i,k,rod}$ between rod $k$ and disk $i$ is also calculable from the robot kinematics. The length $L_{i,k,rod,ss}$ of the rod $k$ subsegment $i$ and its derivative $\dot{L}_{i,k,rod,ss}$ are calculated using Eq. 4.27. The sum of these rod $k$ subsegment velocities from a chosen disk $i$ to the rod's termination disk $N_k$ results in $\dot{d}_{i,k,rod}$, defined recursively in Eq. 4.28.

$$L_{i,k,rod,ss} = \frac{k_i L_0}{k_{i,k}}, \quad \dot{L}_{i,k,rod,ss} = \frac{L_0\left(k_{i,k}\dot{k}_i - k_i\dot{k}_{i,k}\right)}{k_{i,k}^2} \tag{4.27}$$

$$\dot{d}_{i,k,rod} = \begin{cases} 0, & i \geq N_k \\ \dot{L}_{i+1,k,rod,ss} + \dot{d}_{i+1,k,rod}, & i < N_k \end{cases} \tag{4.28}$$

## 4.5 Continuum Robot Loading Model

Four sources of loading contribute to the cable-driven and rod-driven structures' loading $\mathbf{F}_{i,bdy}$ and $\mathbf{M}_{i,bdy}$, as defined in Eq. 4.29: inertial loading ($\mathbf{F}_{i,inr}$ and $\mathbf{M}_{i,inr}$), actuation

loading ($\mathbf{F}_{i,act}$ and $\mathbf{M}_{i,act}$), gravitational loading ($\mathbf{F}_{i,grv}$) and coupling loading ($\mathbf{M}_{i,cpl}$).

$$\mathbf{F}_{i,bdy} = \mathbf{F}_{i,inr} + \mathbf{F}_{i,grv} + \mathbf{F}_{i,act}, \tag{4.29}$$

$$\mathbf{M}_{i,bdy} = \mathbf{M}_{i,inr} + \mathbf{M}_{i,cpl} + \mathbf{M}_{i,act} \tag{4.30}$$

The gravitational loading only consists of a force term since gravity acts at the COM of each tail rigid body. The coupling loading only consists of a moment term since compressive and shear effects are neglected in the presence of the dominant bending effects in both models and torsional effects in the cable-driven model.

### 4.5.1 Inertial Loading

Equations 4.31 and 4.32, define the rigid body $i$ inertial force $\mathbf{F}_{i,inr}$ and moment $\mathbf{M}_{i,inr}$, where $m_{i,bdy}$ is the rigid body $i$ mass and $\mathbf{I}_{i,bdy}$ is the rigid body $i$ moment of inertia. $\mathbf{I}_{i,bdy}$ depends on both the disk orientation and the body-frame fixed radial $I^i_{i,bdy,xx}$ and axial $I^i_{i,bdy,zz}$ moments of inertia, defined in Eq. 4.33.

$$\mathbf{F}_{i,inr} = -m_{i,bdy}\ddot{\mathbf{p}}_i \tag{4.31}$$

$$\mathbf{M}_{i,inr} = -\mathbf{I}_{i,bdy}\dot{\boldsymbol{\omega}}_i - \boldsymbol{\omega}_i \times \mathbf{I}_{i,bdy}\boldsymbol{\omega}_i \tag{4.32}$$

$$\mathbf{I}_{i,bdy} = \mathbf{R}_i \begin{bmatrix} I^i_{i,bdy,xx} & 0 & 0 \\ 0 & I^i_{i,bdy,xx} & 0 \\ 0 & 0 & I^i_{i,bdy,zz} \end{bmatrix} \mathbf{R}_i^T \tag{4.33}$$

### 4.5.2 Gravitational Loading

Gravitational loading accounts for the body forces on the robot due to gravity. The force on each disk $\mathbf{F}_{i,grv}$, defined in 4.34, is applied at each disk's COM, where $g$ is gravitational acceleration.

$$\mathbf{F}_{i,grv} = -m_{i,bdy} g \hat{\mathbf{x}}_0 \tag{4.34}$$

### 4.5.3 Coupling Loading

Coupling loading accounts for the elastic and damping effects between pairs of adjacent rigid bodies. In this analysis, the coupling effects considered include bending and torsional forms of elasticity and damping.

Equation 4.35 defines the disk $i$ coupling moment $\mathbf{M}_{i,cpl}$ based on its adjacent subsegments $i$ and $i+1$ (for the terminal disk $i = 8$, there is no subsegment $i+1 = 9$), where $\mathbf{M}_{i,\{i,i+1\},bnd}$, $\mathbf{M}_{i,\{i,i+1\},tor}$, and $\mathbf{M}_{i,\{i,i+1\},dmp}$ are the elastic bending, elastic torsion and damping moments, respectively, at disk $i$ from subsegment $\{i, i+1\}$. Intermediate disks $i < 8$ are loaded with the difference of the two adjacent subsegments' bending/torsion/damping moments, while the terminal disk $i = 8$ is loaded with the final subsegment's bending/torsion/damping moments. This formulation also ensures that a given subsegment applies equal and opposite loading at its two ends; a requirement for internal loading.

$$\mathbf{M}_{i,cpl} = \begin{cases} \begin{pmatrix} \mathbf{M}_{i,i+1,bnd} + \mathbf{M}_{i,i+1,tor} + \mathbf{M}_{i,i+1,dmp} \\ -\mathbf{M}_{i,i,bnd} - \mathbf{M}_{i,i,tor} - \mathbf{M}_{i,i,dmp} \end{pmatrix} & i < 8 \\ -\mathbf{M}_{i,i,bnd} - \mathbf{M}_{i,i,tor} - \mathbf{M}_{i,i,dmp} & i = 8 \end{cases} \tag{4.35}$$

### Elastic Bending Loading

Bending a continuum tail's subsegment generates an elastic moment on the disks adjacent to that subsegment in opposition to that bending. For both cable-driven and rod-driven structures, the tail's continuum core contributes to that bending elasticity, but in rod-driven structures, the rods' elasticity also contributes. Equation 4.36 provides a general formulation for the subsegment $\{i, i+1\}$ bending moment $\mathbf{M}_{i,\{i,i+1\},bnd}$ acting on disk $i$, with its magnitude $M_{\{i,i+1\},bnd,\{cbl,rod\}}$ uniquely defined for the cable-actuated and rod-actuated structures, and its direction defined as normal to the bending plane.

$$\mathbf{M}_{i,\{i,i+1\},bnd} = M_{\{i,i+1\},bnd,\{cbl,rod\}} \mathbf{R}_{i-1} \begin{bmatrix} -\sin\phi_{\{i,i+1\}} \\ \cos\phi_{\{i,i+1\}} \\ 0 \end{bmatrix} \tag{4.36}$$

For the cable-actuated structure, the only source of bending elasticity is the continuum core. Assuming a linear elastic model, the core's subsegment $i$ bending moment magnitude $M_{i,bnd,core}$ may be defined using Eq. 4.37, where $E_{core}$ and $J_{xx,core}$ are the continuum core's Young's modulus and cross-section second moment of area, respectively. The cable-actuated robot's subsegment bending magnitude $M_{i,bnd,cbl}$ may then be defined using Eq. 4.38.

$$M_{i,bnd,core} = E_{core} J_{xx,core} k_i \tag{4.37}$$

$$M_{i,bnd,cbl} = M_{i,bnd,core} \tag{4.38}$$

For the rod-actuated structure, in addition to the core's bending elasticity, the actuating rods also resist bending. The rod $k$ subsegment $i$ bending moment magnitude $M_{i,k,bnd,rod}$ is defined in Eq. 4.39, where $E_{rod}$ and $J_{xx,rod}$ are the actuation rods' Young's modulus and cross-section second moment of area, respectively, and $k_{i,k}$ is defined in Eq. 4.24. The rod-actuated robot's subsegment bending magnitude $M_{i,bnd,rod}$ may then be defined using Eq. 4.40.

$$M_{i,k,bnd,rod} = E_{rod} J_{xx,rod} k_{i,k} \tag{4.39}$$

$$M_{i,bnd,rod} = M_{i,bnd,core} + \sum_{k=1}^{6} M_{i,k,bnd,rod} \tag{4.40}$$

**Elastic Torsional Loading**

In addition to bending elasticity, torsional elasticity due to the subsegment $\{i, i+1\}$ roll twist angle $\epsilon_{\{i,i+1\}}$ will also contribute to the disk $i$ coupling loading in the cable-driven structure. The subsegment $\{i, i+1\}$ torsional moment $\mathbf{M}_{i,\{i,i+1\},tor}$ acting on rigid body $i$ is defined in Eq. 4.41, where $G_{core}$ and $J_{zz,core}$ are the continuum core's shear modulus and cross-section polar moment of area, respectively.

$$\mathbf{M}_{i,\{i,i+1\},tor} = \frac{G_{core} J_{zz,core}}{L_0} \epsilon_{\{i,i+1\}} \hat{\mathbf{z}}_i \tag{4.41}$$

The rod-driven structure neglects twist along its length (i.e., $\epsilon_i \equiv 0$), and by extension, its torsional elasticity, due to the presence of the actuation rods. Unlike the cable-driven structure supported solely by its single elastic core along its length, the actuation rods at their fixed distances $r_{hl}$ from the disk centers resist subsegment twist.

#### Damping Loading

In addition to the elastic loading, the continuum core and actuation rods also introduce minor damping effects. Inclusion of these effects is critical in simulation to prevent unrealistic marginally stable behaviors. A formulation for $\mathbf{M}_{i,\{i,i+1\},dmp}$ is defined in Eq. 4.42, similar to the elasticity formulations for Eqs. 4.36 and 4.41, where $c_{bnd}$ and $c_{tor}$ are the damping coefficients for bending and twisting, respectively.

$$\mathbf{M}_{i,\{i,i+1\},dmp} = c_{bnd}\dot{k}_{\{i,i+1\}}\mathbf{R}_{i-1}\begin{bmatrix} -\sin\phi_{\{i,i+1\}} \\ \cos\phi_{\{i,i+1\}} \\ 0 \end{bmatrix} + c_{tor}\dot{\epsilon}_{\{i,i+1\}}\hat{\mathbf{z}}_i \tag{4.42}$$

### 4.5.4 Actuation Loading

Actuation loading accounts for the force and moment on each disk due to the tensions of the actuation cables (cable-driven structure) or the axial force of the actuation rods (rod-driven structure), along with the friction generated by these actuation transmission elements' contact with the disks. For the virtual power model formulation, the resulting forces at the disks' cable or rod routing holes are reformulated as a net force and moment acting at the disk COM.

### Cable-Driven Actuation Loading

When considering cable-actuated robots, it is important to ensure that the model does not allow for compressive forces in the actuation cabling. In this model, the tensions of the actuation cables at the base are inputs to the model. By always prescribing these inputs to be positive, the cabling cannot apply a compressive force.

A geometric analysis is used to determine the loading on each disk; Fig. 4.4 shows the cable routing between three disks. Because the cables follow a linear path between holes, the cable routing is formulated using the unit vectors associated with the position vectors $\mathbf{p}_{(i-1)i,k,cbl}$ of the cable $k$ subsegment from disk $i-1$ to $i$ (Eq. 4.18), as shown in Fig. 4.4.

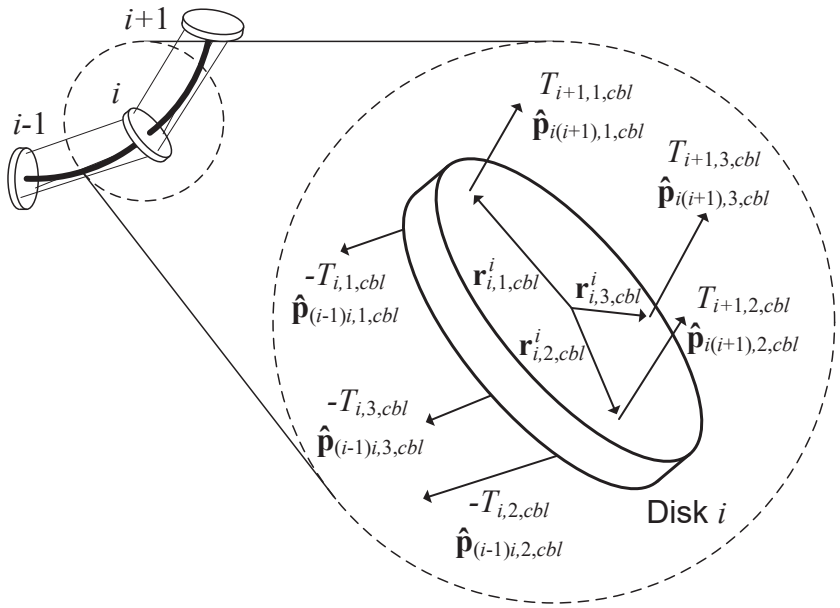


Figure 4.4: Actuation cable loading.

The coupling of the cable tension along the continuum robot and the frictional forces at each disk complicates the analysis. In order to compute the friction at each disk, the tension of the cable before and after the disk is needed. However, in order to compute the cable tensions before and after the disk, the magnitude of the frictional force is needed. Therefore,

an iterative approach is required. The initial assumption will be that tension is constant along the continuum robot. Based on this assumption, the contact friction will be estimated for each cable at each disk. This contact friction estimate will then be used to update the cable tensions in each subsegment along the length of the continuum robot. These updated tensions will then be used to update the friction estimate. Section 4.6.1 will include the analysis on the convergence of the resulting subsegment cable tensions based on the number of iterations of this process and will determine the optimal number to balance the need for an accurate computation with the need to reduce the computational load of the model.

In this analysis, the conventional discontinuous stick-slip friction model will be replaced by a continuous saturated viscous friction model. This enables the model to accurately represent the dynamic sliding friction when the cable sliding velocity is not near zero, while ensuring a continuous force profile when the sliding direction changes. This approach does not allow for a greater static friction than dynamic sliding frictional force, as is normally observed in mechanical systems, but significantly simplifies the dynamic analysis in this study.

Due to the wrap of the cabling around the cable routing holes, as illustrated in Fig. 4.5a, a belt friction model is used in this analysis. Fig. 4.5b shows an illustration of the key model parameters, and Eq. 4.43 analytically defines the model, where $\mu$ is the coefficient of saturated viscous friction and $\psi_{i,k}$ is the cable $k$ contact angle with the disk $i$. Using Eq. 4.43, the friction magnitude $F_{i,k,cbl,fr}$ acting at the the cable $k$ routing hole at disk $i$ is defined in Eq. 4.44. This magnitude is the difference in the left and right tensions $T_{i,k,cbl}$ and $T_{i+1,k,cbl}$ . A key benefit of this approach is that it allows the solver to estimate the frictional force magnitude with estimates for the left and right tensions. For example, in the initial case, the left and right tensions are assumed to be equal, and the difference of these tensions is identically zero. However, Eq. 4.44 estimates the frictional force based on the sum of these two tensions.

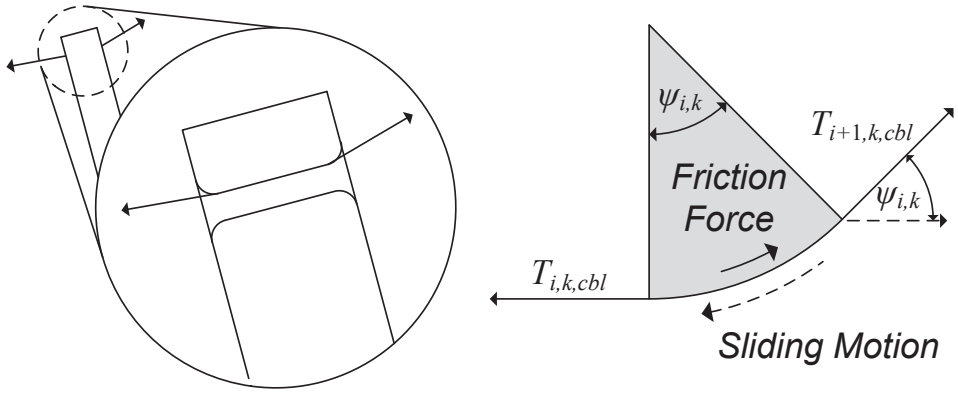


(a) Cut-away view of contact between cable and disk

(b) Belt friction model for cable-disk contact

Figure 4.5: Cable-driven continuum robot cable friction model.

$$\frac{T_{i,k,cbl}}{T_{i+1,k,cbl}} = e^{\mu\psi_{i,k}}, \quad \psi_{i,k} = \cos^{-1}\left(\hat{\mathbf{p}}_{(i-1)i,k,cbl} \cdot \hat{\mathbf{p}}_{i(i+1),k,cbl}\right) \tag{4.43}$$

$$F_{i,k,cbl,fr} = \left(T_{i,k,cbl} + T_{i+1,k,cbl}\right) \frac{e^{\mu\psi_{i,k}} - 1}{e^{\mu\psi_{i,k}} + 1} \tag{4.44}$$

With this estimate of $F_{i,k,cbl,fr}$ and the cable $k$, disk $i$ relative sliding velocities $\dot{d}_{i,k,cbl}$ from Eq. 4.21, the cable tensions in each cable subsegment may be calculated using Eq. 4.45, where sat $(\cdot)$ is the unit saturation function and $\dot{d}_{sat}$ is a constant use to define the continuous transition of friction over zero. Beginning from the tension $T_{k,cbl,base}$ applied at the continuum robot base for each cable $k$, the calculated friction magnitude is subtracted from this tension at each disk until the terminal disk $i = 8$. Because the cabling is rigidly attached to disk $i = 8$, there is no contact friction present at that disk.

$$T_{i,k,cbl} = \begin{cases} T_{k,cbl,base}, & i = 1 \\ T_{i-1,k,cbl} - \text{sat}\left(\frac{\dot{d}_{i,k,cbl}}{\dot{d}_{sat}}\right) F_{i,k,cbl,fr}, & i > 1 \end{cases} \tag{4.45}$$

With these updated values of $T_{i,k,cbl}$, Eq. 4.44 can be used to calculate more accurate estimates of the frictional force magnitude at each disk, which then may be used to calculate more accurate cable tensions using Eq. 4.45.

Once the sufficient number of iterations has occurred, the disk $i$ cable $k$ net contact force $\mathbf{F}_{i,k,cbl}$, which includes the effect of friction, may be determined using Eq. 4.46.

$$\mathbf{F}_{i,k,cbl} = \begin{cases} -T_{i,k,cbl}\hat{\mathbf{p}}_{(i-1)i,k,cbl} + T_{i+1,k,cbl}\hat{\mathbf{p}}_{i(i+1),k,cbl}, & i < 8 \\ -T_{i,k,cbl}\hat{\mathbf{p}}_{(i-1)i,k,cbl}, & i = 8 \end{cases} \tag{4.46}$$

With $\mathbf{F}_{i,k,cbl}$, the disk $i$ net cable actuation force $\mathbf{F}_{i,act}$ and moment $\mathbf{M}_{i,act}$ acting at the disk's COM may be computed using Eq. 4.47.

$$\mathbf{F}_{i,act} = \sum_{k=1}^{3} \mathbf{F}_{i,k,cbl}, \quad \mathbf{M}_{i,act} = \sum_{k=1}^{3} (\mathbf{r}_{i,k,cbl} \times \mathbf{F}_{i,k,cbl}) \tag{4.47}$$

### Rod-Driven Actuation Loading

The rod-driven actuation loading accounts for the force and moment on each disk due to the axial force in each rod and the friction due to the contact forces between the rods and disks. The actuation forces applied may be considered as end forces and contact forces, as shown in Fig. 4.6. The end force $\mathbf{F}_{k,rod,end}$ is applied at the disk $i = N_k$, defined in Eq. 4.48, where $N_k$ is the disk at which rod $k$ terminates and rigidly connects and $T_{k,rod,end}$ is the axial force at the end of rod $k$. In the absence of friction, this force is calculable directly from the axial force input and robot geometry; with friction, this is no longer true.

$$\mathbf{F}_{k,rod,end} = -T_{k,rod,end}\hat{\mathbf{z}}_{N_k} \tag{4.48}$$

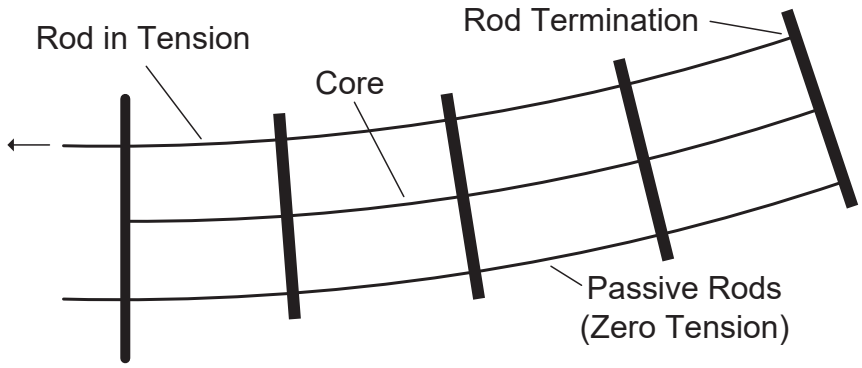


(a) 2D projection of a single-segment rod-driven continuum robot with the upper rod in tension

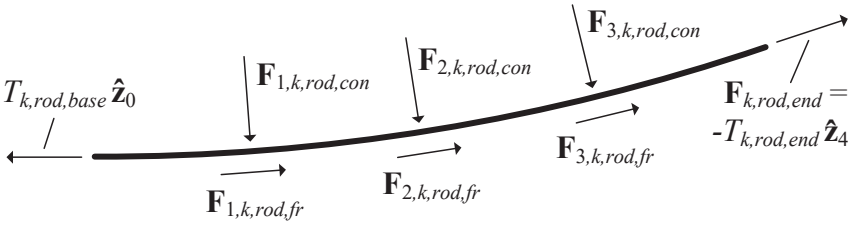


(b) Free-body diagram of the rod under consideration, including friction

Figure 4.6: Continuum robot rod actuation loading.

The coupling of each rod's axial and frictional forces complicates analysis. To compute each disk's friction, the contact force is needed. However, to compute the disks' contact forces, the friction forces are needed. Therefore, similar to cable-driven actuation, an iterative approach is used to converge to the correct values. The starting point assumes the axial force is constant along the rod. From here, the contact forces are estimated for each rod. These contact force estimates are then used to calculate the frictional force at each disk. With these frictional forces, the end force will be updated, and the contact forces will be recalculated. Section 4.6.2 includes analysis on the convergence of the subsegment contact forces based on the iterations of this process and will determine the appropriate iteration count to ensure accurate computation in minimal steps.

The intermediate disk contact forces are calculated from the instantaneous static equilibrium

of each actuation rod. It is assumed the dynamic effects of the rod's mass are negligible. Numerical optimization is used to determine the contact force magnitudes along the segments. A vector of the contact force magnitudes $\|\mathbf{F}_{i,k,rod,con}\|$ for the $i \in \{1, \cdots, N_k\}$ intermediate disk-rod contacts on rod $k$ is the optimization's input. The net equilibrium force $\mathbf{F}_{k,rod,eq}$ is due to the summation of the contact and end forces, shown in Eq. 4.49, where $T_{k,rod,base}$ is the axial force applied at the base and $\hat{\mathbf{F}}_{i,k,rod,con}$ is defined in Eq. 4.25. The net equilibrium moment $\mathbf{M}_{k,rod,eq}$ is calculated relative to the base of the rod in Eq. 4.50, where $\mathbf{p}_{i,k,rod}$ is defined in Eq. 4.26. The rod $k$ objective function $F_{k,rod,obj}$ is the sum of squares of $\mathbf{F}_{k,rod,eq}$ and $\mathbf{M}_{k,rod,eq}$, defined in Eq. 4.51. This model assumes the calculation of at least three contact forces will be required. Furthermore, as the number of contact forces increases beyond the number of terms contributing to the sum of squares, the null-space of the solution will increase, possibly enabling different sets of contact force magnitudes to minimize the objective function.

$$\mathbf{F}_{k,rod,eq} = T_{k,rod,base}\hat{\mathbf{z}}_0 + \sum_{i=1}^{N_k-1}\left(\|\mathbf{F}_{i,k,rod,con}\|\,\hat{\mathbf{F}}_{i,k,rod,con}\right) - T_{k,rod,end}\hat{\mathbf{z}}_{N_k} \tag{4.49}$$

$$\mathbf{M}_{k,rod,eq} = \sum_{i=1}^{N_k-1}\left(\mathbf{p}_{i,k,rod} \times \|\mathbf{F}_{i,k,rod,con}\|\,\hat{\mathbf{F}}_{i,k,rod,con}\right) - \mathbf{p}_{N_k,k,rod} \times (T_{k,rod,end}\hat{\mathbf{z}}_{N_k}) \tag{4.50}$$

$$F_{k,rod,obj} = \mathbf{F}_{k,rod,eq} \cdot \mathbf{F}_{k,rod,eq} + \mathbf{M}_{k,rod,eq} \cdot \mathbf{M}_{k,rod,eq} \tag{4.51}$$

This null-space stems from the fact that the rod geometry is prescribed by the robot geometry, and the contact forces are calculated based on that geometry. In other nondeterministic static equilibrium calculations with a greater number of forces calculated than the number of equations of motion, a constitutive model is used to relate displacement to force, and the coupled forces and displacements are calculated. However, in this case, the displacements

are prescribed by modeling assumptions, and the forces are calculated. In theory, a rod model could be generated with both the core and rod subsegment curvatures as coordinate variables, with compatibility conditions applied between the rods and cables, and coupled solutions of the rod forces and displacements. However, from a practical standpoint, this would significantly increase the number of coordinate variables in the model (for the robot in Fig. 4.1b, the number of coordinates would jump from 16 to 72), likely making the solution intractable. Based on the cross-validation in section 4.6.2, the optimization-based approach provides an acceptable level of accuracy. While this solution may depend on the initial condition of the optimization-based solver, by using this initial condition consistently during a dynamic simulation, the solution's consistency will be maintained and will continue to drive the solution toward the known steady-state configuration.

Based on the model formulation, the contact force magnitudes that minimize $F_{k,rod,obj}$ equal the contact forces applied by the rod on the robot. Due to this, the actuation effects $\mathbf{F}_{i,act}$ and $\mathbf{M}_{i,act}$ may be calculated using Eqs. 4.52 and 4.53. Because the contact forces are parallel to the disk for $i < N_k$, the actuation moment on these disks is zero. However, when friction is considered, there will be a contribution to the disk's actuation moment.

$$\mathbf{F}_{i,act} = \begin{cases} \sum_{k=1}^{6} \left( \|\mathbf{F}_{i,k,rod,con}\| \, \hat{\mathbf{F}}_{i,k,rod,con} \right), & i < 8 \\ \sum_{k=1}^{6} \mathbf{F}_{k,rod,end}, & i = 8 \end{cases} \tag{4.52}$$

$$\mathbf{M}_{i,act} = \begin{cases} 0, & i < 8 \\ \sum_{k=1}^{6} \left( \mathbf{r}_{i,k,rod} \times \mathbf{F}_{k,rod,end} \right), & i = 8 \end{cases} \tag{4.53}$$

The sliding friction arising from the disk-rod contact is calculable from each contact force $\mathbf{F}_{i,k,rod,con}$. However, the frictional forces will change the $T_{k,rod,end}$ used to calculate those

forces. An iterative approach is used to converge on the correct contact forces and friction. Static friction when the sliding velocity equals zero is neglected in the dynamic model due to the difficulty in scaling the sliding velocity zero crossing detection for the numerous rod-disk contacts.

The conventional sliding friction model assumes the rod $k$ disk $i$ contact friction friction magnitude $\|\mathbf{F}_{i,k,rod,fr}\|$ is proportional to the contact force and opposes the sliding motion, as defined in Eq. 4.54, where $\mu$ is the coefficient of friction, $\dot{d}_{i,k,rod}$ is defined in Eq. 4.28, $\text{sat}\,(\cdot)$ is the unit saturation function and $\dot{d}_{sat}$ is a constant use to define the continuous transition of friction over zero. The friction force vector $\mathbf{F}_{i,k,rod,fr}$ is defined based on this magnitude in Eq. 4.55.

$$\|\mathbf{F}_{i,k,rod,fr}\| = \mu \|\mathbf{F}_{i,k,rod,con}\| \,\text{sat}\left(\frac{\dot{d}_{i,k,rod}}{\dot{d}_{sat}}\right) \tag{4.54}$$

$$\mathbf{F}_{i,k,rod,fr} = \|\mathbf{F}_{i,k,rod,fr}\| \,\hat{\mathbf{z}}_i \tag{4.55}$$

Using $\|\mathbf{F}_{i,k,rod,fr}\|$, the rod $k$ end axial force $T_{k,rod,end}$ is updated using Eq. 4.56. The friction opposes the rod motion: when pulled, the friction will reduce the axial force, and when pushed, the friction will increase the axial force.

$$T_{k,rod,end} = T_{k,rod,base} - \sum_{i=1}^{N_k-1} \|\mathbf{F}_{i,k,rod,fr}\| \tag{4.56}$$

The friction will also impact the calculation of the contact force magnitudes, due to the additional force effects on the rods during the calculation of their equilibrium. Equations 4.57 and 4.58 show the modification to Eqs. 4.49 and 4.50 due to friction.

$$\mathbf{F}_{k,rod,eq} = \begin{pmatrix} T_{k,rod,base}\hat{\mathbf{z}}_0 - T_{k,rod,end}\hat{\mathbf{z}}_{N_k} \\ + \sum_{i=1}^{N_k-1} \left( \|\mathbf{F}_{i,k,rod,con}\| \, \hat{\mathbf{F}}_{i,k,rod,con} + \mathbf{F}_{i,k,rod,fr} \right) \end{pmatrix} \tag{4.57}$$

$$\mathbf{M}_{k,rod,eq} = \begin{pmatrix} -\mathbf{p}_{N_k,k,rod} \times (T_{k,rod,end}\hat{\mathbf{z}}_{N_k}) \\ + \sum_{i=1}^{N_k-1} \left( \mathbf{p}_{i,k,rod} \times \left( \|\mathbf{F}_{i,k,rod,con}\| \, \hat{\mathbf{F}}_{i,k,rod,con} + \mathbf{F}_{i,k,rod,fr} \right) \right) \end{pmatrix} \tag{4.58}$$

The resulting frictional forces will modify the force and moment loading on the robot by the rods. The new actuation force and moment are defined in Eqs. 4.59 and 4.60, respectively.

$$\mathbf{F}_{i,act} = \begin{cases} \sum_{k=1}^{6} \left( \|\mathbf{F}_{i,k,rod,con}\| \, \hat{\mathbf{F}}_{i,k,rod,con} + \mathbf{F}_{i,k,rod,fr} \right), & i < 8 \\ \sum_{k=1}^{6} \mathbf{F}_{k,rod,end}, & i = 8 \end{cases} \tag{4.59}$$

$$\mathbf{M}_{i,act} = \begin{cases} \sum_{k=1}^{6} \left( \mathbf{r}_{i,k,rod} \times \mathbf{F}_{i,k,rod,fr} \right), & i < 8 \\ \sum_{k=1}^{6} \left( \mathbf{r}_{i,k,rod} \times \mathbf{F}_{k,rod,end} \right), & i = 8 \end{cases} \tag{4.60}$$

## 4.6 Continuum Robot Results

Results generated using the cable-driven and rod-driven dynamic models are presented in sections 4.6.1 (cable-driven) and 4.6.2 (rod-driven). Various aspects of these simulations are also validated by comparing static and dynamic simulations, analyzing finite element models of the continuum robot structure, and by comparing the results to experiments performed on cable-driven and rod-driven tail prototypes.

### 4.6.1 Cable-Driven Structures

The dynamic behavior of an eight-disk, single-segment, cable-driven continuum robot is analyzed in this section, for which the modeling parameters are defined in Table 4.1. Simulations were performed to compare the dynamic response with alternative methods of analyzing the mechanics. Three case studies were considered: 1) the zero actuation response; 2) the planar actuation response; and 3) the out-of-plane actuation response.

Table 4.1: Material and geometric properties of the cable-driven continuum robot prototype

| | **Property** | **Value** | | **Property** | **Value** |
|---|---|---|---|---|---|
| $m_{i,bdy}$ | Disk and Subsegment Mass | $1.669 \cdot 10^{-3}$ kg | $L_0$ | Initial Subsegment Length (Disk Spacing) | 30 mm |
| $I^i_{i,bdy,xx}$ | Disk and Subsegment Radial Moment of Inertia | $9.821 \cdot 10^{-8}$ kg $\cdot$ m$^2$ | $I^i_{i,bdy,zz}$ | Disk and Subsegment Axial Moment of Inertia | $1.654 \cdot 10^{-7}$ kg $\cdot$ m$^2$ |
| $J_{xx,core}$ | Core Second Moment of Area | $5.743 \cdot 10^{-14}$ m$^4$ | $J_{zz,core}$ | Core Polar Moment of Area | $1.149 \cdot 10^{-13}$ m$^4$ |
| $E_{core}$ | Core Young's Modulus | $2.1 \cdot 10^{11}$ Pa | $G_{core}$ | Core Shear Modulus | $8 \cdot 10^{10}$ Pa |
| $r_{hl}$ | Routing Hole Radius | 12.5 mm | $g$ | Gravitational Acceleration | 9.81m/s$^2$ |
| $\mu$ | Coefficient of Friction | 0.15 | $\dot{d}_{sat}$ | Saturation Velocity Limit | 0.05 m/s |

As discussed in section 4.5.4, the friction model uses an iterative solver to implement the simultaneous calculation of cable-disk contact forces and the tension along the length of the continuum robot. In order to determine the number of iterations for the cable tension/friction force convergence, the static virtual power model is used to track the change in subsegment cable tension at each iteration. Figure 4.7 shows the convergence of the contact forces with a prescribed tension of 10 N in cable $k = 1$ (see Fig. 4.4) at static equilibrium. This 10 N tension is the maximum tension applied in the subsequent analyses, and the maximum number of iterations will be needed for the maximum actuating tension.

Table 4.2 shows the maximum percent error at each iteration for the cable subsegments (in each case, the maximum error was in subsegment 8). Three iterations were chosen to guarantee that the maximum subsegment tension error be less than 1% for the maximum

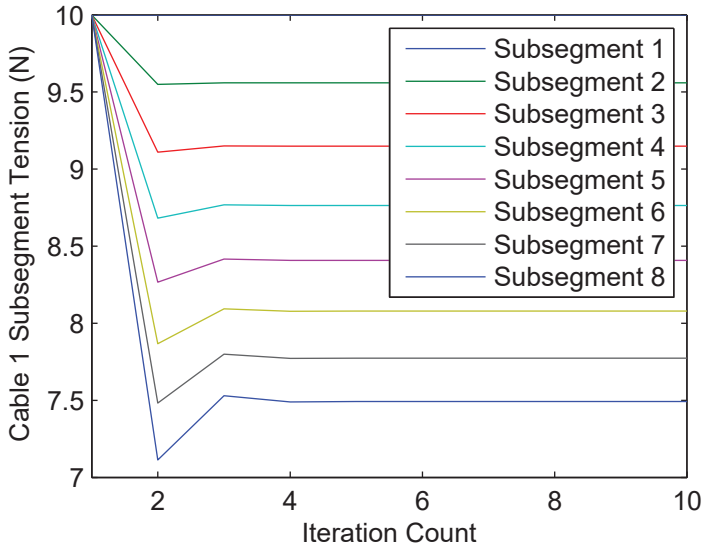


Figure 4.7: Convergence of contact force magnitudes for an eight-disk cable-driven continuum robot over ten iterations.

actuation case in the minimum number of iterations.

Table 4.2: Maximum cable tension error for each iteration

| **Iteration** | **% Error** | **Iteration** | **% Error** | **Iteration** | **% Error** |
|---|---|---|---|---|---|
| 1 | 33.47 | 4 | $3.788 \cdot 10^{-2}$ | 7 | $5.867 \cdot 10^{-6}$ |
| 2 | 5.059 | 5 | $2.338 \cdot 10^{-3}$ | 8 | $2.524 \cdot 10^{-7}$ |
| 3 | $5.028 \cdot 10^{-1}$ | 6 | $1.241 \cdot 10^{-4}$ | 9 | $1.049 \cdot 10^{-8}$ |

### Zero-Actuation Case Study

Figure 4.8 illustrates the dynamic response of the $\beta$ curvatures of the continuum robot's second, fourth, sixth, and eighth subsegments with zero tension in the three cables. This subset of the eight curvature responses presents the curvatures change along the continuum robot without the need to extraneously plot each subsegment's response. The model's initial conditions are $\beta_i = 0.001$ m$^{-1}$, $\gamma_i = 0$ m$^{-1}$ and $\epsilon_i = 0$ rad for subsegments $i = \{1, \cdots, 8\}$. This is equivalent to supporting the robot in this initial condition then removing this support

at time $t = 0$. If damping is neglected, the continuum robot's zero actuation simulation shows sustained oscillations of the continuum robot's curvatures around a stable point. Because the cable tensions are all zero, there is no contact force between the cabling and the disks, resulting in zero friction along the structure. If damping is also neglected, the energy of the continuum robot in the zero actuation simulation is constant. Figure 4.9 shows the first oscillation of the continuum robot after release: the robot initially drops over 0.1342 sec, then springs up over 0.1036 sec.

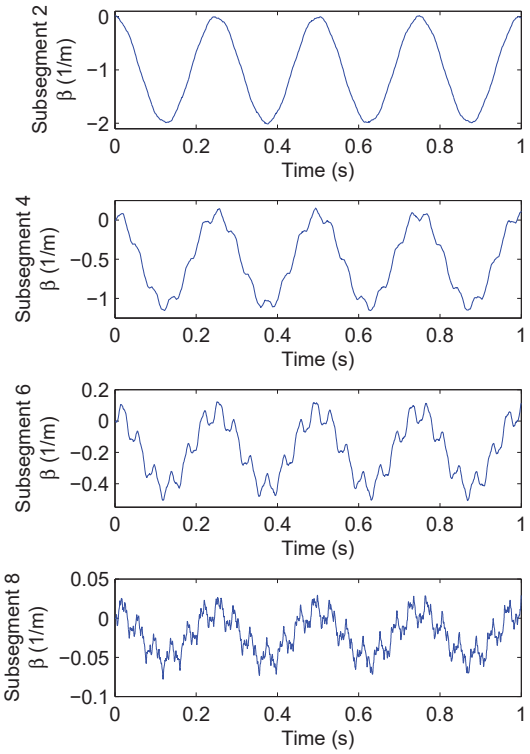


Figure 4.8: Zero actuation response $\beta$ curvatures for subsegments 2, 4, 6, and 8.

Two key properties of the zero actuation dynamic response shown in Fig. 4.8 have been analyzed and compared with alternative methods of modeling. First, the steady-state component of the dynamic response will be compared with the static equilibria generated using two alternative models. Second, frequency domain analysis will compare the transient component of the dynamic response simulated using the virtual power method with the transient

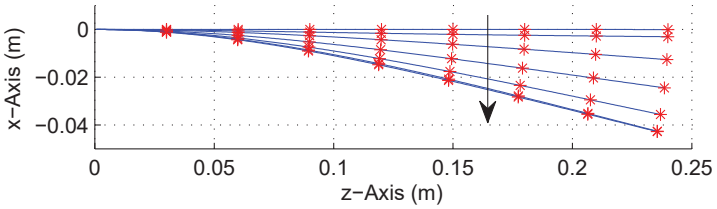


(a) Initial drop over 0.1342 sec

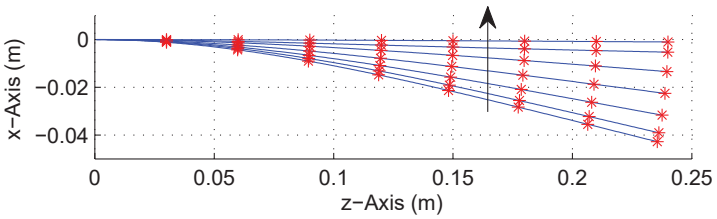


(b) Initial return over 0.1036 sec

Figure 4.9: Time-lapse of zero actuation response. Each frame's seven illustrations are equally spaced over the interval.

response of a dynamic finite-element simulation of the continuum robot.

Figure 4.10 compares three simulations for the zero actuation case of the continuum robot: 1) the steady-state component of the dynamic response; 2) the equilibrium of the static virtual power model; and 3) the equilibrium of a static finite-element model calculated using the COMSOL Structural Mechanics module's 3-D linear elasticity model with a "Fine" mesh. As seen in Fig. 4.10, the three plots are nearly superimposed on one another. Calculating the error of the virtual power simulation disk positions relative to the finite-element simulation (because the FEA simulation is the highest fidelity), the maximum disk position error for the dynamic steady-state response is 0.5188%, and for the virtual power static equilibrium: 0.4848%.

In addition to the steady-state component of the dynamic response, the transient component of the dynamic response is also analyzed. In order to quantify this transient response, a fast Fourier transform (FFT) was performed on the $\mathbf{p}_i$ x-coordinate trajectories computed using:

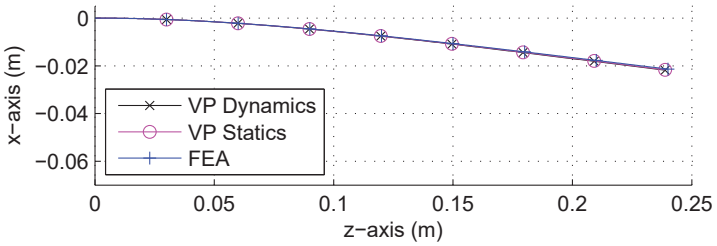


Figure 4.10: Comparison of the zero actuation steady-state component of the dynamic response, the static virtual power equilibrium, and the FEA static equilibrium.

1) the virtual power dynamics model, and 2) the dynamic FEA model. For the virtual power dynamics model, the curvature responses (illustrated in Fig. 4.8) are mapped into time-varying disk displacements. The oscillations of the $\mathbf{p}_i$ x-coordinate for this response are then compared with the simulated response generated using the dynamic FEA. Figure 4.11 illustrates the frequency response for disk 1 in the continuum robot for the two cases. There is a strong correlation between the frequency responses, with a similar zero-frequency magnitude (corresponding to the steady-state response) and a significant peak at the 3.6621 and 4.5776 Hz frequencies. Disk 1's frequency response is representative of the other disks responses.

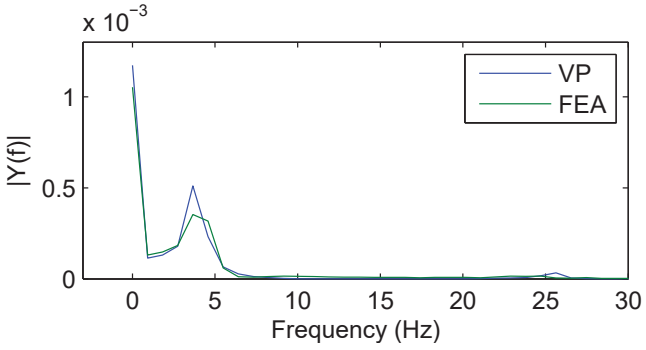


Figure 4.11: Comparison of frequency response magnitudes for disk 1 $\mathbf{p}_i$ x-coordinate trajectories of dynamic virtual power and dynamic finite-element analysis models.

The discrepancy between the two frequency profiles is due to several factors. First, because the virtual power dynamics solver uses a variable time step to solve the dynamics, the

simulation results were resampled at a high frequency (30 kHz) to create a uniform step-size between data points. This resampling used linear interpolation for times at which there was not a matching data point. Second, COMSOL was limited in the number of discrete points the simulation could save during the simulation.

For the 1 s simulation used to characterize the dynamics sampling at a rate of 5 kHz, the results file exceeded 1 GB, due to the mesh density. These 5 kHz results were then resampled like the virtual power dynamic response to 30 kHz to ensure equal fundamental frequencies. Third, the spatial discretizations between the two models differs on the orders of magnitude and will slightly influence the resulting dynamic responses.

### In-Plane Case Study

Figure 4.12 illustrates the dynamic responses of the selected $\beta$ curvatures of the virtual power dynamic model in response to a step input of a 5 N tension in cable $k = 1$ (see Fig. 4.4) from the initial condition of zero actuation static equilibrium. Because the actuation remains in the vertical plane due to the purely x-component of the hole radius $\mathbf{r}^i_{i,1,cbl}$ (Eq. 4.17), the dynamic response will remain in the vertical plane and the $\gamma_i$ and $\epsilon_i$ trajectories will remain zero. Unlike Fig. 4.8, the non-zero actuation will cause a contact force between the cabling and disk, leading to friction that damps the oscillations.

Figure 4.13 shows the two motions of the continuum robot after application of the tension. The robot initially deflects downward over 0.02682 sec, then snaps upward over 0.14292 sec. As in Fig. 4.9, each panel shows seven illustrated configurations equally spanning these two time spans.

Unlike the zero actuation validation, the friction model will cause the damping of the dynamic response toward the steady-state solution, preventing the application of conventional

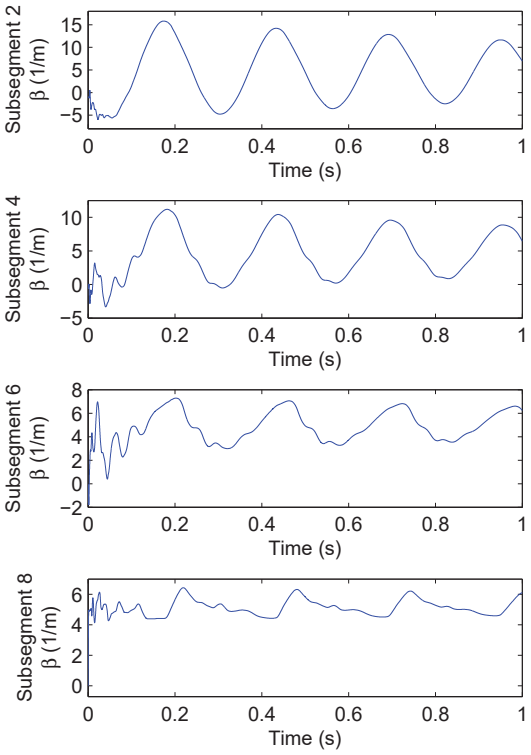


Figure 4.12: Cable 1 actuation $\beta$ curvatures for subsegments 2, 4, 6, and 8.

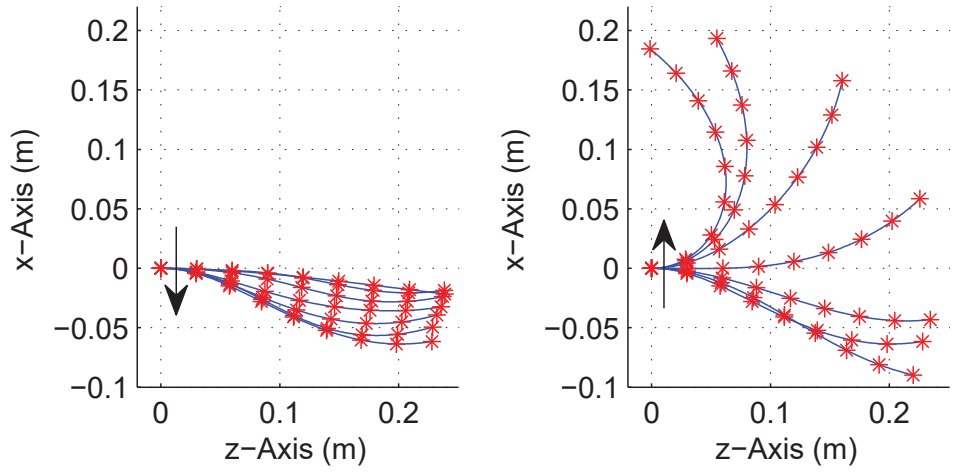


(a) Initial downward motion over 0.0659 sec

(b) Initial upward motion over 0.0988 sec

Figure 4.13: Time-lapse of cable 1 actuation response. Each frame's seven illustrations are equally spaced over the time intervals.

frequency domain analysis methods for the transient response. However, because of the formulation of the friction model for this dynamic model, the friction actually approaches zero as the continuum robot velocity approaches zero. Without the damping, the simulation's steady-state response approaches the zero-friction static equilibrium configuration; however, the introduction of the damping effects causes the response to damp to the lower bound of the virtual power static equilibrium model with friction, as shown in Fig. 4.14. This figure illustrates the steady-state component of the dynamic response, as well as three cases for the static equilibrium: 1) the case with zero friction; 2) the case with the friction saturation (Eq. 4.45) equal to +1; and 3) the case with the friction saturation function equal to 1.

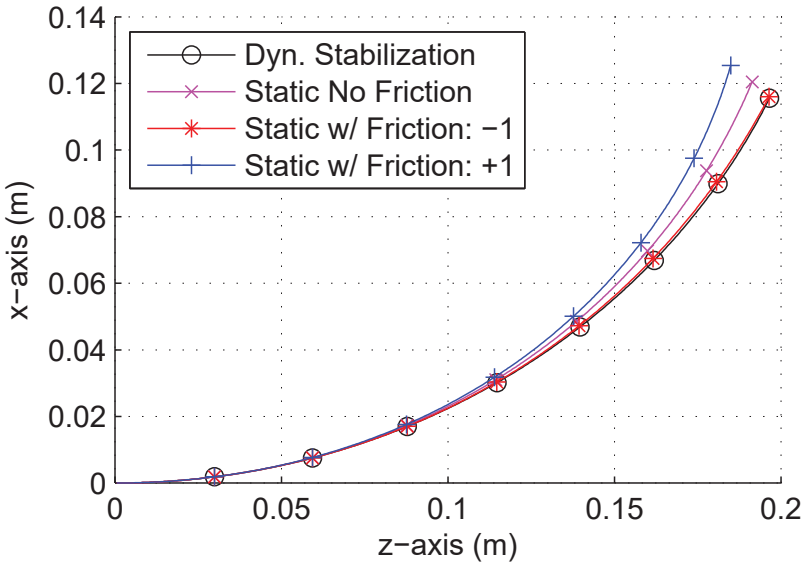


Figure 4.14: Comparison of the stabilization of virtual power dynamic model with friction to static equilibrium models with and without friction for $T_1 = 5$ N.

In addition, these virtual power models have also been compared with experimental results. Fig. 4.15 shows the experimental test platform used to validate the dynamic modeling approach. A spring steel core (ASTM A228, 1.04 mm diameter, 240 mm long) was used with four disks (ABS plastic, 31 mm diameter, 2 mm thick, 30 mm disk spacing) mounted along the core using cyanoacrylate (Loctite 401, Uline). Hanging weights were used to

tension the cables, with PFTE-coated fiberglass thread (0.43 mm diameter) used as the cabling. Three transmission cables were routed through the disks at three equally spaced holes offset 12.5 mm from center. These properties match the properties used to simulate the model presented in Table 4.1. The shape was measured by photographing the disks along the continuum robot in profile, then calculating their angles by postprocessing the images. The bending plane angle $\theta_i$ was found for each subsegment by subtracting the two surrounding disks' angles, and the subsegment curvatures were found by dividing $\theta_i$ by $L_0$ . The error of this image processing step was estimated by determining the angles of gradations on a protractor, then calculating the associated curvature for a given difference in angle. This was compared with the predicted curvature for the known difference in angle. The maximum curvature error was found to be 1.637%.

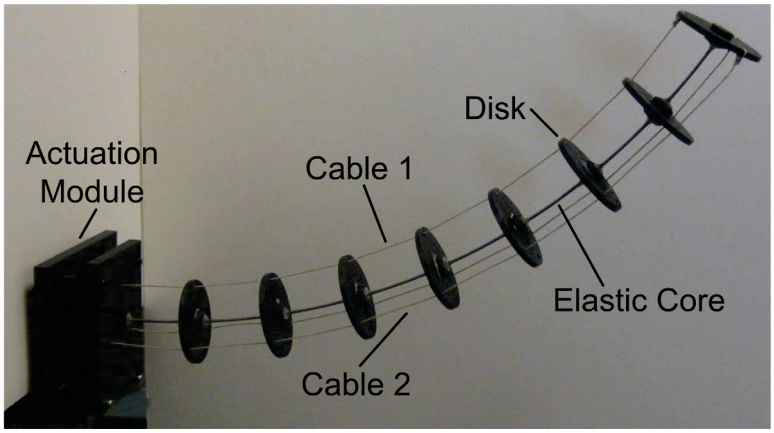


Figure 4.15: Prototype used for experimental validation. Cables are tensioned using hanging weights routed over pulleys in the actuation module.

Figure 4.16 compares the steady-state component of the dynamic virtual power response with the experimental results and static virtual power equilibrium for a 5 N tension applied in cable 1. The maximum error between the disk positions of experimental results and the dynamic virtual power response steady-state component is 2.1961% in disk 8, and between the disk positions of the experimental results and the static virtual power model equilibrium

is 2.4866% in disk 7.

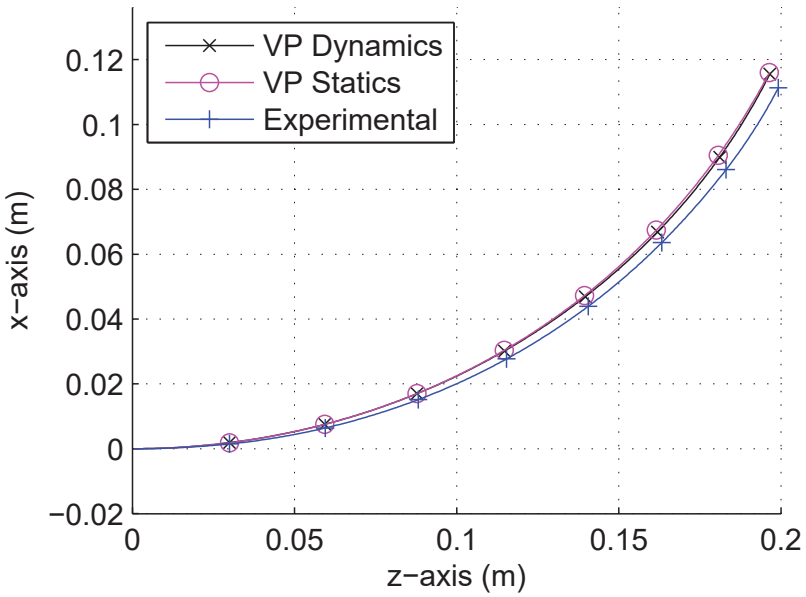


Figure 4.16: Comparison of in-plane actuation dynamic virtual power response steady-state component to the measured static equilibrium of a continuum robot prototype and the calculated static virtual power model equilibrium.

Beyond the single actuation case presented in Fig. 4.16, Fig. 4.17 compares experimental results for a range of actuation tensions ranging from 2.5 to 10 N with the associated calculated static equilibria using the virtual power model. Figure 4.18 quantifies the percent error of the disk positions of the virtual power static equilibrium relative to the experimental results (a positive error correlates to overshooting the experimental configuration, like the 5 N case). Because the error in this type of serial manipulator propagates from the base, the most significant error is the disk 1 errors. A maximum disk 1 position error of 1.2405% was seen in the 5.0 N actuation case. This error is less than the measurement error discussed previously, leading to the conclusion that the errors between the measured and simulated static equilibria are within the measurement range of error.

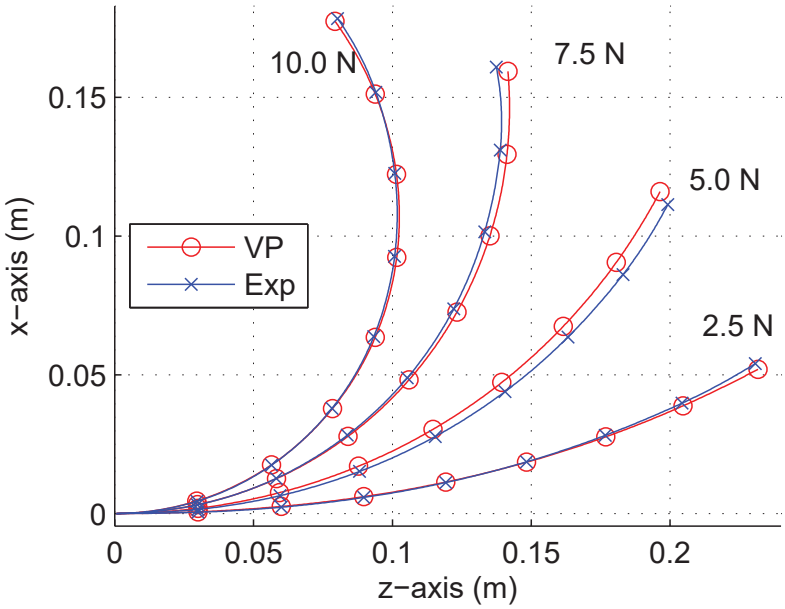


Figure 4.17: Equilibrium configurations of static virtual power continuum robot model with friction compared with experimentally measured static equilibria at cable 1 tensions of 2.5, 5.0, 7.5, and 10.0 N.

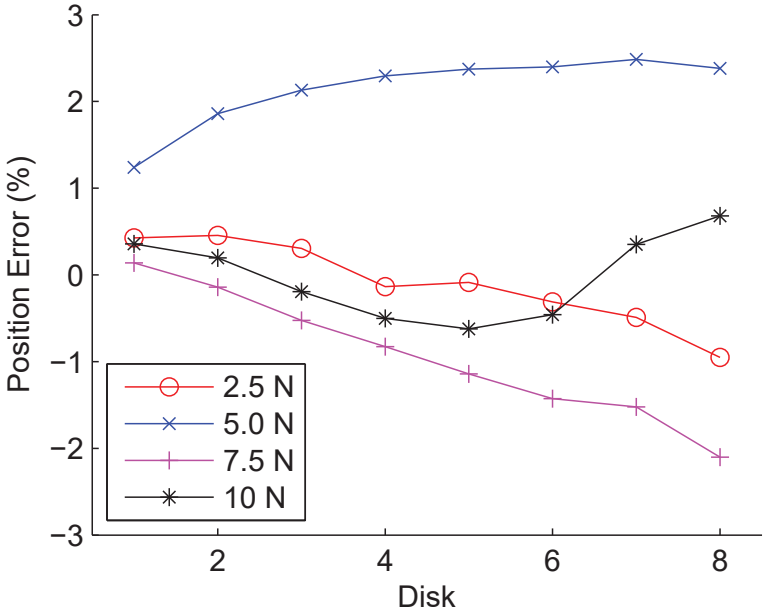


Figure 4.18: Error of disk positions relative to the experimentally measured disk positions for actuation tensions of 2.5, 5, 7.5, and 10 N in cable 1.

### Out-of-Plane Case Study

Figure 4.19 illustrates the dynamic responses of the $\beta$ and $\gamma$ curvatures of a dynamic model in response to a step input of a 5 N tension in cable 2 (see Fig. 4.4) from the initial condition of zero actuation static equilibrium.

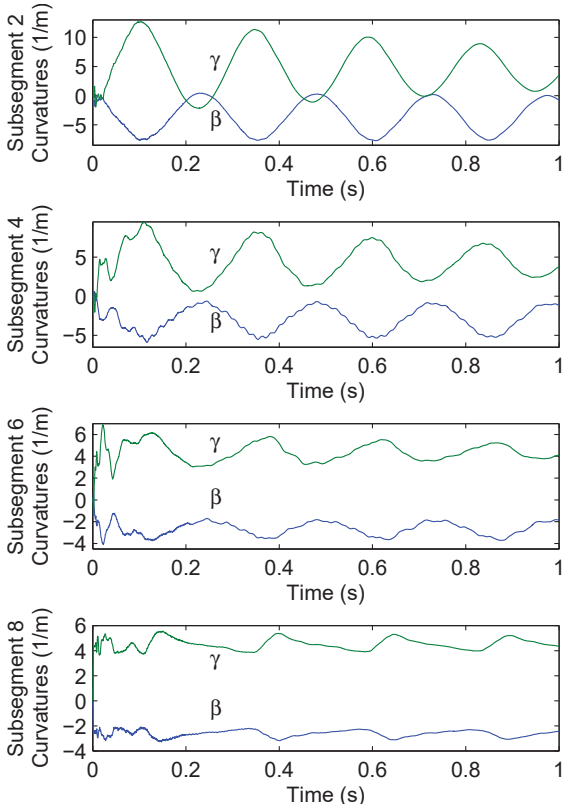


Figure 4.19: Cable 2 actuation curvature trajectories for subsegments 2, 4, 6, and 8.

Figure 4.20 illustrates the dynamic response of the torsional twist angle $\epsilon$. Unlike the first two case studies, because of the out-of-plane actuation, the gravitational loading will cause twist along the length of the subsegments. For the scaling of the current continuum robot, the magnitude and impact of these torsional vibrations is relatively small compared with the impact of variation in curvatures. However, as macro-scale robots are considered and the distributed mass along the continuum arm increases, this effect will significantly impact the continuum robot shape. The robot's damping causes the damping of the high-frequency

oscillations. As a result, as the simulation continues, the oscillations of subsegments 2 and 4 increase in magnitude. This is due to the coupling between the twist angle and the curvatures. As the curvatures oscillate, the geometry of the continuum arm changes, particularly the distance between the disks and the vertical plane. This causes changes in the twist angle. The damping and friction will converge the mutual oscillations to equilibrium over time.

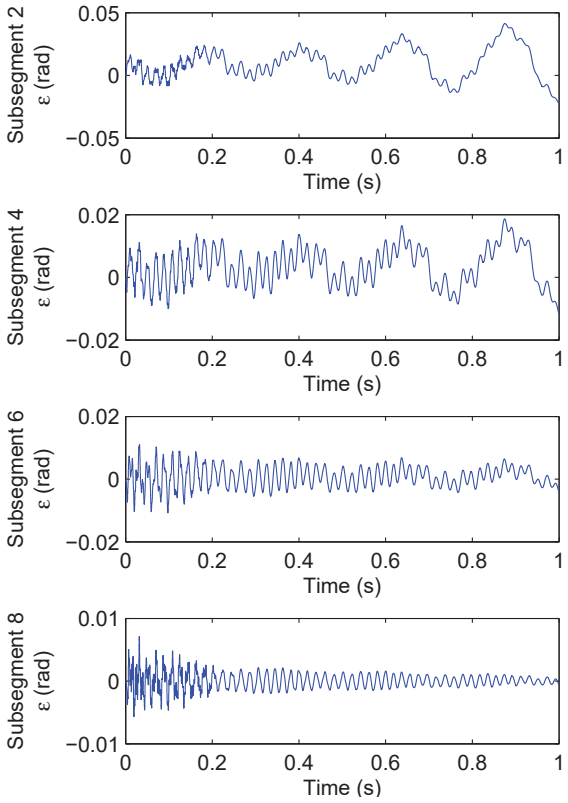


Figure 4.20: Cable 2 twist angle trajectories for subsegment 2, 4, 6, and 8.

The out-of-plane dynamic response tensions cable 2 in the continuum robot, leading to a deformation out of the vertical plane. Unlike the previous section in which the continuum robot was confined to a single plane of motion, the torsional twist along the robot creates a generalized spatial shape for the continuum robot. It is not simply the in-plane response rotated by 120°. As a result, the measurement used for the in-plane case (estimating subsegment curvatures using the disk angle extrapolated from photographs) is not applicable

to this case. However, due to the scaling of this manipulator, the torsional effects are not as significant as they would be in a longer and/or more massive structure. The stabilization of the dynamic response is still compared with the static virtual power, as shown in Fig. 4.21. Due to the interaction between the curvatures and torsional twist angle, there is a greater error between the dynamic model's steady-state response and the static model's static equilibrium compared with the in-plane actuation, but the maximum error remains only 2.0926% at disk 5 for the dynamic steady-state response compared with the static equilibrium.

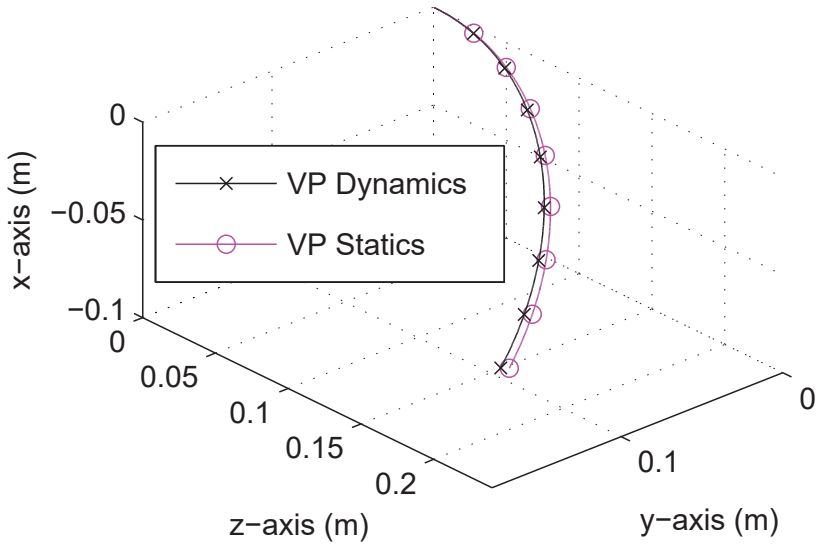


Figure 4.21: Steady-state component of dynamic virtual power model response compared with static virtual power simulation of continuum robot equilibrium with a cable 2 tension of 5 N.

### 4.6.2 Rod-Driven Structures

The dynamic behavior of an eight-disk, two-segment, rod-driven continuum robot is analyzed in this section, for which the modeling parameters are defined in Table 4.3. Dynamic loading profiles were generated for various rod tension inputs, and these results have been compared

to: 1) static models, 2) finite element models, and 3) experimental results.

Table 4.3: Material and geometric properties of the rod-driven continuum robot prototype. S1 and S2 denote segment 1 and segment 2 properties, respectively.

| | Property | Value | | Property | Value |
|---|---|---|---|---|---|
| $m_{i,bdy}$ | Mass | S1: $2.869 \cdot 10^{-3}$ S2: $2.869 \cdot 10^{-3}$ kg | $L_0$ | Subsegment Length (Disk Spacing) | 30 mm |
| $I^i_{i,bdy,xx}$ | Radial Moment of Inertia | S1: $7.690 \cdot 10^{-6}$ S2: $3.894 \cdot 10^{-6}$ $\text{kg} \cdot \text{m}^2$ | $I^i_{i,bdy,zz}$ | Axial Moment of Inertia | S1: $3.531 \cdot 10^{-7}$ S2: $2.593 \cdot 10^{-7}$ $\text{kg} \cdot \text{m}^2$ |
| $J_{xx,core}$ | Core Second Moment of Area | $5.743 \cdot 10^{-14}$ $\text{m}^4$ | $J_{xx,rod}$ | Rod Second Moment of Area | $5.743 \cdot 10^{-14}$ $\text{m}^4$ |
| $E_{core}$ | Core Young's Modulus | $2.1 \cdot 10^{11}$ Pa | $E_{rod}$ | Rod Young's Modulus | $2.1 \cdot 10^{11}$ Pa |
| $r_{hl}$ | Routing Hole Radius | 12.5 mm | $g$ | Gravitational Acceleration | $9.81\text{m/s}^2$ |
| $\mu$ | Coefficient of Friction | 0.3 | $\dot{d}_{sat}$ | Saturation Velocity Limit | 0.05 m/s |

Like the cable-driven structure, as discussed in section 4.5.4, the contact and friction forces calculations are coupled. An iterative model has been formulated to converge on the accurate values of the contact and friction forces; however, the minimum number of iterations needed is required. Based on prototype construction for the experimental validation, a maximum axial force of 30 N was set for the simulations and experiments.

Figure 4.22 shows the convergence of the contact force magnitudes in two cases: (1) planar actuation of the proximal segment with $T_{1,1} = 30$ N and (2) planar actuation of the whole robot with $T_{2,2} = 30$ N. During preliminary simulations, planar actuation was found to converge in more steps than spatial actuation because of the fewer degrees of freedom present for the optimization (three terms in the objective function versus six) of the contact force magnitudes. Furthermore, during preliminary simulations, it was found that the convergence rate increases as the force magnitude increases. Table 4.4 shows the maximum percent error at each iteration of the contact force magnitude relative to the final result at iteration 10 for the two cases. While the segment 2 simulation has higher initial error, it more quickly converges to the final contact force. Therefore, the segment 1 modeling dictates the minimum

number of iterations. As seen in Table 4.4, six iterations results in a solution with less than a 1% difference from the final value. Therefore, in all simulations, six iterations will be utilized.

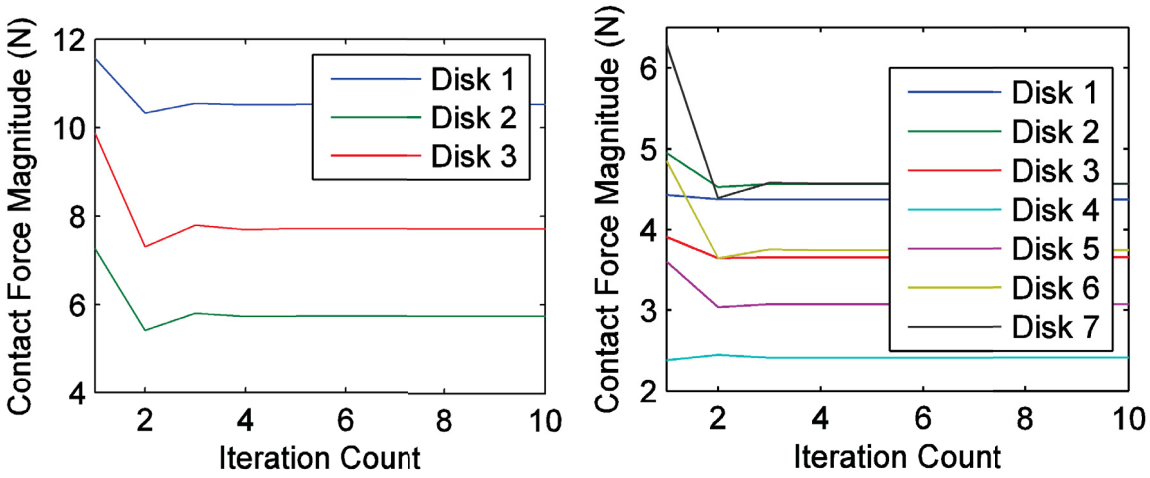


(a) $T_{1,1}$ actuated with 30 N (rod connects at disk 4)

(b) $T_{2,2}$ actuated with 30 N (rod connects at disk 8)

Figure 4.22: Convergence of rod contact force magnitudes for a two segment,eight-disk continuum robot.

Table 4.4: Maximum contact force magnitude error for each iteration for static simulations with $T_{1,1} = 30$ N (S1) or $T_{2,2} = 30$ N (S2).

| **Iteration** | **S1 % Error** | **S2 % Error** | **Iteration** | **S1 % Error** | **S2 % Error** |
|---|---|---|---|---|---|
| 1 | 27.9 | 37.8 | 6 | $8.50 \cdot 10^{-3}$ | $2.76 \cdot 10^{-6}$ |
| 2 | 5.71 | 3.91 | 7 | $1.68 \cdot 10^{-3}$ | $8.42 \cdot 10^{-8}$ |
| 3 | 1.12 | $2.32 \cdot 10^{-1}$ | 8 | $3.16 \cdot 10^{-4}$ | $2.24 \cdot 10^{-8}$ |
| 4 | $2.21 \cdot 10^{-1}$ | $8.96 \cdot 10^{-3}$ | 9 | $7.71 \cdot 10^{-5}$ | $2.20 \cdot 10^{-9}$ |
| 5 | $4.34 \cdot 10^{-2}$ | $2.13 \cdot 10^{-4}$ | | | |

### Dynamic Response Analysis

Dynamic simulations were generate using the virtual power model for three case studies: 1) zero-actuation in the rods, 2) rod $k = 1$ actuated with a 10 N tension, and 3) rod $k = 5$ actuated with a 10 N tension. Figure 4.23 illustrates the dynamic response of the

$\beta$ curvatures of the continuum robot's subsegments with zero axial force in the rods. The simulation results in sustained oscillations of the continuum robot's curvatures around a stable point when damping is neglected. Because the axial forces are all zero, there is no contact force between the rods and disks, resulting in zero friction along the arm. In this case, the rod's bending is due to the moment applied by the terminal disk and transmitted along the rod. The elastic effects of these passive rods are then incorporated into the elastic loading. Because sliding friction due to the contact forces is the only dissipative force in the model, the vibrations are not damped and remain sustained over the interval.

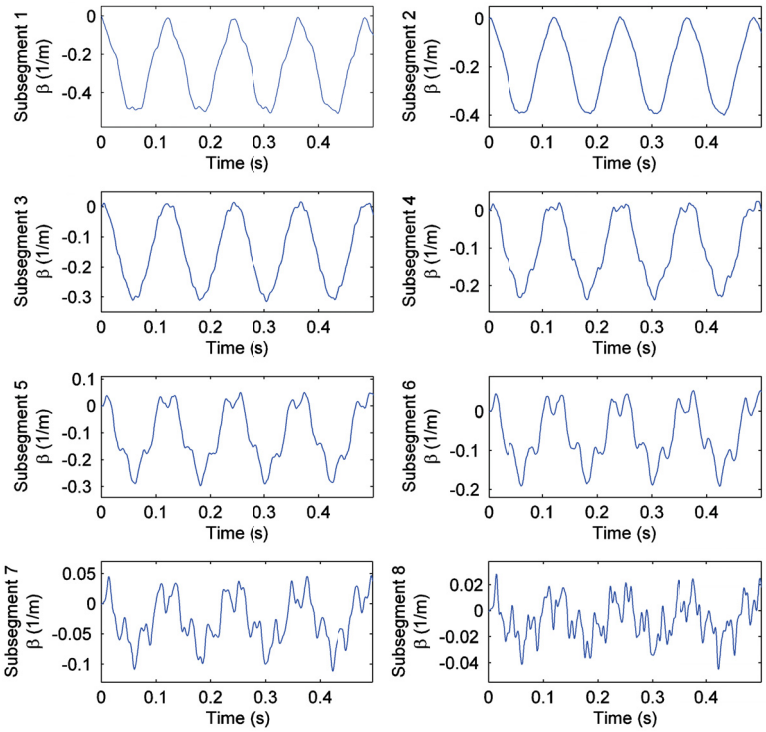


Figure 4.23: Zero actuation virtual power dynamic model response $\beta$ curvatures. These curvature profile correspond to tip oscillations with peak-to-peak amplitude of 9.48 mm around a setpoint of 24.74 mm.

Figure 4.24 illustrates the dynamic response of the robot with rod $k = 1$ (the first rod that terminates in the first segment) actuated with a tension of 10 N. Because the actuation remains in-plane, only the $\beta$ curvatures are non-zero. In addition, due to the contact forces

between the actuation rods and the disks, friction damps the responses. Because rod $k = 1$ terminates at disk 4, only subsegments 1 through 4 will have appreciably different steady-state curvature values. However, all subsegments experience vibration attenuation. For segment 1, this is due to the contact friction between rod $k = 1$ and the disks adjacent to its subsegments. However, for segment 2, the dissipation is indirect due to the internal force loading of segment 1 on segment 2. When the segment 2 internal forces and moments are applied to segment 1, the frictional force will oppose the resulting motion. This frictional opposition results in reduction of the internal forces and moments, which results in reduced vibrations in segment 2.

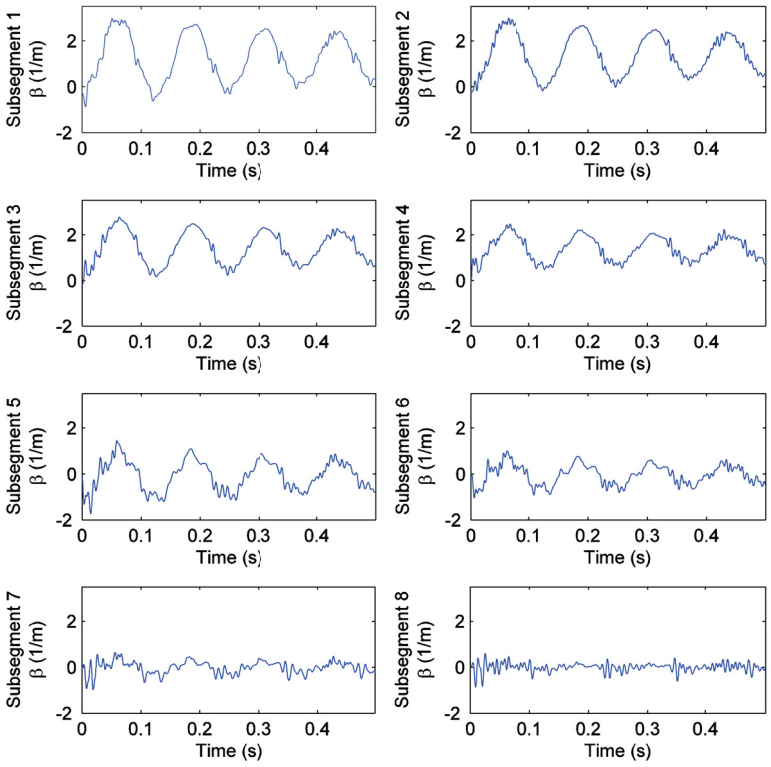


Figure 4.24: Rod $k = 1$ actuation (10 N) dynamic virtual power model $\beta$ curvature responses.

The actuation of the segment 2 rods results in deformation along the entire robot, due to their routing through the proximal segment 1. Figure 4.25 illustrates the dynamic response of the continuum robot with rod $k = 5$ (the second rod that terminates in the second segment)

actuated with a tension of 10 N (same as the segment 1 dynamic response) from the initial condition of the zero actuation static equilibrium.

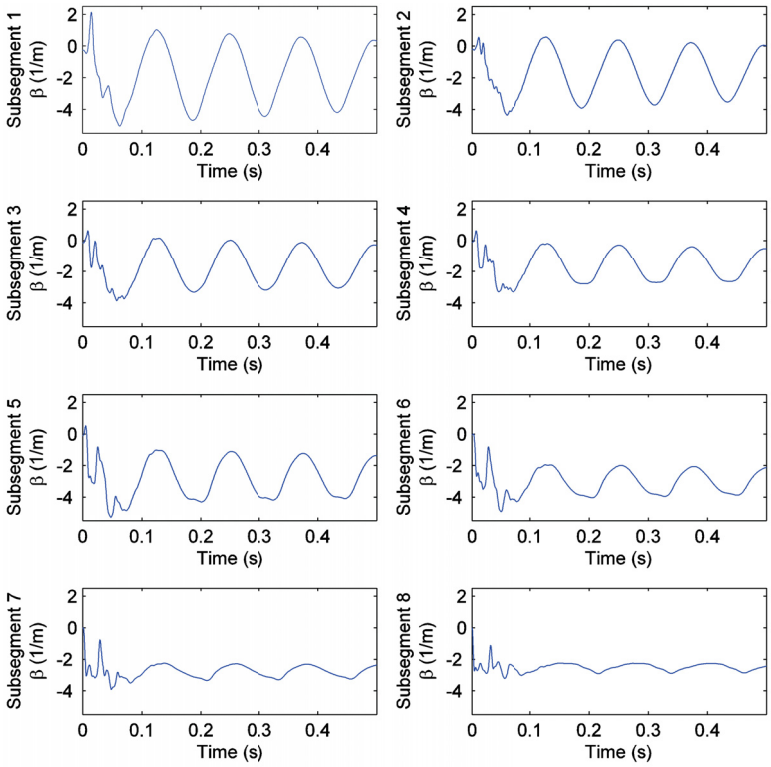


Figure 4.25: Rod $k = 5$ actuation (10 N) dynamic virtual power model $\beta$ curvature responses.

### Static Versus Dynamic Virtual Power Model Comparison

As an initial point of comparison, the steady-state component of the dynamic virtual power model response (i.e., the constant values of the response around which the transient response oscillates) can be compared to the equilibrium configuration calculated by the static virtual power model. Figure 4.26 compares these for a 10 N tension in rod $k = 1$. As shown, they are nearly identical. The maximum position error is 0.2939% in disk 8, enabling interchangeable use of the static equilibrium model for the steady-state component of the dynamic response.

Figure 4.27 compares the dynamic model steady-state response to the static model equilib-

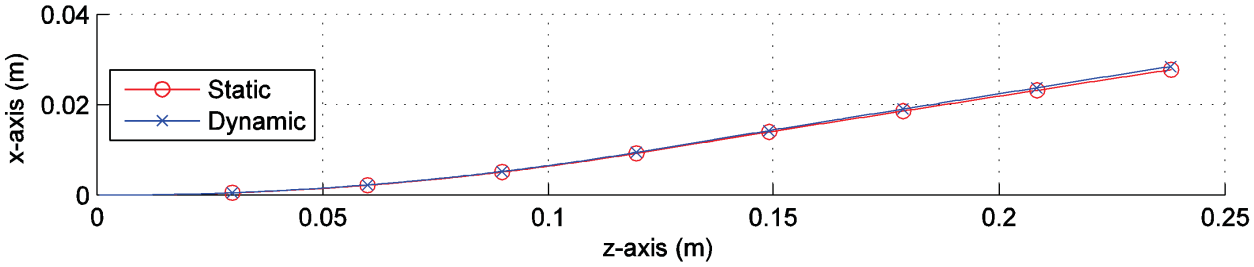


Figure 4.26: Comparison of the calculated static virtual power model equilibrium to the steady-state component of the dynamic virtual power model response for actuation of 10 N in rod $k = 1$.

rium for actuation of rod $k = 5$ with 10 N tension. Although there is slightly more variation between these two configurations than in Fig. 4.26, the maximum error in disk 8 position is still 2.2165%, or 5.3 mm. Table 4.5 provides the error of the steady-state dynamic response component relative to the static equilibrium. In addition, it is seen that for identical tension inputs, the segment 2 rods will cause greater overall deflection.

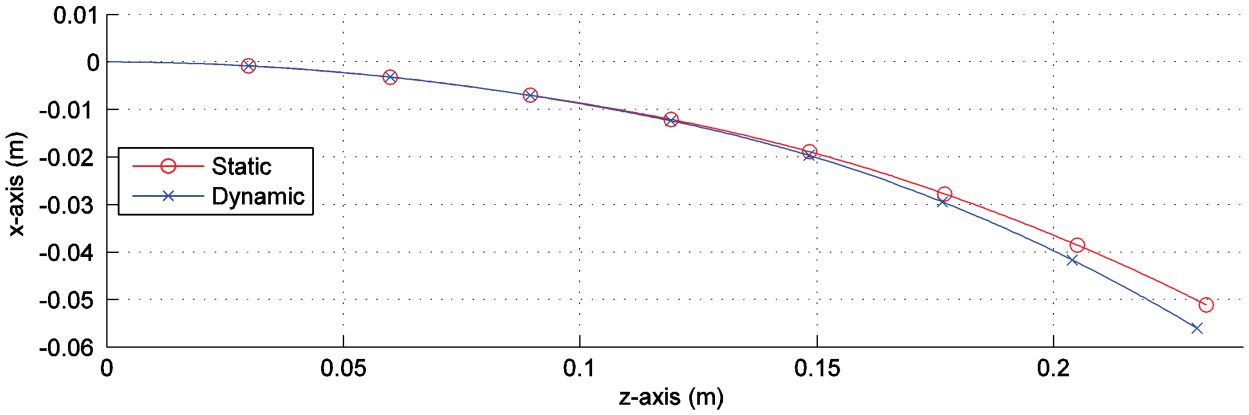


Figure 4.27: Comparison of the calculated static virtual power model equilibrium to the steady-state component of the dynamic virtual power model response for actuation of 10 N in rod $k = 5$.

### Finite Element Analysis Validation of Virtual Power Model

Two properties of the zero actuation dynamic response shown in Fig. 4.23 have been analyzed: the magnitude of the steady-state component and the frequency response of the

Table 4.5: Percent error of dynamic response steady-state component relative to static equilibrium for actuation of 10 N in rod $k = 5$.

| **Disk** | **% Error** | **Disk** | **% Error** | **Disk** | **% Error** | **Disk** | **% Error** |
|---|---|---|---|---|---|---|---|
| 1 | 0.0735 | 3 | 0.0502 | 5 | 0.5221 | 7 | 1.5957 |
| 2 | 0.0684 | 4 | 0.2448 | 6 | 0.9805 | 8 | 2.2165 |

transient component. Figure 4.28 compares the dynamic response's steady-state component to: (1) the static virtual power model equilibrium, and (2) the equilibrium of a static FEA model of the continuum robot. This FEA model was generated using COMSOL's Structural Mechanics module. A 3D linear elasticity material model was chosen, and the geometry was discretized using a "Fine" mesh. As shown in Fig. 4.28, the three plots are practically superimposed on one another. The maximum disk position error for both the dynamic response steady-state component and the static equilibrium model relative to the FEA simulation is 0.2958%.

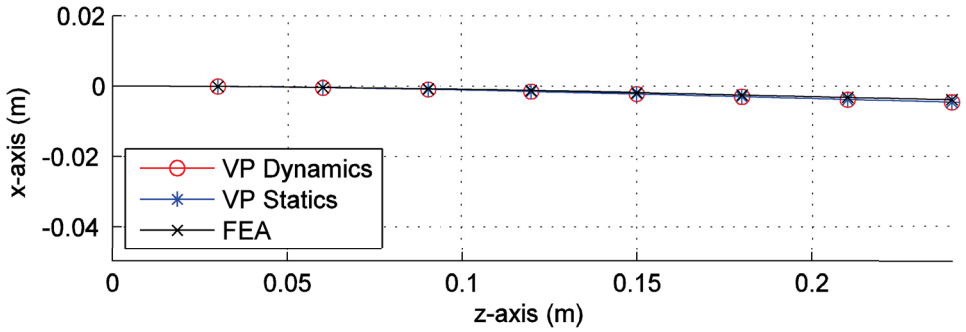


Figure 4.28: Comparisons of the zero actuation dynamic virtual power model response steady-state component to the calculated equilibria using the static virtual power model and the static finite element analysis model.

The frequency response of the virtual power dynamic response was compared to a dynamic FEA simulation in COMSOL. A fast Fourier transform using MATLAB was performed on the oscillations of the x-components of displacement of the disks' centers-of-mass to quantify the frequency response. For the dynamic virtual power model, the curvature responses illustrated in Fig. 4.23 were mapped into disk trajectories, based on the kinematic analysis

in section 4.4.

Figure 4.29 illustrates the frequency responses of the first and eighth disk in the robot. As illustrated, the frequency response profiles' shapes between the two disks' oscillations are similar and differ primarily in their magnitudes. However, there is a slight difference in the peak frequency of the first mode: the FEA simulation exhibits a greater fundamental frequency (9.76 Hz) than the virtual power model (7.81 Hz). This is primarily due to the difference in discretization between the two models: the dynamic virtual power model is defined by 32 variables, whereas the FEA uses a model composed of 6964 elements. In addition, the model discretization makes several assumptions for model simplicity that change the mass properties of the robot. The first half of the core and rods in subsegment 1 are not explicitly modeled, due to the lumping of these masses elsewhere with their immediately surrounding disks. On the other hand, at disk 4, the mass properties are assumed to be the same as the three previous disks, but one triplet of rods does not continue past disk 4. Likewise, at disk 8, rods are modeled as continuing beyond the disk, when in actuality they do not. The redistribution of this mass would have an effect on the dynamic properties of the robot and likely contributes to this error.

### Experimental Validation of Virtual Power Model

Experimental validation is used to verify the accuracy of the actuated case studies of the virtual power model. Figure 4.30 shows the experimental test platform utilized. A spring steel core (ASTM A228, 1.04 mm diameter, 240 mm long) was used with eight disks (ABS plastic, 30 mm diameter, 2 mm thick, 30 mm disk spacing) mounted along the core using cyanoacrylate (Loctite 401). The actuation rods are also spring steel (ASTM A228, 1.04 mm diameter), route through holes in the disk of 1.75 mm diameter, and terminate and are connected to the fourth or eighth disk using the above cyanoacrylate. Hanging weights are

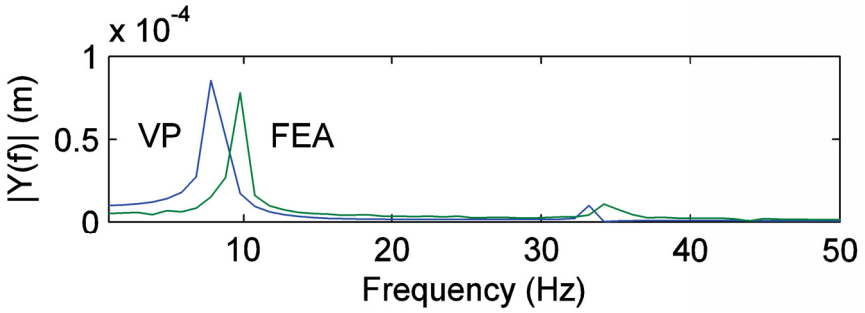


(a) Disk 1

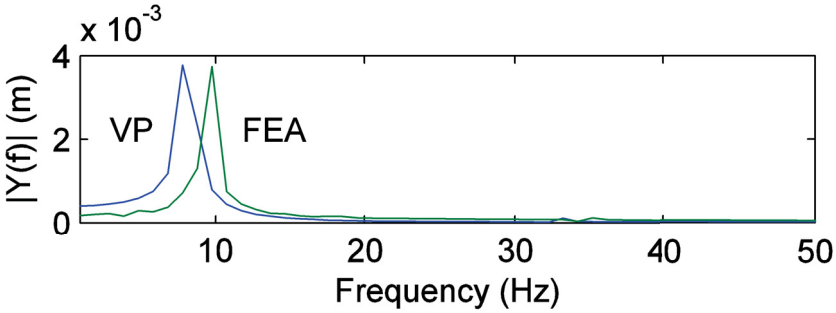


(b) Disk 8

Figure 4.29: Comparison of frequency response magnitudes for disk 1 and 8 x-coordinate trajectories of dynamic virtual power and dynamic finite-element analysis models.

used to tension the rods, with an adapter mounted on the rod with polytetrafluoroethylene-coated fiberglass thread tied on and routed over a spool supported by ball bearings. The actuation rods were routed through the disks offset 12.5 mm from the center. The properties of this prototype match the properties used in the numerical models shown in Table 4.3.

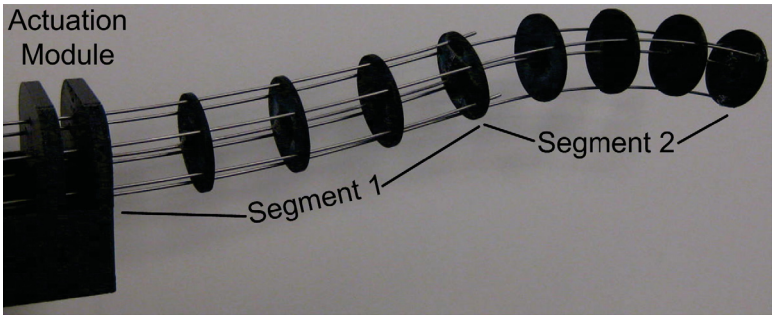


Figure 4.30: Rod-driven, two-segment prototype used for validating actuated case studies.

The shape was measured by photographing the disks in profile, then indirectly calculating the

curvature from the relative angle between the two disks adjacent to each subsegment. The bending plane angle $\theta_i$ was found for each subsegment by subtracting the two adjacent disks' angles, and the subsegment curvature was found by dividing $\theta_i$ by $L_0$. The error of this image processing step was estimated by determining the angle of gradations on a protractor, then determining the associated curvature for each given difference in angle. This was compared to the predicted curvature for the known difference in angle. The maximum curvature error was found to be 1.637%.

Figure 4.31 compares the experimentally measured continuum robot static equilibria to the calculated static equilibria from the virtual power model for tensions of 10, 20, and 30 N applied to rod $k = 1$. In each case, a pattern is observed where for each tension, the experimental results exhibit greater curvature in subsegment 1 than the virtual power simulation, reduced curvature in subsegment 2 compared to the virtual power simulation, and similar curvatures for subsegments 3 and 4, as shown in Fig. 4.32. This is due primarily to the assumption in the model that the actuation rods are held horizontal at the base of the robot. In the experimental prototype, the clearance between the routing holes for the rods allows for slight variation from horizontal. As a result, the elastic loading in the model is greater than the actual elastic loading in the prototype. This could be compensated for by adjusting the assumed boundary condition of the model at the base of the robot. However, even with this slight discrepancy, the errors of the modeled positions of the disks relative to the experimental results are all still less than 5%, with a maximum error of 4.89% occurring in disk 8 for the 30 N case.

Figure 4.33 compares the experimentally measured static equilibria to the calculated static equilibria from the virtual power model for tensions of 5, 10, and 15 N in rod $k = 5$. As seen in Fig. 4.32, the reduced elastic moment generated in subsegment 1 seen in the experimental prototype causes the measured configuration to consistently extend beyond the predicted

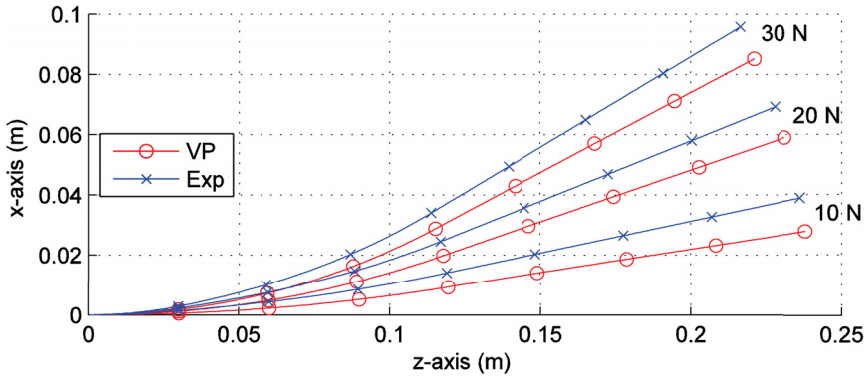


Figure 4.31: Comparison of the experimentally measured static equilibrium and the calculated static virtual power model equilibrium for tensions of 10, 20, and 30 N in rod $k = 1$.

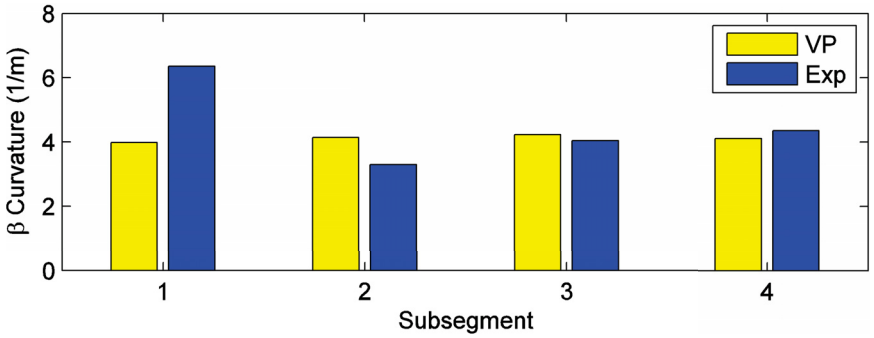


Figure 4.32: Comparison of $\beta$ curvatures for subsegments 14 for the experimentally measured static equilibrium and the calculated static virtual power model equilibrium for 30 N tension in rod $k = 1$.

shape. The maximum disk position error of 5.53% is seen in disk 8 for the 10 N actuation case.

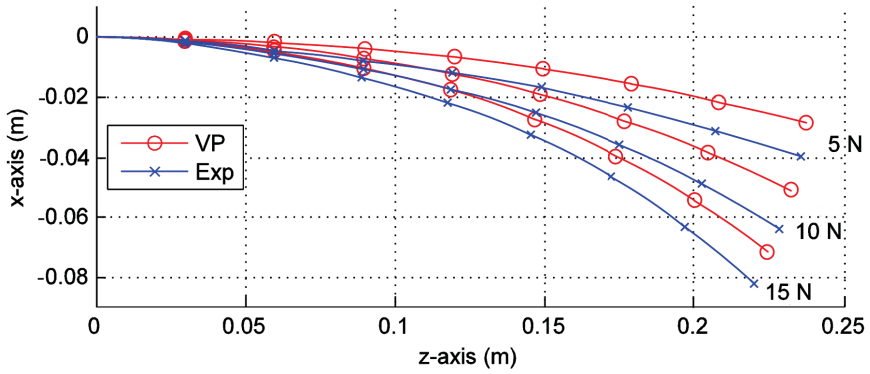


Figure 4.33: Comparison of the experimentally measured static equilibrium and the calculated static virtual power model equilibrium for tensions of 5, 10, and 15 N in rod $k = 5$.

The mutual actuation of rods $k = 1$ and $k = 5$ results allows for the quasi-independent control of these two segments. To validate this model, the impact of segment 2 loading on a robot with fixed segment 1 loading was considered. Rod $k = 1$ was tensioned with 25 N, and the tension in rod $k = 5$ was varied from 5 N to 15 N. Because of the previously demonstrated correlation between the steady-state component of the dynamic responses and the static equilibria, the static models are directly compared to the experimental results generated for the previously described loading conditions. Figure 4.34 illustrates the resulting experimental results and calculated static equilibria for the loading described above. The maximum error occurs of 8.02% occurs in disk 7 of the 5 N actuation case.

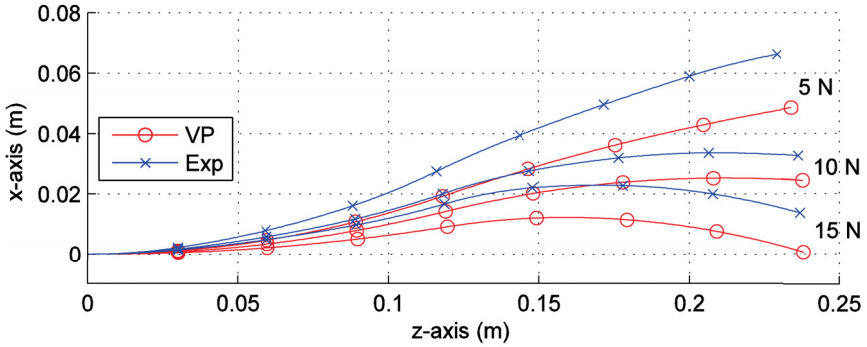


Figure 4.34: Comparison of the experimentally measured static equilibrium and the calculated static virtual power model equilibrium for a tension of 25 N in rod $k = 1$ and tensions of 5, 10, and 15 N in rod $k = 5$.

# Chapter 5

# Serpentine Tail Designs

When the continuum robotic structure was set aside, existing serpentine tail designs from the literature were considered. However, no existing design satisfied all of the design criteria, highlighted in chapter 3. To address this shortcoming, two novel serpentine tail designs meeting these criteria have been conceptualized, implemented and prototyped.

This chapter details the design concepts, mechanical designs, electrical designs and prototype implementation of the Roll-Revolute-Revolute Robotic Tail (R3RT, section 5.1) and the Universal-Spatial Robotic Tail (USRT, section 5.2).

## 5.1 Roll-Revolute-Revolute Robotic Tail (R3RT)

### 5.1.1 R3RT Design Concept

The Roll-Revolute-Revolute Robotic Tail, or R3RT, is a robotic tail capable of rotating its planar serpentine tail structure about a roll axis at its base. Its name stems from the tail's

three independent degrees of freedom: a roll joint at its base, and two segments comprised of links connected by parallel revolute joints capable of independent articulated bending. The defining characteristic of the tail structure is the use of nested cylindrical surfaces to route pairs of antagonistic cables along its length. As the R3RT's joints rotate, the antagonistic cable pair paths on these circular surfaces will lengthen and shorten by equal amounts, owing to the equal radii of the routing surfaces. In addition, the R3RT is also defined by the kinematic coupling used to enforce equal relative joint angles between the links comprising each of its actuated segments.

Details on the implementation of this R3RT concept as a mechanical design are discussed in section 5.1.2, its associated electrical design is provided in section 5.1.3, and its prototype implementation is shown in section 5.1.4.

### 5.1.2 R3RT Mechanical Design

The R3RT mechanical design, shown in Fig. 5.1, consists of a rigid housing, actuation unit and tail segments. The rigid housing connects to the load cell or legged robot and consists of two frames connected together with steel rods to provide lightweight, structural support to the R3RT. The actuation unit is supported by two coaxial bearings mounted to the ends of the rigid housing, and an internal gear mounted to the rear rigid housing support meshes with the actuation unit spur gear (Fig. 5.2) to enable the roll-DOF rotation. This roll angle is measured by an absolute encoder mounted to the rear frame and coupled to the actuation unit via a timing belt. A high-current-capacity, miniature slip ring (Orbex 300 Series) transmits control signals and motor current to the actuation unit while allowing for continuous roll rotation of the actuation module.

The tail actuation unit (Fig. 5.2) consists of three gear motors: one to actuate the roll-DOF,

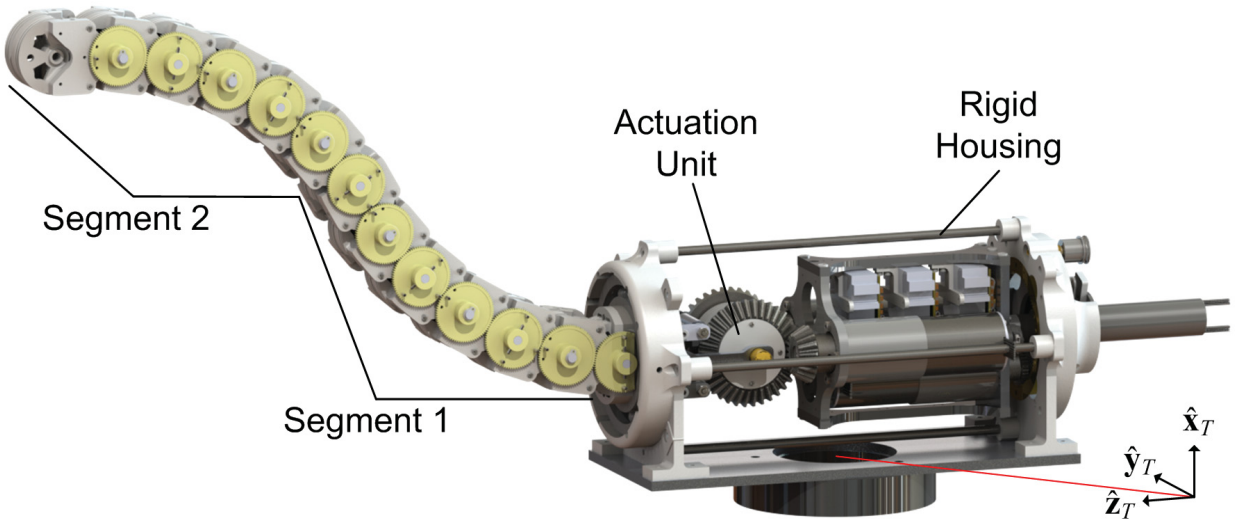


Figure 5.1: R3RT mechanical CAD design.

and two to actuate the tail segment bending DOFs. The roll-DOF motor is attached to a spur gear that meshes with the rigid housing's internal gear. The two tail segment bending gear motors are each coupled to a two-channel pulley (not visible in Fig. 5.2, located behind the bevel gear) through a pinion/bevel gear reduction. The pulleys are rigidly connected to both the bevel gear and the antagonistic cable pair used to actuate the motor's tail segment. Four adjustable tensioning mechanisms with passive rollers provide a means to individually tension each of the four cables (two antagonistic cables per actuated segment) to ensure a straight home configuration and minimize backlash.

Figure 5.1 shows the overall tail design concept. Twelve identical rigid bodies (links 1-12) are connected serially to create a two-segment robotic tail capable of "bending" in a rotating plane. Link 1 is connected to link 0 through a pitch-direction (when the roll angle is zero) revolute joint, which is rigidly attached to the actuation unit's segment plate (Fig. 5.2).

The remaining 11 links are connected by revolute joints parallel to the joint between links 0 and 1. As a consequence of this design, when the roll angle is $\pm 90°$, the tail remains in its configuration without requiring cable actuation. Distinct segments are created by

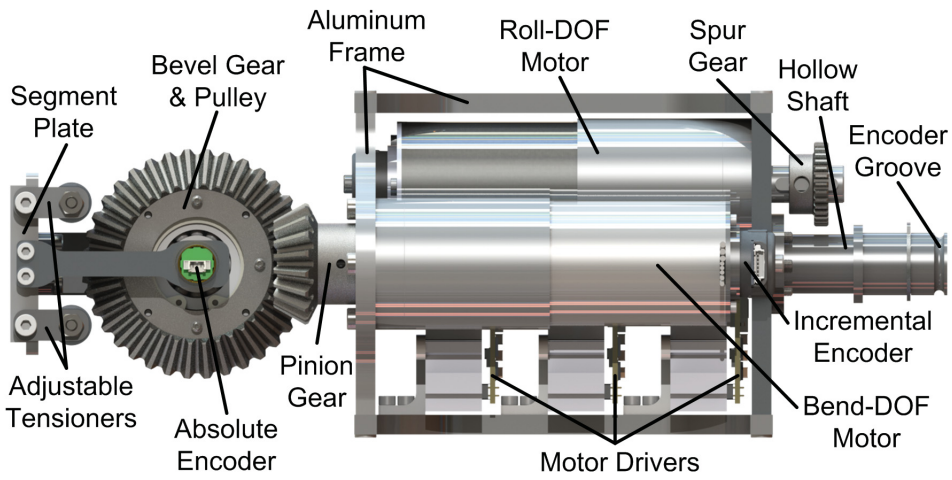


Figure 5.2: R3RT actuation module CAD design.

terminating pairs of antagonistic cables along the robot: in Fig. 5.1, two segments are created by terminating cable pairs at links 6 and 12. The two segment structure measures 500 mm in length, has a 50 x 70 mm cross-section, and has a minimum mass of 0.91 kg.

The R3RT decouples its segment actuation and ensures equal and opposite antagonistic cable displacements through its link design and cable routing scheme. Cables are routed along nested cylindrical surfaces designed into the links to ensure equal cable extension/retraction of the antagonistic cable pair during tail motion. Figure 5.3a illustrates this configuration and shows cable routing for a four-link segment that resembles the cable routing scheme used to actuate segment 1 (where two cables are terminated at the end link within the tail segment and the left link is considered fixed ground). The antagonistic cable displacements are defined by the linear relationship $\pm r_{cbl}\theta_j$, where $r_{cbl}$ is the radius of the cylindrical contour and $\theta_j$ is the relative rotations between links $i = j - 1$ and $i = j$. The nested cylinder cable routing approach enables the use of a single pulley to control the extension and retraction of an antagonistic cable pair without the need to account for variations in cable extension and retraction. This is because the joint angles increases and decreases the cable path by equal angles on each side over the same radius.

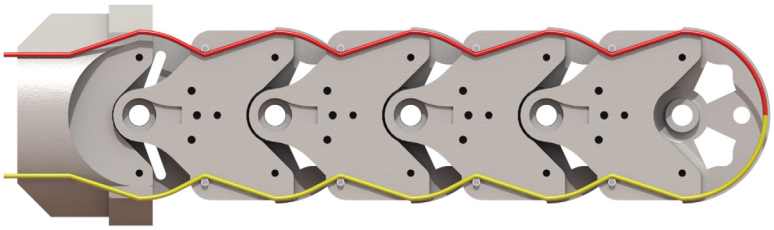

(a) Cable routing to generate bending motion in segment

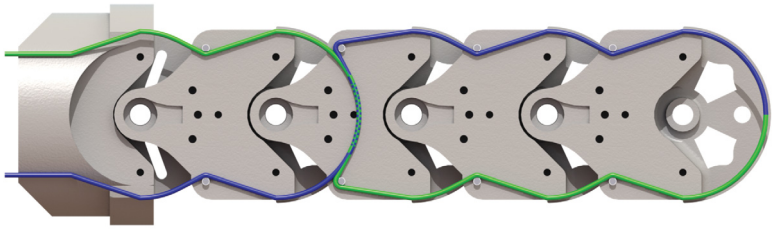

(b) Cable routing to generate zero cable displacement due to segment motion

Figure 5.3: R3RT cabling.

To simplify control, the actuation of segments 1 and 2 are mechanically decoupled. Two cables terminate at link 12 in segment 2 and route through segment 2 similar to segment 1 shown in Fig. 5.3a. However, in segment 1, the segment 2 cabling routes along an S-path and cross in the middle of segment 1 as shown in Fig. 5.3b. With this S-path routing, the first half of the cable path will extend by some length and the second half of the cable path will shorten by the same length, or vice versa (the first and second halves will shorten and extend, respectively). This routing creates a null space for the segment 2 actuation cabling with respect to the motion of segment 1. However, this assumes that the joint angles along the segment are all equal.

To ensure the 6 joint angles are equal within a segment, the R3RT utilizes 5 gear pairs mounted along the segment. The gears in each pair are mounted on two links separated by a single link, as shown in Fig. 5.4a. For example, in gear pair 1, the first gear (red) meshes with the second gear (purple) with an intermediate link (yellow) separating the gears' associated rigid bodies.

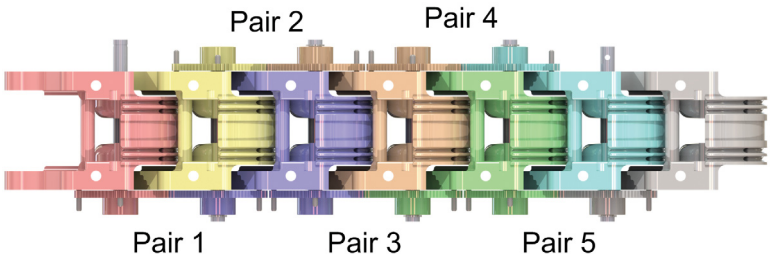


(a) Single-segment gear arrangement

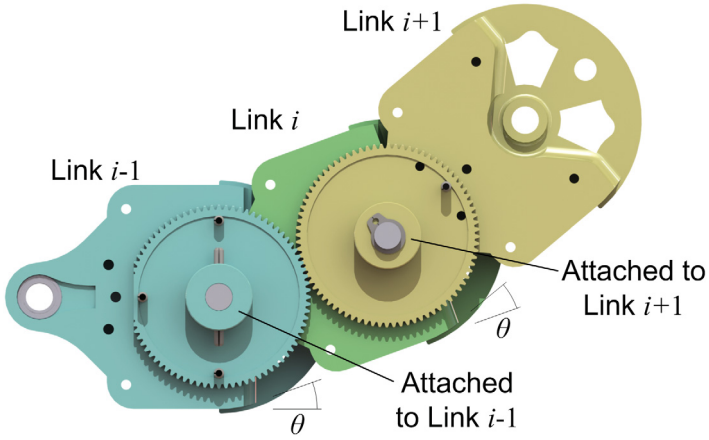


(b) Angle constraint from gear pair. Parts sharing a color are rigidly attached.

Figure 5.4: R3RT gearing.

To ensure equal angles along the segment, the gears in each pair have equal pitch diameters. For the gear pair associated with three sequential links $i-1$, $i$ and $i+1$, shown in Fig. 5.4b, gears are rigidly attached to links $i-1$ and $i+1$, with link $i$ separating the links. If link $i-1$ is held fixed, link $i$ will rotate by angle $\theta$ relative to link $i-1$, and link $i+1$ will rotate by $\theta$ relative to link $i$. This is done for the five sequential triplets of links 0-6 (segment 1) and 6-12 (segment 2).

### 5.1.3 R3RT Electrical Design

Figure 5.5 shows the R3RT's electrical design. To control the system, two Teensy 3.2 ARM microcontrollers (MCUs) are used, with one acting as master and the other as slave. These MCUs communicate over an UART connection through the slip ring. The master MCU is mounted to the rigid housing and connects the user PC and the slave MCU. The master MCU receives the tail's actuation input trajectories from the user and transfer to the slave MCU through the UART connection. The master MCU also allows the user to exercise software control over motor power through a high side MOSFET switch. The master MCU housing also connects the power supply to the slip ring through an emergency cut-off switch.

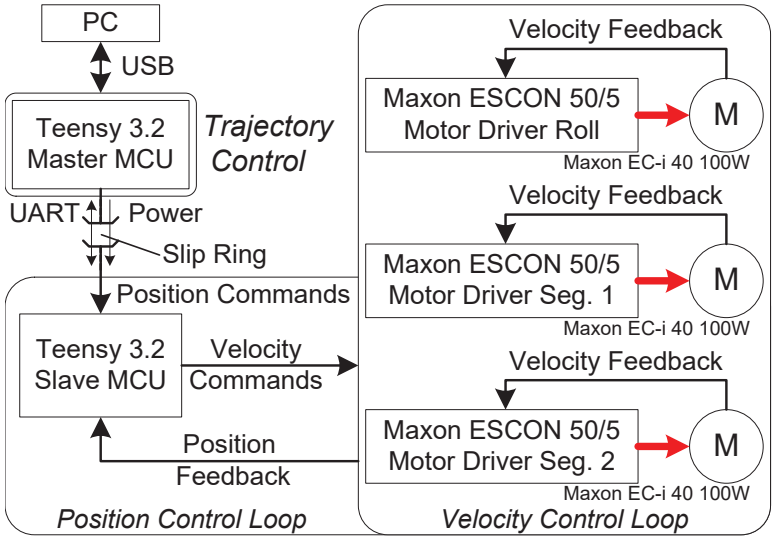


Figure 5.5: R3RT electrical design with inner-loop velocity control and outer-loop position control. M denotes motor.

The slave MCU is incorporated into the actuation module to ensure stable connections with the sensors and motor drivers. The slave MCU maps the inputs from the master MCU into analog voltage commands to the motor drivers prescribing either motor speed or motor torque commands. Each motor is controlled by a motor driver (Maxon ESCON 50/5) operating either a PI motor velocity control loop or a motor current control loop.

### 5.1.4 R3RT Prototype Implementation

Figure 5.6 shows the R3RT experimental prototype. The tail links and rigid housing frames were printed using ABS plastic. The remaining custom structural components were fabricated from metal (steel for shafts, aluminum for other components). Braided nylon cables (MagicShield) rated for 441 N (100 lbs) were used to actuate the tail; segment 1 actuation required double routed cable lines to accommodate the high impulsive tensions generated during tail motions. During integration, the cable routing was optimized though a series of experimental iterations to minimize friction effects by relieving aggressive cable routing angles about the small sized pins with passive rollers.

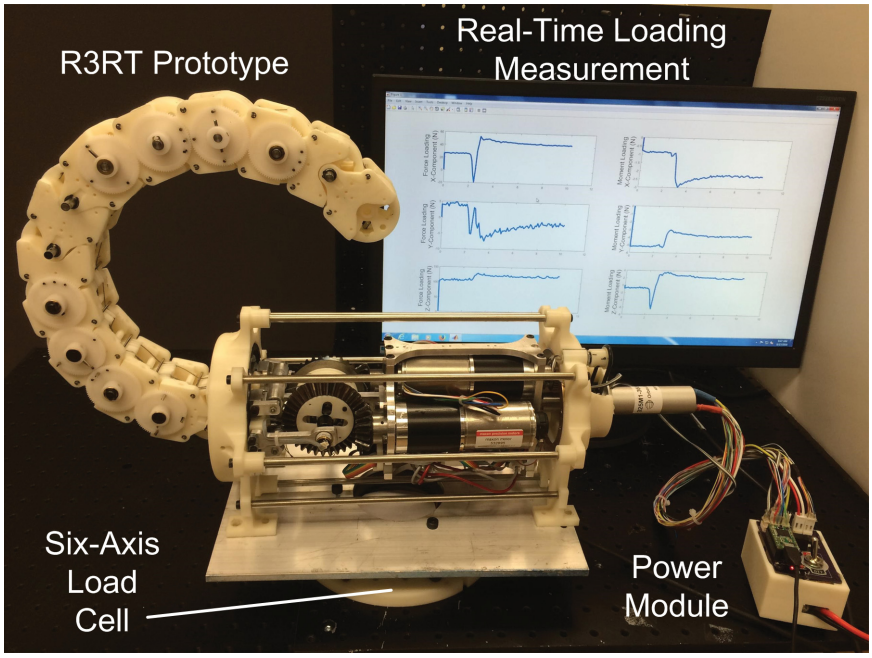


Figure 5.6: R3RT experimental prototype.

To generate high inertial loading, the R3RT is actuated using three Maxon 100 W brushless DC motors (EC-i 40). These motors were chosen to exceed the torque requirements for the experiments considered in this work to provide an experimental test platform capable of analyzing a wide variety of potential tail structures with various dimensions and mass

properties. Gear reductions were selected to balance considerations for cable speed and force requirements estimated for a range of possible robotic tails.

As discussed in section III-C, two of the three motors control the independent bending of the R3RT segments through antagonistically-actuated cable mechanisms. A bevel gear train with 2:1 reduction drives the cable pulley, and a gearbox with reduction 15:1 drives the pinion gear. The pulley radius matches the cylindrical cable routing radius $r_{cbl}$ of the linkages, which makes the pulley rotation and segment bending angle equal (e.g., if the segment 1 pulley rotates 45°, segment 1 will bend 45°). The third motor controls the R3RT actuation module roll-angle using a spur gear coupled to an internal gear (with a gear reduction of 3:1 in addition to a 15:1 gearbox). Incorporating the roll motor within the actuation unit reduces the rigid housing cross-section at the cost of increased power required to produce roll motion due to the additional inertia. However, in this design, the motors are close to the roll axis, minimizing their contributions to the net actuation unit inertia.

## 5.2 Universal-Spatial Robotic Tail (USRT)

### 5.2.1 USRT Design Concept

The Universal-Spatial Robotic Tail, or USRT, is a robotic tail capable of intrinsically spatial pitch and yaw bending of its quasi-independently actuated segments. Its name stems from the universal joints that comprise the structure, and the inherently spatial workspace they provide. Unlike the R3RT, which can only bend in two directions from its extended configuration without rotating the bending plane, the USRT can intrinsically bend in any direction from its extended configuration. However, the USRT also requires three additional motors (six total) controlling the coupled motion of individual actuation cables, instead of the three

motors controlling the R3RT's three decoupled DOFs.

The tail's behavior is similar to the elastic core continuum robots considered in Chapter 4, with one key differences: the universal joints constrain the relative roll (or twist) between disks, which eliminates a significant source of undesired sag in the mechanism. Although the combined motion of the pitch and yaw joints can create roll-like tail motions that can sag the structure when bent out of plane, this is no longer aided by twist between disks.

Unlike other similar serpentine robot designs, such as [6, 19, 28], the USRT is designed for cantilevered operation. The tail's elastic loading is asymmetric in the vertical and horizontal directions, with non-zero elastic loading at the joint's zero-angle configuration to counteract the gravitational moment induced in each joint. In addition, the vertical elastic loading is also scaled along the length of the USRT: toward the tip, lower elastic loading reflects the reduced gravitational loading acting at those joint, whereas higher stiffness springs are used toward the base.

Details on the implementation of this USRT concept as a mechanical design are discussed in section 5.2.2, its associated electrical design is provided in section 5.2.3, and its prototype implementation is shown in section 5.2.4.

### 5.2.2 USRT Mechanical Design

The USRT, shown in Fig. 5.7, is composed of a serial chain of six links connected by universal joints that permit relative pitch and yaw. The six links are organized into two quasi-independently actuated segments 1 and 2. Figure 5.8 shows joint $j$ between disks $i = j - 1$ and $i = j$. In addition to the universal joint between these links, two springs are mounted (extension and compression), along with actuation cabling, two distance sensors, and a joint angle limit.

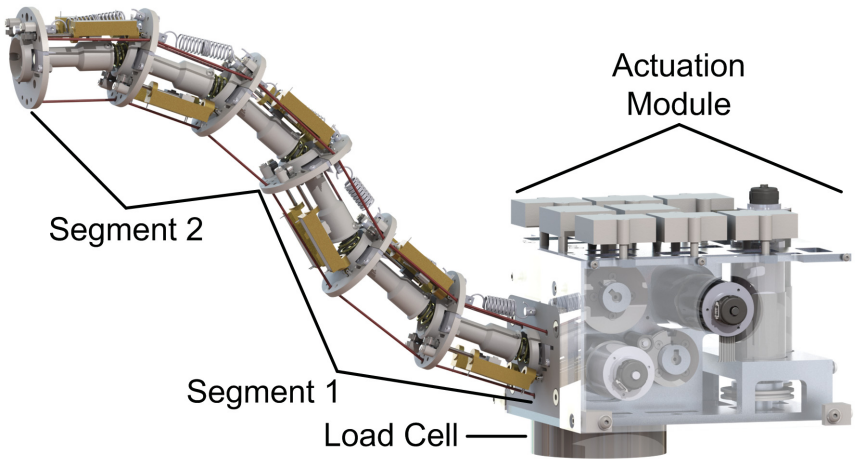


Figure 5.7: USRT mechanical design.

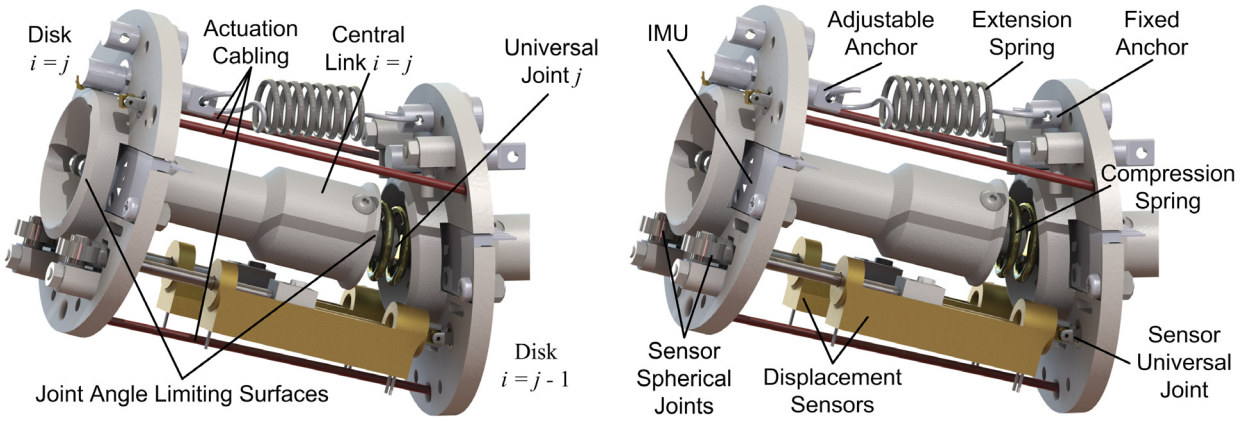


(a) Structure and actuation

(b) Elasticity and sensing

Figure 5.8: USRT joint design.

The joint angle limit prevents the angular displacement of the universal joint from exceeding a fixed maximum. To implement the joint limit, a pair of axisymmetric beveled surfaces are incorporated into the designs of disk $i = j - 1$ and the base of central link $i = j$. The beveled surfaces are parallel and in contact when the joint angle limit is reached, and the axisymmetric design allows the surface to "roll" along the mated beveled surfaces at the maximum deflection as the pitch and yaw angles are varied. This provides a uniform maximum workspace for each joint when planning tail motions and prevents the need for the displacement sensors to stop joint motion at their limits.

In addition, although the universal joints only permit relative pitch and yaw between links, a rolling motion can be created by multiple joints acting together, as shown in Fig. 5.9. In this illustration, the pitch and yaw angles are varied sinusoidally to roll the tail COM around the mounting plate centerline.

### USRT Elasticity

Two sources of elastic loading are incorporated into each joint: (1) a compression spring surrounding the universal joint that resists bending equally in all directions as the universal joint pitches and yaws, and (2) an extension spring mounted between adjacent links to help compensate for gravitational loading.

The compression spring provides a compact means of distributing actuation loading within an actuated segment. These springs provide axisymmetric mechanical coupling between links to prevent the cable actuation from only causing bending in a single joint (the extension spring only acts in the pitch direction). The compression spring is housed within the central link, and the portion exposed between adjacent links contributes to the bending resistance.

The extension spring modifies the joint's elasticity in the pitch direction to help offset the

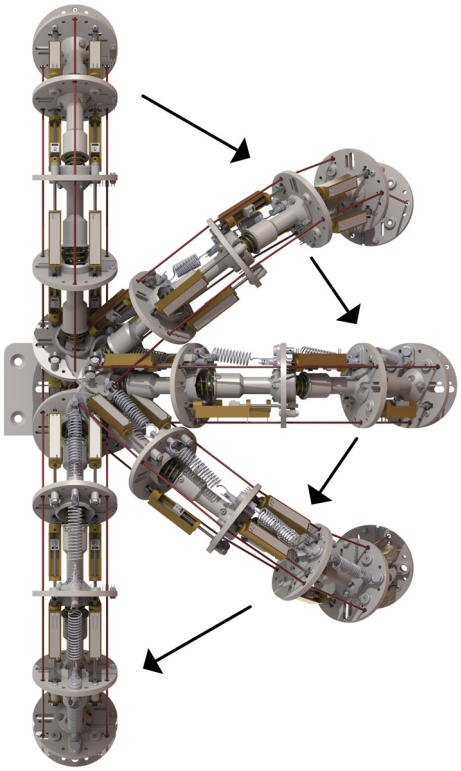

Figure 5.9: Stroboscopic composite of a USRT rolling motion through $-180°$ with tail bent $180°$, shown in $45°$ increments.

effect of gravity. Because of the differences in gravitational moments at joints along the tail (i.e., the gravitational moments near the base is significantly higher than the gravitational moment near the tip), the elastic loading required from this spring varies. This can be achieved by varying the springs' stiffnesses, unloaded lengths and/or anchor-point distances. Spring stiffness and unloaded length are functions of the spring chosen for inclusion in the design; for a fixed unloaded length, higher stiffness correlates to higher force, and for a fixed stiffness, shorter unloaded length generate higher force for a fixed distance between anchor points. As shown in Fig. 5.8b, the USRT design incorporates an adjustable anchor to allow for variation of the distance between anchor points. The fixed anchor in Fig. 5.8b is designed such that the spring anchor point is an equal distance from the disk surface as the central universal joint. This minimizes the effect of the extension spring on yaw-direction loading.

### USRT Actuation

A spool is mounted to the output shaft of each gearmotor, and a cable routed along the USRT is attached to this spool. An actuated segment is created by ending/tying off sets of three actuation cables at a specific disk. The first actuated segment is from the tail base to the first disk to which cables are tied off, and subsequent segments are from the previous segment's terminal link to the next link at which cables are tied off. Actuation is applied by three cables routed through holes at a fixed radius with 120° between holes around the disk center.

Cables terminating in different segments are co-routed through the same holes to simplify control. For example, if prescribing the desired cable velocities for a two-segment structure, to account for the change in cable path lengths in segment 1 for the segment 2 cabling, the prescribed segment 1 cable velocities can be added to the desired segment 2 cable velocities. This feature will also aid in the formulation of the cable tensioning contribution of the USRT's inner-loop controller in section 7.3.2.

During operation, in each segment, two of the three cables will actively contribute to the tail segment motion. These active cables generate the desired motion of the segment and dictate its shape. The passive cable will either follow the segment trajectory established by the other two cables or maintain a nominal tension during operation. It is important that the passive cable not over-slack as the subset of two active cables may change during tail motion.

### USRT Sensors

Sensors integrated along the tail allow for estimation of the joint angles and velocities of each universal joint. Two displacement sensors (Fig. 5.8b) are mounted between the disks

separated by each joint to measure the distances between pairs of fixed points on each disk. These distances can be used to analytically calculate the pitch and yaw joint angles of the universal joint, providing a mechanism for sensing the real-time tail configuration.

An inertial measurement unit (IMU, Fig 5.8b) that includes a gyroscope is also mounted to each link. Utilizing the body-fixed angular velocity measurements from the gyroscope, along with the estimates of the relative pitch and yaw of adjacent links from the displacement sensors, the universal joint pitch and yaw velocities may also be estimated.

### 5.2.3 USRT Electrical Design

The tail motors are controlled by six ESCON 50/5 Maxon motor drivers operating in either a PI velocity control mode or a motor current control mode. Sensor feedback for each motor control loop is a US Digital Miniature Optical Kit Encoder (part #E4T-360-236-DHMB) mounted to the motor shaft and Hall effect sensors incorporated into the motor. For the desired tail motion, LabView was used generated to transmit desired velocity or motor current trajectories at 10 ms intervals (100 Hz) to an ARM Cortex M4 microcontroller that interfaces with the six motor drivers. The tail was powered using a 37 V LiPo battery connected to the motors drivers through the R3RT's power regulator.

### 5.2.4 USRT Prototype Implementation

Figure 5.10 shows the USRT experimental test platform. Structural components of the tail were made of thermoplastic using a Stratasys uPrint 3D printer and were connected by commercial universal joints from SDP/SI (Molded Universal Joints, 3/8 inch OD with 3/16 inch Bore Insert, part #A-5Z-8-D306). Commercial compression and extension springs with properties defined in Tables 6.2 and 6.3 were utilized, and spring anchor positions were

adjusted so that the tail is extended (approximately straight) in the absence of actuation.

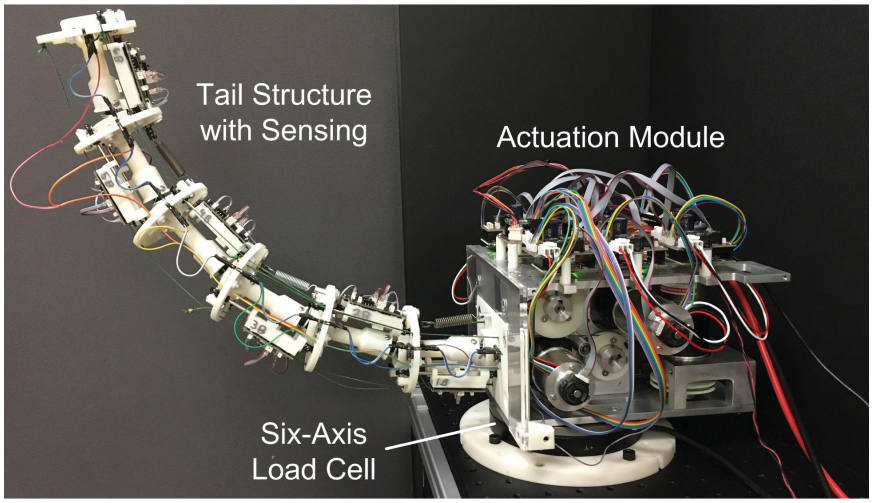


Figure 5.10: USRT experimental prototype.

Six brushless EC-i 40 Maxon motors (36 V) were used to actuate the prototype: three 100W brushless motors for segment 1 (part #496661), and three 70W motors for segment 2 (part #496655). The segment 1 motors are higher power than the segment 2 motors due to the increased inertial loading acting on the segment 1 joints due to the presence of segment 2. Gear reductions (15:1 for segment 1, 26:1 for segment 2) and cable spool diameters (34 mm for segment 1, 49 mm for segment 2) were chosen so that the tail would be capable of bending from 0 to 180° in 0.25 sec without exceeding the motors' velocity limits. The gear reduction and spool diameter were chosen to accomplish this goal with maximum gear ratio and minimum spool diameter, to maximize the force the cable can support given the motor's torque limitations.

# Chapter 6

# Serpentine Tail Dynamics

Based on the R3RT and USRT designs presented in Chapter 5, kinematic and dynamic models for the R3RT (section 6.1) and USRT (section 6.2) have been defined. These sections define the state vectors, control inputs and equations of motion of the tails, formulate the tails' kinematic and loading models, calculate the loading the tails applies at their bases, simulate the tails' loading capabilites and compare these simulations to experimental results.

Owing to the limited number of Latin and Greek characters, the same variables can have different meanings for the continuum tail, R3RT and USRT models. As a result, each of these sets of models should be considered independently of one another. As a consequence of this, there are some formulations for the R3RT and USRT models (such as the inertial and gravitational loading) that are nearly duplicated in their respective R3RT and USRT sections. This is to avoid "crossing the streams" and allows sections 6.1 and 6.2 to stand on their own to represent their tail models.

## 6.1 Roll-Revolute-Revolute Robotic Tail Model

### 6.1.1 R3RT State, Control and Equations of Motion

The R3RT's kinematic state may be represented by three variables: the roll angle $\phi$ and the segment 1 and 2 relative joint angles $\beta_1$ and $\beta_2$. Only two relative joint angles are needed to represent the state of the 12-DOF tail structure due to the 10 kinematic constraints imposed by the 10 gear pairs. These state variables are collected into the state vector $\mathbf{q}$ defined in Eq. 6.1.

$$\mathbf{q} = \begin{bmatrix} \phi \\ \beta_1 \\ \beta_2 \end{bmatrix} \tag{6.1}$$

The R3RT's three control inputs are the actuation module torque $\tau$, the segment 1 cable tension $T_1$ and the segment 2 cable tension $T_2$. These scalar values are collected into the control input vector $\mathbf{u}$ defined in Eq. 6.2.

$$\mathbf{u} = \begin{bmatrix} \tau \\ T_1 \\ T_2 \end{bmatrix} \tag{6.2}$$

The R3RT's 13 revolute joints lead to 13 equations of motion. If the net moment $\mathbf{M}_{j,jnt}$ is calculated at the joint $j$ center, the projection of $\mathbf{M}_{j,jnt}$ onto the joint $j$ axis unit vector $\hat{\boldsymbol{\xi}}_j$ equals zero, shown in Eq. 6.3, as a revolute joint cannot support a moment about its joint axis.

$$\hat{\boldsymbol{\xi}}_j \cdot \mathbf{M}_{j,jnt} = 0, \quad j \in \{0, \cdots, 12\} \tag{6.3}$$

These 13 equations are a set of differential-algebraic equations defined by three differential variables ($\mathbf{q}$) and ten algebraic variables (the gear pairs' contact forces). Algebraic manipulation can be used to reduced these 13 differential-algebraic equations into the three ordinary differential equations defined by Eq. 6.4, where $\mathbf{M}(\mathbf{q})$ is the tail's inertia matrix, $\mathbf{C}(\mathbf{q}, \dot{\mathbf{q}})\,\dot{\mathbf{q}}$ is the tail's centripetal and Coriolis loading effects, $\mathbf{g}(\mathbf{q})$ is the tail's gravitational loading, and $\mathbf{T}(\mathbf{q})$ is the tail's actuation transmission matrix.

$$\mathbf{M}(\mathbf{q})\,\ddot{\mathbf{q}} + \mathbf{C}(\mathbf{q}, \dot{\mathbf{q}})\,\dot{\mathbf{q}} + \mathbf{g}(\mathbf{q}) = \mathbf{T}(\mathbf{q})\,\mathbf{u} \tag{6.4}$$

### 6.1.2 R3RT Kinematic Analysis

First, to aid in the recursive formulation of the kinematic analysis, $\beta_1$ and $\beta_2$ are mapped into the joint $j$ angle $\theta_j$, defined in Eq. 6.5.

$$\theta_j = \begin{cases} \beta_1, & 1 \leq j \leq 6, \\ \beta_2, & 7 \leq j \leq 12 \end{cases} \tag{6.5}$$

Using these angles, the orientation $\mathbf{R}_i$ of link $i$ with respect to the inertial tail frame is defined using Eq. 6.6, where $\mathbf{R}_Z(\cdot)$ and $\mathbf{R}_Y(\cdot)$ are rotation matrices for z- and y-axis rotations, respectively, by the angle $(\cdot)$. The link $i$ orientations can be used to calculate revolute joint $j$ axis unit vector $\hat{\boldsymbol{\xi}}_j$, as shown in Eq. 6.7, where $\hat{\mathbf{z}}_j^j$ and $\hat{\mathbf{y}}_j^j$ are the frame $j$ z- and y-axis unit vectors, respectively.

$$\mathbf{R}_i = \begin{cases} \mathbf{R}_Z(\phi), & i = 0, \\ \mathbf{R}_{i-1}\mathbf{R}_Y(\theta_i), & 1 \leq i \leq 12 \end{cases} \tag{6.6}$$

$$\hat{\boldsymbol{\xi}}_j = \begin{cases} \mathbf{R}_j \hat{\mathbf{z}}_j^j, & j = 0 \\ \mathbf{R}_j \hat{\mathbf{y}}_j^j, & 1 \leq j \leq 12 \end{cases} \tag{6.7}$$

The position vectors from the inertial tail frame origin to the joint $j$ center $\mathbf{p}_{j,jnt}$ and link $i$ COM $\mathbf{p}_{i,COM}$ are defined in Eqs. 6.8 and 6.9, respectively, where $\mathbf{p}_{T0,jnt}$ is the position from the inertial tail frame origin to the joint 0 center, $\mathbf{p}^0_{01,jnt}$ is the position from the joint 0 center to the joint 1 center, $L_{JJ}$ is the distance each link's joint centers, $\mathbf{p}^0_{0,JC}$ is the position from the joint 0 center to the link 0 COM and $L_{JC}$ is the distance between a link's proximal joint center and its COM. In addition, $\mathbf{p}_{j,i,JC}$ in Eq. 6.10 defines the position from joint $j$ to the link $i$ COM.

$$\mathbf{p}_{j,jnt} = \begin{cases} \mathbf{p}_{T0,jnt}, & j = 0, \\ \mathbf{p}_{0,jnt} + \mathbf{R}_0 \mathbf{p}^0_{01,jnt}, & j = 1 \\ \mathbf{p}_{j-1,jnt} + L_{JJ}\mathbf{R}_{j-1}\hat{\mathbf{z}}_{j-1}^{j-1}, & 2 \leq j \leq 12 \end{cases} \tag{6.8}$$

$$\mathbf{p}_{i,COM} = \begin{cases} \mathbf{p}_{0,jnt} + \mathbf{R}_0 \mathbf{p}^0_{0,JC}, & i = 0 \\ \mathbf{p}_{i,jnt} + L_{JC}\mathbf{R}_i \hat{\mathbf{z}}_i^i, & 1 \leq i \leq 12 \end{cases} \tag{6.9}$$

$$\mathbf{p}_{j,i,JC} = \mathbf{p}_{i,COM} - \mathbf{p}_{j,jnt} \tag{6.10}$$

For the rotational kinematics, the link $i$ angular velocities $\boldsymbol{\omega}_i$ are defined in Eq. 6.11 based

on the roll DOF between the rigid housing and link 0 and the pitch DOFs between links $i-1$ and $i$ for $1 \leq i \leq 12$, where $\dot{\phi}$ denotes the time derivative of $\phi$.

$$\boldsymbol{\omega}_i = \begin{cases} \dot{\phi}\hat{\boldsymbol{\xi}}_i, & i = 0, \\ \boldsymbol{\omega}_{i-1} + \dot{\theta}_i\hat{\boldsymbol{\xi}}_i, & 1 \leq i \leq 12 \end{cases} \tag{6.11}$$

### 6.1.3 R3RT Loading Analysis

Four loading effects contribute to $\mathbf{M}_{j,jnt}$: inertia ($\mathbf{M}_{j,inr}$), gravity ($\mathbf{M}_{j,grv}$), gearing ($\mathbf{M}_{j,gear}$), and actuation ($\mathbf{M}_{j,act}$), shown in Eq. 6.12.

$$\mathbf{M}_{j,jnt} = \mathbf{M}_{j,inr} - \mathbf{M}_{j,grv} - \mathbf{M}_{j,gear} - \mathbf{M}_{j,act} \tag{6.12}$$

#### R3RT Inertial Loading

The inertial moment $\mathbf{M}_{j,inr}$ depends on the links "downstream" of the joint. For joint $j$, Eq. 6.13 defines the inertial moment generated by links $i = j$ through $i = 12$, where $\mathbf{F}_{i,inr,bdy}$ and $\mathbf{M}_{i,inr,bdy}$ are the link $i$ inertial force and moment, respectively.

$$\mathbf{M}_{j,inr} = \sum_{i=j}^{12} (\mathbf{M}_{i,inr,bdy} + \mathbf{p}_{j,i,JC} \times \mathbf{F}_{i,inr,bdy}) \tag{6.13}$$

These link $i$ inertial forces and moments are defined in Eqs. 6.14 and 6.15, where $m_{i,bdy}$ is the link $i$ mass, $\mathbf{I}_{i,bdy}$ is the link $i$ inertia tensor defined in Eq. 6.16, $\mathbf{I}^i_{i,bdy}$ is the constant body-frame-fixed link $i$ inertia tensor, $\ddot{\mathbf{p}}_{i,COM}$ is the link $i$ COM linear acceleration and $\dot{\boldsymbol{\omega}}_i$ is the link $i$ angular acceleration.

$$\mathbf{F}_{i,inr,bdy} = m_{i,bdy}\ddot{\mathbf{p}}_{i,COM} \tag{6.14}$$

$$\mathbf{M}_{i,inr,bdy} = \mathbf{I}_{i,bdy}\dot{\boldsymbol{\omega}}_i + \boldsymbol{\omega}_i \times \mathbf{I}_{i,bdy}\boldsymbol{\omega}_i \tag{6.15}$$

$$\mathbf{I}_{i,bdy} = \mathbf{R}_i\mathbf{I}^i_{i,bdy}\mathbf{R}_i^T \tag{6.16}$$

To formulate the $\mathbf{M}$ and $\mathbf{C}$ matrices, Jacobian-based formulations of $\ddot{\mathbf{p}}_{i,COM}$, $\boldsymbol{\omega}_i$ and $\dot{\boldsymbol{\omega}}_i$ are needed, as defined in Eqs. 6.17, 6.18 and 6.19, where $\mathbf{J}_{\mathbf{p},i}$ is the link $i$ COM linear velocity Jacobian and $\mathbf{J}_{\boldsymbol{\omega},i}$ is the link $i$ angular velocity Jacobian.

$$\ddot{\mathbf{p}}_{i,COM} = \mathbf{J}_{\mathbf{p},i}\ddot{\mathbf{q}} + \dot{\mathbf{J}}_{\mathbf{p},i}\dot{\mathbf{q}} \tag{6.17}$$

$$\boldsymbol{\omega}_i = \mathbf{J}_{\boldsymbol{\omega},i}\dot{\mathbf{q}} \tag{6.18}$$

$$\dot{\boldsymbol{\omega}}_i = \mathbf{J}_{\boldsymbol{\omega},i}\ddot{\mathbf{q}} + \dot{\mathbf{J}}_{\boldsymbol{\omega},i}\dot{\mathbf{q}} \tag{6.19}$$

With these, $\mathbf{F}_{i,inr,bdy}$ and $\mathbf{M}_{i,inr,bdy}$ can be reformulated as shown in Eqs. 6.20 and 6.21, and used in conjunction with Eq. 6.13 to calculate $\mathbf{M}$ and $\mathbf{C}$ using Eqs. 6.22 and 6.23.

$$\mathbf{F}_{i,inr,bdy} = m_{i,bdy}\mathbf{J}_{\mathbf{p},i}\ddot{\mathbf{q}} + m_{i,bdy}\dot{\mathbf{J}}_{\mathbf{p},i}\dot{\mathbf{q}} \tag{6.20}$$

$$\mathbf{M}_{i,inr,bdy} = \mathbf{I}_{i,bdy}\mathbf{J}_{\boldsymbol{\omega},i}\ddot{\mathbf{q}} + \left(\mathbf{I}_{i,bdy}\dot{\mathbf{J}}_{\boldsymbol{\omega},i} + \boldsymbol{\omega}_i \times \mathbf{I}_{i,bdy}\mathbf{J}_{\boldsymbol{\omega},i}\right)\dot{\mathbf{q}} \tag{6.21}$$

$$\mathbf{M} = \begin{bmatrix} \hat{\boldsymbol{\xi}}_0 \cdot \sum_{i=0}^{12} \left( \mathbf{I}_{i,bdy} \mathbf{J}_{\boldsymbol{\omega},i} + m_{i,bdy} \mathbf{p}_{0,i,JC} \times \mathbf{J}_{\mathbf{p},i} \right) \\ \sum_{j=1}^{6} \left( \hat{\boldsymbol{\xi}}_j \cdot \sum_{i=j}^{12} \left( \mathbf{I}_{i,bdy} \mathbf{J}_{\boldsymbol{\omega},i} + m_{i,bdy} \mathbf{p}_{j,i,JC} \times \mathbf{J}_{\mathbf{p},i} \right) \right) \\ \sum_{j=7}^{12} \left( \hat{\boldsymbol{\xi}}_j \cdot \sum_{i=j}^{12} \left( \mathbf{I}_{i,bdy} \mathbf{J}_{\boldsymbol{\omega},i} + m_{i,bdy} \mathbf{p}_{j,i,JC} \times \mathbf{J}_{\mathbf{p},i} \right) \right) \end{bmatrix} \tag{6.22}$$

$$\mathbf{C} = \begin{bmatrix} \hat{\boldsymbol{\xi}}_0 \cdot \sum_{i=0}^{12} \left( \mathbf{I}_{i,bdy} \dot{\mathbf{J}}_{\boldsymbol{\omega},i} + \boldsymbol{\omega} \times \mathbf{I}_{i,bdy} \mathbf{J}_{\boldsymbol{\omega},i} + m_{i,bdy} \mathbf{p}_{0,i,JC} \times \dot{\mathbf{J}}_{\mathbf{p},i} \right) \\ \sum_{j=1}^{6} \left( \hat{\boldsymbol{\xi}}_j \cdot \sum_{i=j}^{12} \left( \mathbf{I}_{i,bdy} \dot{\mathbf{J}}_{\boldsymbol{\omega},i} + \boldsymbol{\omega}_i \times \mathbf{I}_{i,bdy} \mathbf{J}_{\boldsymbol{\omega},i} + m_{i,bdy} \mathbf{p}_{j,i,JC} \times \dot{\mathbf{J}}_{\mathbf{p},i} \right) \right) \\ \sum_{j=7}^{12} \left( \hat{\boldsymbol{\xi}}_j \cdot \sum_{i=j}^{12} \left( \mathbf{I}_{i,bdy} \dot{\mathbf{J}}_{\boldsymbol{\omega},i} + \boldsymbol{\omega}_i \times \mathbf{I}_{i,bdy} \mathbf{J}_{\boldsymbol{\omega},i} + m_{i,bdy} \mathbf{p}_{j,i,JC} \times \dot{\mathbf{J}}_{\mathbf{p},i} \right) \right) \end{bmatrix} \tag{6.23}$$

### R3RT Gravitational Loading

Similar to $\mathbf{M}_{j,inr}$, the gravitational moment $\mathbf{M}_{j,grv}$ at joint $j$ is due to the gravitational forces $\mathbf{F}_{i,grv,bdy}$ acting on links $i = j$ through $i = 12$. Equations 6.24 and 6.25 define $\mathbf{M}_{j,grv}$ and $\mathbf{F}_{i,grv,bdy}$, respectively, where $g$ is gravitational acceleration and $\hat{\mathbf{x}}_T$ is the inertial tail frame x-axis unit vector.

$$\mathbf{M}_{j,grv} = \sum_{i=j}^{12} \left( \mathbf{p}_{j,i,JC} \times \mathbf{F}_{i,grv,bdy} \right) \tag{6.24}$$

$$\mathbf{F}_{i,grv,bdy} = -m_{i,bdy} g \hat{\mathbf{x}}_T \tag{6.25}$$

Equation 6.26 uses $\mathbf{M}_{j,grv}$ in conjunction with the joint $j$ axes $\hat{\boldsymbol{\xi}}_j$ to formulate the $\mathbf{g}$ vector.

$$\mathbf{g} = \begin{bmatrix} \hat{\boldsymbol{\xi}}_0 \cdot \mathbf{M}_{0,grv} \\ \sum_{j=1}^{6} \left( \hat{\boldsymbol{\xi}}_j \cdot \mathbf{M}_{j,grv} \right) \\ \sum_{j=7}^{12} \left( \hat{\boldsymbol{\xi}}_j \cdot \mathbf{M}_{j,grv} \right) \end{bmatrix} \tag{6.26}$$

### R3RT Coupling Loading

Each gear pair's contact forces will induce moments in the two joints separating that gear pair. Figure 6.1 shows that the force applied on link $i+1$ contributes to the gear moment at joints $j = i$ and $j = i+1$. The impact of each gear force $F_{l,\{1,\cdots,5\},gear}$ (from gear pair $\{1,\cdots,5\}$ in segment $l$) is mapped into two terms defined in Eqs. 6.27 and 6.28: $M_{j,1,gear}$ accounts for the link $i+1$ gear force acting on joint $j = i$, and $M_{j,2,gear}$ accounts for the link $i+1$ gear force acting on joint $j = i+1$, with the assumption that the gear force acts tangentially to the gear's pitch diameters. For each joint $j$, Eq. 6.29 defines $\mathbf{M}_{j,gear}$.

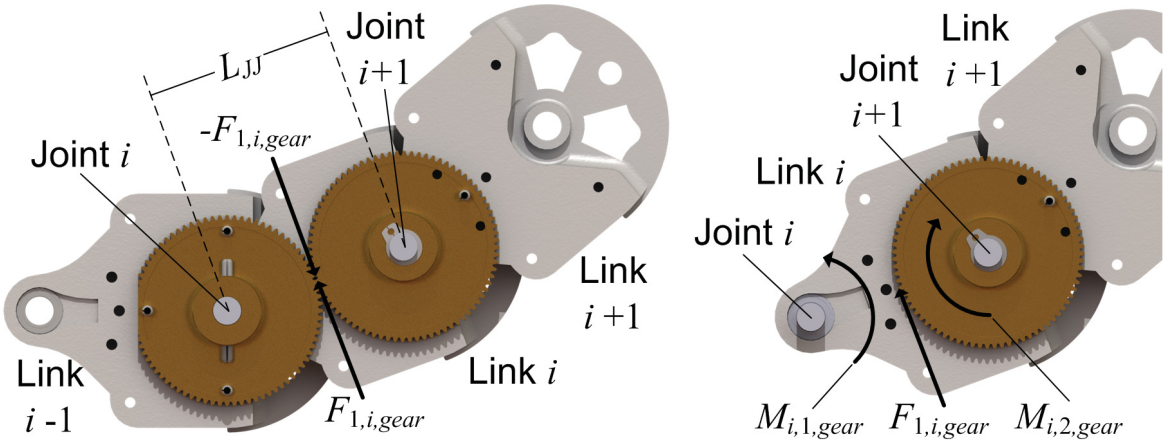


(a) Gear pair $i \in \{1,\cdots,5\}$ in segment $l = 1$ (b) Joint moments due to gear force

Figure 6.1: R3RT gear model.

$$M_{j,1,gear} = \begin{cases} 0, & j = \{0,6,12\}, \\ 0.5L_{JJ}F_{1,j,gear}, & j = \{1,\cdots,5\}, \\ 0.5L_{JJ}F_{2,j-6,gear}, & j = \{7,\cdots,11\} \end{cases} \tag{6.27}$$

$$M_{j,2,gear} = \begin{cases} 0, & j = \{0,1,7\}, \\ -0.5L_{JJ}F_{1,j-1,gear}, & j = \{2,\cdots,6\}, \\ -0.5L_{JJ}F_{2,j-7,gear}, & j = \{8,\cdots,12\} \end{cases} \tag{6.28}$$

$$\mathbf{M}_{j,gear} = (M_{j,1,gear} + M_{j,2,gear})\,\hat{\boldsymbol{\xi}}_j \tag{6.29}$$

A vector representation of $\hat{\boldsymbol{\xi}}_j \cdot \mathbf{M}_{j,gear}$ in terms of $F_{l,\{1,\cdots,5\},gear}$ is shown in Eq. 6.30. By adding together rows 1-6 and rows 7-12, the $F_{l,\{1,\cdots,5\},gear}$ variables are eliminated, allowing for the formulation of the three reduced equations of motion in Eq. 6.4. This simple formulation is only possible because the gear efficiencies are neglected as a modeling assumption; if efficiencies were considered, Gaussian elimination would need to be performed to eliminate the $F_{l,\{1,\cdots,5\},gear}$ variables. However, the same principle would apply: the joint 1-6 equations could be reduced into a single segment 1 equation, and the joint 7-12 equations could be reduced into a single segment 2 equation.

$$\begin{bmatrix} \hat{\boldsymbol{\xi}}_0 \cdot \mathbf{M}_{0,gear} \\ \hat{\boldsymbol{\xi}}_1 \cdot \mathbf{M}_{1,gear} \\ \hat{\boldsymbol{\xi}}_2 \cdot \mathbf{M}_{2,gear} \\ \hat{\boldsymbol{\xi}}_3 \cdot \mathbf{M}_{3,gear} \\ \hat{\boldsymbol{\xi}}_4 \cdot \mathbf{M}_{4,gear} \\ \hat{\boldsymbol{\xi}}_5 \cdot \mathbf{M}_{5,gear} \\ \hat{\boldsymbol{\xi}}_6 \cdot \mathbf{M}_{6,gear} \\ \hat{\boldsymbol{\xi}}_7 \cdot \mathbf{M}_{7,gear} \\ \hat{\boldsymbol{\xi}}_8 \cdot \mathbf{M}_{8,gear} \\ \hat{\boldsymbol{\xi}}_9 \cdot \mathbf{M}_{9,gear} \\ \hat{\boldsymbol{\xi}}_{10} \cdot \mathbf{M}_{10,gear} \\ \hat{\boldsymbol{\xi}}_{11} \cdot \mathbf{M}_{11,gear} \\ \hat{\boldsymbol{\xi}}_{12} \cdot \mathbf{M}_{12,gear} \end{bmatrix} = \begin{bmatrix} 0 & & & & & \\ & \begin{bmatrix} L_{JJ}/2 & 0 & 0 & 0 & 0 \\ -L_{JJ}/2 & L_{JJ}/2 & 0 & 0 & 0 \\ 0 & -L_{JJ}/2 & L_{JJ}/2 & 0 & 0 \\ 0 & 0 & -L_{JJ}/2 & L_{JJ}/2 & 0 \\ 0 & 0 & 0 & -L_{JJ}/2 & L_{JJ}/2 \\ 0 & 0 & 0 & 0 & -L_{JJ}/2 \end{bmatrix} & \begin{bmatrix} F_{1,1,gear} \\ F_{1,2,gear} \\ F_{1,3,gear} \\ F_{1,4,gear} \\ F_{1,5,gear} \end{bmatrix} \\ & \begin{bmatrix} L_{JJ}/2 & 0 & 0 & 0 & 0 \\ -L_{JJ}/2 & L_{JJ}/2 & 0 & 0 & 0 \\ 0 & -L_{JJ}/2 & L_{JJ}/2 & 0 & 0 \\ 0 & 0 & -L_{JJ}/2 & L_{JJ}/2 & 0 \\ 0 & 0 & 0 & -L_{JJ}/2 & L_{JJ}/2 \\ 0 & 0 & 0 & 0 & -L_{JJ}/2 \end{bmatrix} & \begin{bmatrix} F_{2,1,gear} \\ F_{2,2,gear} \\ F_{2,3,gear} \\ F_{2,4,gear} \\ F_{2,5,gear} \end{bmatrix} \end{bmatrix} \tag{6.30}$$

### R3RT Actuation Loading

The actuation moment $\mathbf{M}_{j,act}$ takes different forms depending on the joint, as shown in Eq. 6.31, where $r_{cbl}$ is the radius of the nested cylindrical cable routing surfaces within the tail. For joint $j = 0$, the roll torque $\tau$ acts directly on the joint, but for joints $j = 1$ through $j = 12$, the actuation cable tensions generate a joint moment.

$$\mathbf{M}_{j,act} = \begin{cases} \tau\hat{\boldsymbol{\xi}}_0, & j = 0, \\ (T_1 + T_2)\, r_{cbl}\hat{\boldsymbol{\xi}}_j, & 1 \leq j \leq 3, \\ (T_1 - T_2)\, r_{cbl}\hat{\boldsymbol{\xi}}_j, & 4 \leq j \leq 6, \\ T_2 r_{cbl}\hat{\boldsymbol{\xi}}_j, & 7 \leq j \leq 12 \end{cases} \tag{6.31}$$

For each antagonistic cable pair, a single real-valued variable $T_l$ for $l \in \{1, 2\}$ represents the non-zero tension in each cable pair. Because cabling cannot carry a negative tension, the symmetric antagonistic cabling allows for equal and opposite bi-directional tensioning: the "upper" cable is in tension when $T_l > 0$, and the "lower" cable is in tension when $T_l < 0$, as shown in Fig. 6.2. The mapping of the cable tension into a joint moment is illustrated in Fig. 6.2: the cable tension vector aligns with the actuation cabling between links $i = j - 1$ and $i = j$ and the orthogonal distance from this force to the joint axis is assumed to be $r_{cbl}$. In Eq. 6.31, the difference in $\mathbf{M}_{j,act}$ definitions for joints $1-3$ and $4-6$ is due to the S-path routing: as the segment 2 cabling routes through segment 1, its impact on joints $1-3$ and $4-6$ are equal and opposite.

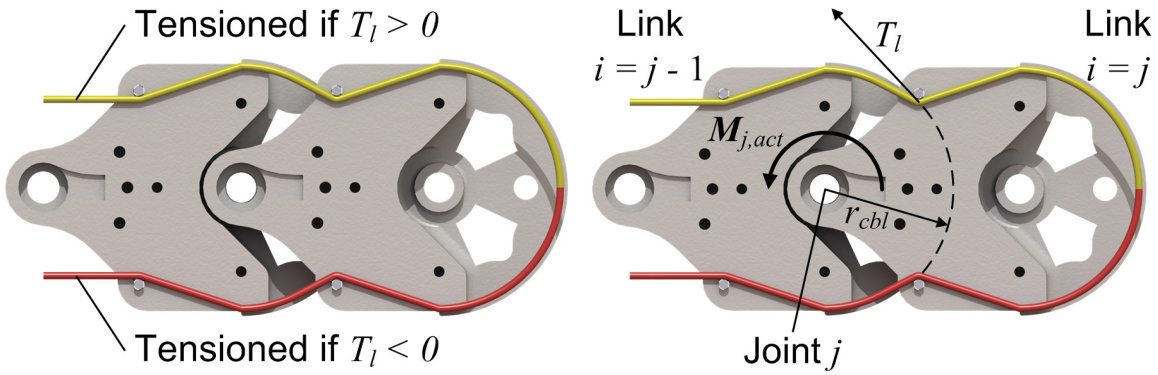


(a) Single-variable segment $l$ cable tension representation

(b) Joint moment due to segment $l$ cable tension

Figure 6.2: R3RT cable model.

Equation 6.32 uses $\mathbf{M}_{j,act}$ in conjunction with the joint $j$ axes $\hat{\boldsymbol{\xi}}_j$ to formulate the $\mathbf{T}$ matrix.

$$\mathbf{Tu} = \begin{bmatrix} \hat{\boldsymbol{\xi}}_0 \cdot \mathbf{M}_{0,act} \\ \sum_{j=1}^{6} \left( \hat{\boldsymbol{\xi}}_j \cdot \mathbf{M}_{j,act} \right) \\ \sum_{j=7}^{12} \left( \hat{\boldsymbol{\xi}}_j \cdot \mathbf{M}_{j,act} \right) \end{bmatrix} \rightarrow \mathbf{T} = \begin{bmatrix} 1 & 0 & 0 \\ 0 & 6r_{cbl} & 0 \\ 0 & 0 & 6r_{cbl} \end{bmatrix} \tag{6.32}$$

### 6.1.4 R3RT Tail Base Loading

When the tail is mounted to a load cell or mobile robot, an internal force $\mathbf{F}_T$ and moment $\mathbf{M}_T$ acting on the rigid housing is generated, along with equal and opposite loading acting on the load cell or robot. The loading $\mathbf{F}_T$ and $\mathbf{M}_T$ depends on the inertia of the tail's moving links and the gravitational forces acting at the tail's fixed and moving link COMs. All of these calculations are performed with respect to the inertial tail frame. As the gear and actuation loading are internal loading effects, they do not contribute to $\mathbf{F}_T$ or $\mathbf{M}_T$.

Equations 6.33 and 6.34 define $\mathbf{F}_T$ and $\mathbf{M}_T$, where $\mathbf{F}_{RH,grv}$ is the rigid housing's gravitational loading defined in Eq. 6.35, $m_{RH,bdy}$ is the mass of the rigid housing and $\mathbf{p}_{RH,COM}$ is the position from the inertial tail frame origin to the rigid housing COM.

$$\mathbf{F}_T = -\mathbf{F}_{RH,grv} + \sum_{i=0}^{12} \left( \mathbf{F}_{i,inr,bdy} - \mathbf{F}_{i,grv,bdy} \right), \tag{6.33}$$

$$\mathbf{M}_T = \begin{pmatrix} -\mathbf{p}_{RH,COM} \times \mathbf{F}_{RH,grv} \\ + \sum_{i=0}^{12} \left( \mathbf{M}_{i,inr,bdy} + \mathbf{p}_{i,COM} \times \left( \mathbf{F}_{i,inr,bdy} - \mathbf{F}_{i,grv,bdy} \right) \right) \end{pmatrix} \tag{6.34}$$

$$\mathbf{F}_{RH,grv} = -m_{RH,bdy} g \hat{\mathbf{x}}_T \tag{6.35}$$

### 6.1.5 R3RT Simulations

In order to utilize the R3RT's kinematic and dynamic models to simulate the tail base loading, the parameters used to calculate $\mathbf{F}_T$ and $\mathbf{M}_T$ in Eqs. 6.33 and 6.34 are provided in Table 6.1. These properties match the prototype in section 5.1.4, to allow comparison of the simulated and measured results.

Table 6.1: Mass and geometric properties of the R3RT prototype.

| **Variable** | **Value** | **Variable** | **Value** |
|---|---|---|---|
| $r_{cbl}$ | 25 mm | $I^0_{0,bdy,xx}$ | 0.01197 kg-m$^2$ |
| $L_{JJ}$ | 40 mm | $I^0_{0,bdy,yy}$ | 0.01205 kg-m$^2$ |
| $L_{JC}$ | 32.7 mm | $I^0_{0,bdy,zz}$ | 0.004202 kg-m$^2$ |
| $m_{0,bdy}$ | 3.144 kg | $I^{\{1,\cdots,12\}}_{\{1,\cdots,12\},bdy,xx}$ | 0.0001868 kg-m$^2$ |
| $m_{\{1,\cdots,12\},bdy}$ | 0.0759 kg | $I^{\{1,\cdots,12\}}_{\{1,\cdots,12\},bdy,yy}$ | 0.0000813 kg-m$^2$ |
| $\mathbf{p}_{T0,jnt}$ | 92.1 $\hat{\mathbf{x}}$ mm | $I^{\{1,\cdots,12\}}_{\{1,\cdots,12\},bdy,zz}$ | 0.0001626 kg-m$^2$ |
| $\mathbf{p}^0_{01,jnt}$ | 159.24 $\hat{\mathbf{z}}$ mm | $\mathbf{p}^0_{0,JC}$ | $[-3.52,\ 0,\ -7.33]^T$ mm |

In addition, trajectories of $\phi$, $\beta_1$ and $\beta_2$ are required. To aid in the formulation of trajectories for these variables, a placeholder variable $\psi$ will be defined for which the interpolation is defined and can be used to define either variable bending or variable rolling trajectories. A sixth-order interpolation is defined for $\psi$, as shown in Eq. 6.36, where $t$ is the simulation time, $t_0$ and $t_f$ are the trajectory start and end times, $\psi_0$ and $\psi_f$ are the values of $\psi$ at $t_0$ and $t_f$, respectively, and $a_n$ is the polynomial's $n$th-order term coefficient. Values for $a_n$ are found using the trajectory's boundary conditions defined in Eq. 6.37.

$$\psi = \begin{cases} \sum_{n=0}^{5} \left(a_n \left(t - t_0\right)^n\right), & t_0 \leq t \leq t_f \\ \psi_f, & t > t_f \end{cases} \tag{6.36}$$

$$\begin{aligned} \psi(t_0) = \psi_0, \quad \dot{\psi}(t_0) = 0, \quad \ddot{\psi}(t_0) = 0, \\ \psi(t_f) = \psi_f, \quad \dot{\psi}(t_f) = 0, \quad \ddot{\psi}(t_f) = 0 \end{aligned} \tag{6.37}$$

Two case studies are considered: 1) dynamic tail bending for a set of fixed roll angles, and 2) dynamic tail roll for a set of fixed bending angles. For both case studies, the tail's static loading when $\phi = \beta_1 = \beta_2 = 0$ is subtracted from the calculated loading profile trajectories to show the loading as it would impact the legged robot on which the tail is mounted. In addition, in cases where $\beta_1 = \beta_2$, the variable $\beta$ will be used to reference both.

Figure 6.3 illustrates the $\mathbf{F}_T$ and $\mathbf{M}_T$ profiles for the first case, where $(t_0, t_f) = (0, 0.5)$ sec, $(\psi_0, \psi_f) = (0, 90)^\circ$ and $\beta = \psi$ at three fixed values of $\phi = \{0, 45, 90\}^\circ$. The z-component of $\mathbf{F}_T$, $(\mathbf{F}_T)_z$, due primarily to centripetal acceleration, is invariant to $\phi$, given that the roll axis is the tail frame z-axis; for $(\mathbf{M}_T)_z$, as roll increases from $\phi = 0$, the gravitational forces acting over y-axis distances generate a moment at the base. For $(\mathbf{F}_T)_x$ and $(\mathbf{F}_T)_y$, due to the centripetal and tangential accelerations of the tail masses, as $\phi$ increases, the time-varying component of $(\mathbf{F}_T)_x$ re-allocates to $(\mathbf{F}_T)_y$. The moments $(\mathbf{M}_T)_x$ and $(\mathbf{M}_T)_y$ are due to several factors: the moments due to the links' angular acceleration, the moments due to inertial forces from the links' linear acceleration, and the moments due to gravity. Gravity primarily impacts $(\mathbf{M}_T)_y$: the gravitational moment is greatest when $\psi = 0$ and least when $\psi = 90^\circ$. As with force, the roll angle re-allocates the inertial component between $(\mathbf{M}_T)_x$ and $(\mathbf{M}_T)_y$.

Figure 6.4 illustrates the loading profiles for the second case, where $(t_0, t_f) = (0, 0.5)$ sec, $(\psi_0, \psi_f) = (0, 90)^\circ$ and $\phi = \psi$ with $(\beta_1, \beta_2) = \{(45, 45)^\circ, (90, 90)^\circ, (-21.75, 90)^\circ\}$. The set $(\beta_1, \beta_2) = (-21.75, 90)^\circ$ corresponds to a tail configuration with the tail COM located along the roll axis similar to a reaction wheel. For this case, the tail COM does not move during rotation, hence zero force. However, since the tail is not axisymmetric (i.e., there

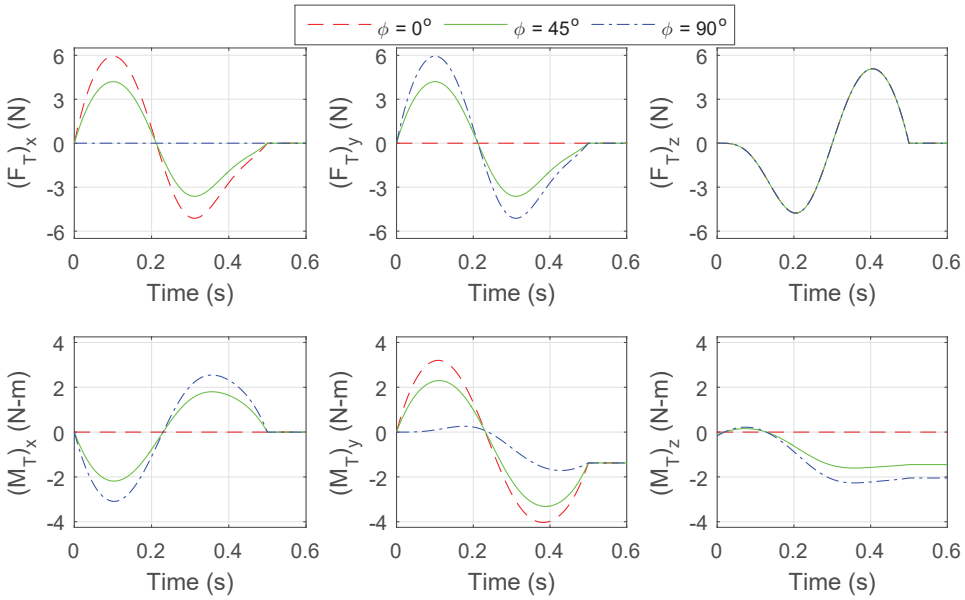


Figure 6.3: R3RT simulation results: loading due to dynamic tail bending motion at fixed tail roll angles.

are off-diagonal terms in the tail's inertia tensor), moments are generated in the x-, y- and z-directions.

For the $\beta = \{45, 90\}^\circ$ cases, the tail COM is held at a fixed distance along the z-axis, which ensures there is zero $(\mathbf{F}_T)_z$, and $(\mathbf{F}_T)_x$ and $(\mathbf{F}_T)_t$ are due to centripetal and tangential accelerations. However, gravity will generate moments in $(\mathbf{M}_T)_y$ and $(\mathbf{M}_T)_z$. For $(\mathbf{M}_T)_y$, the non-zero initial moments are due to the reduced tail COM distance from the tail base for $\beta = \{45, 90\}^\circ$ compared to $\beta = 0$ (the static loading for $\phi = \beta = 0$ includes a y-axis moment component). For $(\mathbf{M}_T)_z$, as $\psi$ increases from 0 to 90°, the y-axis distance between the COM and inertial tail frame increases, creating a gravitational moment. For the inertial components of $(\mathbf{M}_T)_x$ and $(\mathbf{M}_T)_y$, the magnitude of the inertial component of loading initially increases in magnitude ($\beta = 45^\circ$), and then decreases ($\beta = 90^\circ$), due to the varying of the z-axis tail COM coordinate and the distance of the tail COM from the z-axis as $\beta$ increases. For the inertial component of $(\mathbf{M}_T)_z$, the tail's tangential acceleration generates a slight

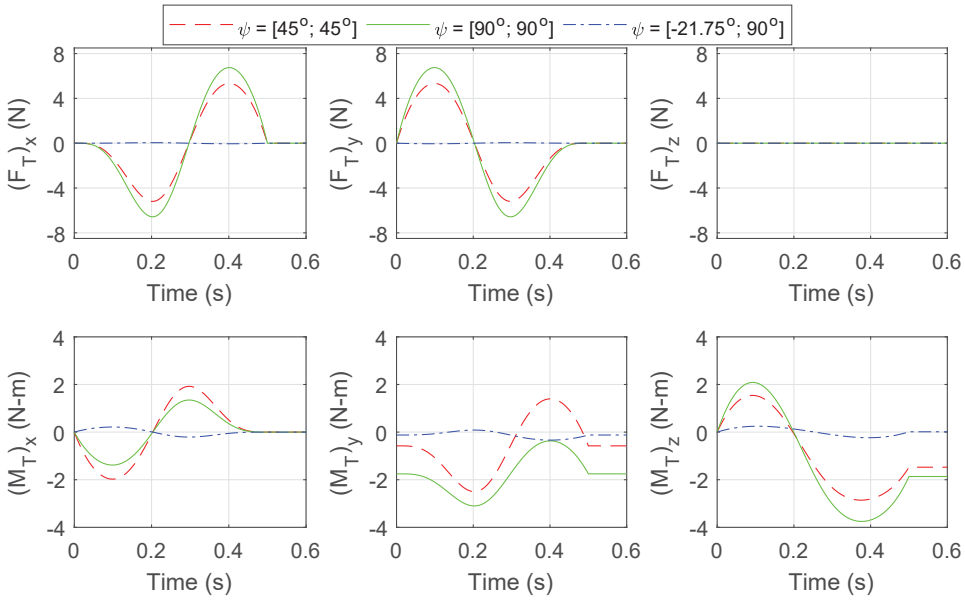


Figure 6.4: R3RT simulation results: loading due to dynamic tail rolling motion at fixed tail bending angles.

inertial moment that is secondary to the change due to gravity as $\beta$ increases.

### 6.1.6 R3RT Experiments

Experiments were performed to measure the tail's ability to generate dynamic loading using a 6-axis load cell. Sensor measurements were sampled at 400 Hz using a PCI data acquisition card. A moving window mean low-pass filter with a 50 sample points width was used to filter out high frequency sensor noise from the measured data; sufficient data was collected preceding the start of the tail motion to uniformly filter the relevant time span.

The tail bending motion case studies from section 6.1.5 were implemented experimentally to compare measured loading profiles with computed simulation results (sensor errors associated with the roll DOF sensing at the time precluded experimental implementation of the tail rolling motion case studies). Figure 6.5 illustrates the measured loading profiles. Each case

scenario was conducted three times with results averaged. From the plot, it can be observed that tail curvature motion is completed in 0.8 sec, after which the tail experiences vibrations that dissipate to steady state conditions.

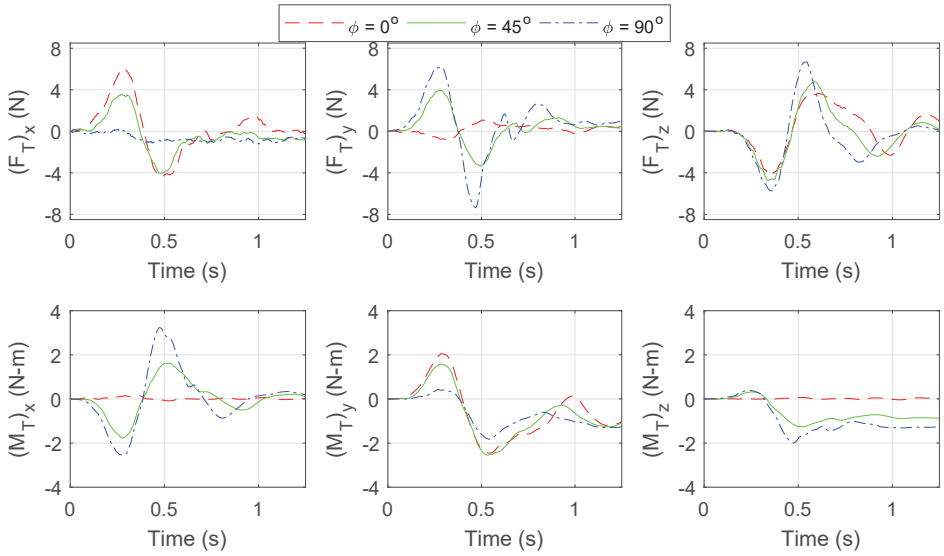


Figure 6.5: R3RT experimental results: loading due to dynamic tail bending motion at fixed tail roll angles.

Compared to computed results in Fig. 6.3, the measured loading profiles exhibit similar loading as the roll angle is varied: force loading about the z-axis shows an approximate invariance to various roll angles, gravitational moment loading offsets about the y- and z-axis at final tail configurations approximately match computed results, and profiles qualitatively match the shape of computed profiles, but do not exactly match the smooth contours.

A shortcoming observed in the experiments is a lag between the prescribed and resulting trajectories. This is due to the motor driver's position control loop that prescribes the pulley rotation angle, as opposed to the quadratic splines used to compute the loading profiles in section VI-C. Since the PD position controller's output depends on position and velocity errors, a delay is introduced while sufficient error is accumulated to overcome friction and gravity. This delay distorts the loading profile with respect to commanded profile.

Measured peak loading profile values, equal to 6 N and 3.1 N-m, fall slightly below computed values because the experimental tail motion duration was slightly longer than the 0.5 s time span used in computed results. This is expected since inertial loading decreases as the time spans of tail motions are lengthened.

## 6.2 Universal-Spatial Robotic Tail Model

### 6.2.1 USRT State, Control and Equations of Motion

The USRT's kinematic state may be represented by twelve variables: six pitch angles and six yaw angles. For universal joint $j \in \{1, \cdots, 6\}$, $\phi_j$ is the joint $j$ pitch angle and $\theta_j$ is the joint $j$ yaw angle. These state variables are collected into the state variable $\mathbf{q}$ defined in Eq. 6.38.

$$\mathbf{q} = [\phi_1, \quad \cdots, \quad \phi_6, \quad \theta_1, \quad \cdots, \quad \theta_6]^T \tag{6.38}$$

The USRT's control inputs are six non-negative cable tensions $T_k$ for $k \in \{1, \cdots, 6\}$ that maintain a minimum tension of $T_{min}$ and are collected into the control input vector $\mathbf{u}$ defined in Eq. 6.39.

$$\mathbf{u} = \begin{bmatrix} T_1 \\ \vdots \\ T_6 \end{bmatrix}, \quad T_k \geq T_{min} \tag{6.39}$$

The USRT's 6 universal joints (or 12 revolute joints) lead to 12 equations of motion. If the net moment $\mathbf{M}_{j,jnt}$ is calculated at the joint $j$ center, the projections of $\mathbf{M}_{j,jnt}$ onto the joint

$j$ pitch axis unit vector $\boldsymbol{\rho}_j$ and yaw axis unit vector $\boldsymbol{\gamma}_j$ equal zero, as shown in Eq. 6.40, since a universal joint cannot support a moment about its joint axes.

$$\begin{cases} \hat{\boldsymbol{\rho}}_j \cdot \mathbf{M}_{j,jnt} = 0, \\ \hat{\boldsymbol{\gamma}}_j \cdot \mathbf{M}_{j,jnt} = 0, \end{cases} \quad j \in \{1, \cdots, 6\} \tag{6.40}$$

Alternatively, the tail's 12 dynamic equations of motion may be represented by Eq. 6.41, where $\mathbf{M}(\mathbf{q})$ is the tail's inertia matrix, $\mathbf{C}(\mathbf{q}, \dot{\mathbf{q}})\,\dot{\mathbf{q}}$ is the tail's Coriolis and centripetal loading, $\mathbf{d}(\mathbf{q}, \dot{\mathbf{q}})$ is the tail's joint damping loading, $\mathbf{k}(\mathbf{q})$ is tail's joint coupling loading, $\mathbf{g}(\mathbf{q})$ is the tail's gravitational loading, and $\mathbf{T}(\mathbf{q})$ is the tail's actuation transmission matrix.

$$\mathbf{M}(\mathbf{q})\,\ddot{\mathbf{q}} + \mathbf{C}(\mathbf{q}, \dot{\mathbf{q}})\,\dot{\mathbf{q}} + \mathbf{d}(\mathbf{q}, \dot{\mathbf{q}}) + \mathbf{k}(\mathbf{q}) + \mathbf{g}(\mathbf{q}) = \mathbf{T}(\mathbf{q})\,\mathbf{u} \tag{6.41}$$

In addition to the state vector $\mathbf{q}$, an additional state vector $\mathbf{z} \in \mathbb{R}^4$ is defined in Eq. 6.42 in terms of the segment $l$ net pitch $\psi_l$ and yaw $\eta_l$ bending angles, where $\boldsymbol{\mu}$ is a 4-by-12 matrix that maps $\mathbf{q}$ into $\mathbf{z}$, $\mathbf{1}_{1\times3}$ is a 1-by-3 row vector of ones and $\mathbf{0}_{1\times3}$ is a 1-by-3 row vector of zeros. The three cables used to actuate each segment only allow for control of two DOFs [85]; $\psi_l$ and $\eta_l$ for segment $l \in \{1, 2\}$ parameterize the controllable workspace of the tail.

$$\mathbf{z} = \begin{bmatrix} \psi_1 \\ \psi_2 \\ \eta_1 \\ \eta_2 \end{bmatrix} = \boldsymbol{\mu}\mathbf{q} = \begin{bmatrix} \mathbf{1}_{1\times3} & \mathbf{0}_{1\times3} & \mathbf{0}_{1\times3} & \mathbf{0}_{1\times3} \\ \mathbf{0}_{1\times3} & \mathbf{1}_{1\times3} & \mathbf{0}_{1\times3} & \mathbf{0}_{1\times3} \\ \mathbf{0}_{1\times3} & \mathbf{0}_{1\times3} & \mathbf{1}_{1\times3} & \mathbf{0}_{1\times3} \\ \mathbf{0}_{1\times3} & \mathbf{0}_{1\times3} & \mathbf{0}_{1\times3} & \mathbf{1}_{1\times3} \end{bmatrix} \mathbf{q} \tag{6.42}$$

### 6.2.2 USRT Kinematic Analysis

Using these pitch and yaw angles, the orientation and position kinematics can be defined. Frames for the tail base ($T$) and a tail link (4) are shown in Fig. 6.6. The relative orientation $\mathbf{R}_{(i-1)i}^{i-1}$ between links $i-1$ and $i$ and the link $i$ orientation $\mathbf{R}_i$ with respect to the inertial tail frame are defined in Eqs. 6.43 and 6.44, respectively, where $\mathbf{E}_3$ is the 3-by-3 identity matrix, $\mathbf{R}_Y(\cdot)$ is the rotation matrix for a y-axis rotation by angle $(\cdot)$, and $\mathbf{R}_X(\cdot)$ is the rotation matrix for an x-axis rotation by angle $(\cdot)$.

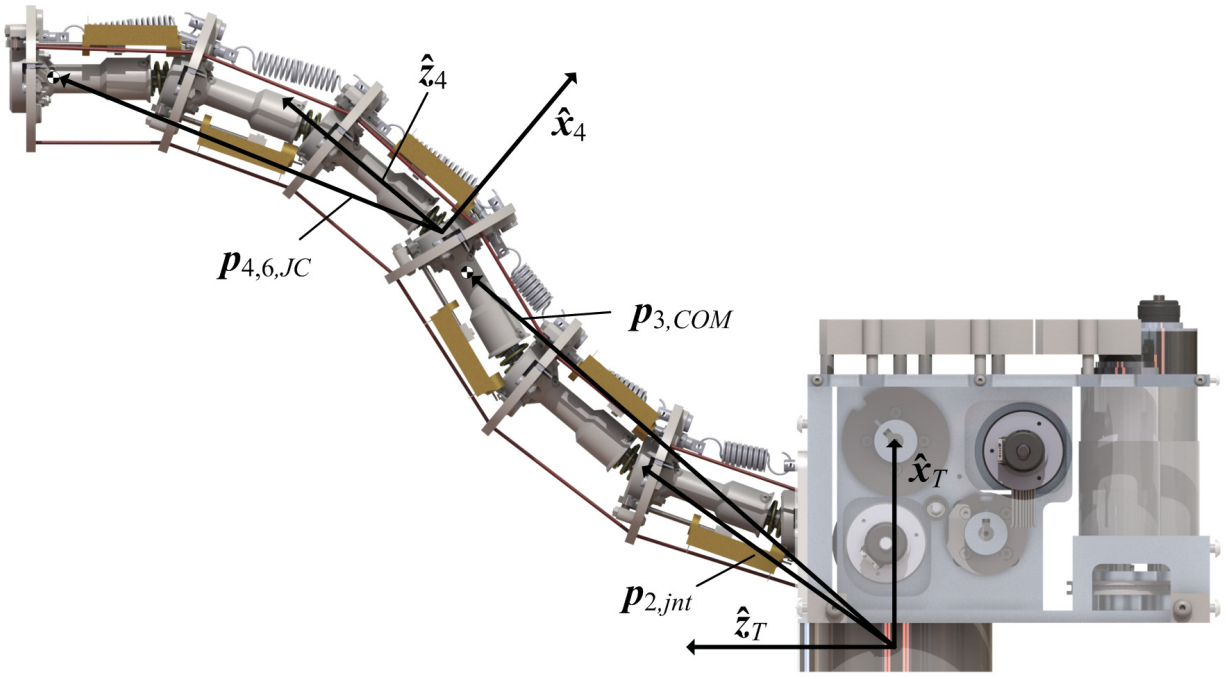


Figure 6.6: USRT frame definitions and joint/link COM position vectors.

$$\mathbf{R}_{(i-1)i}^{i-1} = \mathbf{R}_Y(\phi_i)\,\mathbf{R}_X(\theta_i) \tag{6.43}$$

$$\mathbf{R}_i = \begin{cases} \mathbf{E}_3, & i = 0, \\ \mathbf{R}_{i-1}\mathbf{R}_{(i-1)i}^{i-1}, & 1 \le i \le 6 \end{cases} \tag{6.44}$$

The joint $j$ axes $\boldsymbol{\rho}_j$ and $\boldsymbol{\gamma}_j$ are defined in Eqs. 6.45 and 6.46.

$$\boldsymbol{\rho}_j = \mathbf{R}_{j-1}\hat{\mathbf{y}}_{j-1}^{j-1} \tag{6.45}$$

$$\boldsymbol{\gamma}_j = \mathbf{R}_j\hat{\mathbf{x}}_j^j \tag{6.46}$$

Using these orientations, the position vectors from the inertial tail frame origin to joint $j$ ($\mathbf{p}_{j,jnt}$) and the link $i$ COM ($\mathbf{p}_{i,COM}$), shown in Fig. 6.6, may be calculated using Eqs. 6.47 and 6.48, where $\mathbf{p}_{T1,jnt}$ is the position vector from the inertial tail frame origin to the joint 1 center, $L_{JJ}$ is the distane between a link's joint centers, $\mathbf{p}_{0,JC}$ is the position vector from the inetial tail frame origin to the link 0 COM and $L_{JC}$ is the distance between a link's proximal joint center and its COM (shown in Fig. 6.7).

$$\mathbf{p}_{j,jnt} = \begin{cases} \mathbf{p}_{T1,jnt}, & j = 1, \\ \mathbf{p}_{j-1,jnt} + L_{JJ}\mathbf{R}_j\hat{\mathbf{z}}_j^j, & 1 \leq j \leq 6 \end{cases} \tag{6.47}$$

$$\mathbf{p}_{i,COM} = \begin{cases} \mathbf{p}_{0,JC}, & i = 0 \\ \mathbf{p}_{i,jnt} + L_{JC}\mathbf{R}_i\hat{\mathbf{z}}_i^i, & 1 \leq i \leq 6 \end{cases} \tag{6.48}$$

The link $i$ angular velocity may be defined relative to link $i-1$ ($\boldsymbol{\omega}_{(i-1)i}^{i-1}$) and the inertial tail frame ($\boldsymbol{\omega}_i$) using Eqs. 6.49 and 6.50, where $\dot{\phi}$ denotes the first time derivative of $\phi$.

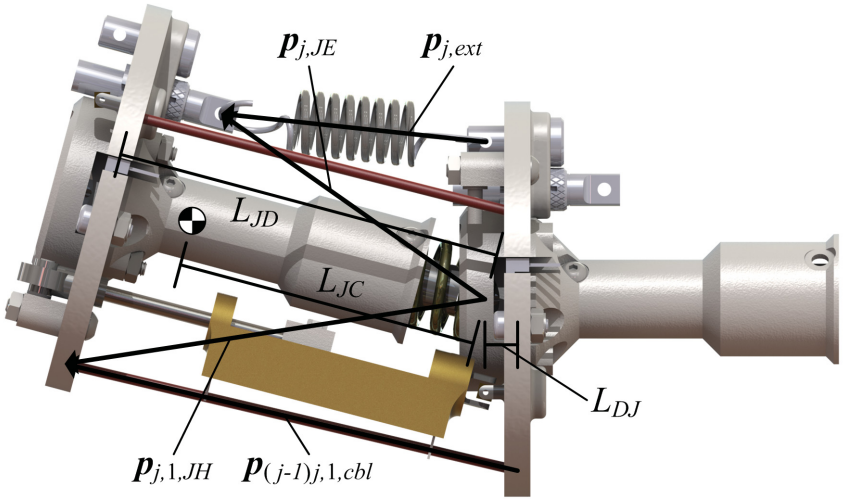


Figure 6.7: USRT joint kinematics definitions.

$$\boldsymbol{\omega}_{(i-1)i}^{i-1} = \dot{\phi}_i \boldsymbol{\rho}_i^{i-1} + \dot{\theta}_i \boldsymbol{\gamma}_i^{i-1} \tag{6.49}$$

$$\boldsymbol{\omega}_i = \begin{cases} \mathbf{0}_{3\times 1}, & i = 0, \\ \boldsymbol{\omega}_{i-1} + \mathbf{R}_{i-1}\boldsymbol{\omega}_{(i-1)i}^{i-1}, & i > 0 \end{cases} \tag{6.50}$$

An additional set of kinematic variables are also needed to characterize the bending angle and bending plane of each universal joint for calculating the coupling loading. The angle $\beta_j > 0$ between the frame $j-1$ z-axis and the frame $j$ z-axis is defined in Eq. 6.51, along with the unit vector $\boldsymbol{\lambda}_j^{j-1}$ along the common normal between these two axes (assuming they are not coincident).

$$\beta_j = \cos^{-1}\left(\hat{\mathbf{z}}_{j-1}^{j-1} \cdot \mathbf{R}_{(j-1)j}^{j-1} \hat{\mathbf{z}}_j^j\right), \tag{6.51}$$

$$\boldsymbol{\lambda}_j^{j-1} = \frac{\hat{\mathbf{z}}_{j-1}^{j-1} \times \mathbf{R}_{(j-1)j}^{j-1} \hat{\mathbf{z}}_j^j}{\sin\beta_j} \tag{6.52}$$

The product $\dot{\beta}_j \boldsymbol{\lambda}_j^{j-1}$ for the universal joint damping may be formulated in terms of the relative angular velocity between links $i = j-1$ and $i = j$ using Eq. 6.53, which isolates the x- and y-components of the relative angular velocity using the outer products $\otimes$ of the x- and y-axis unit vectors.

$$\dot{\beta}_j \boldsymbol{\lambda}_j^{j-1} = \left(\hat{\mathbf{x}}_{j-1}^{j-1} \otimes \hat{\mathbf{x}}_{j-1}^{j-1} + \hat{\mathbf{y}}_{j-1}^{j-1} \otimes \hat{\mathbf{y}}_{j-1}^{j-1}\right) \boldsymbol{\omega}_{(j-1)j}^{j-1} \tag{6.53}$$

To aid in calculating the gravitational and inertial moments, position vectors from joint $j$ to the link $i$ COM are defined as $\mathbf{p}_{j,i,JC}$ in Eq. 6.54 and shown in Fig. 6.6.

$$\mathbf{p}_{j,i,JC} = \mathbf{p}_{i,COM} - \mathbf{p}_{j,jnt} \tag{6.54}$$

For the joint $j$ extension spring, Eq. 6.55 defines $\mathbf{p}_{j,ext}^{j-1}$ as the position from the spring's base to tip, shown in Fig. 6.7, and Eq. 6.56 defines $\mathbf{p}_{j,JE}^{j}$ as the position from joint $j$ to the spring's tip anchor, where $\mathbf{p}_{j-1,ext,B}^{j-1}$ is the position from the link $i = j-1$ disk center to the joint $j$ extension spring base, $L_{DJ}$ is the distance between a link's disk center and its distal joint center, $L_{JD}$ is the distance between a link's proximal joint center and its disk center and $\mathbf{p}_{i,ext,T}^{i}$ is the position from the link $i = j$ disk center to the joint $j$ extension spring tip.

$$\mathbf{p}_{j,ext}^{j-1} = -\mathbf{p}_{j-1,ext,B}^{j-1} + L_{DJ}\hat{\mathbf{z}}_{j-1}^{j-1} + \mathbf{R}_{(j-1)j}^{j-1}\mathbf{p}_{j,JE}^{j}, \tag{6.55}$$

$$\mathbf{p}_{j,JE}^{j} = L_{JD}\hat{\mathbf{z}}_{j}^{j} + \mathbf{p}_{j,ext,T}^{j} \tag{6.56}$$

For the actuation cabling, Eq. 6.57 defines $\mathbf{p}_{(j-1)j,k,cbl}^{j-1}$ as the cable $k$ position from link $i = j-1$ to link $i = j$, shown in Fig. 6.7, and Eq. 6.58 defines $\mathbf{p}_{j,k,JH}^{i}$ as the position vector

from the joint $j$ center to the cable routing hole $k$, where $\mathbf{p}^{j}_{j,k,hl}$ is the position vector in disk $i = j$ from the disk center to cable routing hole $k$. The displacement $\delta_k$ of cable $k$ due to the tail configuration is defined by Eq. 6.59, where $l$ is the segment in which cable $k$ terminates.

$$\mathbf{p}^{j-1}_{(j-1)j,k,cbl} = -\mathbf{p}^{j-1}_{j-1,k,hl} + L_{DJ}\hat{\mathbf{z}}^{j-1}_{j-1} + \mathbf{R}^{j-1}_{(j-1)j}\mathbf{p}^{i}_{j,k,JH}, \tag{6.57}$$

$$\mathbf{p}^{i}_{j,k,JH} = L_{JD}\hat{\mathbf{z}}^{j}_{j} + \mathbf{p}^{j}_{j,k,hl} \tag{6.58}$$

$$\delta_k = \sum_{j=1}^{3l}\left(\left\|\mathbf{p}^{j-1}_{(j-1)j,k,cbl}\right\| - L_{JJ}\right), \quad l = \begin{cases} 1, & 1 \leq k \leq 3 \\ 2, & 4 \leq k \leq 6 \end{cases} \tag{6.59}$$

Furthermore, although the universal joints does not allow for relative roll between links, a rolling tail motion can be generated by coordinating the motion of the joints' yaw and pitch angles. To parameterize this motion with respect to the segment motions, three additional variables are introduced: a bending plane angle $\xi$, and two segment bending angles $\chi_1$ (for joints 1-3) and $\chi_2$ (for joints 4-6). An implicit relationship between $\{\xi, \chi_{\{1,2\}}\}$ and $\{\psi_{\{1,2\}}, \eta_{\{1,2\}}\}$ is defined by Eq. 6.60, and either set of angles can be solved from the other subject to the angles' constraints: $\xi \in [-180°, 180°]$, $\chi_{\{1,2\}} \in [0, 3\beta_{lim}]$, $\{\psi_{\{1,2\}}, \eta_{\{1,2\}}\} \in [-3\beta_{lim}, 3\beta_{lim}]$.

$$\mathbf{R}_Z(\xi)\,\mathbf{R}_Y\left(\chi_{\{1,2\}}/3\right)\begin{bmatrix}0\\0\\1\end{bmatrix} = \mathbf{R}_Y\left(\psi_{\{1,2\}}/3\right)\mathbf{R}_X\left(\eta_{\{1,2\}}/3\right)\begin{bmatrix}0\\0\\1\end{bmatrix} \tag{6.60}$$

### 6.2.3 USRT Loading Analysis

Four types of loading are considered in the dynamics model: inertia, gravity, coupling and actuation. To compute the tail's dynamic equilibrium, the net moment at each joint $j$ due to inertia ($\mathbf{M}_{j,inr}$), gravity ($\mathbf{M}_{j,grv}$), coupling ($\mathbf{M}_{j,cpl}^{j-1}$) and actuation ($\mathbf{M}_{j,act}^{i-1}$) will be found. The joint $j$ net moment $\mathbf{M}_{j,jnt}$ is defined in Eq. 6.61.

$$\mathbf{M}_{j,jnt} = \mathbf{M}_{j,inr} - \mathbf{M}_{j,grv} - \mathbf{R}_{j-1}\left(\mathbf{M}_{j,cpl}^{j-1} + \mathbf{M}_{j,act}^{j-1}\right) \tag{6.61}$$

#### USRT Inertial Loading

A joint's inertial moment is due to the inertial loading acting on the COMs of links "downstream" of the joint. Equations 6.62 and 6.63 define the link $i$ inertial force $\mathbf{F}_{i,inr,bdy}$ and moment $\mathbf{M}_{i,inr,bdy}$, where $m_{i,bdy}$ is the link $i$ mass, $\mathbf{I}_{i,bdy}$ is the link $i$ inertia defined in the tail base frame (Eq. 6.64) and $\mathbf{I}_{i,bdy}^{i}$ is the constant link $i$ body-frame inertia. The resulting joint $j$ inertial moment $\mathbf{M}_{j,inr}$ is due to the loading acting on links $i = j$ through $i = 6$, as defined in Eq. 6.65.

$$\mathbf{F}_{i,inr,bdy} = m_{i,bdy}\ddot{\mathbf{p}}_{i,COM} \tag{6.62}$$

$$\mathbf{M}_{i,inr,bdy} = \mathbf{I}_{i,bdy}\dot{\boldsymbol{\omega}}_i + \boldsymbol{\omega}_i \times \mathbf{I}_{i,bdy}\boldsymbol{\omega}_i \tag{6.63}$$

$$\mathbf{I}_{i,bdy} = \mathbf{R}_i\mathbf{I}_{i,bdy}^{i}\mathbf{R}_i^T \tag{6.64}$$

$$\mathbf{M}_{j,inr} = \sum_{i=j}^{6}\left(\mathbf{M}_{i,inr,bdy} + \mathbf{p}_{j,i,JC} \times \mathbf{F}_{i,inr,bdy}\right) \tag{6.65}$$

As with the R3RT, the formulation of the USRT's $\mathbf{M}$ and $\mathbf{C}$ matrices requires implicit formulations of $\ddot{\mathbf{p}}_{i,COM}$, $\boldsymbol{\omega}_i$ and $\dot{\boldsymbol{\omega}}_i$, defined in Eqs. 6.66, 6.67 and 6.68, where $\mathbf{J}_{\mathbf{p},i}$ and $\mathbf{J}_{\boldsymbol{\omega},i}$ are the link $i$ COM linear and angular velocity Jacobians, respectively.

$$\ddot{\mathbf{p}}_{i,COM} = \mathbf{J}_{\mathbf{p},i}\ddot{\mathbf{q}} + \dot{\mathbf{J}}_{\mathbf{p},i}\dot{\mathbf{i}} \tag{6.66}$$

$$\boldsymbol{\omega}_i = \mathbf{J}_{\boldsymbol{\omega},i}\dot{\mathbf{q}} \tag{6.67}$$

$$\dot{\boldsymbol{\omega}}_i = \mathbf{J}_{\boldsymbol{\omega},i}\ddot{\mathbf{q}} + \dot{\mathbf{J}}_{\boldsymbol{\omega},i}\dot{\mathbf{q}} \tag{6.68}$$

With these, $\mathbf{F}_{i,inr,bdy}$ and $\mathbf{M}_{i,inr,bdy}$ can be reformulated as shown in Eqs. 6.69 and 6.70.

$$\mathbf{F}_{i,inr,bdy} = m_{i,bdy}\mathbf{J}_{\mathbf{p},i}\ddot{\mathbf{q}} + m_{i,bdy}\dot{\mathbf{J}}_{\mathbf{p},i}\dot{\mathbf{q}} \tag{6.69}$$

$$\mathbf{M}_{i,inr,bdy} = \mathbf{I}_{i,bdy}\mathbf{J}_{\boldsymbol{\omega},i}\ddot{\mathbf{q}} + \left(\mathbf{I}_{i,bdy}\dot{\mathbf{J}}_{\boldsymbol{\omega},i} + \boldsymbol{\omega}_i \times \mathbf{I}_{i,bdy}\mathbf{J}_{\boldsymbol{\omega},i}\right)\dot{\mathbf{q}} \tag{6.70}$$

Using Eqs. 6.65, 6.69 and 6.70, formulations for $\mathbf{M}$ and $\mathbf{C}$ defined in terms of the matrices' row $r$ are defined using Eqs. 6.71 and 6.72.

$$(\mathbf{M})_{r,:} = \begin{cases} \hat{\boldsymbol{\rho}}_r \cdot \sum_{i=r}^{6} \left(\mathbf{I}_{i,bdy}\mathbf{J}_{\boldsymbol{\omega},i} + \mathbf{p}_{r,i,JC} \times m_{i,bdy}\mathbf{J}_{\mathbf{p},i}\right), & 1 \leq r \leq 6 \\ \hat{\boldsymbol{\gamma}}_{r-6} \cdot \sum_{i=r-6}^{6} \left(\mathbf{I}_{i,bdy}\mathbf{J}_{\boldsymbol{\omega},i} + \mathbf{p}_{r-6,i,JC} \times m_{i,bdy}\mathbf{J}_{\mathbf{p},i}\right), & 7 \leq r \leq 12 \end{cases} \tag{6.71}$$

$$(\mathbf{C})_{r,:} = \begin{cases} \hat{\boldsymbol{\rho}}_r \cdot \sum_{i=r}^{6} \left(\mathbf{I}_{i,bdy}\dot{\mathbf{J}}_{\boldsymbol{\omega},i} + \boldsymbol{\omega}_i \times \mathbf{I}_{i,bdy}\mathbf{J}_{\boldsymbol{\omega},i} + \mathbf{p}_{R,i,JC} \times m_{i,bdy}\dot{\mathbf{J}}_{\mathbf{p},i}\right), & 1 \leq r \leq 6 \\ \hat{\boldsymbol{\gamma}}_{r-6} \cdot \sum_{i=r-6}^{6} \left(\mathbf{I}_{i,bdy}\dot{\mathbf{J}}_{\boldsymbol{\omega},i} + \boldsymbol{\omega}_i \times \mathbf{I}_{i,bdy}\mathbf{J}_{\boldsymbol{\omega},i} + \mathbf{p}_{r-6,i,JC} \times m_{i,bdy}\dot{\mathbf{J}}_{\mathbf{p},i}\right), & 7 \leq r \leq 12 \end{cases} \tag{6.72}$$

### USRT Gravitational Loading

Like a joint's inertial moment, a joint's gravitational moment is due to the gravitational forces acting on the COMs of links "downstream" of the joint. Equation 6.73 defines the link $i$ gravitational force $\mathbf{F}_{i,grv,bdy}$, where $g$ is gravitational acceleration, and Eq. 6.74 defines the joint $j$ gravitational moment $\mathbf{M}_{j,grv}$ due to gravity acting on links $i = j$ through $i = 6$.

$$\mathbf{F}_{i,grv,bdy} = -m_{i,bdy} g \hat{\mathbf{x}}_T, \tag{6.73}$$

$$\mathbf{M}_{j,grv} = \sum_{i=j}^{6} (\mathbf{p}_{j,i,JC} \times \mathbf{F}_{i,grv,bdy}) \tag{6.74}$$

Equation 6.75 uses $\mathbf{M}_{j,grv}$ in conjunction with the joint $j$ pitch $\hat{\boldsymbol{\rho}}_j$ and yaw $\hat{\boldsymbol{\gamma}}_j$ axis unit vectors to formulate rows $r \in \{1, \cdots, 12\}$ of the $\mathbf{g}$ vector.

$$(\mathbf{g})_r = \begin{cases} \hat{\boldsymbol{\rho}}_r \cdot \mathbf{M}_{r,grv}, & 1 \leq r \leq 6 \\ \hat{\boldsymbol{\gamma}}_{r-6} \cdot \mathbf{M}_{r-6,grv}, & 7 \leq r \leq 12 \end{cases} \tag{6.75}$$

### USRT Coupling Loading

The joint $j$ coupling moment, defined in Eq. 6.76, is due to the loading acting between links $i = j-1$ and $i = j$. Moments due to four sources of loading are included in Eq. 6.76: $\mathbf{M}^{j-1}_{j,ext}$ for the extension spring, $\mathbf{M}^{j-1}_{j,cmp}$ for the compression spring, $\mathbf{M}^{j-1}_{j,dmp}$ for the joint damping and $\mathbf{M}^{j-1}_{j,lim}$ for the joint angle limit.

$$\mathbf{M}^{j-1}_{j,cpl} = \mathbf{M}^{j-1}_{j,ext} + \mathbf{M}^{j-1}_{j,cmp} + \mathbf{M}^{j-1}_{j,dmp} + \mathbf{M}^{j-1}_{j,lim} \tag{6.76}$$

For the joint $j$ extension spring, $\mathbf{M}_{j,ext}^{j-1}$ is defined in Eq. 6.77, where $\mathbf{p}_{j,JE}^{j-1} = \mathbf{R}_{(j-1)j}^{j-1}\mathbf{p}_{j,JE}^{i}$, $\mathbf{p}_{j,JE}^{j}$ is defined in Eq. 6.56, $\mathbf{F}_{j,ext}^{j-1}$ is the force applied by the joint $j$ extension spring on its link $i = j$ anchor (defined in Eq. 6.78), $k_{j,ext}$ is the joint $j$ extension spring stiffness, $L_{j,ext}$ is the joint $j$ extension spring unloaded length, $F_{j,ext,pre}$ is the joint $j$ extension spring pretension and $\mathbf{p}_{j,ext}^{j-1}$ is defined in Eq. 6.55.

$$\mathbf{M}_{j,ext}^{j-1} = \mathbf{p}_{j,JE}^{j-1} \times \mathbf{F}_{j,ext}^{j-1}, \tag{6.77}$$

$$\mathbf{F}_{j,ext}^{j-1} = -\left(k_{j,ext}\left(\left\|\mathbf{p}_{j,ext}^{j-1}\right\| - L_{j,ext}\right) + F_{j,ext,pre}\right)\hat{\mathbf{p}}_{j,ext}^{j-1} \tag{6.78}$$

The joint $j$ compression spring generates a moment $\mathbf{M}_{j,cmp}^{j-1}$ that resists the joint's net bending $\beta_j$ (Eq. 6.51), as defined in Eq. 6.79, where $k_{j,cmp}$ is the joint $j$ compression spring bending stiffness [86] and $\boldsymbol{\lambda}_j^{j-1}$ is the common normal of the frame $j-1$ and $j$ z-axes, as defined in Eq. 6.52. Equation 6.80 defines the joint damping $\mathbf{M}_{j,dmp}^{j-1}$, which represents the energy loss during joint motion due to dissipative effects (e.g., friction) in the universal joint, where $c_{dmp}$ is the effective damping and $\dot{\beta}_j\boldsymbol{\lambda}_j^{j-1}$ is defined in Eq. 6.53.

$$\mathbf{M}_{j,cmp}^{j-1} = -k_{j,cmp}\beta_j\boldsymbol{\lambda}_j^{j-1}, \tag{6.79}$$

$$\mathbf{M}_{j,dmp}^{j-1} = -c_{j,dmp}\dot{\beta}_j\boldsymbol{\lambda}_j^{j-1} \tag{6.80}$$

The joint $j$ limit that prevents $\beta_j$ from exceeding an angle $\beta_{lim}$ generates the moment $\mathbf{M}_{j,lim}^{j-1}$ with respect to the joint when the calculated $\beta_j$ exceeds $\beta_{lim}$. This limit is modeled as a nonlinear spring-damper, with zero loading when $\beta_j \leq \beta_{lim}$, and continuously increasing loading if $\beta_j > \beta_{lim}$, as defined in Eq. 6.81, where $k_{lim}$ is the limit's additional stiffness and

$c_{lim}\left(\beta_j - \beta_{lim}\right)$ is the limit's additional damping.

$$\mathbf{M}_{j,lim}^{j-1} = \begin{cases} \mathbf{0}_{3\times 1}, & \beta_j \leq \beta_{lim}, \\ \left(-k_{lim} - c_{lim}\dot{\beta}_j\right)\left(\beta_j - \beta_{lim}\right)\boldsymbol{\lambda}_j^{j-1}, & \beta_j > \beta_{lim} \end{cases} \tag{6.81}$$

Unlike the R3RT dynamic model, in which the coupling loading was algebraically manipulated out of Eq. 6.4, the USRT's coupling loading contributes to both $\mathbf{d}$ and $\mathbf{k}$.

Equations 6.82 and 6.83 define formulations of the non-linear elasticity vector $\mathbf{k}$ and the non-linear damping vector $\mathbf{d}$, respectively, in terms of those vectors' row $r \in \{1, \cdots, 12\}$ elements. The moments due to the extension spring, compression spring and joint limit all contribute to $\mathbf{k}$, and the moment due to the universal joint damping contributes to $\mathbf{d}$. A more conventional formulation of one or more of these loading effects defined as a matrix multiplying $\mathbf{q}$ or $\dot{\mathbf{q}}$ cannot be achieved due to the geometric nonlinearity of the coupled motion of the universal joint angles during joint displacement.

$$\left(\mathbf{k}\right)_r = \begin{cases} \hat{\boldsymbol{\rho}}_r^{r-1} \cdot \left(\mathbf{M}_{r,ext}^{r-1} + \mathbf{M}_{r,cmp}^{r-1} + \mathbf{M}_{r,lim}^{r-1}\right), & 1 \leq r \leq 6 \\ \hat{\boldsymbol{\gamma}}_{r-6}^{r-7} \cdot \left(\mathbf{M}_{r-6,ext}^{r-7} + \mathbf{M}_{r-6,cmp}^{r-7} + \mathbf{M}_{r-6,lim}^{r-7}\right), & 7 \leq r \leq 12 \end{cases} \tag{6.82}$$

$$\left(\mathbf{d}\right)_r = \begin{cases} \hat{\boldsymbol{\rho}}_r^{r-1} \cdot \mathbf{M}_{r,dmp}^{r-1}, & 1 \leq r \leq 6 \\ \hat{\boldsymbol{\gamma}}_{r-6}^{r-7} \cdot \mathbf{M}_{r-6,dmp}^{r-7}, & 7 \leq r \leq 12 \end{cases} \tag{6.83}$$

### USRT Actuation Loading

The joint $j$ actuation loading is due to the six ($1 \leq j \leq 3$) or three ($4 \leq j \leq 6$) cables routing between disks $i = j - 1$ and $i = j$. Each cable $k \in \{1, \cdots, 6\}$ is defined by a tension $T_k$ prescribed at the base (this tension may be zero), with coefficients $\mu_{j,k}$ scaling that tension

along the tail. If $\mu_{j,k} = 0$, cable $k$ is not present between disks $i = j-1$ and $i = j$ and does not affect the joint $j$ loading; if $0 < \mu_{j,k} < 1$, the cable $k$ tension affecting joint $j$ is lessened by friction compared to $T_k$; and if $\mu_{j,k} = 1$, the cable $k$ tension affecting joint $j$ is $T_k$ (i.e., the cable routes without friction). The resulting joint $j$ actuation moment $\mathbf{M}^{j-1}_{j,act}$ is defined in Eq. 6.84, where $\mathbf{p}^{j-1}_{j,k,JH} = \mathbf{R}^{j-1}_{(j-1)j}\mathbf{p}^{j}_{j,k,JH}$, $\mathbf{p}^{j}_{j,k,JH}$ is defined in Eq. 6.58, $\mathbf{F}^{j-1}_{j,k,cbl}$ is the cable $k$ force acting across joint $j$ (defined in Eq. 6.85) and $\mathbf{p}^{j-1}_{(j-1)j,k,cbl}$ is defined in Eq. 6.57.

$$\mathbf{M}^{j-1}_{j,act} = \sum_{k=1}^{6} \left(\mathbf{p}^{j-1}_{j,k,JH} \times \mathbf{F}^{j-1}_{j,k,cbl}\right), \tag{6.84}$$

$$\mathbf{F}^{j-1}_{j,k,cbl} = -\mu_{j,k} T_k \hat{\mathbf{p}}^{j-1}_{(j-1)j,k,cbl} \tag{6.85}$$

The coefficients $\mu_{j,k}$ are defined in two stages. First, $\mu_{j,k}$ is defined as zero for each joint $j$ a given cable $k$ does not affect. For the tail under consideration, this condition is defined in Eq. 6.86 for the coefficients of cables $k \in \{1,2,3\}$ for joints $j \in \{4,5,6\}$.

$$\mu_{j,k} = 0, \quad (j,k) = (\{4,5,6\},\{1,2,3\}) \tag{6.86}$$

Second, a belt-friction model [79] is assumed at each cable routing hole, and the cumulative friction losses in cable subsegment tensions are propagated along the length of the tail. For the belt friction model, this is a geometric scaling, defined in Eq. 6.87, where $\mu$ is the coefficient of friction and $\psi_{j,k}$ is the cable $k$ link $i = j$ contact angle.

$$\mu_{j,k} = \begin{cases} 1, & j = 0, \\ \mu_{j-1,k} e^{-\mu\psi_{j,k}}, & 1 \le j \le 6 \end{cases}, \quad \psi_{j,k} = \cos^{-1}\left(\hat{\mathbf{p}}^{j-1}_{(j-1)j,k,cbl} \cdot \hat{\mathbf{p}}^{j-1}_{j(j+1),k,cbl}\right) \tag{6.87}$$

The actuation transmission matrix $\mathbf{T}$ is defined by extracting the cable tensions $T_k$ from the formulations of Eqs. 6.84 and 6.85. A formulation for the row $r$ and column $c$ value of $\mathbf{T}$ is defined in Eq. 6.88.

$$(\mathbf{T})_{r,c} = \begin{cases} \hat{\boldsymbol{\rho}}_r \cdot \left( \mathbf{p}_{r,c,JH}^{r-1} \times \left( -\mu_{r,c} \hat{\mathbf{p}}_{(r-1)r,c,cbl}^{r-1} \right) \right), & 1 \leq r \leq 6 \\ \hat{\boldsymbol{\gamma}}_{r-6} \cdot \left( \mathbf{p}_{r-6,c,JH}^{r-7} \times \left( -\mu_{r-6,c} \hat{\mathbf{p}}_{(r-7)(r-6),c,cbl}^{r-7} \right) \right), & 7 \leq r \leq 12 \end{cases} \tag{6.88}$$

### 6.2.4 USRT Tail Base Loading

In this analysis, it will be assumed that the tail's base frame is coincident with the center of the load cell mounted to the USRT shown in Fig. 6.6 to aid in the comparison to experimental results. This load cell records the force and moment acting between the USRT and its mounting; this loading is analogous to the loading the tail applies to a stationary mobile robot. The orientation of the tail base frame $T$ with respect to the load cell frame $LC$ is defined in Eq. 6.89.

$$\mathbf{R}_{(LC)T}^{LC} = \begin{bmatrix} 0 & 0 & 1 \\ 0 & -1 & 0 \\ 1 & 0 & 0 \end{bmatrix} \tag{6.89}$$

Two types of loading will contribute to the force and moment between the USRT actuation module and the load cell: gravity and inertia. Given that both of these effects are modeled at the link COMs, the position vector $\mathbf{p}_{i,COM}$ (Eq. 6.48) is used to relate this point to the inertial tail frame/load cell frame origin. Equations 6.90 and 6.91 define the force $\mathbf{F}_T^{LC}$ and moment $\mathbf{M}_T^{LC}$ applied on the USRT by the tail base/load cell, and the USRT applies an equal and opposite force/moment pair on the load cell.

$$\mathbf{F}_T^{LC} = \mathbf{R}_{(LC)T}^{LC}\left(\sum_{i=0}^{6}\left(\mathbf{F}_{i,inr,bdy} - \mathbf{F}_{i,grv,bdy}\right)\right) \tag{6.90}$$

$$\mathbf{M}_T^{LC} = \mathbf{R}_{(LC)T}^{LC}\left(\sum_{i=0}^{6}\left(\mathbf{M}_{i,inr,bdy} + \mathbf{p}_{i,j,JC} \times \left(\mathbf{F}_{i,inr,bdy} - \mathbf{F}_{i,grv,bdy}\right)\right)\right) \tag{6.91}$$

The loading trajectories will be normalized with respect to the loading of the tail when fully extended. This will emphasize how the tail loading changes due to the motion, and how it modifies the loading acting on the legged platform.

### 6.2.5 USRT Simulations

The geometric, mass and elastic properties used in these simulations have been extracted from the USRT prototype (section 5.2.4) and its associated CAD model. Tables 6.2 and 6.3 define the tail properties. The moments of inertia of links 1-6 are sufficiently small that they may be neglected, and friction is assumed to be negligible along the length of the USRT.

Table 6.2: Mass, geometric and elastic properties of the USRT prototype.

| Variable | Value | Variable | Value |
|---|---|---|---|
| $L_{JJ}$ | 80 mm | $\mathbf{p}_{01,jnt}$ | $[62.85,\ 0,\ 53.5]^T$ mm |
| $L_{JD}$ | 74 mm | $\mathbf{p}_{0,JC}$ | $[84.64,\ 0,\ -56.13]^T$ mm |
| $L_{JC}$ | 46.6 mm | $\mathbf{p}_{j-1,ext,B}^{j-1}$ | $[30.5,\ 0,\ 6]^T$ mm |
| $L_{DJ}$ | 6 mm | $k_{cmp}$ | 2.82 N-m/rad |
| $m_{0,bdy}$ | 6507 g | $c_{dmp}$ | 0.1 N-m-s/rad |
| $m_{\{1,\cdots,6\},bdy}$ | 85 g | $\beta_{lim}$ | 35° |
| $r_{hl}$ | 32.5 mm | $k_{lim}$ | 100 N-m/rad |
| $\mu$ | 0 | $c_{lim}$ | 0.1 N-m-s/rad |

Three case studies will be considered in this analysis: yaw-direction bending, pitch-direction bending, and bending through a rolling motion. For each of these case studies, a kinematic

Table 6.3: Joint-specific geometric and elastic properties of the USRT prototype.

| **Joint** | $k_{j,ext}$ **(N/m)** | $L_{j,ext}$ **(mm)** | $F_{j,ext,pre}$ **(N)** | $\mathbf{p}^{j}_{j,ext,T}$ **(mm)** |
|---|---|---|---|---|
| 1 | 1460.6 | 38.354 | 3.47 | $[20.8,\ 0,\ -14.26]^T$ |
| 2 | 1460.6 | 38.354 | 3.47 | $[20.8,\ 0,\ -16.18]^T$ |
| 3 | 684.7 | 36.830 | 4.27 | $[20.8,\ 0,\ -13.45]^T$ |
| 4 | 455.3 | 36.830 | 2.98 | $[20.8,\ 0,\ -13.39]^T$ |
| 5 | 122.6 | 37.592 | 1.02 | $[20.8,\ 0,\ -15.38]^T$ |
| 6 | 122.6 | 37.592 | 1.02 | $[20.8,\ 0,\ -15.57]^T$ |

model will be used to derive desired cable trajectory inputs, which will be applied to the tail's dynamic model. For planning the cable trajectories, it will be assumed that the six pitch and yaw angles in the tail are equal to $\phi_{des}$ and $\theta_{des}$, respectively. However, individual joint angles in the tail trajectories may not match these desired joint angle trajectories, due to the variable effects of gravitational and elastic loading along the tail. Each case study below describes how its $\phi_{des}$ and $\theta_{des}$ trajectories are defined; using these trajectories, the kinematic model described in section 6.2.2 is used to calculate $\delta_{k,des}$ using Eq. 6.59, for which $\mathbf{p}^{j-1}_{(j-1)j,k,cbl}$ is calculated using $\phi_j = \phi_{des}$ and $\theta_j = \theta_{des}$.

### USRT Yaw-Angle Bending

For yaw-angle bending, the joints' desired pitch angles are held fixed at 0, and the joints' desired yaw angles are determined by prescribing a desired acceleration profile and integrating from initial positions/velocities.

The desired joint acceleration profile $\ddot{\theta}_{des}$ is a sine wave defined for a single period $T_{0f}$ from time $t_0$ to $t_f$, as shown in Eq. 6.92, where $\ddot{\theta}_{pk}$ is the sine wave's peak acceleration magnitude, $\theta_{des,0}$ and $\theta_{des,f}$ are the initial and final yaw angles, and $\dot{\theta}_{des,0}$ is the initial yaw velocity. Trajectories for the yaw angle and velocity are calculated by integrating $\ddot{\theta}_{des}$ from

the initial conditions $\theta_{des,0}$ and $\dot{\theta}_{des,0}$.

$$\ddot{\theta}_{des} = \begin{cases} \ddot{\theta}_{pk} \sin\left(2\pi \frac{t-t_0}{T_{0f}}\right), & t_0 \leq t \leq t_f \\ 0, & t > t_f \end{cases}, \quad \ddot{\theta}_{pk} = 2\pi \frac{\theta_{des,f} - \theta_{des,0} - \dot{\theta}_{des,0} T_{0f}}{T_{0f}^2} \tag{6.92}$$

The first set of simulations prescribes tail bending of 90° in 0.3, 0.5 and 0.7 sec, with trajectory parameters defined in Eq. 6.93. Figure 6.8 illustrates the joint trajectories associated with the $T_{0f} = 0.5$ sec trajectory. As previously discussed, the behavior in the pitch and yaw angles does not match the behavior planned for when generating the trajectory; the tail dynamics cause variation in the joint angles along the length. For example, since the simulation parameters are taken from the experimental prototype shown in Fig. 5.10, the pitch angles in segment 1 are not perfectly balanced such that their magnitudes are zero at the initial condition. However, the sum of these three angles does approximate zero within the segment. Despite these minor variations, the various joint angles track trajectories similar to those prescribed.

$$\theta_{des,0} = 0, \quad \theta_{des,f} = 15°, \quad \dot{\theta}_{des,0} = 0, \quad T_{0f} = \{0.3, 0.5, 0.7\} \text{ sec} \tag{6.93}$$

Loading results for the three case studies are illustrated in Fig. 6.9. Negligible loading is observed in $\left(\mathbf{F}_T^{LC}\right)_z$, the x-component of $\mathbf{F}_T^{LC}$, due to the minimal change in the tail's vertical COM position, whereas nontrivial loading is observed in $\left(\mathbf{F}_T^{LC}\right)_x$ and $\left(\mathbf{F}_T^{LC}\right)_y$, due to the x- and y-direction tail COM displacement. For the moment loading, minor steady-state variations in $\left(\mathbf{M}_T^{LC}\right)_x$ and $\left(\mathbf{M}_T^{LC}\right)_y$ due to gravity are observed, but the most significant dynamic loading occurs in $\left(\mathbf{M}_T^{LC}\right)_z$, as desired.

A second set of simulations is also performed for a net 150° bend in 0.5, 0.75 and 1.0 sec; the trajectory parameters for these simulations are defined in Eq. 6.94. The 0.5 sec case

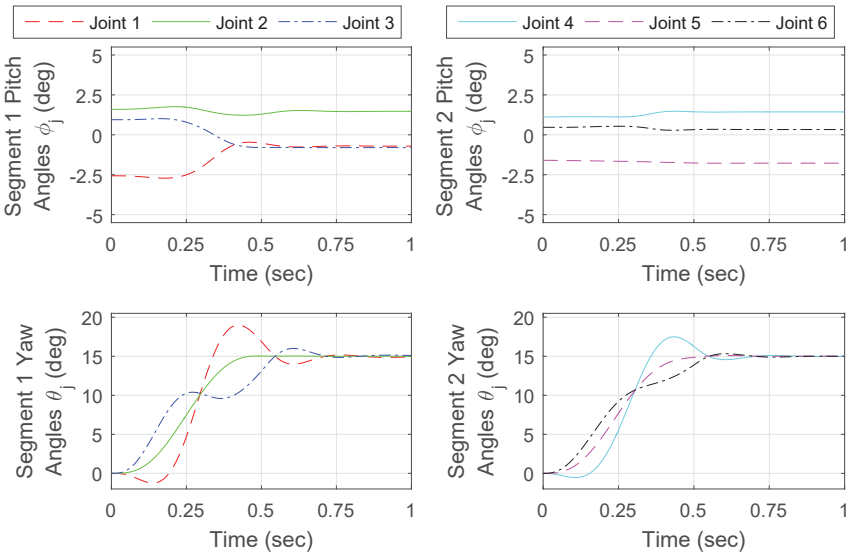


Figure 6.8: USRT simulation results: joint angle trajectories for 90° yaw bending in 0.5 sec.

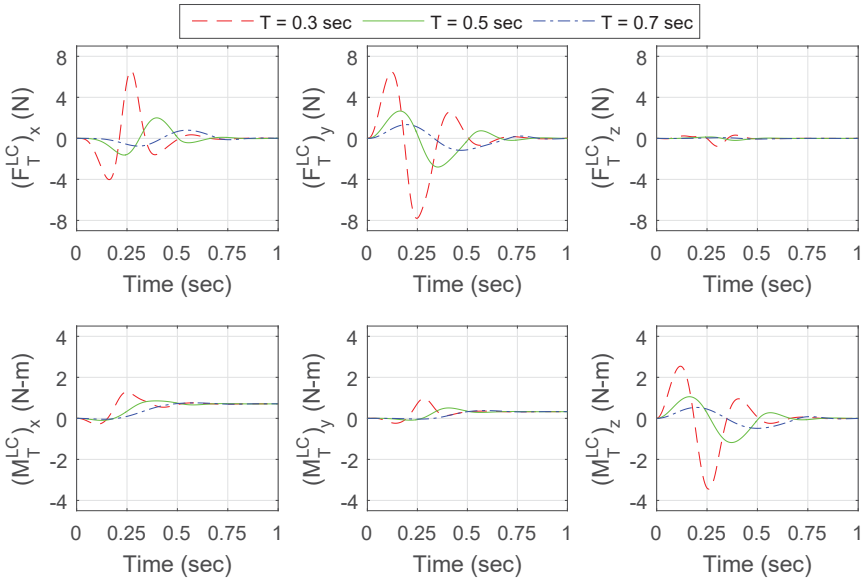


Figure 6.9: USRT simulation results: yaw bending loading for 90° bend.

represents a similar effective velocity of the tail as the previous 0.3 sec simulation (i.e., moving 90° in 0.3 sec and moving 150° in 0.5 sec both correspond to an effective velocity of 300°/sec), which shows the impact of additional tail "stroke" on the dynamic loading.

$$\theta_{des,0} = 0, \quad \theta_{des,f} = 25°, \quad \dot{\theta}_{des,0} = 0, \quad T_{0f} = \{0.5, 0.75, 1.0\} \text{ sec} \tag{6.94}$$

Figure 6.10 illustrates the loading results for these three cases. Qualitatively, the loading behavior is similar to the 90° yaw bending loading, but with reduced magnitudes in $\left(\mathbf{F}_T^{LC}\right)_x$, $\left(\mathbf{F}_T^{LC}\right)_y$ and $\left(\mathbf{M}_T^{LC}\right)_z$. Despite similar bending rates, the reduced time span in the 90° bending generates greater magnitude loading. Higher magnitude loading for a given yaw-direction tail displacement is beneficial for overcoming friction, as discussed in [69], whereas greater stroke is necessary for higher net rotation in the absence of friction.

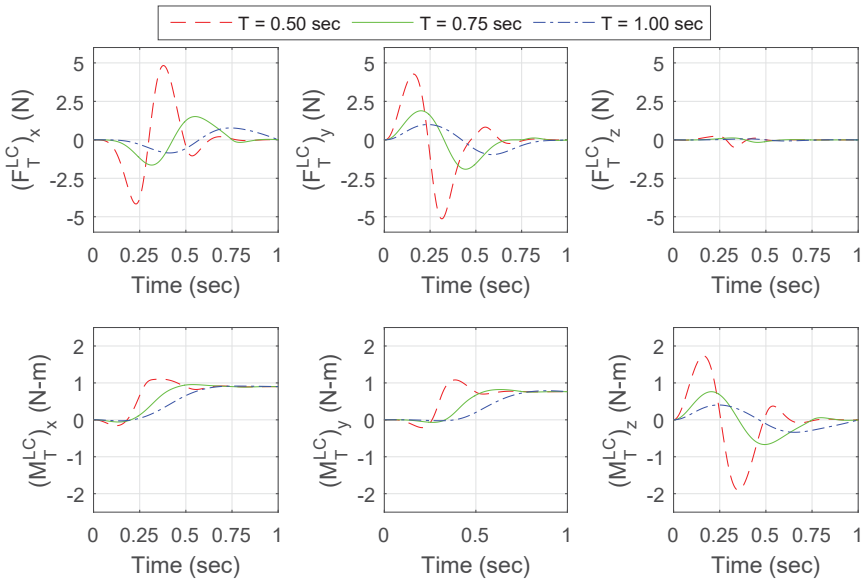


Figure 6.10: USRT simulation results: yaw bending loading for 150° bend.

### USRT Pitch-Angle Bending

The trajectory planning for the pitch angle bending is identical to that for yaw angle bending except $\theta$ and $\phi$ are switched: $\theta_{des}$ is fixed at zero, and $\ddot{\phi}_{des}$ is defined by Eq. 6.92. Likewise, two sets of simulations are carried out for the pitch-angle behavior of the robot using the same trajectories defined by the parameters in Eqs. 6.93 and 6.94, with $\phi$ substituted for $\theta$. Unlike the yaw-direction motion, in which there was multi-degree pitch motion due to variations in gravitational loading, there is no significant out-of-plane loading in this case to cause the yaw angles to vary during simulation (slight variations due to rounding errors do occur but are corrected for by the elastic loading of the compression spring). Therefore, only the pitch angle trajectories, $\left(\mathbf{F}_T^{LC}\right)_x$, $\left(\mathbf{F}_T^{LC}\right)_z$ and $\left(\mathbf{M}_T^{LC}\right)_y$ are shown; the yaw angle trajectories and other three loading components are negligible.

Figure 6.11 illustrates the pitch angle trajectories for the 90° tail bending motion in 0.5 sec. Due to the impact of changing gravitational loading as the tail bends, along with the variations in extension spring stiffness along the tail, the similarity in joint trajectories within a given segment is less than the yaw angle trajectories for the previous case. In the yaw case, the equal stiffness compression springs were the primary mechanism by which loading was balanced within a segment, and unequal inertia at the tail joints caused variation; in this pitch case, there is a more complex relationship between the effects of the compression springs, extension springs, gravity and inertia, leading to greater variation within the segment.

Figure 6.12 illustrates the nontrivial loading associated with the pitch direction case studies. Despite the reduced similarity of the joint angle trajectories in comparison to yaw-angle trajectories in Fig. 6.8, the loading profiles for the pitch motion are very similar to those for the yaw motion. The yaw and pitch $\left(\mathbf{F}_T^{LC}\right)_x$ trajectories correlate, as do the yaw $\left(\mathbf{F}_T^{LC}\right)_y$ and pitch $\left(\mathbf{F}_T^{LC}\right)_z$ trajectories; the yaw and pitch $\left(\mathbf{M}_T^{LC}\right)_z$ and $\left(\mathbf{M}_T^{LC}\right)_y$ trajectories are

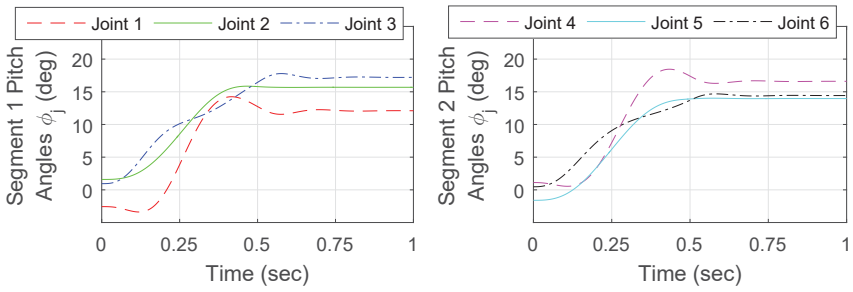


Figure 6.11: USRT simulation results: joint angle trajectories for 90° pitch bending in 0.5 sec.

approximately equal and opposite. This shows a strong correlation between the kinematically planned trajectory and the applied loading, with the tail dynamics merely perturbing the loading predicted by the applied kinematic trajectory.

### USRT Rolling Motion While Bending

To simulate the rolling motion depicted in Fig. 5.9, an alternative set of joint coordinates are used to plan the trajectory, which were then mapped into the desired pitch and yaw angle trajectories. The coordinates on which the alternative trajectory was defined were a desired bending plane angle $\kappa_{des}$ and a bending angle $\beta_{des}$ (analogous to $\beta_i$ in Eq. 6.51). The desired link $i$ z-axis orientation relative to frame $i-1$ is defined by Eq. 6.95.

$$\hat{\mathbf{z}}^{i-1}_{(i-1)i,des} = \mathbf{R}_Z\left(\kappa_{des}\right)\mathbf{R}_Y\left(\beta_{des}\right)\hat{\mathbf{z}}^{i}_{i} \tag{6.95}$$

In these coordinates, the rolling motion is prescribed by holding $\beta_{des}$ at a fixed value, while $\kappa_{des}$ follows a trajectory similar to $\theta_{des}$ from the yaw-bending case, from an initial angle of $\kappa_{des,0}$ to a final angle of $\kappa_{des,f}$ starting from a velocity of $\dot{\kappa}_{des,0}$, defined by Eq. 6.92, for which $\kappa$ is substituted for $\theta$.

The angles $\kappa_{des}$ and $\beta_{des}$ are mapped into $\phi_{des}$ and $\theta_{des}$ using Eq. 6.96, where $\hat{\mathbf{z}}^{i-1}_{(i-1)i,des}$ is

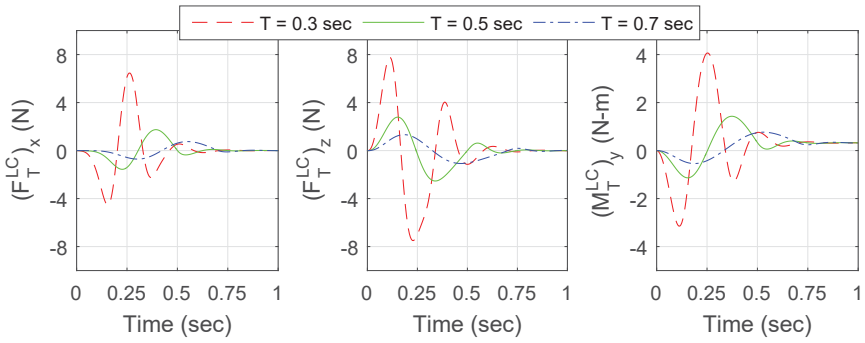


(a) 90° bend

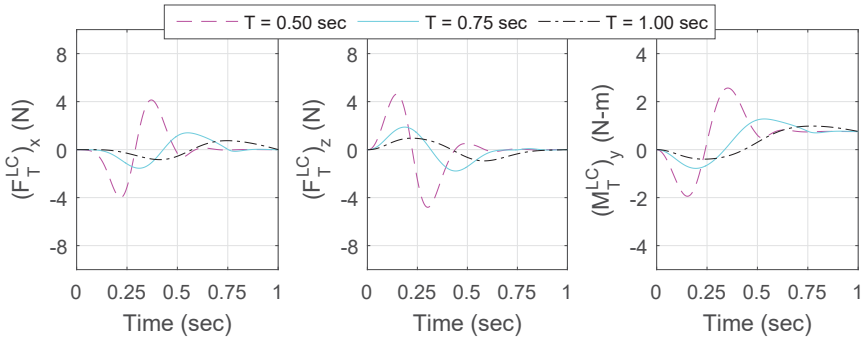


(b) 150° bend

Figure 6.12: USRT simulation results: pitch bending loading for 90° and 150° bends.

known as a function of $\kappa_{des}$ and $\beta_{des}$ from Eq. 6.95. The three transcendental equations in Eq. 6.96 may be uniquely solved for $\phi_{des}$ and $\theta_{des}$ in the domain $\{\phi_{des}, \theta_{des}\} \in [-\beta_{lim}, \beta_{lim}]$.

$$\hat{\mathbf{z}}_{(i-1)i,des}^{i-1} = \mathbf{R}_Y\left(\phi_{des}\right)\mathbf{R}_X\left(\theta_{des}\right)\hat{\mathbf{z}}_i^i \tag{6.96}$$

Three sets of simulations were run to analyze the impact of the initial bending angle on the loading generated by a $-180°$ rolling motion at a fixed $\beta_{des}$ of 15°. In the first set, the tail was rolled from a zero-yaw, positive pitch initial condition using the trajectory parameters in Eq. 6.97. In the second set, the tail was rolled from a zero-pitch, negative yaw initial condition using the trajectory parameters defined in Eq. 6.98. In the third set, the tail was rolled from a zero-yaw, negative pitch initial condition using the trajectory parameters in Eq. 6.99.

$$\kappa_{des,0} = 0, \quad \kappa_{des,f} = -180°, \quad \dot{\kappa}_{des_0} = 0, \quad T_{0f} = \{0.6, 0.8, 1.0\} \text{ sec} \tag{6.97}$$

$$\kappa_{des,0} = 90°, \quad \kappa_{des,f} = -90°, \quad \dot{\kappa}_{des_0} = 0, \quad T_{0f} = \{0.6, 0.8, 1.0\} \text{ sec} \tag{6.98}$$

$$\kappa_{des,0} = 180°, \quad \kappa_{des,f} = 0, \quad \dot{\kappa}_{des_0} = 0, \quad T_{0f} = \{0.6, 0.8, 1.0\} \text{ sec} \tag{6.99}$$

Figures 6.13, 6.14 and 6.15 show the loading for the three sets of roll motion simulations. In each case, $\left(\mathbf{F}_T^{LC}\right)_x$ is minimal, as the tail COM is not prescribed motion in this direction (dynamic effects during tail motion introduce slight x-coordinate motions which cause slight perturbations in this loading). Given that all three trajectories consist of a clockwise, $-180°$ rotation of the tail COM, the dynamic components of $\left(\mathbf{M}_T^{LC}\right)_x$ of the three figures are similar. However, variations are caused by the fact that for the zero-initial pitch case, since the initial and final configurations bend away from the vertical plane, there are non-zero static offsets for the loading. In addition, the variation in how the tail must act with or against gravity for different initial angles changes the magnitude of the loading generated by each tail.

The loading trajectories of $\left(\mathbf{F}_T^{LC}\right)_y$, $\left(\mathbf{F}_T^{LC}\right)_z$, $\left(\mathbf{M}_T^{LC}\right)_y$ and $\left(\mathbf{M}_T^{LC}\right)_z$ for Fig. 6.15 are of opposite sign than those of Fig. 6.15, given that the two tail motions move in opposite directions. However, the magnitudes of these trajectories are not equal, due to the effect of gravity acting with the tail motion in Fig. 6.13 and against the tail motion in Fig. 6.15. In terms of acceleration, for Fig. 6.13, gravity acts against acceleration and with deceleration; for Fig. 6.15, gravity acts with acceleration and against deceleration. However, for Fig. 6.14, both acceleration and deceleration act against gravity; this leads to the highest magnitude peak loading for each of the four components under consideration. This shows that $\kappa_{des,0}$ provides a means to adjust the secondary loading the tail applies on the robot during a rolling motion; for a given roll, $\kappa_{des,0}$ may be chosen such that $\left(\mathbf{F}_T^{LC}\right)_y$, $\left(\mathbf{F}_T^{LC}\right)_z$, $\left(\mathbf{M}_T^{LC}\right)_y$ and $\left(\mathbf{M}_T^{LC}\right)_z$

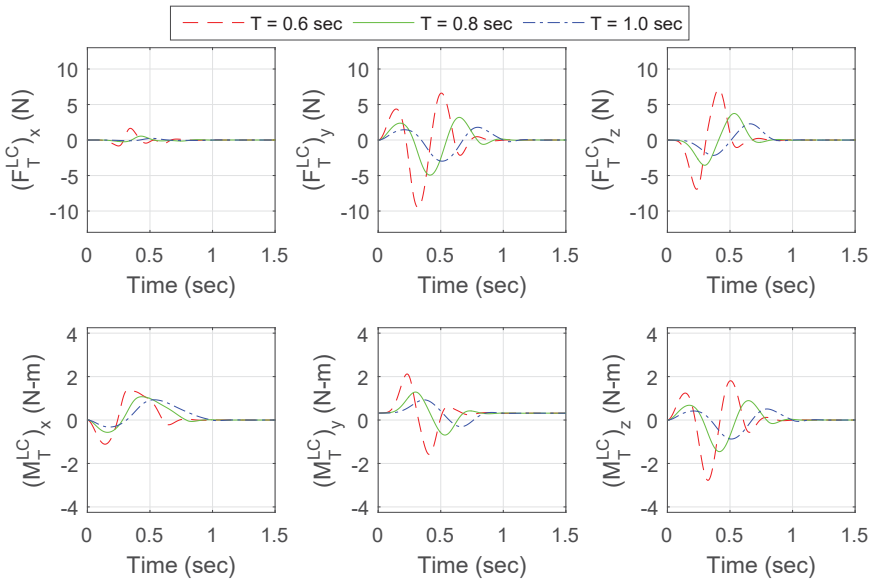


Figure 6.13: USRT simulation results: $-180°$ roll motion loading with $90°$ tail bend for zero-yaw, positive pitch initial condition.

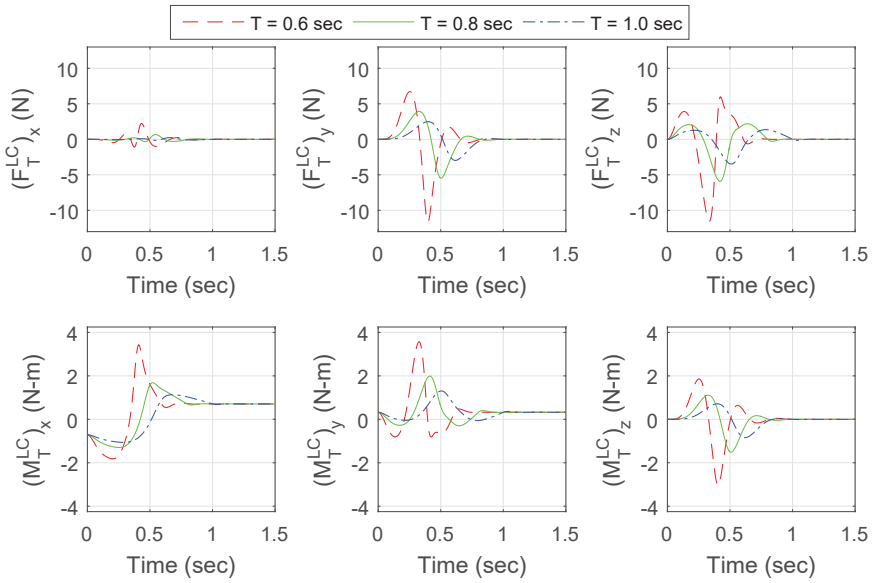


Figure 6.14: USRT simulation results: $-180°$ roll motion loading with $90°$ tail bend for zero-pitch, negative yaw initial condition.

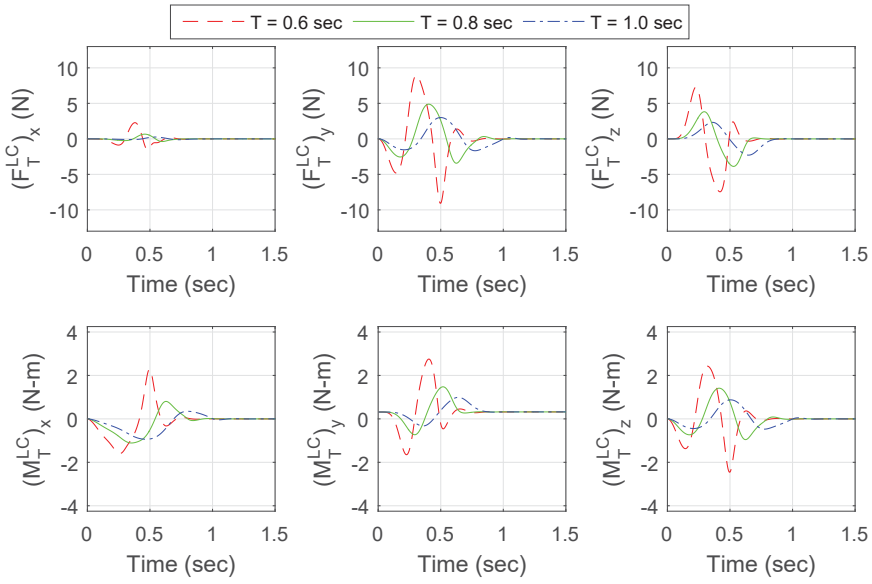


Figure 6.15: USRT simulation results: $-180°$ roll motion loading with $90°$ tail bend for zero-yaw, negative pitch initial condition.

do not destabilize the robot in addition to applying the desired $\left(\mathbf{M}_T^{LC}\right)_x$. However, unlike the previous two case studies, the loading generated by the rolling tail motion generates yaw, pitch and moment loading of comparable magnitude, requiring greater consideration of the destabilizing effects of the pitch and yaw moments during a roll motion.

### 6.2.6 USRT Experiments

Loading results were generated using trajectories considered in the three case studies analyzed in section 6.2.5. Measured results were filtered using the MATLAB 'filter' function to implement a moving-average filter, with a window size of 50 samples for samples recorded at approximately 400 Hz. As with the simulated loading, the results shown are normalized to the measured loading of the USRT in its initially extended configuration. In addition, the tail motion is initiated after at least 50 samples have been measured, so that the filter has sufficient samples preceding the dynamic loading profile to effectively filter.

For the yaw angle case study, the tail was driven through a 90° bend in 0.5 sec. The measured joint trajectories and loading are shown in Figs. 6.16 and 6.17, along with the simulated results. Although the simulations approximate the general pattern of the results, there are variations in the joint trajectories and loading. For the joint trajectories, the implementation of the compression spring mounting leads to slight yaw variations along the length of the tail in its nominally straight configuration, as evidenced by the non-zero initial yaw angles in Fig. 6.16. The next generation of USRT will modify the compression spring mounting design to reduce these undesired initial yaw angle variations.

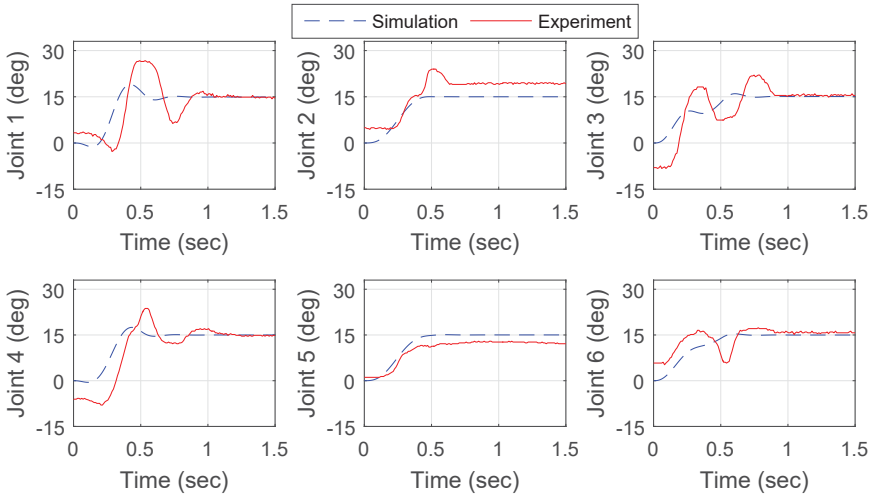


Figure 6.16: USRT experimental results: joint angle trajectories for 90° yaw bending in 0.5 sec.

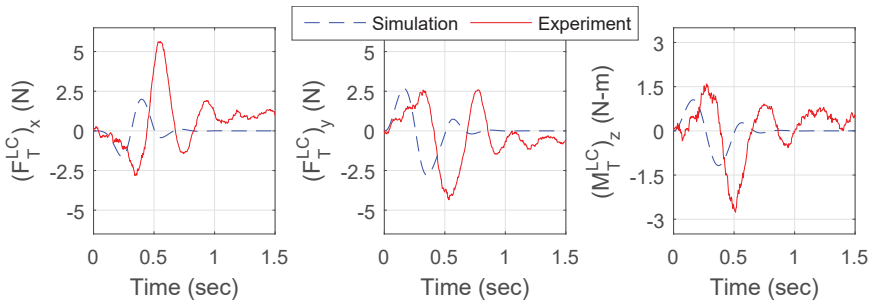


Figure 6.17: USRT experimental results: loading trajectories for 90° yaw bending in 0.5 sec.

Greater overshoot and vibration is also seen in the experimental results (both joint trajecto-

ries and loading) than the simulated results. As discussed in [71], the cable tension profiles during dynamic motion vary greatly due to the need to accelerate and decelerate the tail during a motion. Because the motor controller generates spool torque/cable tension based on prescribed velocity inputs, the controller cannot anticipate the highly dynamic changes in torque requirements to match the desired trajectory. Thus, more advanced control of the system, in which motor torques (or, interchangeably, motor currents) are prescribed to the motor driver instead of velocity commands implemented using a closed loop. The inclusion of a feedforward control component in this controller will also help with the observed lag; given that the motor velocity controller only utilizes feedback to prescribe motor current, a lag is necessary to generate the error that provides impetus to prescribe current to actuate the motor.

For the pitch angle case study, the tail was driven through a 90° bend in 0.5 sec. The measured joint trajectories and loading are shown in Figs. 6.18 and Fig. 6.19, along with the simulated results. The experimental joint angle trajectories show variations from the simulated trajectories similar to those for the yaw-bending case study, but with higher-magnitude vertical offset from the desired trajectories. For the yaw-direction bending, the compression spring is the primary means of distributing loading. However, in this pitch-direction motion, particularly in joints close to the base, the extension spring plays a similar or greater role in the dynamics than the compression spring. Furthermore, this variation in elastic loading along the length, while necessary for minimizing the actuation for supporting the USRT in its cantilevered-mode, reduces the uniformity in bending along the tail.

Although the pitch-motion joint trajectories show greater variation from their nominal values than the yaw-motion joint trajectories, the loading in Fig. 6.19 shows greater correlation to the predicted loading than the yaw-motion loading. Because the tail is moving up against gravity, gravity will help decelerate the USRT, reducing the overshoot in the loading com-

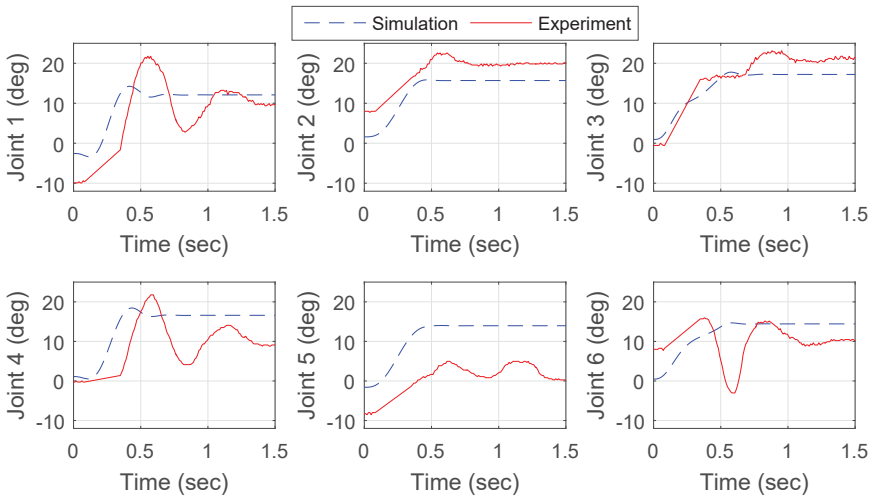


Figure 6.18: USRT experimental results: joint angle trajectories for 90° pitch bending in 0.5 sec.

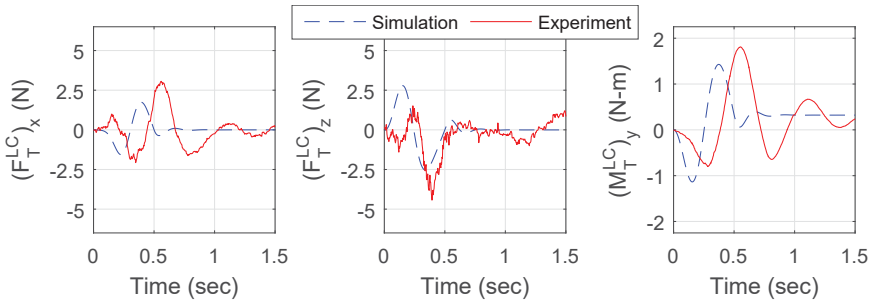


Figure 6.19: USRT experimental results: loading trajectories for 90° pitch bending in 0.5 sec.

pared to the yaw-direction bending. As before, the measured trajectories exhibit lag and increase oscillation in comparison to the simulated values due to the inner-loop motor velocity controller; a torque/current controller that utilizes both feedforward and feedback control elements will reduce these variations. Minor variations are observed in the tail's yaw-angle trajectories, $\left(\mathbf{F}_T^{LC}\right)_y$, $\left(\mathbf{M}_T^{LC}\right)_x$ and $\left(\mathbf{M}_T^{LC}\right)_z$, due to the non-zero initial yaw-angle configuration, as discussed for the yaw-direction case study. However, the magnitude of these effects are secondary in comparison to those shown in Fig. 6.19.

For the roll angle case study, the tail was driven through a $-180°$ rolling motion at a

prescribed bend of 90° ($\beta_{des} = 15°$) in 0.5 sec starting from zero yaw angle and positive pitch. The measured joint trajectories and loading are shown in Figs. 6.20, 6.21 and 6.22, along with simulated results. The joint trajectories show significant variations from their predicted value, due to the simultaneous, highly dynamic variation of pitch and yaw during the motion. In addition, since the trajectory did not start from the nominally straight configuration, additional errors were introduced in the positioning of the USRT into the initial configuration. Despite these errors, the correlation between the measured and predicted loading is the strongest amongst the three case studies. Because the tail is not moving monotonically in a single direction, there is less accumulated velocity that leads to overshoot. The most significant variation is in $\left(\mathbf{F}_T^{LC}\right)_x$, due to unmodeled motion of the tail COM along the x-axis. Controller improvements will lead to stable higher speed tail motions being possible, improving the loading capacity of the tail.

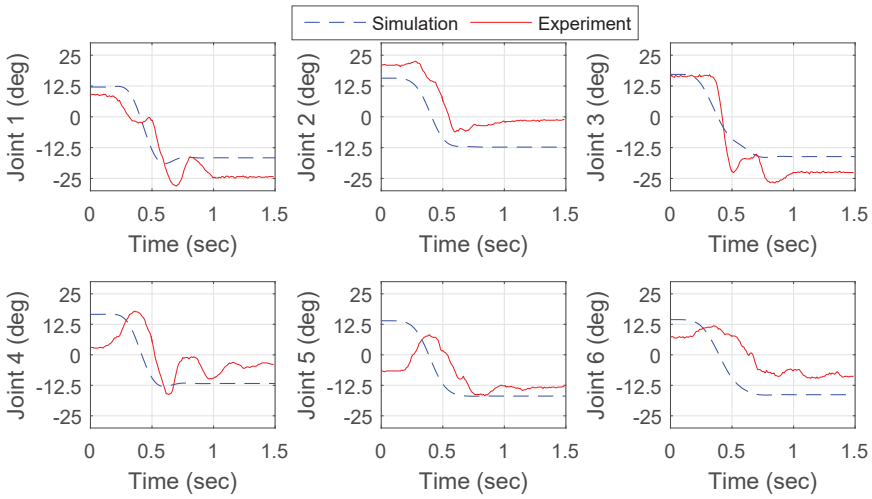


Figure 6.20: USRT experimental results: pitch angle trajectories for 180° roll rotation at a 90° bend in 0.8 sec.

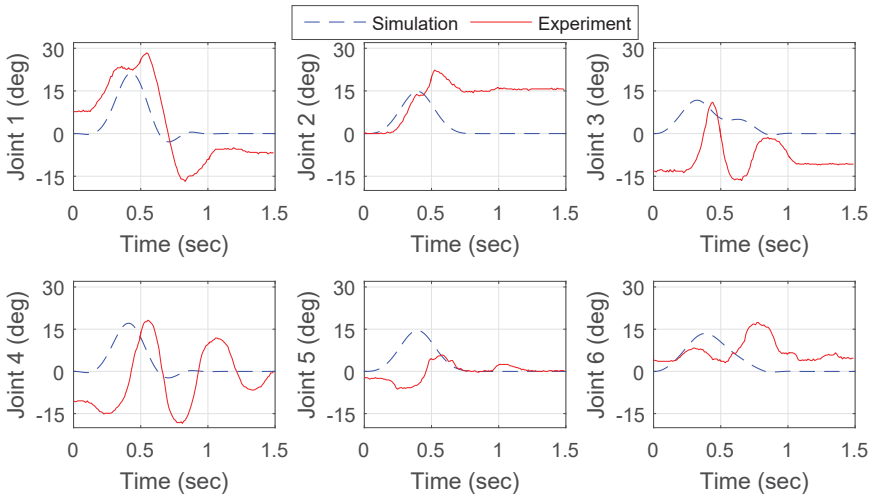


Figure 6.21: USRT experimental results: yaw angle trajectories for 180° roll rotation at a 90° bend in 0.8 sec.

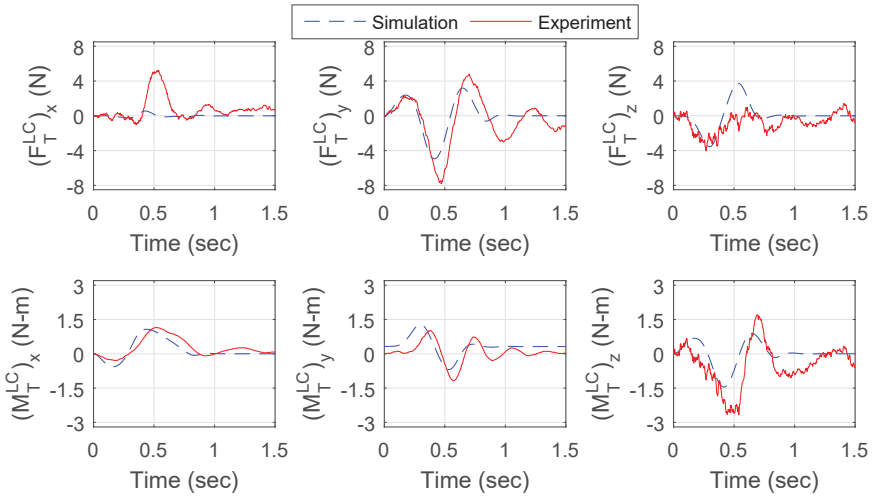


Figure 6.22: USRT experimental results: loading trajectories for 180° roll rotation at a 90° bend in 0.8 sec.

# Chapter 7

# Serpentine Tail Sensing and Control

In Chapter 6, the R3RT and USRT simulations were driven by kinematic constraints, and the R3RT and USRT experiments were driven by feedback-only velocity control loops implemented within the motor driver. To more effectively operate the R3RT and USRT and to use these tails to implement desired maneuvering and stabilization behaviors, analysis of outer-loop and inner-loop controllers for the R3RT and USRT are needed.

In this analysis, the phrase outer-loop control refers to the calculation of desired tail trajectories to implement a desired behavior, and the phrase inner-loop control refers to the calculation of control inputs to implement the desired tail trajectories (R3RT and USRT) and maintain cable tension in the six actuation cables (USRT).

This section is outlined as follows: Section 7.1 highlights the sensing associated with the R3RT and USRT, and analyzes the state estimation procedure for mapping the USRT sensor data into estimates of the joint angles and velocities. Section 7.2 presents the outer-loop controllers that will be used generate quadruped and biped maneuvering and stabilization behaviors with the R3RT and USRT. Section 7.3 defines the inner-loop controllers used to

generate control inputs for the R3RT, using feedback linearization to implement the desired motions for both tails, and a null space analysis to implement tensioning behavior in the USRT.

## 7.1 Tail Sensing and State Estimation

### 7.1.1 R3RT Sensing and State Estimation

Two types of joint-space sensing are integrated into the R3RT's actuation module: angular position (roll or cable pulleys) and motor rotor speed. The three position measurements are generated by absolute encoders (US Digital MA3-P10-125-N) coupled between the rigid housing and actuation module (for the roll angle) and between the actuation module and spools (for the spool angles). The roll-DOF encoder fits into the rear frame of the rigid housing and is coupled to the actuation module using a timing belt mounted to the groove shown in Fig. 5.2. The two segment-DOF encoders are coupled to the bevel gear in Fig. 5.2, which is rigidly connected to the pulley. Motor rotor angular velocity for each motor is estimated by an incremental encoder (US Digital E4T-360-236-DHMB) mounted to the gearmotor rotor's rear shaft. The absolute encoder measurement directly corresponds to the measured angular position, and the motor driver internally processes the incremental encoder measurements into an analog output scaled to the motor shaft velocity; no additional state estimation is required.

### 7.1.2 USRT Sensing and State Estimation

This section highlights the two types of sensing incorporated into the USRT design for state estimation: 12 linear displacement sensors (two per joint) to indirectly estimate the universal

joint angles, and seven inertial measurement units to indirectly estimate the universal joint velocities.

### Analytical Formulation

Figure 7.1 illustrates two joints of the USRT with two pairs of distance sensors. To accommodate the sensors for each joint, the sensors are alternatively placed "above" and "below" the universal joint along the tail. In both configurations, the position vectors from the disk center to the center of the sensor mount are at 45° angles with respect to the disk's x-axis unit vector $\hat{\mathbf{x}}_i^i$, ensuring a 90° separation of the sensor pair, which maximizes the sensor fidelity within the joint workspace.

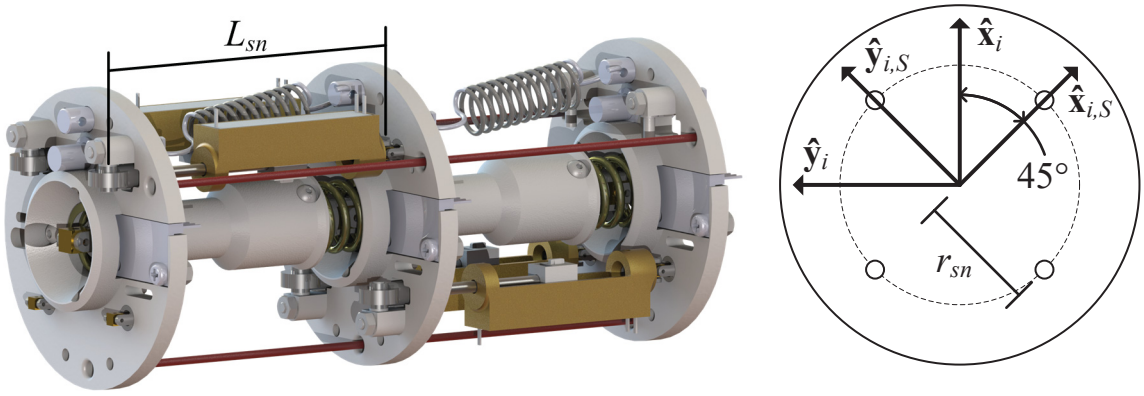


(a) Displacement sensor arrangement for adjacent joints

(b) Disk $i$ sensor frame definition

Figure 7.1: USRT joint angle sensing.

The joint $j$ sensor pair is mounted to link $i = j - 1$ with a universal joint and to link $i = j$ with a spherical joint, shown in Fig. 5.8b, to ensure fixed sensor endpoint positions with respect to the two disks without overconstraining the sensor.

For the joint $j \in \{1, \cdots, 6\}$ sensor $m \in \{1, 2\}$, the forward kinematics (calculating the sensor distances $d_{j,m,sn}$ from $\phi_j$ and $\theta_j$) are calculated using the positions from the link $i = j - 1$

sensor $m$ base to joint $j$ ($\mathbf{p}^{j-1}_{j,m,SJ}$, Eq. 7.1) and from joint $j$ to the link $i = j$ sensor $m$ tip ($\mathbf{p}^{j}_{j,m,JS}$, Eq. 7.2), where $\mathbf{p}^{j-1}_{j,m,sn,B}$ is the position from the link $i = j-1$ disk center to the joint $j$ sensor $m$ base, $L_{DJ}$ is the distance between a link's disk center and its distal universal joint center, $L_{JD}$ is the distance between a link's proximal universal joint center and its disk center, and $\mathbf{p}^{j}_{j,m,sn,T}$ is the position from the link $i = j$ disk center to the joint $j$ sensor $m$ tip.

$$\mathbf{p}^{j-1}_{j,m,SJ} = -\mathbf{p}^{j-1}_{j,m,sn,B} + L_{DJ}\hat{\mathbf{z}}^{j-1}_{j-1} \tag{7.1}$$

$$\mathbf{p}^{j}_{j,m,JS} = L_{JD}\hat{\mathbf{z}}^{j}_{j} + \mathbf{p}^{j}_{j,m,sn,T} \tag{7.2}$$

The position $\mathbf{p}^{j-1}_{j,m,sn}$ from the joint $j$ sensor $m$ base to tip is defined in Eq. 7.3, and the distance $d_{j,m,sn}$ is defined in Eq. 7.4.

$$\mathbf{p}^{j-1}_{j,m,sn} = \mathbf{p}^{j-1}_{j,m,SJ} + \mathbf{R}^{j-1}_{(j-1)j}\mathbf{p}^{j}_{j,m,JS} \tag{7.3}$$

$$d_{j,m,sn} = \left\|\mathbf{p}^{j-1}_{j,m,sn}\right\| \tag{7.4}$$

To analytically calculate the inverse kinematics, further constraints are necessary, as defined in Eq. 7.5: (i) the disk-frame z-coordinate displacement between the sensor $m$ base and joint $j$ is zero, (ii) the disk-frame sensor base and tip x-coordinates are equal, and (iii) the disk-frame sensor base and tip y-coordinates are equal.

$$\hat{\mathbf{z}}^{j-1}_{j-1} \cdot \mathbf{p}^{j-1}_{j,m,SJ} = 0, \quad \hat{\mathbf{x}}^{j-1}_{j-1} \cdot \mathbf{p}^{j-1}_{j,m,SJ} = \hat{\mathbf{x}}^{j}_{j} \cdot \mathbf{p}^{j}_{j,m,JS}, \quad \hat{\mathbf{y}}^{j-1}_{j-1} \cdot \mathbf{p}^{j-1}_{j,m,SJ} = \hat{\mathbf{y}}^{j}_{j} \cdot \mathbf{p}^{j}_{j,m,JS} \tag{7.5}$$

With these constraints, an analytical formulation for the $\phi_j$ and $\theta_j$ may be found by considering the disk $i = j$ sensor frame $j, S$ shown in Fig. 7.1. These frames are generated by rotating the disk $i = j$ frame by $-45°$ about the $\hat{\mathbf{z}}_j^j$ axis. The positions $\mathbf{p}_{j,m,SJ}^{j-1,S}$ and $\mathbf{p}_{j,m,JS}^{j,S}$ are defined with respect to frames $j-1, S$ and $j, S$, respectively, using Eqs. 7.6 and 7.7, where $r_{sn}$ is the sensor mounting radius, shown in Fig. 7.1, and $L_{sn}$ is the zero-angle sensor length, shown in Fig. 7.1. The $(-1)^j$ term accounts for the alternating placement of the sensors above and below the universal joint.

$$\mathbf{p}_{j,m,SJ}^{j-1,S} = \begin{cases} (-1)^j \, r_{sn} \hat{\mathbf{y}}_{j-1,S}^{j-1,S}, & m = 1 \\ (-1)^j \, r_{sn} \hat{\mathbf{x}}_{j-1,S}^{j-1,S}, & m = 2 \end{cases} \tag{7.6}$$

$$\mathbf{p}_{j,m,JS}^{j,S} = \begin{cases} (-1)^j \, r_{sn} \hat{\mathbf{y}}_{j,S}^{j,S} + L_{sn} \hat{\mathbf{z}}_{j,S}^{j,S}, & m = 1 \\ (-1)^j \, r_{sn} \hat{\mathbf{x}}_{j,S}^{j,S} + L_{sn} \hat{\mathbf{z}}_{j,S}^{j,S}, & m = 2 \end{cases} \tag{7.7}$$

A new relative orientation matrix $\mathbf{R}_{(j-1,S)(j,S)}^{j-1,S}$ between frames $j-1, S$ and $j, S$ is defined in Eq. 7.8, where $\rho_j$ and $\gamma_j$ are the joint $j$ sensor-frame pitch and yaw angles, respectively. With this, a formulation for the sensor position $\mathbf{p}_{j,m,sn}^{j-1,S}$ from base to tip may be formulated using Eq. 7.9.

$$\mathbf{R}_{(j-1,S)(j,S)}^{i-1,S} = \mathbf{R}_Y(\rho_i) \, \mathbf{R}_X(\gamma_i) \tag{7.8}$$

$$\mathbf{p}_{j,m,sn}^{j-1,S} = \mathbf{p}_{j,m,SJ}^{j-1,S} + \mathbf{R}_{(j-1,S)(j,S)}^{j-1,S} \mathbf{p}_{j,m,JS} \tag{7.9}$$

The scalar sensor length $d_{j,m,sn}$ is invariant to the frame in which the sensor position vector is expressed, enabling expression of $d_{j,m,sn}$ in terms of $\rho_j$ and $\gamma_j$. Equations 7.10 and 7.11

expand $\left\|\mathbf{p}_{j,m,sn}^{j-1,S}\right\|^2$ for sensors $m \in \{1,2\}$. Because Eq. 7.11 is solely a function of $\gamma_j$, it may be solved for uniquely in the domain $\gamma_j \in (-90,90)^\circ$. Using this value for $\gamma_j$ in Eq. 7.10, $\rho_j$ may also be calculated uniquely in the domain $\rho_j \in (-90,90)^\circ$.

$$\left\|\mathbf{p}_{j,1,sn}^{j,1,S}\right\|^2 = d_{j,1,sn}^2 = 2r_{sn}^2 + L_{sn}^2 - 2r_{sn}^2\cos\psi_j - 2r_{sn}L_{sn}\sin\psi_j\cos\gamma_j \tag{7.10}$$

$$\left\|\mathbf{p}_{j,2,sn}^{j-1,S}\right\|^2 = d_{j,2,sn}^2 = 2r_{sn}^2 + L_{sn}^2 - 2r_{sn}^2\cos\gamma_j + 2r_{sn}L_{sn}\sin\gamma_j \tag{7.11}$$

The joint angles $\rho_j$ and $\gamma_j$ may be mapped into $\phi_k$ and $\theta_j$ by equating implicit formulations of the universal joint z-axes $\hat{\mathbf{z}}_{j,S}^{j,S}$ and $\hat{\mathbf{z}}_j^j$, as shown in Eq. 7.12.

$$\begin{aligned}\mathbf{R}_{(j-1)(j-1,S)}^{j-1}\mathbf{R}_{(j-1,S)(j,S)}^{j-1,S}\hat{\mathbf{z}}_{j,S}^{j,S} &= \mathbf{R}_{(j-1)j}^{j-1}\hat{\mathbf{z}}_j^j \\ \mathbf{R}_Z\left(-45^\circ\right)\mathbf{R}_{(j-1,S)(j,S)}^{j-1,S}\hat{\mathbf{z}}_{j,S}^{j,S} &= \mathbf{R}_{(j-1)j}^{j-1}\hat{\mathbf{z}}_j^j\end{aligned} \tag{7.12}$$

The link $i$ IMU measures the link $i$ angular velocity vector $\boldsymbol{\omega}_i^i$ with respect to the link-fixed frame $i$. Using the estimated joint $j$ relative orientation matrix $\mathbf{R}_{(j-1)j}^{j-1}$ from the joint angle estimates, the universal joint $j$ relative velocity $\boldsymbol{\omega}_{(j-1)j}^{j-1}$ may be calculated using Eq. 7.13 as the joint $j$ relative angular velocity between links $i = j-1$ and $j$.

$$\boldsymbol{\omega}_{(j-1)j}^{j-1} = \mathbf{R}_{(j-1)j}^{j-1}\boldsymbol{\omega}_j^j - \boldsymbol{\omega}_{j-1}^{j-1} \tag{7.13}$$

Based on Eq. 6.49, $\dot{\phi}_j$ and $\dot{\theta}_j$ may be extracted from $\boldsymbol{\omega}_{(j-1)j}^{j-1}$, as shown in Eqs. 7.14 and 7.15, due to the orthogonality of $\boldsymbol{\rho}_j^{j-1}$ and $\boldsymbol{\gamma}_j^{j-1}$.

$$\dot{\phi}_j = \boldsymbol{\rho}_j^{j-1} \cdot \boldsymbol{\omega}_{(j-1)j}^{j-1} \tag{7.14}$$

$$\dot{\theta}_j = \boldsymbol{\gamma}_j^{j-1} \cdot \boldsymbol{\omega}_{(j-1)j}^{j-1} \tag{7.15}$$

**Embedded Formulation**

For joints $j \in \{1, \cdots, 6\}$, Eq. 7.16 defines a linear relationship between the distance sensor measurements $d_{j,m,sn}$ for $m \in \{1, 2\}$ and the joint angles $\phi_j$ and $\theta_j$.

$$\begin{bmatrix} d_{j,1,sn} \\ d_{j,2,sn} \end{bmatrix} = \mathbf{A} \begin{bmatrix} \phi_j \\ \theta_j \end{bmatrix} + \mathbf{b} = \begin{bmatrix} (\mathbf{A})_{1,1} & (\mathbf{A})_{1,2} \\ (\mathbf{A})_{2,1} & (\mathbf{A})_{2,2} \end{bmatrix} \begin{bmatrix} \phi_j \\ \theta_j \end{bmatrix} + \begin{bmatrix} (\mathbf{b})_1 \\ (\mathbf{b})_2 \end{bmatrix} \tag{7.16}$$

The coefficients $\mathbf{A}$ and offsets $\mathbf{b}$ are determined using a kinematic analysis in three stages. First, the zero-angle configuration of the joint when $\phi_j = \theta_j = 0$ dictates that the $\mathbf{b}$ coefficients equal $L_{sn}$, the nominal length of the distance sensor.

Second, the pitch angle coefficients $(\mathbf{A})_{1,1}$ and $(\mathbf{A})_{2,1}$ are calculated over the domain of $\phi_j \in [-\beta_{lim}, \beta_{lim}]$ for zero-yaw ($\theta_j = 0$) using linear regression. Due to the symmetry of the anchor placements, this regression shows that these two coefficients are both equal to a nominal value $K_\phi$.

Third, the yaw angle coefficients ($(\mathbf{A})_{1,2}$ and $(\mathbf{A})_{2,2}$) are calculated using an array of equally spaced pitch and yaw joint angle pairs within the universal joint workspace. Because of the symmetric placement of the spring anchors with respect to the links' vertical planes and the 90° spacing of the spring anchors, these coefficients are equal and opposite, such that $(\mathbf{A})_{1,2} = K_\theta$ and $(\mathbf{A})_{2,2} = -K_\theta$. These calculated coefficients lead to the simplified expressions for calculating $\phi_j$ and $\theta_j$ shown in Eq. 7.17.

$$\begin{aligned} \phi_j &= \left(d_{j,1,sn} + d_{j,2,sn} - 2L_{sn}\right)/2K_\phi \\ \theta_j &= \left(d_{j,1,sn} - d_{j,2,sn}\right)/2K_\theta \end{aligned} \tag{7.17}$$

Comparisons of the analytical and linear calculations of the joint angles using valid distance sensor value pairs within the workspace of the USRT joint are shown in Fig. 7.2. Linearization errors in the ranges of -2.01° to 2.66° in the pitch joint and −1.17° to 1.17° in the yaw joint were calculated at the boundaries of the workspace, and average error magnitudes across the total workspace were 0.36° in the pitch joint and 0.19° in the yaw joint.

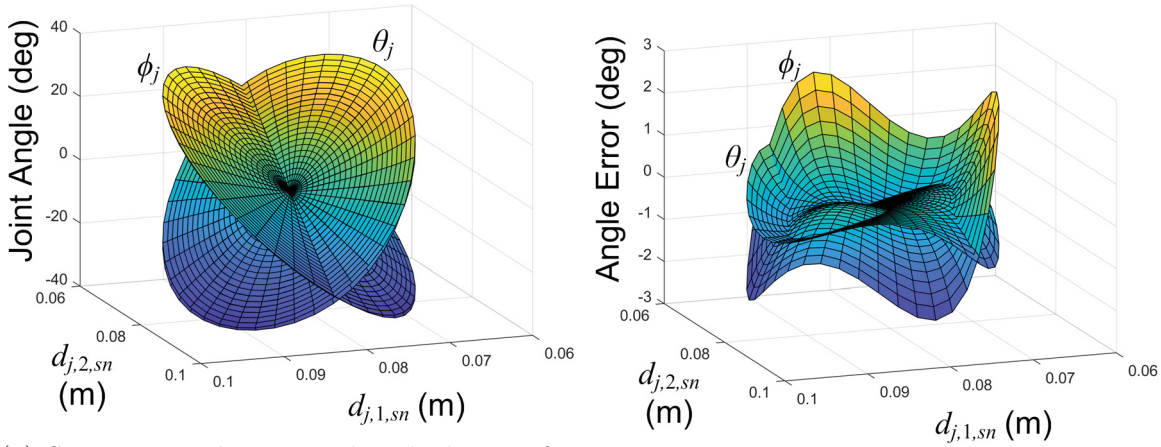


(a) Superimposed joint angle calculations for pitch ($\phi_j$) and yaw ($\theta_j$) using analytical and linearized models

(b) Angle error between analytical and linear joint angle calculations for $\phi_j$ and $\theta_j$

Figure 7.2: USRT joint angle state estimation linearization error analysis.

For simplifying the joint velocity calculation, the relative angular velocity between links $i = j - 1$ and $i = j$ is defined in terms of the link-frame angular velocities in Eq. 7.18 and in terms of the joint velocities in Eq. 7.19. Equating Eqs. 7.18 and 7.19 and taking the dot products of each side with $\hat{\boldsymbol{\rho}}_j^{j-1}$ and $\hat{\boldsymbol{\gamma}}_j^{j-1}$ results in simplified formulations for $\dot{\phi}_j$ and $\dot{\theta}_j$, respectively, as shown in Eq. 7.20.

$$\boldsymbol{\omega}_{(j-1)j}^{j-1} = \mathbf{R}_{(j-1)j}^{j-1}\boldsymbol{\omega}_{j}^{j} - \boldsymbol{\omega}_{j-1}^{j-1} \tag{7.18}$$

$$= \dot{\phi}_j \hat{\boldsymbol{\rho}}_j^{j-1} + \dot{\theta}_j \hat{\boldsymbol{\gamma}}_j^{j-1} \tag{7.19}$$

$$\begin{aligned} \dot{\phi}_j &= \left(\boldsymbol{\omega}_{\boldsymbol{j}}^{\boldsymbol{j}}\right)_y \cos\theta_j - \left(\boldsymbol{\omega}_{\boldsymbol{j-1}}^{\boldsymbol{j-1}}\right)_y - \left(\boldsymbol{\omega}_{\boldsymbol{j}}^{\boldsymbol{j}}\right)_z \sin\theta_j \\ \dot{\theta}_j &= \left(\boldsymbol{\omega}_{\boldsymbol{j}}^{\boldsymbol{j}}\right)_x - \left(\boldsymbol{\omega}_{\boldsymbol{j-1}}^{\boldsymbol{j-1}}\right)_x \cos\phi_j + \left(\boldsymbol{\omega}_{\boldsymbol{j-1}}^{\boldsymbol{j-1}}\right)_z \sin\phi_j \end{aligned} \tag{7.20}$$

## 7.2 Outer-Loop Tail Control

### 7.2.1 Quadruped and Biped Maneuvering Behavior

The maneuvering controller in this case study will generate a dynamic tail motion capable of changing the heading angle of the quadruped or biped without destabilizing locomotion. Although this functionality has been studied in various forms by the author [69, 70, 76], this analysis will focus on a method of trajectory planning that is designed to more intelligently allocate the tail's acceleration during the tail motion to minimize peaks in motor power consumption in favor of a more uniform power consumption throughout the trajectory. Qualitatively, this is done by prescribing greater tail accelerations when the tail velocity is low, and lower angular accelerations when tail velocity is high.

Furthermore, tail-based maneuvering will occur while the legged platform is airborne, as discussed in section 8.1.2, to avoid the need for the tail to act against friction at the legged robots' feet. As a result, the biped's rotation depends only on the tail's displacement and not the trajectory over which that displacement occurs.

In addition, although the treatment of the R3RT and USRT has been kept separate throughout this work, this is the one instance in which both will be considered jointly. The trajectory planning process for the R3RT's $\beta_l$ angle trajectories for $l \in \{1, 2\}$ is identical to that for the USRT's $\eta_l$ angle trajectories. The only difference is the range over which the trajectories are calculated: the R3RT $\beta_l$ moves from 0 to 15°, whereas the USRT $\eta_l$ moves from 0 to 90°. To avoid repeating the same analysis, the maneuvering tail trajectory is formulated in terms of the R3RT's $\beta_l$, for which the USRT's $\eta_l$ may be substituted.

In this approach, the segment bending angles are prescribed to be equal ($\beta = \beta_1 = \beta_2$), and the joint angle trajectories are defined based on a prescribed $\ddot{\beta}$ trajectory designed to hold the product $\dot{\beta}\ddot{\beta}$ at a fixed nominal value value throughout the tail motion trajectory, as shown in Fig. 7.3. This product is a kinematic analog to the motor's power output, as there is a direct relationship between angular acceleration and motor torque.

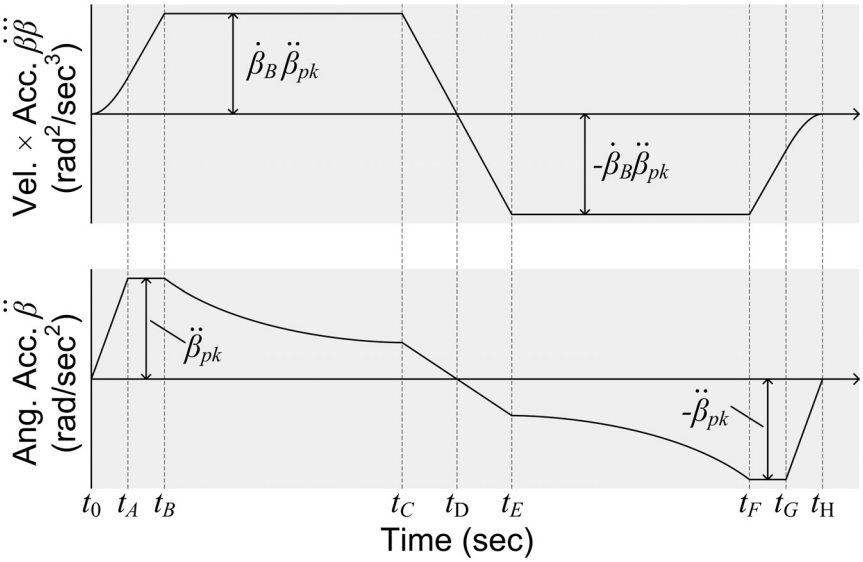


Figure 7.3: Desired trajectories for joint velocity/acceleration product and joint acceleration.

From $t_0$ to $t_B$, the acceleration increases the product $\dot{\beta}\ddot{\beta}$ from zero to the nominal fixed value $\dot{\beta}_B\ddot{\beta}_{pk}$, as defined in Eq. 7.21, where $\dot{\beta}_B = \dot{\beta}(t_B)$ is the joint angle velocity at time $t_B$ and $\ddot{\beta}_{pk}$ is the peak joint angle acceleration.

$$\ddot{\beta} = \begin{cases} \ddot{\beta}_{pk}\frac{t-t_0}{t_A-t_0}, & t_0 \leq t \leq t_A \\ \ddot{\beta}_{pk}, & t_A < t \leq t_B \end{cases} \tag{7.21}$$

From $t_B$ to $t_C$, $\ddot{\beta}$ is defined to maintain a constant product of $\dot{\beta}\ddot{\beta} = \dot{\beta}_B\ddot{\beta}_{pk}$ as defined in Eq. 7.22. From $t_C$ to $t_D$, the defined $\ddot{\beta}$ is linearly scaled to zero to ensure $\ddot{\beta}_D = 0$ at the midpoint of the trajectory.

$$\ddot{\beta} = \begin{cases} \dot{\beta}_B\ddot{\beta}_{pk}/\dot{\beta}, & t_B \leq t \leq t_C \\ \frac{\dot{\beta}_B\ddot{\beta}_{pk}}{\dot{\beta}}\frac{t_D-t}{t_D-t_C}, & t_C < t \leq t_D \end{cases} \tag{7.22}$$

Equation 7.23 defines the trajectory from $t_D$ to $t_H$, which is the inverse mirror trajectory of the $\ddot{\beta}$ trajectory from $t_0$ to $t_D$, as shown in Fig. 7.3.

$$\ddot{\beta} = \begin{cases} -\frac{\dot{\beta}_B\ddot{\beta}_{pk}}{\dot{\beta}}\frac{t-t_D}{t_E-t_D}, & t_D < t \leq t_E \\ -\dot{\beta}_B\ddot{\beta}_{pk}/\dot{\beta}, & t_E < t \leq t_F \\ -\ddot{\beta}_{pk}, & t_F < t \leq t_G \\ -\ddot{\beta}_{pk}\frac{t_H-t}{t_H-t_G}, & t_G < t \leq t_H \end{cases} \tag{7.23}$$

The desired $\dot{\beta}$ and $\beta$ trajectories are found by integrating the defined $\ddot{\beta}$ trajectory once and twice from the initial conditions $\dot{\beta}_0$ and $\beta_0$.

For fixed time span parameters, there is a functional relationship between the joint angle displacement $\beta_H - \beta_0$ and $\ddot{\beta}_{pk}$ (i.e., $\beta_H - \beta_0 = fn\left(\ddot{\beta}_{pk}\right)$). Simulations over a range of $\ddot{\beta}_{pk}$ values can be used characterize this functional relationship and invert it, allowing for a $\ddot{\beta}_{pk}$ value to be selected to implement the desired change in heading angle, similar to the single-tail motion analysis in [70].

From these trajectories, a desired R3RT state trajectory $\mathbf{q}_{des}$ and its derivatives $\dot{\mathbf{q}}_{des}$ and $\ddot{\mathbf{q}}_{des}$ may be calculated by setting $\phi = 90°$. Likewise, a desired USRT reduced state trajectory $\mathbf{z}_{des}$ and its derivatives $\dot{\mathbf{z}}_{des}$ and $\ddot{\mathbf{z}}_{des}$ may be calculated by setting $\psi_1 = \psi_2 = 0$.

### 7.2.2 Quadruped Stabilization Behavior

The stabilization controller in this case study will prescribe a tail motion that utilizes the tail's inertial and gravitational loading to counteract a destabilizing load applied to the quadruped. Based on the quadruped's geometry and mass distribution, the moment of inertia with respect to its roll axis is significantly lower than that of the pitch axis, making roll angle destabilization more likely for a lower magnitude disturbance. Therefore, the stabilization controller is designed to counteract a destabilizing moment about this roll axis.

Roll destabilization can be detected from the quadruped's roll angle $\rho$. During steady-state locomotion, slight variations in $\rho$ are expected, and the range of acceptable roll angles without requiring tail intervention (i.e., the $\rho$ angle deadzone) can be defined as $\rho \in [-\rho_{dz}, \rho_{dz}]$. Beyond these limits, the tail should be actuated to oppose the destabilizing roll influence. The required stabilizing tail actuation is parameterized by the variable $\kappa \in [-1, 1]$, defined in Eq. 7.24 and shown in Fig. 7.4, where $\rho_{lim}$ is the roll angle magnitude beyond which $|\kappa| = 1$, 'sat' is the unit saturation function, and 'sgn' is the signum function. The $-\text{sgn}(\rho)$ term ensures that stabilizing control action acts in opposition to the quadruped's roll angle.

$$\kappa = \begin{cases} 0, & |\rho| \leq \rho_{dz} \\ \text{sat}\left(-\text{sgn}(\rho)\, \frac{|\rho| - \rho_{dz}}{\rho_{lim} - \rho_{dz}}\right), & |\rho| > \rho_{dz} \end{cases} \tag{7.24}$$

When $|\kappa| > 0$, a methodology for mapping $\kappa$ into a second-order continuous tail trajectory is needed; the variable $\chi$ is used to parameterize this continuous trajectory. A unit damped

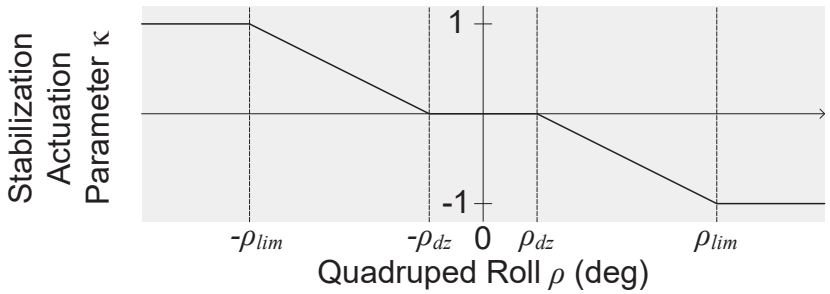


Figure 7.4: Stabilization actuation parameter $\kappa$ definition.

harmonic oscillator for $\chi$ is defined in Eq. 7.25 with $\kappa$ as its forcing function, where $\xi$ and $\omega_n$ are the oscillator's damping ratio and natural frequency, respectively. To minimize the system's settling time without overshoot, $\xi$ is set equal to 1, and $\omega_n$ is defined in section 8.3.

$$\frac{1}{\omega_n^2}\ddot{\chi} + \frac{2\xi}{\omega_n}\dot{\chi} + \chi = \kappa, \quad \{\chi_0, \dot{\chi}_0\} = 0 \tag{7.25}$$

The $\chi$ trajectory is used to continuously transition the desired tail state $\mathbf{q}_{des}$ from its nominal tail configuration $\mathbf{q}_0$ during steady-state locomotion to the stabilization steady-state configuration $\mathbf{q}_{st}$, as defined in Eq. 7.26, where $\odot$ defines element-by-element multiplication. The states $\mathbf{q}_0$ and $\mathbf{q}_{st}$ are determined based on considerations for (1) symmetry, (2) gravity, and (3) conservation of angular momentum. To simplify analysis, $\beta_1 \geq 0$, to avoid equivalent tail states such as $\mathbf{q} = [0,\ \beta_1,\ \beta_2] = [180°,\ -\beta_1,\ -\beta_2]$. In addition, the discussion below will assume $\rho > 0$; an equivalent analysis can be made for $\rho < 0$.

$$\mathbf{q}_{des} = \mathbf{q}_0 + (\mathbf{q}_{st} - \mathbf{q}_0) \odot \begin{bmatrix} \chi \\ |\chi| \\ |\chi| \end{bmatrix} \tag{7.26}$$

First, based on symmetry, $\phi_0 = \{0,\ \pm 180°\}$ so that the tail can respond equivalently in either direction. Second, to maximize the gravitational loading at $\mathbf{q}_{st}$ with respect to the

roll axis, define $\mathbf{q}_{st} = [-90°, 15°, 0]$. Third, conservation of angular momentum dictates that the relative rotation $\phi_{st} - \phi_0$ should be the same sign as $\rho$ to induce rotation in the opposite direction in the quadruped. Based on these conditions, $\mathbf{q}_0$ and $\mathbf{q}_{st}$ are defined in Eq. 7.27, with free choices of $(\beta_1)_0$ and $(\beta_2)_0$ based on other considerations. This analysis will define $(\beta_1)_0 = 15°$ and $(\beta_2)_0 = 0$ to minimize the required tail motion during stabilization.

$$\mathbf{q}_0 = \begin{bmatrix} -180° \\ (\beta_1)_0 \\ (\beta_2)_0 \end{bmatrix}, \quad \mathbf{q}_{st} = \begin{bmatrix} -90° \\ 15° \\ 0 \end{bmatrix} \tag{7.27}$$

### 7.2.3 Biped Stabilization Behavior

The stabilization controller in this case study will prescribe a tail motion that utilizes the tail's inertial and gravitational loading to counteract the roll angle destabilzation induced by the cyclic lifting of the biped's legs. Assuming a symmetric biped design with respect to its saggital plane, and assuming that its feet do not cross this saggital plane and interfere with one another, the effective gravitational force acting at the biped COM will generate a non-zero rolling moment with respect to an edge of one of the biped foot support polygons when the other foot is lifted. In addition, the vertical acceleration of the lift phase foot induces an additional undesired inertial roll moment with respect to the same support polygon edge. These moments induce undesired roll rotation during the steady-state locomotion of the biped. However, the tail can be used to generate cyclic loading during steady-state locomotion to act against this destabilizing moment and maintain a more consistent biped roll angle.

The tail generates two types of loading that may be used to oppose this destabilizing moment: inertia and gravity. In terms of inertia, a tail rolling motion accelerating in the direction of

the roll destabilization will induce a moment opposing the roll destabilization on the biped. In terms of gravity, the reduced tail state with maximum gravitational loading opposed to the destabilizing moments are defined in Eq. 7.28.

$$\mathbf{z}_{grv,max} = \begin{bmatrix} 0 \\ 0 \\ \pm 90^\circ \\ 0 \end{bmatrix} \tag{7.28}$$

To illustrate: when the biped's leg configuration induces a roll destabilization in the negative $\hat{\mathbf{z}}_T$ direction, the desired inertial loading can be generated by prescribing $\ddot{\xi} > 0$ (Eq. 6.60) during this gait half-cycle, and the desired gravitational loading can be generated by enforcing $\eta_1 > 0$ during this gait half-cycle. Conversely, when the biped's leg configuration induces the opposite destabilization, enforce $\ddot{\xi} < 0$ and $\eta_1 < 0$. Based on Eqs. 6.42 and 6.60, $\eta_1 > 0$ correlates to $\xi < 0$, and vice versa.

A single biped gait cycle may be defined using three time points: the cycle start at time $t_A$, in which leg A enters its support phase and leg B enters its lift phase, the cycle's midpoint at time $t_C$, in which the legs switch phases, and the cycle end at time $t_E$, which is also the next gait cycle's $t_A$. By definition, $t_C = (t_A + t_E)/2$. In addition, to aid the model formulation, times $t_B = (t_A + t_C)/2$ and $t_D = (t_C + t_E)/2$ are defined as the midpoints of the first and second gait half-cycles.

To implement the desired $\ddot{\xi}$ behavior ($\ddot{\xi} > 0$ when leg A is lifted; $\ddot{\xi} < 0$ when leg B is lifted), $\ddot{\xi}$ is defined by a sinusoidal wave of period $T_{AE} = t_E - t_A$ in Eq. 7.29, where $\ddot{\xi}_{pk}$ is the peak $\xi$ acceleration. Single- and double-integration of this equation results in formulations for $\dot{\xi}$ (Eq. 7.30) and $\xi$ (Eq. 7.31), where $\xi_A$ and $\dot{\xi}_A$ are the initial roll angle and roll velocity at time $t_A$. Choices for $\ddot{\xi}_{pk}$, $\dot{\xi}_A$ and $\xi_A$ are dictated by the gravitational loading considerations.

$$\ddot{\xi} = \ddot{\xi}_{pk} \sin\left(2\pi \frac{t - t_A}{T_{AE}}\right) \tag{7.29}$$

$$\dot{\xi} = \dot{\xi}_A + \frac{T_{AE}}{2\pi}\ddot{\xi}_{pk}\left(1 - \cos\left(2\pi \frac{t - t_A}{T_{AE}}\right)\right) \tag{7.30}$$

$$\xi = \xi_A + \left(\dot{\xi}_A + \frac{T_{AE}}{2\pi}\ddot{\xi}_{pk}\right) t - \left(\frac{T_{AE}}{2\pi}\right)^2 \ddot{\xi}_{pk} \sin\left(2\pi \frac{t - t_A}{T_{AE}}\right) \tag{7.31}$$

First, whenever the legs change gait phase, there is a corresponding change in the sign of $\xi$. To accommodate this, $\xi_A = \xi_C = \xi_E = 0$. In addition to this condition defining $\xi_A$, evaluating Eq. 7.31 at $t_C$ and equating it to $\xi_C = 0$ results in the coupling condition between $\ddot{\xi}_{pk}$ and $\dot{\xi}_A$ defined in Eq. 7.32.

$$\dot{\xi}_A = -\frac{T_{AE}}{2\pi}\ddot{\xi}_{pk} \tag{7.32}$$

With these constraints, $\xi$ has maximum magnitude at times $t_B$ and $t_D$; therefore, $\xi_B$ and $\xi_D$ should be scaled such that the tail state $\mathbf{z}_{grv,max}$ (Eq. 7.28) is prescribed at this angle. For $t_B$, at which leg B is lifted, $\xi_B = 90°$ allows for $\eta_1 = -90°$ when $\beta_1 = 90°$. For $t_D$, at which leg A is lifted, $\xi_D = -90°$ allows for $\eta_1 = 90°$ when $\beta_1 = 90°$. Both of these conditions dictate the Eq. 7.33 definition of $\ddot{\xi}_{pk}$.

$$\ddot{\xi}_{pk} = -90° \left(\frac{2\pi}{T_{AE}}\right)^2 \tag{7.33}$$

In addition to the $\xi$ trajectory, formulations for $\beta_1$ and $\beta_2$ are also needed. To isolate the impact of the tail's rolling motion on stability, the angles are fixed as $\beta_1 = 90°$ and $\beta_2 = 0$ to ensure that the tail state matches $\mathbf{z}_{grv,max}$ at $t_B$ and $t_D$.

## 7.3 Inner-Loop Tail Control

### 7.3.1 R3RT Inner-Loop Controller

The R3RT's inner-loop controller is a model-based feedback linearization controller that prescribes both feedforward inputs based on the modeled tail dynamics and feedback inputs based on the measured tail error. Equation 7.34 defines the feedback linearizing controller, where $\bar{(\cdot)}$ denotes the estimate of the corresponding matrix or vector from Eq. 6.4, $\tilde{\mathbf{q}}$ is the error $\mathbf{q} - \mathbf{q}_{des}$ between the measured and desired states and $\mathbf{K}_0$ and $\mathbf{K}_1$ are outer-loop linear feedback gains. This analysis will assume that the estimates of a given matrix or vector matches the actual matrix or vector (i.e., $\bar{\mathbf{M}} - \mathbf{M} = \mathbf{0}_{3\times3}$).

$$\mathbf{u} = \bar{\mathbf{T}}^{-1}\left(\bar{\mathbf{M}}\left(\ddot{\mathbf{q}}_{des} - \mathbf{K}_0\tilde{\mathbf{q}} - \mathbf{K}_1\dot{\tilde{\mathbf{q}}}\right) + \hat{\mathbf{C}}\dot{\mathbf{q}} + \hat{\mathbf{g}}\right) \tag{7.34}$$

This controller leads to the closed-loop system dynamics shown in Eq. 7.35, which is canonically asymptotically stable if $\mathbf{K}_0$ and $\mathbf{K}_1$ are positive definite.

$$\ddot{\tilde{\mathbf{q}}} + \mathbf{K}_1\dot{\tilde{\mathbf{q}}} + \mathbf{K}_0\tilde{\mathbf{q}} = \mathbf{0}_{3\times1} \tag{7.35}$$

### 7.3.2 USRT Inner-Loop Controller

For the USRT, the tail's inner-loop controller has two considerations for calculating the desired $\mathbf{u}$: (1) achieving the desired tail motion, and (2) ensuring each cable maintains a minimum tension $T_{min}$ at all times during the tail motion. As a result, $\mathbf{u} = \mathbf{u}_{act} + \mathbf{u}_{ten}$, where $\mathbf{u}_{act}$ is the tail actuation control contribution and $\mathbf{u}_{ten}$ is the cable tensioning control contribution.

### USRT Cable Actuating Control Contribution

Ideally, a feedback linearizing controller of the form shown in Eq. 7.36 would be used to calculate $\mathbf{u}_{act}$, where $\bar{(\cdot)}$ denotes an estimate of the associated matrix or vector from Eq. 6.41, $\mathbf{a}_{OL}$ is the prescribed outer-loop acceleration and $\bar{\mathbf{V}}\left(\mathbf{q}, \dot{\mathbf{q}}, \ddot{\mathbf{q}}\right)$ is a vector of the estimated non-actuation loading effects. However, the USRT's underactuation precludes the calculation of $\mathbf{u}_{act}$ directly using Eq. 7.36, as the 12-by-6 matrix $\bar{\mathbf{T}}$ is not invertible.

$$\bar{\mathbf{T}}\mathbf{u}_{act} = \bar{\mathbf{M}}\mathbf{a}_{OL} + \bar{\mathbf{C}}\dot{\mathbf{q}} + \bar{\mathbf{d}} + \bar{\mathbf{k}} + \bar{\mathbf{g}} = \bar{\mathbf{V}}\left(\mathbf{q}, \dot{\mathbf{q}}, \ddot{\mathbf{q}}\right) \tag{7.36}$$

Based on the geometry of the cable actuation, the rank of $\bar{\mathbf{T}}$ can only be guaranteed to be 4 within the tail's workspace (two of columns 1-3 are linearly independent, two of columns 4-6 are linearly independent). To compress the 12 equations of motions into 4, both sides of Eq. 7.36 are multiplied by $\boldsymbol{\mu}$, as shown in Eq. 7.37. The $\boldsymbol{\mu}\bar{\mathbf{T}}$ term is now a 4-by-6 matrix of rank 4.

$$\boldsymbol{\mu}\bar{\mathbf{T}}\mathbf{u}_{act} = \boldsymbol{\mu}\bar{\mathbf{V}} \tag{7.37}$$

To extract an invertible 4-by-4 matrix from $\boldsymbol{\mu}\bar{\mathbf{T}}$, two of the cable tensions in $\mathbf{u}_{act}$ are set as zero, and the tensions for the remaining four cables $A$, $B$, $C$ and $D$ are solved for using Eq. 7.38, where $\mathbf{u}_{ABCD}$ is the 4-by-1 vector of non-zero cable tensions from $\mathbf{u}_{act}$ and $\left(\boldsymbol{\mu}\bar{\mathbf{T}}\right)_k$ is column $k$ of $\boldsymbol{\mu}\bar{\mathbf{T}}$. The segment 1 cables $A$ and $B$ are defined such that $A \in \{1, 2, 3\}$ and $B \in \{1, 2, 3 \mid B \neq A\}$, and the segment 2 cables $C$ and $D$ are defined similarly for cables 4, 5 and 6.

$$\mathbf{u}_{ABCD} = \begin{bmatrix} \left(\boldsymbol{\mu}\bar{\mathbf{T}}\right)_A & \left(\boldsymbol{\mu}\bar{\mathbf{T}}\right)_B & \left(\boldsymbol{\mu}\bar{\mathbf{T}}\right)_C & \left(\boldsymbol{\mu}\bar{\mathbf{T}}\right)_D \end{bmatrix}^{-1} \boldsymbol{\mu}\bar{\mathbf{V}} \tag{7.38}$$

At least one set of the nine unique combinations of $A$, $B$, $C$ and $D$ will produce an actuating tension vector for which all six terms are greater than or equal to zero, satisfying the constraint that cables cannot support a compressive load.

### USRT Cable Tensioning Control Contribution

Since the calculation of $\mathbf{u}_{act}$ by definition prescribes at least two cable tensions as zero, a methodology for uniformly scaling up the prescribed cable tensions with minimal changes to the dynamic behavior of the tail is needed. This is done by exploiting the null space of $\boldsymbol{\mu}\bar{\mathbf{T}}$ due to its rank deficiency.

As before, the 12-by-6 $\bar{\mathbf{T}}$ cannot be used directly to calculate $\mathbf{u}_{ten}$ using $\bar{\mathbf{T}}\mathbf{u}_{ten} = \mathbf{0}_{12\times1}$. As shown in Eq. 7.39, $\boldsymbol{\mu}$ is used to consider the impact of $\mathbf{u}_{ten}$ on the tail segments' pitch and yaw bending as a whole. While the resulting $\bar{\mathbf{T}}\mathbf{u}_{ten}$ is not identically equal to zero, it may be approximated as such.

$$\boldsymbol{\mu}\bar{\mathbf{T}}\mathbf{u}_{ten} = \mathbf{0}_{4\times1} \rightarrow \bar{\mathbf{T}}\mathbf{u}_{ten} \approx \mathbf{0}_{12\times1} \tag{7.39}$$

The rows of matrix $\boldsymbol{\mu}\bar{\mathbf{T}}$ may be rearranged as shown in Eq. 7.40, where $\left(\boldsymbol{\mu}\bar{\mathbf{T}}\right)_{r,l}$ is the 1-by-3 row $r$ vector for the segment $l$ cables, $\mathbf{u}_{ten,123}$ is the vector of segment 1 cable tensions and $\mathbf{u}_{ten,456}$ is the vector of segment 2 cable tensions.

$$\begin{bmatrix} \left(\boldsymbol{\mu}\bar{\mathbf{T}}\right)_{1,1} & \left(\boldsymbol{\mu}\bar{\mathbf{T}}\right)_{1,2} \\ \left(\boldsymbol{\mu}\bar{\mathbf{T}}\right)_{3,1} & \left(\boldsymbol{\mu}\bar{\mathbf{T}}\right)_{3,2} \\ \mathbf{0}_{1\times3} & \left(\boldsymbol{\mu}\bar{\mathbf{T}}\right)_{2,2} \\ \mathbf{0}_{1\times3} & \left(\boldsymbol{\mu}\bar{\mathbf{T}}\right)_{4,2} \end{bmatrix} \begin{bmatrix} \mathbf{u}_{ten,123} \\ \mathbf{u}_{ten,456} \end{bmatrix} = \begin{bmatrix} \mathbf{0}_{2\times1} \\ \mathbf{0}_{2\times1} \end{bmatrix} \tag{7.40}$$

For the segment 2 cable tensions, rows 3 and 4 from Eq. 7.40 may be reformulated as $\left(\boldsymbol{\mu}\bar{\mathbf{T}}\right)_{24,2}\mathbf{u}_{ten,456} = \mathbf{0}_{2\times1}$, where $\left(\boldsymbol{\mu}\bar{\mathbf{T}}\right)_{24,2}$ is the 2-by-3 segment 2 actuation transmission matrix. The unit vector $\hat{\mathbf{u}}_{ten,456}$ is the basis of the null space of $\left(\boldsymbol{\mu}\bar{\mathbf{T}}\right)_{24,2}$, and the magnitude $\|\mathbf{u}_{ten,456}\|$ is scaled such that the minimum segment 2 cable tension $\mathbf{u}_{456} = \mathbf{u}_{act,456} + \mathbf{u}_{ten,456}$ equals the minimum desired cable tension $T_{min}$.

For the segment 1 cable tensions, rows 1 and 2 from Eq. 7.40 may be further simplified based on the knowledge that the segment 1 and 2 cables route through the same holes in segment 1. Therefore, $\left(\boldsymbol{\mu}\bar{\mathbf{T}}\right)_{\{1,3\},1} = \left(\boldsymbol{\mu}\bar{\mathbf{T}}\right)_{\{1,3\},2}$, and the 2-by-3 segment 1 actuation transmission matrix $\left(\boldsymbol{\mu}\bar{\mathbf{T}}\right)_{13,12}$ may be defined using Eq. 7.41 based on rows 1 and 2 from Eq. 7.40.

$$\left(\boldsymbol{\mu}\bar{\mathbf{T}}\right)_{13,12}\left(\mathbf{u}_{ten,123} + \mathbf{u}_{ten,456}\right) = \mathbf{0}_{2\times1} \tag{7.41}$$

Since the segment 2 cables routes through segment 1, their effect must be accounted for when calculating $\mathbf{u}_{ten,123}$. For this segment, the unit basis of the $\left(\boldsymbol{\mu}\bar{\mathbf{T}}\right)_{13,12}$ null space is no longer the unit vector $\hat{\mathbf{u}}_{ten,123}$, but rather the unit vector of the sum $\mathbf{u}_{ten,1} = \mathbf{u}_{ten,123} + \mathbf{u}_{ten,456}$. Therefore, the magnitude $|\mathbf{u}_{ten,1}|$ should be selected to ensure that the minimum segment 1 cable tension $\mathbf{u}_{123} = \mathbf{u}_{act,123} + \mathbf{u}_{ten,123}$ equals the minimum desired cable tension $T_{min}$. As an intermediate step, $\mathbf{u}_{ten,123}$ is calculated using Eq. 7.42, based on the prescribed $|\mathbf{u}_{ten,1}|$.

$$\mathbf{u}_{ten,123} = |\mathbf{u}_{ten,1}|\,\hat{\mathbf{u}}_{ten,1} - \mathbf{u}_{ten,456} \tag{7.42}$$

### USRT Controller Stability

Owing to its underactuation, stability for the USRT is not evaluated with respect to the full state vector $\mathbf{q}$. Instead, stability is shown on the reduced state $\mathbf{z}$, and the USRT's internal dynamics guide the state $\mathbf{q}$ to a stable equilibrium. The closed-loop system dynamics are defined in Eq. 7.43 by multiplying Eq. 6.41 by $\boldsymbol{\mu}$ and substituting $\boldsymbol{\mu}\mathbf{T}\mathbf{u} = \boldsymbol{\mu}\bar{\mathbf{T}}\mathbf{u}_{act} + \boldsymbol{\mu}\bar{\mathbf{T}}\mathbf{u}_{ten}$ from Eqs. 7.37 and 7.39. In this analysis, it will be assumed that the estimated tail dynamics vectors and matrices exactly match the actual tail dynamics (e.g., $\bar{\mathbf{M}} = \mathbf{M}$).

$$\boldsymbol{\mu}\mathbf{M}\ddot{\mathbf{q}} + \boldsymbol{\mu}\mathbf{C}\dot{\mathbf{q}} + \boldsymbol{\mu}\mathbf{d} + \boldsymbol{\mu}\mathbf{k} + \boldsymbol{\mu}\mathbf{g} = \boldsymbol{\mu}\bar{\mathbf{M}}\mathbf{a}_{OL} + \boldsymbol{\mu}\bar{\mathbf{C}}\dot{\mathbf{q}} + \boldsymbol{\mu}\bar{\mathbf{d}} + \boldsymbol{\mu}\bar{\mathbf{k}} + \boldsymbol{\mu}\bar{\mathbf{g}} \tag{7.43}$$

As desired, the tensioning term does not impact the closed-loop dynamics, and the feedback linearization controller reduces the nonlinear open-loop dynamics into the linear double-integrator shown in Eq. 7.44. The desired outer-loop acceleration $\mathbf{a}_{OL}$ is defined in Eq. 7.45, where $\mathbf{K}_0$ and $\mathbf{K}_1$ are proportional and derivative control gain matrices, respectively.

$$\ddot{\mathbf{q}} = \mathbf{a}_{OL} \tag{7.44}$$

$$\mathbf{a}_{OL} = \frac{1}{3}\boldsymbol{\mu}^T\left(\ddot{\mathbf{z}}_{des} - \mathbf{K}_0\tilde{\mathbf{z}} - \mathbf{K}_1\dot{\tilde{\mathbf{z}}}\right) \tag{7.45}$$

Substituting Eq. 7.45 into Eq. 7.44 and multiplying both sides by $\boldsymbol{\mu}$ results in the closed-loop dynamics represented in the canonical form shown in Eq. 7.46. Stability for this type of system is guaranteed as long as $\mathbf{K}_0$ and $\mathbf{K}_1$ are positive definite.

$$\ddot{\tilde{\mathbf{z}}} + \mathbf{K}_1\dot{\tilde{\mathbf{z}}} + \mathbf{K}_0\tilde{\mathbf{z}} = \mathbf{0}_{4\times 1} \tag{7.46}$$

# Chapter 8

# Quadruped and Biped Case Studies for Maneuvering and Stabilization

Using the controllers defined in Chapter 7, case studies are implemented that demonstrate the desired maneuvering and stabilization behaviors. First, section 8.1 discusses the quadrupedal and bipedal legged robot simulations on which the tails' loading acts, along with considerations for hardware-in-the-loop simulations combining the virtual legged robot and experimental tail loading. Then, the remaining four sections present the results associated with the quadruped maneuvering (section 8.2), quadruped stabilization (section 8.3), biped maneuvering (section 8.4) and biped stabilization (section 8.5) case studies.

## 8.1 Legged Platform Design and Simulation

### 8.1.1 Robotic Modular Leg Design

The Robotic Modular Leg, or RMLeg, was chosen to implement the quadrupedal and bipedal legged platforms used to analyze the outer-loop tail controllers. Figure 8.1 illustrates a side view of an RMLeg module; it is composed of two independently actuated four-bar mechanisms used to control the foot's planar position relative to its hip link. The two four-bar mechanisms have parallelogram topologies (opposite links have equal lengths), which results in double-rocker behavior. This behavior constrains the RMLeg's foot link orientation to remain parallel to the hip link as the thigh and shin links move. This guarantees a parallel flat foot orientation with respect to the hip without needing an additional actuator between the shin and foot links. On flat surfaces, flat feet provide a more stable support polygon compared to feet with a point or line contact.

One of the main benefits of using a four-bar mechanism is actuation decoupling. The thigh is actuated directly by a motor mounted within the hip link, and the shin is actuated by a motor mounted on one of the two thigh links. A timing belt transmits the thigh motor actuation to the shin. Mounting the shin motor to the thigh instead of the hip allows this actuator to control the relative motion between the thigh and shin links and not have to compensate for the thigh actuation.

Four compliant toes are incorporated into the foot to help maintain planar contact between the foot and ground even when the leg's hip is not parallel to the ground. Instead of tipping along one of the sides of the foot, the toes will extend and retract in response to the quadruped's pitch and rolling. However, once these toes reach their displacement limits, loss of contact between one or more toes and/or feet will occur.

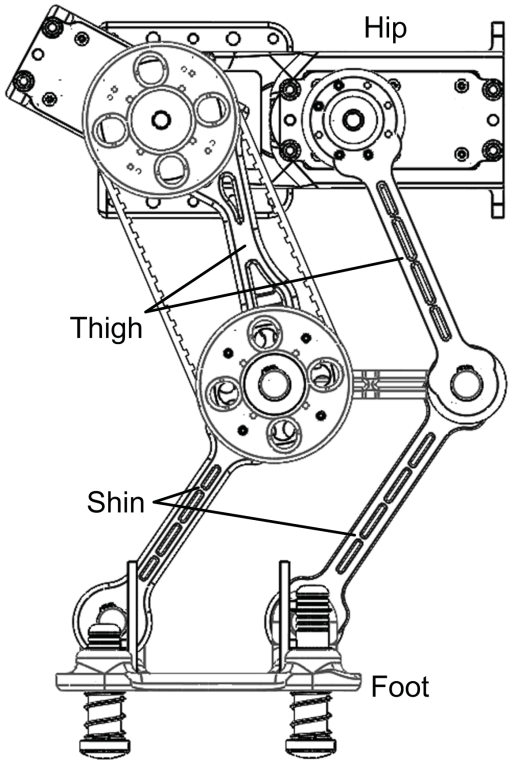


Figure 8.1: Robotic Modular Leg (RMLeg) design.

### 8.1.2 Quadrupedal Robot with R3RT

Figure 8.2 shows the tailed-quadruped composed of four RMLeg modules used to analyze the R3RT's maneuvering and stabilization outer-loop controllers. The quadruped is designed to provide forward locomotion along a single direction, with the tail capable of performing steering (maneuvering) and disturbance rejection (stabilization) functions. To realize a forward quasi-static walking gait, a trot gait pattern is utilized in which pairs of legs alternate between a support phase, in which the foot is in contact with the ground, and a lift phase, in which it is airborne. The support phase foot trajectory is a straight line with constant velocity, and the lift phase is designed to raise the foot and move it in front of its hip for its next support phase.

Trot gaits provide quadrupeds with planar foot contact a quasi-statically stable walking gait

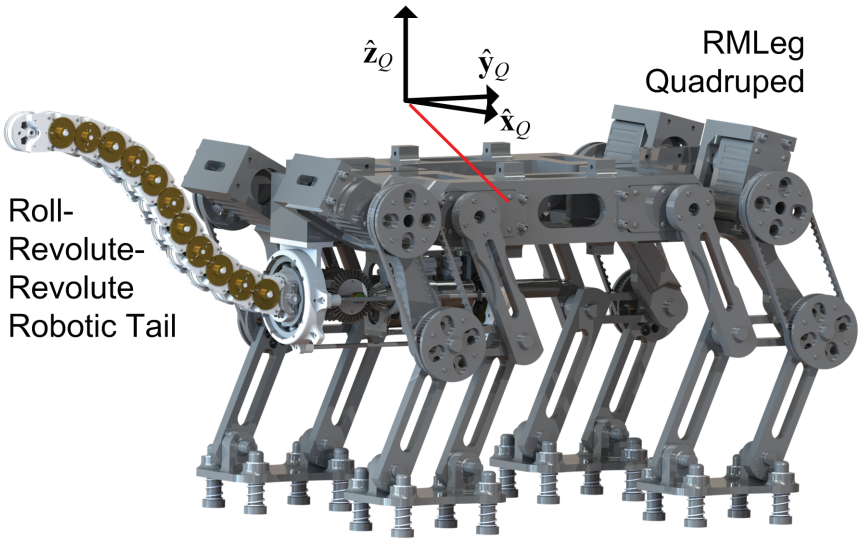


Figure 8.2: RMLeg quadruped with R3RT.

if the quadruped's zero-moment point falls within the support polygon created by the geometric boundary created by all of the ground contact points at a given time. The quadruped alternates between diagonal pairs of legs in contact with the ground. Therefore, two support phase feet move cooperatively (i.e., in the same direction) for forward walking and the system zero-moment point can be configured such that it always falls within the support polygon.

During preliminary simulations for the maneuvering case study, it was found that the friction at the feet was a severely limiting factor for effective turning with a reasonable tail mass. With a dynamically stable gait, this challenge could be mitigated by choosing to actuate the tail during an airborne gait phase in which all legs are lifted from the ground. However, for the quasi-statically stable gait currently under consideration, at least two legs are in contact with the ground at all time.

To mimic an airborne gait phase in this analysis, a hop is added during the walking trajectory to lift the quadruped off the ground for 0.45 seconds and move the tail during this time. In addition, due to the absence of friction between the ground and quadruped during this time, the net rotation of the quadruped depends only on the net rotation of the tail and not the

duration over which that motion occurs. However, this ground friction is beneficial when returning the tail from its bent configuration after maneuvering to its nominal configuration: if the system were airborne during this return, the generated yaw rotation would be undone.

A 3D CAD model of the RMLeg quadruped was created in Solidworks and exported to MSC ADAMS, a multi-body dynamic simulation software. This software enables a comprehensive simulation and motion analysis capable of solving for the kinematics and dynamics of the quadruped.

In addition to the system's inertial loading effects based on the imported CAD mass properties and geometry, loading effects are incorporated into the model for the tail loading, gravity, and contact between the 16 toes and ground. The contact loading between the toes and ground are defined by setting stiffness, force exponent, damping and penetration depth, and the associated friction is defined using a continuous velocity-dependent calculation of the friction coefficient. The desired leg trajectories are prescribed as kinematic constraints on the hip and knee joints of each leg and implicitly calculate the joint torques used to drive the associated joints' motors.

Although the quadruped design is inspired by a physical RMLeg prototype, the mass properties of the simulated system need to match the loading capacity available for the existing R3RT prototype. To accomplish this, the mass of the quadruped frame and legs were scaled down to 30% of their nominal values to enable the tail to achieve meaningful yaw rotation with a single tail motion. Connectors were needed between the fore and aft pairs of legs to provide sufficient spacing for the feet, and an additional proof mass in the head was added to help balance the cantilevered tail. The nominal quadruped mass $m_Q$ and body-frame inertia $\mathbf{I}_Q^Q$ are defined in Eq. 8.1 at the quad COM. This inertia does change during locomotion due to the leg motion, but this is calculated and accounted for automatically by ADAMS.

$$m_Q = 4.876 \text{ kg},$$

$$\mathbf{I}_Q^Q = \begin{bmatrix} 0.1723 & 0.0007 & -0.4000 \\ 0.0007 & 0.4343 & 0.0001 \\ -0.4000 & 0.0001 & 0.4291 \end{bmatrix} \text{kg-m}^2 \tag{8.1}$$

The quadruped's nominal gait during both simulations generate an average forward velocity of 750 mm/s with a step length of 250 mm (1.5 gait cycles per second) and a maximum foot lift of 50 mm.

### 8.1.3 Bipedal Robot with USRT

Figure 8.3 shows the tailed-biped composed of two RMLeg modules used to analyze the USRT's maneuvering and stabilization outer-loop controllers. MSC ADAMS is used to model the dynamics of the biped, based on the geometry and mass properties of a 3D CAD model exported from Solidworks. Kinematic constraints are used to prescribe desired joint velocities at the biped's hip and knee joints, and the multi-body dynamics model automatically calculates the associated torques required to implement these trajectories. External loading effects representing ground contact, gravity and tail loading are incorporated into the dynamic model, in addition to the inertial loading effects generated by the CAD's mass and geometric properties. Ground contact at each toe generates a normal force based on a damped elastic model acting against the toe penetrating the ground and a friction force opposing the toe's sliding velocity and calculated using a velocity-dependent friction coefficient to mimic stiction behavior. To mimic the effect of the tail, a rigid-body is fixed to the biped hip to account for the tail's effective mass and inertia, and a force/moment input is used to prescribe the tail's effective loading to the biped.

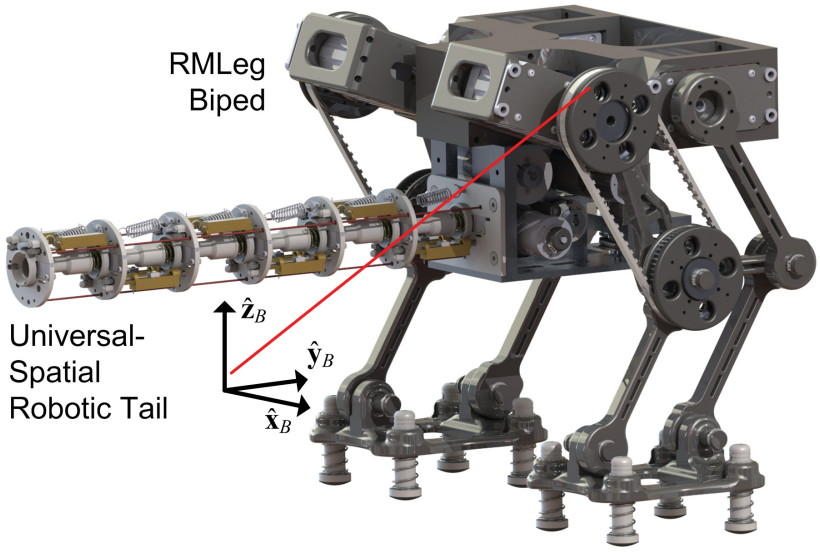


Figure 8.3: RMLeg biped with USRT.

This analysis focuses on analyzing controllers that generate specific stabilization and maneuvering behaviors in a tailed-biped system. As a result, leg motions are planned that demonstrate those behaviors without the need for full-scale demonstration of the biped's steady-state walking ability.

For stabilization, the biped's quasi-static trot gait alternates its feet between a support phase, in which one of the feet is in contact with the ground and pushes the quadruped forward, and a lift phase, in which the other foot is not in contact with the ground and returns to the starting point of its support phase. For the stabilization case study, only the vertical motion of the leg is considered.

During the support phase, a foot remains at a fixed vertical distance $h_S$ relative to the hip. During the lift phase, the foot starts from its fixed vertical distance $h_S$, reaches its maximum height midway through the lift phase at the distance $h_L$ relative to the hip, and returns to the distance $h_S$ at the end of the lift phase. A seventh-order polynomial is used to interpolate the lift-phase foot trajectory; the seven coefficient constraints are the three position constraints, two zero velocity constraints at the trajectory start and end and two

acceleration constraints at the trajectory start and end.

For maneuvering, friction at the biped's toes provide a high barrier to overcome to generate meaningful yaw-angle rotation. For bipeds exhibiting dynamically stable gaits with an aerial phase in which neither of the legs are in contact with the ground, friction can be avoided by actuating the tail during this time. For the quasi-statically stable RMLeg biped under consideration, an aerial phase may be mimicked by actuating the legs to generate a jumping motion.

The hopping motion is generated by actuating the legs in parallel to generate a vertical velocity in the biped, and then discontinously stopping the leg actuation so that the biped's momentum lifts the biped off the ground. A fifth-order polynomial is used to generate the hopping motion: constraints include two position constraints so that the trajectory starts and ends when the foot is $h_S$ from the hip, two zero-velocity and zero-acceleration constraints at the start of the trajectory, and a desired biped velocity $\dot{h}_H$ at the end of the trajectory.

For both the stabilization and maneuvering cases, an inverse kinematics model of the leg is used to map the foot trajectories into joint trajectories.

In order to facilitate experimental validation, the mass and inertia of the simulated RMLeg biped are scaled down by 40% to enable the existing USRT prototype to appreciably impact its dynamics. The mass of the biped $m_B$ and its inertia $\mathbf{I}_B^B$ in its nominal standing configuration are defined in Eq. 8.2 at the biped COM. As the biped links move during the simulation, this inertia will slightly change, but these perturbations are automatically accounted for in ADAMS.

$$m_B = 6.511 \text{ kg},$$

$$\mathbf{I_B^B} = \begin{bmatrix} 0.1864 & 0.0003 & 0.0080 \\ -0.0003 & 0.1538 & -0.2659 \\ 0.0080 & -0.2659 & 0.1830 \end{bmatrix} \text{ kg-m}^2 \tag{8.2}$$

### 8.1.4 Hardware-in-the-Loop Analysis

For both the quadruped and biped case studies, MSC ADAMS/Control is used to export the legged robot simulation to a Simulink block with six inputs (three components each for tail force and moment) and four outputs (quadruped forward velocity and yaw/pitch/roll angles). Initially, simulated tail loading calculated by the serpentine tail models (Chapter 6) are used to analyze the performance of the tails' outer-loop controllers.

To augment these simulation-based studies, a series of hardware-in-the-loop simulations were also performed. Hardware-in-the-loop (HIL) simulations use real, physical system hardware to replace one or more simulated subsystems in an analysis. Although HIL simulations typically utilizes a physical embedded system in conjunction with a mechanical plant simulation, the distinct mechanical subsystems of the tailed legged platforms lend themselves to this type of analysis. In this analysis, R3RT and USRT prototypes are used in conjunction with the simulated RMLeg quadruped and biped to analyze the stabilization and maneuvering behaviors of the tails' outer-loop controllers.

Figure 8.4 illustrates an example of the experimental setup used in this section. The R3RT prototype is mounted on a six-axis load cell (Sunrise Instruments M3716B) to measure the force and moment generated by the tail, which is then mapped into the equivalent force and moment at the tail frame origin (this is the loading the simulated tail calculated).

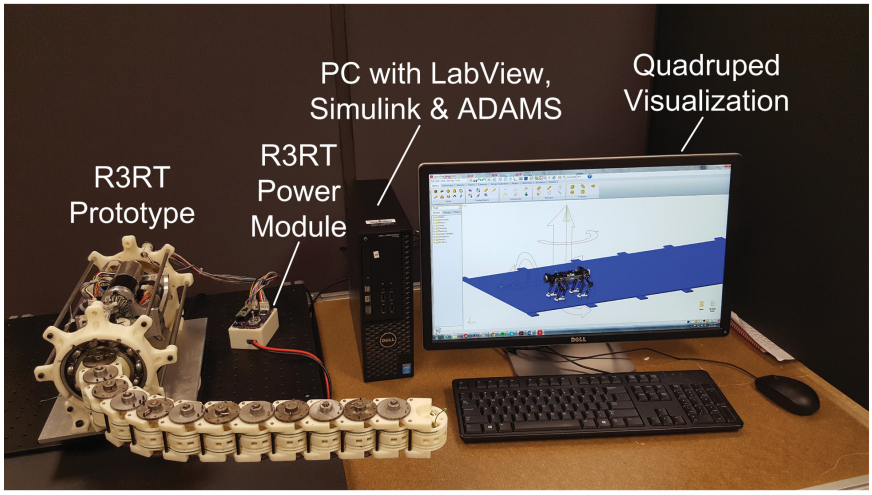


Figure 8.4: R3RT hardware-in-the-loop setup.

For the R3RT, control inputs for the tail experiments are generated by recording the calculated control input trajectories $\mathbf{u}$ and state vector accelerations $\ddot{\mathbf{q}}$ during a simulation. Using dynamic models of the actuation transmission mechanisms between the actuation inputs and motors for the R3RT and USRT, $\mathbf{u}$ and $\ddot{\mathbf{q}}$ are mapped into motor current commands. In addition, an empirical current offset was also added to overcome the friction within the actuation transmission mechanism and along the tail.

For the USRT, the present implementation of the USRT has impeded implementation of the prescribed torque/current inner-loop controller analyzed in section 7.3.2. As a result, the velocity controller used to implement the tail trajectories in section 6.2.6 is used to experimentally analyze the single-motion outer-loop maneuvering behavior. However, the multi-motion USRT stabilization behavior cannot be effectively implemented using the velocity inner-loop controllers, for these cases, the simulation results stand alone.

The tail prototypes' functional performances are assessed in two ways: 1) the loading calculated by the simulated tails are compared to the loading measured from the prototype tails, and 2) the performance of the prototype tail in terms of maneuvering and stabilization is

assessed using a HIL simulation.

## 8.2 Quadruped Maneuvering Case Study

For the maneuvering case study, the loading generated by a single tail motion was applied to the quadruped during locomotion to observe the resulting quadruped yaw rotation.

Figure 8.5 illustrates the change in yaw-angle heading due to a tail bend of 90° in segments 1 and 2. Unlike the maneuvering results in [69, 70], the heading angle magnitude monotonically increases. In those cases, friction acting against the desired motion of the quadruped caused the quadruped angular velocity to reach zero before the tail velocity reached zero during the tail's deceleration. Then, the tail's continuing deceleration induced an undesired rotation in the quadruped in the undesired direction. In this case, angular momentum between the tail and quadruped is conserved.

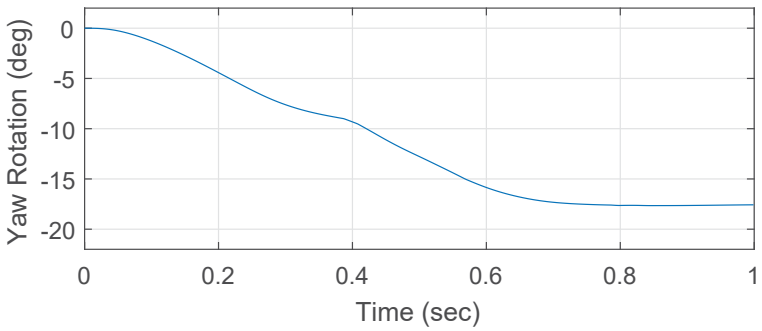


Figure 8.5: Quad with R3RT maneuvering case study yaw-angle rotation.

A key requirement of a robotic tail is that the loading generated by the tail does not induce instabilities in the DOFs orthogonal to the one under consideration. Figure 8.6 illustrates the associated pitch and roll angle trajectories of the quadruped due to the yawing tail motion. As shown, while the tail motion does induce slight undesired displacements in each, these do not cause destabilization.

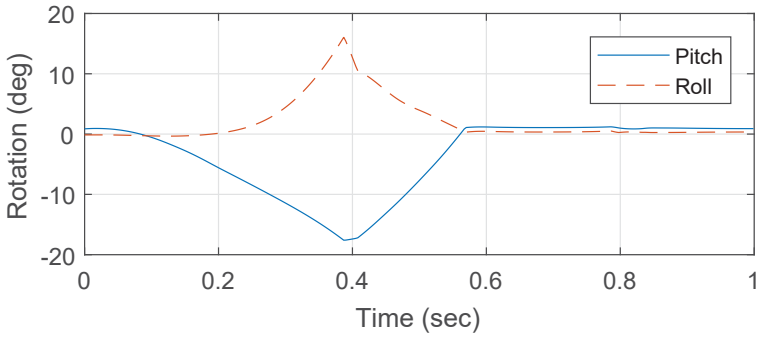


Figure 8.6: Quad with R3RT maneuvering case study pitch- and roll-angle trajectories.

Net changes to the quadruped's yaw heading angle in excess of the rotation that can be generated by a single tail motion may be generated by performing multiple tail motions in sequence. As discussed in section 7.2.1, the functional relationship between the net change in yaw-angle heading and $\ddot{\beta}_{pk}$ may be developed using simulations, to allow use of the multiple tail motion maneuvering algorithm described in [70].

Figure 8.7 compares the simulated and experimentally measured loading generated by the maneuvering tail motion, and Fig. 8.8 compares the simulated yaw-angle rotation due to the simulated and experimentally measured loading. To reduce the noise in the experimentally measured trajectories, three experiments for each tail motion were performed and the resulting loading averaged together.

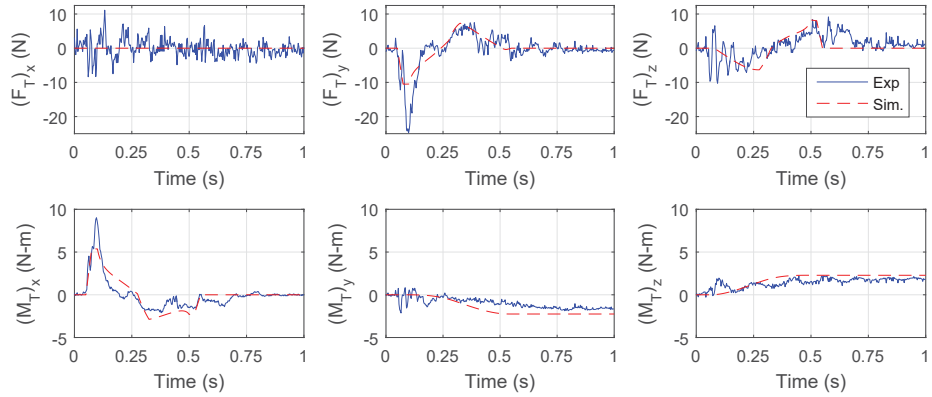


Figure 8.7: Quad with R3RT maneuvering case study simulated and experimental loading.

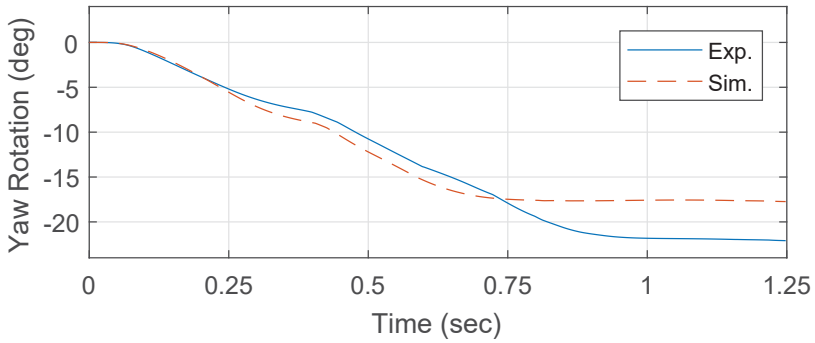


Figure 8.8: Quad with R3RT maneuvering case study simulated and experimental quadruped yaw-angle trajectories.

The x-component of moment is the most critical in this case study, and the increase in peak moment magnitude in the acceleration phase coupled with a lower magnitude moment and longer duration of the deceleration phase leads to the increased rotation observed in the yaw angle for the experimental loading case. The feedback linearization inner-loop controller used to generate the motor torque inputs in this analysis also shows significant improvement in terms of lag time compared to the inner-loop velocity controller results shown in section 6.1.6. In those results, the initial peak loading was predicted to occur at 0.1 sec, but the experimentally measured initial peak loading didn't occur until 0.3 sec. As shown in Fig. 8.7, the initial peak error is on the order of hundredths of a second, on par with the sampling rate.

The friction compensation current offsets required for bending the segments was significantly higher than anticipated, and likely resulted in shortcomings in the tracking of the desired dynamic trajectory.

## 8.3 Quadruped Stabilization Case Study

For the stabilization case study, an impulsive moment of magnitude $M_\delta$ is applied for 0.2 seconds in the roll direction of the quadruped during locomotion. Without active tail control, depending on the magnitude of $M_\delta$, one of three scenarios will occur.

1. The quadruped's gravitational loading will reject the disturbance without significant change in roll angle. This occurs in the range $M_\delta \in [0, 10.1]$ N-m, in which the quadruped's roll angle $|\rho|$ remains less than 3°. Thus, the moment disturbance threshold for non-trivial roll-angle variations is $M_{\delta,0} = 10.1$ N-m.

2. The quadruped will experience non-trivial roll displacement ($|\rho| > 3°$), but the disturbance is not sufficient to tip the quadruped and destabilize it. This occurs in the range $M_\delta \in [M_{\delta,0}, M_{\delta,0} + 15.5]$. Thus, the additional moment disturbance beyond $M_{\delta,0}$ the quadruped can accommodate without destabilizing is $M_{\delta,Q} = 15.5$ N-m.

3. The disturbance is sufficient to tip the quadruped and destabilize the system in the roll DOF. Without active stabilization, this occurs when $M_\delta > M_{\delta,0} + M_{\delta,Q}$. However, when the tail is used to actively stabilize the quadruped, a significant improvement in roll angle stability is observed.

The parameters used for the controller are defined in Eq. 8.3: no control action is taken for roll angle disturbances less than 3°, full control action is applied once the roll is greater than 13°, and the settling time of the tail position is $3\xi/\omega_n = 0.15$ sec.

$$\rho_{dz} = 3°, \quad \rho_{lim} = 13°, \quad \omega_n = 20 \text{ rad/sec} \tag{8.3}$$

Figure 8.9 illustrates the roll-angle trajectory of the quadruped for a disturbance of magni-

tude $M_\delta = M_{\delta,0} + M_{\delta,Q}$. Active tail-based stabilization provided a 68% reduction in peak roll-angle in relation to the passive case, which allows the system to further accommodate additional disturbance loading.

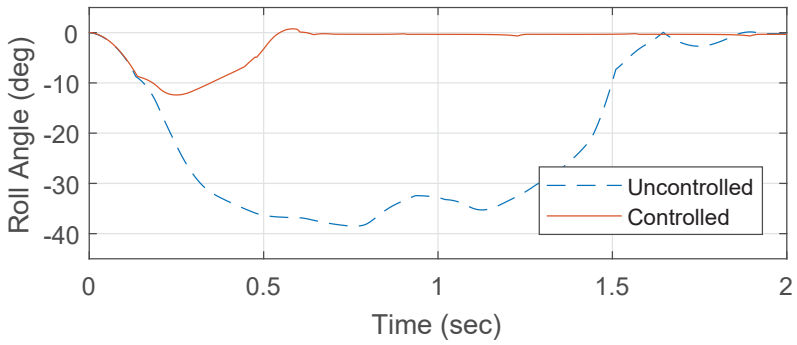


Figure 8.9: Quad with R3RT stabilization case study quadruped marginal stability with and without tail control action.

Figure 8.10 illustrates the roll-angle $\rho$ and control action parameter $\kappa$ trajectories for disturbances of magnitude $M_\delta = M_{\delta,0} + M_{\delta,Q} + \Delta M$ for which $\Delta M \in \{0, 1.5, 3.0, 4.6, 4.7\}$ N-m. The maximum $\Delta M$ allowable before the tailed-quadruped destabilizes is $M_{\delta,T} = 4.6$ N-m, which represents a 30% improvement to $M_{\delta,Q}$.

As with the maneuvering case, the roll-stabilizing control action should not destabilize the tailed-quadruped in the pitch or yaw direction. Figure 8.11 illustrates the system's pitch and yaw trajectories due to the stabilizing tail motion when $M_\delta = M_{\delta,0} + M_{\delta,Q} + M_{\delta,T}$. Although the tail does not destabilize the system in the pitch direction, it does result in a net non-zero yaw angle after the tail returns to its nominal configuration. This heading error can then be compensated for using an appropriately scaled maneuvering tail motion.

For the experimental validation, the $\mathbf{u}$ and $\ddot{\mathbf{q}}$ used to compute the motor current commands for the experimental validation were calculated for the case in which $M_\delta = M_{\delta,0} + M_{\delta,Q} + M_{\delta,T}$.

Figure 8.12 compares the simulated and experimentally measured loading generated by the stabilizing tail motion, and Fig. 8.13 compares the simulated roll-angle rotation due to

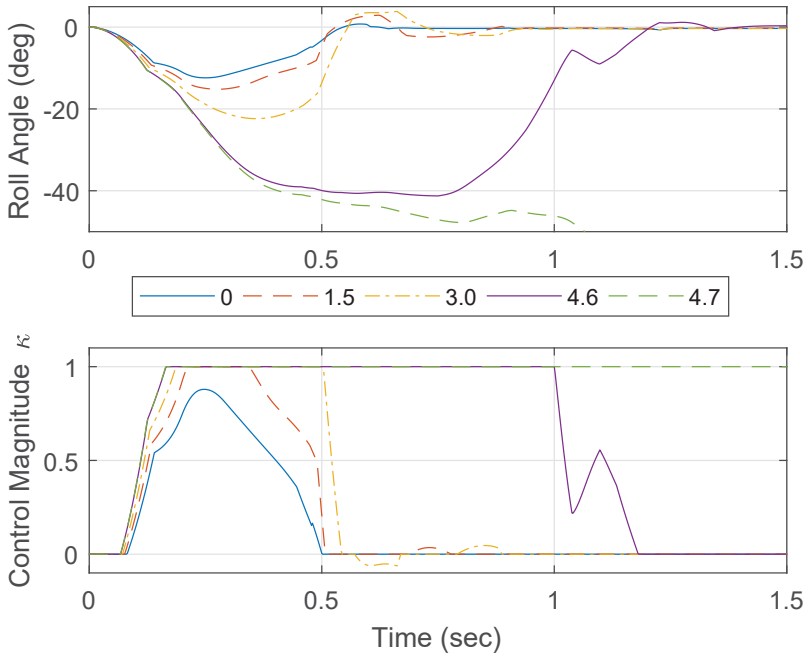


Figure 8.10: Quad with R3RT stabilization case study $\rho$ and $\kappa$ trajectories for varying disturbance magnitudes $M_\delta = M_{\delta,0} + M_{\delta,Q} + \Delta M$.

the simulated and experimentally measured loading. For the experimental loading HIL simulation, the magnitude of the disturbance was reduced by 0.1 N-m, as the system was unstable for the simulation's $M_\delta$.

The z-component of moment is the most critical in this case study; like the stabilization case, the tail simulation underestimated the moment's maximum and minimum magnitudes, but the impact of this variation on the simulation's predicted performance of the robot is significantly less than the stabilization case. The simpler actuation transmission mechanism between the motor and roll DOF also required less friction compensation in relation to the bending tail motions, providing for a more accurate simulation of the tail behavior.

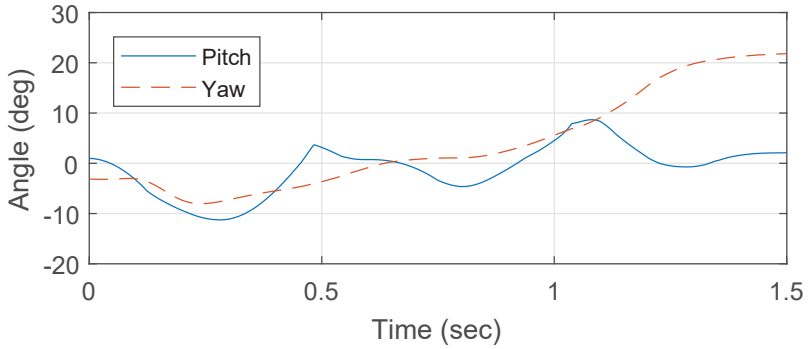


Figure 8.11: Quad with R3RT stabilization case study pitch- and yaw-angle trajectories.

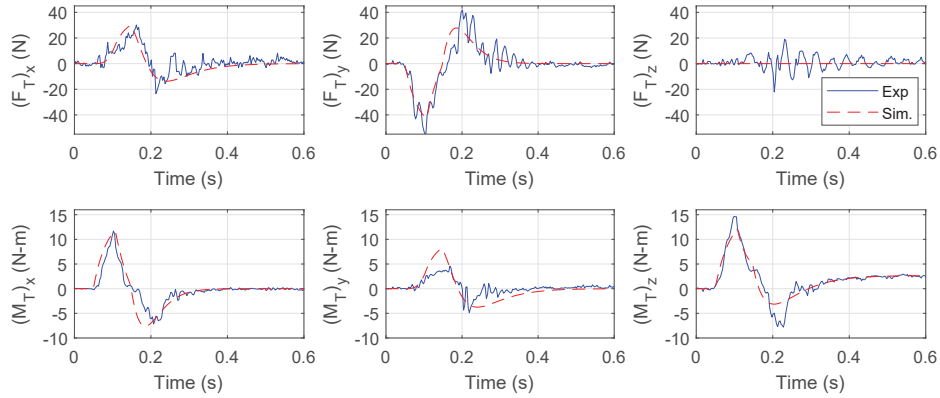


Figure 8.12: Quad with R3RT stabilization case study simulated and experimental loading.

## 8.4 Biped Maneuvering Case Study

For the biped maneuvering case study, the loading generated by a single tail motion was applied to the biped during a hopping motion to observe the resulting biped yaw rotation.

Figure 8.14 illustrates the change in yaw-angle heading due to a yaw-angle bending of 90° in segments 1 and 2. Due to the similar formulations of their driving tail motions, the results for this case study are similar to those for the quadruped maneuvering. Likewise, Fig. 8.15 shows the biped's pitch and roll angle trajectories due to the bipedal tail motion. Of particular importance for the biped is the pitch behavior, as the biped lacks the quadruped's fore set of legs to help prevent forward tipping. As shown, the tail loading does not introduce

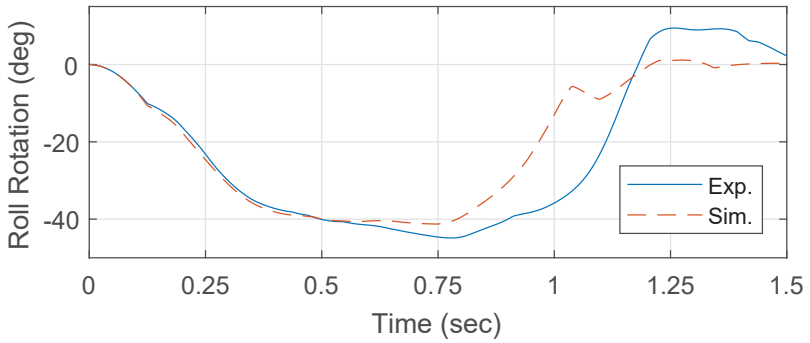


Figure 8.13: Quad with R3RT stabilization case study simulated and experimental quadruped roll-angle trajectories.

instabilities to its auxiliary DOFs.

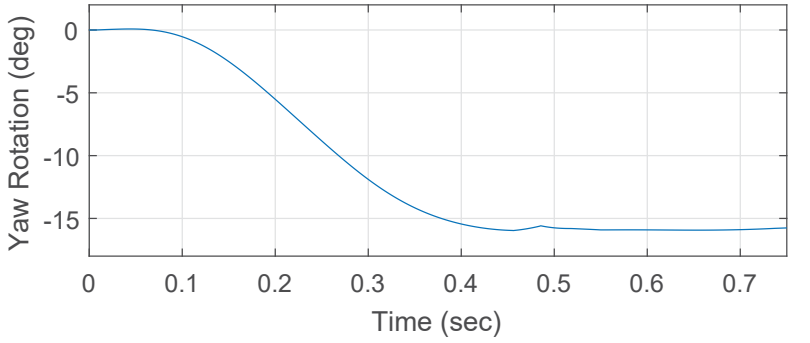


Figure 8.14: Biped with USRT maneuvering case study simulated biped yaw-angle trajectory.

Figure 8.16 compares the simulated and experimentally measured loading generated by the maneuvering tail motion, and Fig. 8.17 compares the simulated biped yaw-angle rotation due to the simulated and experimentally measured tail loading. Although undesirable, these results clearly emphasize the benefit of the feedforward current controller used in section 8.2 for the quadruped maneuvering case study. Instead of the increase in loading magnitudes and net rotation seen in the R3RT, the motor's velocity controller induces lag, reduces the peak loading magnitude and less efficiently actuates the robot during its aerial phase, resulting in reduced yaw-angle rotation.

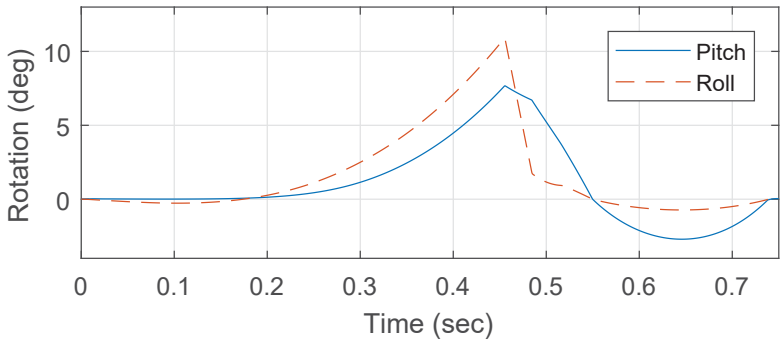


Figure 8.15: Biped with USRT maneuvering case study simulated biped pitch- and roll-angle trajectories.

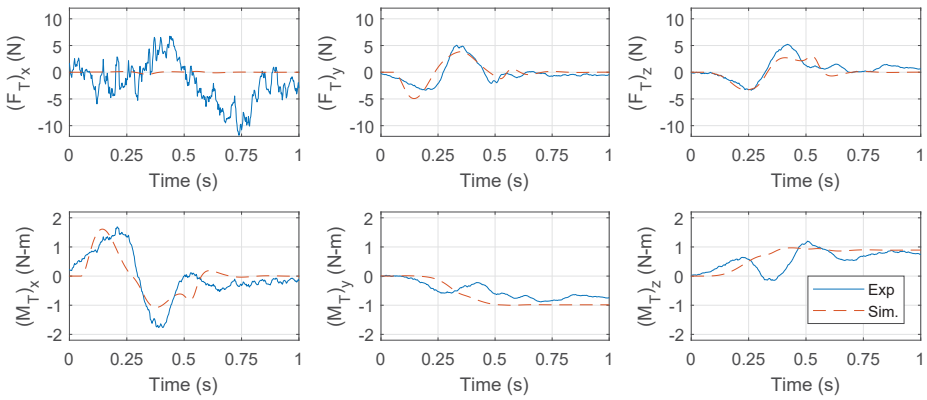


Figure 8.16: Biped with USRT maneuvering case study simulated and experimental tail loading.

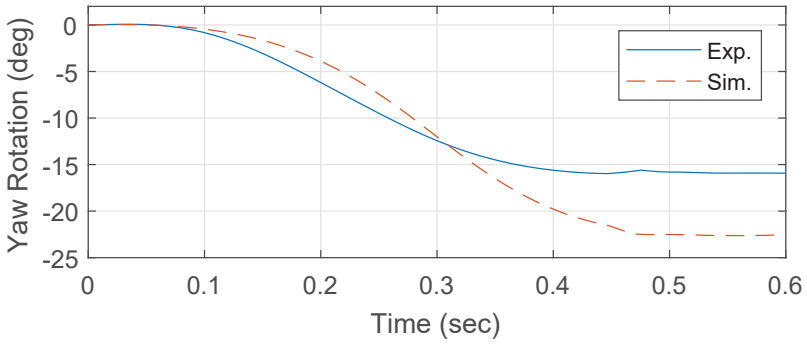


Figure 8.17: Biped with USRT maneuvering case study biped yaw-angle trajectories for simulated and experimental tail loading.

## 8.5 Biped Stabilization Case Study

Figure 8.18 illustrates the roll-angle trajectories of the biped during a single gait cycle with and without the stabilizing tail action. In the absence of the tail actuation, as the biped begins to lift one of its legs, it begins rolling to the side for which the leg is lifted. As the biped rolls, the leg continues its motion, and at the peak of the roll magnitude, the leg comes in contact with the ground once again, earlier than the anticipated switch between leg contacts at 0.5 second intervals. For the remainder of this gait half-cycle, the foot is in contact with the ground, and is pushing up the biped to its nominal configuration. Alternatively, the controlled biped motion shows a minor roll variation ($< 1°$) immediately after the gait transition, but otherwise maintains a stable roll angle throughout the gait cycle.

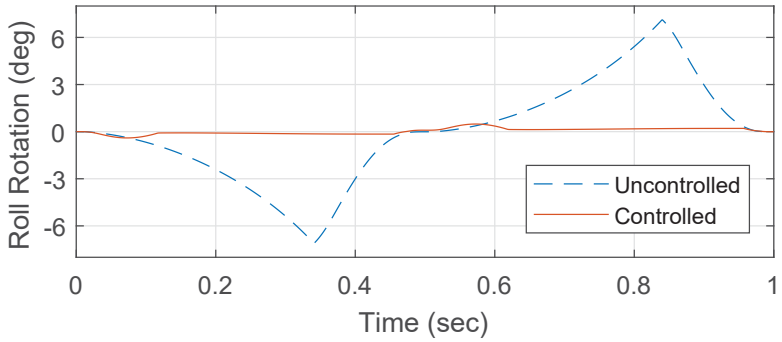


Figure 8.18: Biped with USRT stabilization case study biped roll-angle trajectories with and without tail action.

Figure 8.19 illustrates the ancillary pitch- and yaw-angle trajectories of the biped during the stabilizing tail motion. As anticipated, the rolling tail motion causes no apparent change in the biped's pitch, whereas the biped's yaw cyclically adjusts due to the cyclic horizontal motion of the tail's COM during the stabilizing roll motion. This yaw angle trajectory variation causes no net change in heading angle when averaged over the gait cycle, but slightly reduces the efficiency of locomotion.

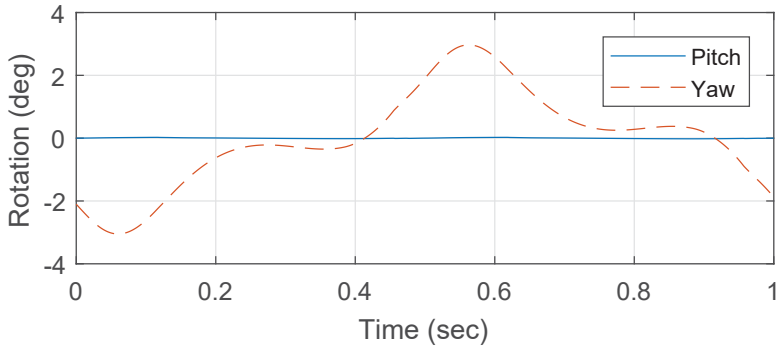


Figure 8.19: Biped with USRT stabilization case study biped pitch- and yaw-angle trajectories.

Although experimental loading profiles are not generated for this case study, the simulated loading profiles are generated to show the behavior of the tail's z-component of moment, which correlates to the biped's roll axis. As desired, the tail generates a consistent stabilizing moment in each half of the gait cycle. Use of an alternative formulation for the tail's motion could modify this profile if necessary, but the result is strong considering its source is a simple sinusoidal waveform.

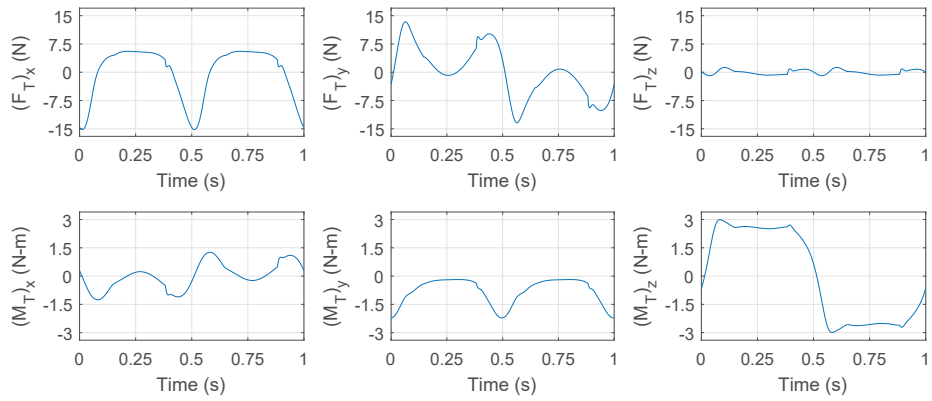


Figure 8.20: Biped with USRT stabilization case study simulated tail loading.

# Chapter 9

# Conclusion

## 9.1 Summary

This dissertation has presented research into the design, modeling, sensing and control of hyperredundant robotic structures for use as robotic tails on-board quadrupedal and bipedal legged robots. A high-fidelity lumped parameter model was derived for a class of cable- and rod-driven continuum robots, and the dynamic equations of motion of this model were formulated using the method of virtual power. Simulation results for the cable- and rod-driven actuation structures were generated, and cross-validated using finite element analysis and experimental results.

Two novel serpentine tails—the Roll-Revolute-Revolute Robotic Tail (R3RT) and the Universal Spatial Robotic Tail (USRT)–were presented, including the overall design concept, the detailed mechanical and electrical designs, and the prototype integration. Kinematic and dynamic models were formulated for these two tails, including a model for calculating the loading applied by the tail to its legged platform, and the accuracy of these models

were compared to experimental results generated using the R3RT and USRT prototypes and measured using a six-axis load cell.

Considerations for tail sensing and control were also addressed: in terms of sensing, a means of estimating position and velocity data for each tail were presented, along with outer-loop and inner-loop analyses for each tail structure. Outer-loop controllers for the tails were designed to generate desired tail trajectories that implement the desired maneuvering and stabilizing behaviors. Inner-loop controllers for each tail then mapped the desired tail trajectories into control inputs that implemented the desired trajectory and maintained minimum cable tension (for the USRT).

Case studies were implemented using quadrupeds and bipeds constructed from four and two Robotic Modular Leg (RMLeg) units, respectively, with the quadruped considered with R3RT and the biped considered with the USRT. For maneuvering, yaw angle rotations were induced by the tail in the quadruped and biped during a hopping motion. For stabilization, the rejection of a rolling moment disturbance in the quadruped was improved by a stabilizing tail action, and the undesired roll angle motion in the biped due to the cyclic lifting of its two legs was compensated for. Both simulated and experimental tail loading was utilized in the case studies, with the case studies involving latter serving as hardware-in-the-loop validation of the tail's abilities.

## 9.2 Future Work

As the work described in this dissertation represented the creation of several new design concepts, modeling frameworks and control laws, there are clear directions in how this research can progress in the future. First, the most important consideration that needs to be made with regards to tailed-legged-robots is the joint consideration of the dynamics. In this

research, the tail dynamics were formulated with respect to an inertial tail base frame, and neither the motion of the tail nor the loading generated by its were impacted by the motion of the legged platform. This will require the formulation of the legged platform's floating-base equations of motion in the same modeling framework as the tail dynamics, accounting for inertia, ground contact, and the implicit connection between the legs and tail.

In relation to the tail prototypes, further iteration on the tail designs, particularly the actuation modules, should be done to better facilitate their integration with legged robots. In addition, simplifying the designs of key tail components (particularly the R3RT links) should be done to facilitate their fabrication out of metal instead of 3D printed plastic. The USRT's electrical design should also be re-assessed to better understand the errors that prevented implementation of inner-loop torque control.

In relation to the tails' inner-loop controllers, full-scale implementation of the feedforward and feedback control loops on an embedded system driving the tails is needed to fully demonstrate the tails' capabilities. Further characterization of both sensor error and modeling errors in the feedback linearizing controller could also be used to synthesize additional tail control inputs to help offset these errors. In addition, better characterization of friction within both the actuation transmission mechanisms and the tail structures themselves would aid in formulating feedforward control actions that anticipate these potential sources of error and preemptively act against them.

In relation to the tails' outer-loop controllers, additional tail motions to generate the desired legged platform behavior should be studied and compared to one another to assess a more systematic method of generating tail trajectories. Furthermore, maneuvering and stabilization behaviors should be jointly considered to allow for continuous operation of the legged robot.

Finally, the full-scale integration of a tailed-legged robot will conclusively demonstrate the feasibility of this idea. Whether an experimental implementation of the RMLeg quadruped or biped considered as a part of this work, or another quasi-statically or dynamically stable legged robot, this would provide a baseline for comparison to existing tail-free quadrupeds and bipeds.

# Appendices

# Appendix A

# Nomenclature

This appendix details the nomenclature of the symbols, marks and variables used throughout the paper for the analyses of the continuum robots and serpentine tails. Owing to the limited number of Latin and Greek characters, there are some variables defined differently for different categories of robots.

Four categories of robots are considered: a cable-driven continuum robot (CC), a rod-driven continuum robot (CR), the Roll-Revolute-Revolute Robotic Tail (R3) and the Universal-Spatial Robotic Tail (US). In addition, 'C' is used to represent both categories of continuum robots (CC and CR), 'S' is used to represent both categories of serpentine robots (R3 and US), and 'All' implies that the variable definition is applicable to all four categories.

In addition, a superscript other than $T$ denotes the frame in which a vector or matrix is defined; if a superscript is omitted, that vector or matrix is defined with respect to the inertial base frame (continuum) or inertial tail frame (serpentine).

Table A.1: Nomenclature, Marks and Symbols

| Mark | Meaning | Symbol | Meaning |
|---|---|---|---|
| $\|\mathbf{x}\|$ | Euclidian norm of $\mathbf{x}$ | $\cdot$ | Inner product |
| $\hat{\mathbf{x}}$ | Unit vector of $\mathbf{x}$ | $\times$ | Cross product |
| $\bar{\mathbf{x}}$ | Estimate of $\mathbf{x}$ | $\otimes$ | Outer product |
| $\tilde{\mathbf{x}}$ | Error of $\mathbf{x}$, $\mathbf{x} - \mathbf{x}_{des}$ | $\odot$ | Element-by-element multiplication |
| $\mathbf{x}^T$ | Transpose of $\mathbf{x}$ | sgn | Signum function |
| $\dot{\mathbf{x}}$ | First time derivative of $\mathbf{x}$ | sat | Unit saturation function |
| $\ddot{\mathbf{x}}$ | Second time derivative of $\mathbf{x}$ | | |

Table A.2: Nomenclature, A through E

| Variable | Structure | Description |
|---|---|---|
| $\mathbf{A}$ | US | Sensor model linearization coefficient matrix for pitch and yaw angles |
| $(\mathbf{A})_{r,c}$ | US | Sensor model linearization coefficient for row $r$ and column $c$ of matrix $\mathbf{A}$ |
| $A$ | US | Cable index, for which $A \in \{1, 2, 3\}$ |
| $a_n$ | R3 | Coefficient for polynomial interpolation for trajectory planning |
| $\mathbf{a}_{OL}$ | US | Prescribed outer-loop acceleration |
| $B$ | US | Cable index, for which $B \in \{1, 2, 3 \mid B \neq A\}$ |
| $\mathbf{b}$ | US | Sensor model linearization offset vector |
| $(\mathbf{b})_r$ | US | Sensor model linearization offset for row $r$ of vector $\mathbf{b}$ |
| $\mathbf{C}$ | S | Coriolis and centripetal effects matrix for the equations of motion |
| $(\mathbf{C})_{r,:}$ | US | Row $r$ of matrix $\mathbf{C}$ |
| $C$ | US | Cable index, for which $C \in \{4, 5, 6\}$ |
| $c$ | US | Index for matrix column |
| $c_{bnd}$ | C | Damping coefficient for continuum core subsegment bending |
| $c_{dmp}$ | US | Damping coefficient for universal joint displacement |
| $c_{lim}$ | US | Damping coefficient for joint limit model |
| $c_{tor}$ | CC | Damping coefficient for continuum core subsegment twisting |
| $D$ | US | Cable index, for which $D \in \{4, 5, 6 \mid D \neq C\}$ |
| $\mathbf{d}$ | US | Damping loading vector for the equations of motion |
| $(\mathbf{d})_r$ | US | Row $r$ of vector $\mathbf{d}$ |
| $\dot{d}_{i,k,cbl}$ | CC | Sliding velocity of cable $k$ through its disk $i$ routing hole |
| $\dot{d}_{i,k,rod}$ | CR | Sliding velocity of rod $k$ through its disk $i$ routing hole |
| $d_{j,m,sn}$ | US | Distance measured by joint $j$ sensor $m$ |
| $\dot{d}_{sat}$ | C | Continuous friction direction transition constant |
| $\mathbf{E}_3$ | All | 3-by-3 identity matrix |
| $E_{core}$ | C | Young's modulus of the continuum core |
| $E_{rod}$ | CR | Young's modulus of the actuation rod |

Table A.3: Nomenclature, F through I

| Variable | Structure | Description |
|---|---|---|
| $\mathbf{F}_{i,act}$ | C | Actuation force of rigid body $i$ |
| $\mathbf{F}_{i,bdy}$ | C | Net force of rigid body $i$ |
| $\mathbf{F}_{i,k,cbl}$ | CC | Contact force due to cable $k$ on disk $i$ |
| $\mathbf{F}_{j,k,cbl}$ | US | Force of cable $k$ acting across joint $j$ |
| $\mathbf{F}_{j,ext}$ | US | Force of joint $j$ extension spring acting on link $i = j$ |
| $\mathbf{F}_{i,inr}$ | C | Inertial force of rigid body $i$ |
| $\mathbf{F}_{i,inr,bdy}$ | S | Inertial force of link $i$ |
| $\mathbf{F}_{i,grv}$ | C | Gravitational force of rigid body $i$ |
| $\mathbf{F}_{i,grv,bdy}$ | S | Gravitational force of link $i$ |
| $\mathbf{F}_{RH,grv}$ | R3 | Gravitational force of rigid housing |
| $\mathbf{F}_{i,k,rod,con}$ | CR | Contact force between rod $k$ and disk $i$ |
| $\mathbf{F}_{k,rod,end}$ | CR | Force between rod $k$ and its terminal disk $N_k$ |
| $\mathbf{F}_{k,rod,eq}$ | CR | Net equilibrium force of rod $k$ |
| $\mathbf{F}_{i,k,rod,fr}$ | CR | Friction force due to rod $k$ contact with disk $i$ |
| $\mathbf{F}_T$ | S | Tail base force |
| $(\mathbf{F}_T)_{\{x,y,z\}}$ | S | $\{x, y, z\}$-component of tail base force |
| $F_{i,k,cbl,fr}$ | CC | Friction force due to cable $k$ contact with disk $i$ |
| $F_{j,ext,pre}$ | US | Pretension force of joint $i$ extension spring |
| $F_{l,\{1,\cdots,5\},gear}$ | R3 | Contact force for gear pair $\{1, \cdots, 5\}$ in segment $l$ |
| $F_{k,rod,obj}$ | CR | Objective function for rod $k$ equilibrium |
| $G_{core}$ | CC | Shear modulus of the continuum core |
| $\mathbf{g}$ | S | Gravitational loading vector for the equations of motion |
| $(\mathbf{g})_r$ | US | Row $r$ of vector $\mathbf{g}$ |
| $g$ | All | Gravitational acceleration |
| $\dot{h}_H$ | US | Relative velocity between biped hip and ankle at end of hop-initiating trajectory |
| $h_L$ | US | Minimum distance between biped hip and ankle during leg lift phase |
| $h_S$ | US | Distance between biped hip and ankle during leg support phase |
| $\mathbf{I}_B$ | US | Inertia tensor of biped |
| $\mathbf{I}_{i,bdy}$ | All | Inertia tensor of rigid body $i$ |
| $\mathbf{I}_Q$ | R3 | Inertia tensor of quadruped |
| $I_{i,bdy,xx}$ | C | Radial inertia of rigid body $i$ in body-fixed frame |
| $I_{i,bdy,zz}$ | C | Axial inertia of rigid body $i$ in body-fixed frame |
| $I^i_{i,bdy,\{xx,yy,zz\}}$ | S | {x,y,z}-axis moment of inertia of rigid body $i$ in body-fixed frame |
| $i$ | C | Index over the number of rigid bodies or subsegments |
| $i$ | S | Index over a number of links |

Table A.4: Nomenclature, J through L

| Variable | Structure | Description |
|---|---|---|
| $\mathbf{J}_{\mathbf{p},i}$ | All | Jacobian of the link $i$ COM linear velocity |
| $(\mathbf{J}_{\mathbf{p},i})_{\{1,\cdots,n\}}$ | C | Column $\{1,\cdots,n\}$ of $\mathbf{J}_{\mathbf{p},i}$ |
| $\mathbf{J}_{\boldsymbol{\omega},i}$ | All | Jacobian of the link $i$ angular velocity |
| $(\mathbf{J}_{\boldsymbol{\omega},i})_{\{1,\cdots,n\}}$ | C | Column $\{1,\cdots,n\}$ of $\mathbf{J}_{\boldsymbol{\omega},i}$ |
| $J_{xx,core}$ | C | Second moment of area of the continuum core |
| $J_{xx,rod}$ | CR | Second moment of area of the actuating rod |
| $J_{zz,core}$ | CC | Polar moment of area of the continuum core |
| $j$ | S | Index over the number of joints |
| $\mathbf{K}_0$ | S | Linear feedback gain for state position error |
| $\mathbf{K}_1$ | S | Linear feedback gain for state velocity error |
| $K_\theta$ | US | Sensor model linearization yaw-angle coefficient |
| $K_\phi$ | US | Sensor model linearization pitch-angle coefficient |
| $\mathbf{k}$ | US | Coupling loading vector for the equations of motion |
| $(\mathbf{k})_r$ | US | Row $r$ of vector $\mathbf{k}$ |
| $k$ | C | Index over the number of cables or rods |
| $k$ | US | Index over the number of cables |
| $k_i$ | C | Spatial curvature of elastic core subsegment $i$ |
| $k_{i,k}$ | CR | Spatial curvature of rod $k$ subsegment $i$ |
| $k_{j,cmp}$ | US | Bending stiffness of joint $j$ compression spring |
| $k_{j,ext}$ | US | Stiffness of joint $j$ extension spring |
| $k_{lim}$ | US | Stiffness of joint limit model |
| $L_0$ | C | Subsegment length |
| $L_{i,k,cbl,ss}$ | CC | Length of cable $k$ in subsegment $i$ |
| $L_{i,k,rod,ss}$ | CR | Length of rod $k$ in subsegment $i$ |
| $L_{DJ}$ | US | Distance between a link's disk center and its distal universal joint center |
| $L_{j,ext}$ | US | Nominal length of joint $j$ extension spring |
| $L_{JC}$ | S | Distance between a link's proximal joint center and its COM |
| $L_{JD}$ | US | Distance between a link's proximal universal joint center and its disk center |
| $L_{JJ}$ | S | Distance between a link's joint centers |
| $L_{sn}$ | US | Sensor distance when universal joint pitch and yaw are zero |
| $l$ | S | Index over the number of segments |

Table A.5: Nomenclature, M

| Variable | Structure | Description |
|---|---|---|
| $\mathbf{M}$ | S | Mass matrix for the equations of motion |
| $(\mathbf{M})_{r,:}$ | US | Row $r$ of matrix $\mathbf{M}$ |
| $\mathbf{M}_{i,act}$ | C | Actuation moment of rigid body $i$ |
| $\mathbf{M}_{j,act}$ | S | Actuation moment of joint $j$ |
| $\mathbf{M}_{i,bdy}$ | C | Net moment of rigid body $i$ |
| $\mathbf{M}_{i,\{i,i+1\},bnd}$ | C | Bending moment due to subsegment $\{i, i+1\}$ on rigid body $i$ |
| $\mathbf{M}_{j,cmp}$ | US | Compression spring moment of joint $j$ |
| $\mathbf{M}_{i,cpl}$ | C | Coupling moment of rigid body $i$ |
| $\mathbf{M}_{j,cpl}$ | US | Coupling moment of joint $j$ |
| $\mathbf{M}_{i,\{i,i+1\},dmp}$ | C | Damping moment due to subsegment $\{i, i+1\}$ on rigid body $i$ |
| $\mathbf{M}_{j,dmp}$ | US | Damping moment of joint $j$ |
| $\mathbf{M}_{j,ext}$ | US | Extension spring moment of joint $j$ |
| $\mathbf{M}_{j,gear}$ | R3 | Gearing moment of joint $j$ |
| $\mathbf{M}_{j,grv}$ | S | Gravitational moment of joint $j$ |
| $\mathbf{M}_{i,inr}$ | C | Inertial moment of rigid body $i$ |
| $\mathbf{M}_{j,inr}$ | S | Inertial moment of joint $j$ |
| $\mathbf{M}_{i,inr,bdy}$ | S | Inertial moment of link $i$ |
| $\mathbf{M}_{j,jnt}$ | S | Net moment of joint $j$ |
| $\mathbf{M}_{j,lim}$ | US | Joint limit moment of joint $j$ |
| $\mathbf{M}_{k,rod,eq}$ | CR | Net equilibrium moment of rod $k$ |
| $\mathbf{M}_T$ | S | Tail base moment |
| $(\mathbf{M}_T)_{\{x,y,z\}}$ | S | $\{x, y, z\}$-component of tail base moment |
| $\mathbf{M}_{i,\{i,i+1\},tor}$ | CC | Torsional moment due to subsegment $\{i, i+1\}$ on rigid body $i$ |
| $M_{i,bnd,cbl}$ | CC | Bending moment magnitude of cable-driven subsegment $i$ |
| $M_{i,bnd,core}$ | C | Bending moment magnitude of continuum core subsegment $i$ |
| $M_{i,bnd,rod}$ | CR | Bending moment magnitude of rod-driven subsegment $i$ |
| $M_{i,k,bnd,rod}$ | CR | Bending moment magnitude of rod $k$ subsegment $i$ |
| $M_{j,\{1,2\},gear}$ | R3 | Gear moment $\{1, 2\}$ of joint $j$ |
| $M_\delta$ | R3 | Destabilizing roll moment on quadruped |
| $M_{\delta,0}$ | R3 | Maximum $M_\delta$ for which $\lvert\rho\rvert \leq \rho_{dz}$ without a stabilizing tail motion |
| $M_{\delta,Q}$ | R3 | Maximum addition to $M_\delta = M_{\delta,0}$ for which the quadruped remains stable without a stabilizing tail motion |
| $M_{\delta,T}$ | R3 | Maximum addition to $M_\delta = M_{\delta,0} + M_{\delta,Q}$ for which the quadruped remains stable with a stabilizing tail motion |
| $m$ | US | Index for the number of distance sensors |
| $m_B$ | US | Mass of biped |
| $m_{i,bdy}$ | All | Mass of rigid body $i$ |
| $m_{RH,bdy}$ | R3 | Mass of rigid housing |
| $m_Q$ | R3 | Mass of quadruped |

Table A.6: Nomenclature, N through Q

| Variable | Structure | Description |
|---|---|---|
| $N_k$ | CR | Disk to which rod $k$ attaches |
| $n$ | C | Number of state coordinates |
| $n$ | R3 | Index for polynomial interpolation |
| $P$ | C | Net virtual power acting on the tail |
| $\mathbf{p}_i$ | C | Position vector from inertial base frame origin to disk $i$ center/COM |
| $\mathbf{p}_{(i-1)i}$ | C | Position vector from disk $i-1$ center/COM to disk $i$ center/COM |
| $\mathbf{p}_{(i-1)i,k,cbl}$ | CC, US | Position vector of cable $k$ subsegment from disk $i-1$ to disk $i$ |
| $\mathbf{p}_{i,COM}$ | S | Position vector from inertial tail frame origin to link $i$ COM |
| $\mathbf{p}_{j,ext}$ | US | Position vector from base to tip of joint $j$ extension spring |
| $\mathbf{p}_{i,ext,B}$ | US | Position vector in link $i$ from disk center to joint $j=i+1$ extension spring base |
| $\mathbf{p}_{i,ext,T}$ | US | Position vector in link $i$ from disk center to joint $j=i$ extension spring tip |
| $\mathbf{p}_{i,k,hl}$ | US | Position vector in link $i$ from disk center to cable $k$ routing hole |
| $\mathbf{p}_{j,i,JC}$ | S | Position vector from joint $j$ center to link $i$ COM |
| $\mathbf{p}_{0,JC}$ | R3 | Position vector from joint 0 center to link 0 COM |
| $\mathbf{p}_{0,JC}$ | US | Position vector from inertial tail frame origin to link 0 COM |
| $\mathbf{p}_{j,JE}$ | US | Position vector from joint $j$ center to joint $j$ extension spring tip |
| $\mathbf{p}_{j,k,JH}$ | US | Position vector from joint $j$ center to link $i=j$ cable $k$ routing hole |
| $\mathbf{p}_{j,jnt}$ | S | Position vector from inertial tail frame origin to joint $j$ center |
| $\mathbf{p}_{T0,jnt}$ | R3 | Position vector from inertial tail frame origin to joint 0 center |
| $\mathbf{p}_{T1,jnt}$ | US | Position vector from inertial tail frame origin to joint 1 center |
| $\mathbf{p}_{01,jnt}$ | R3 | Position vector from joint 0 center to joint 1 center |
| $\mathbf{p}_{j,m,JS}$ | US | Position vector from joint $j$ center to joint $j$ sensor $m$ tip |
| $\mathbf{p}_{RH,COM}$ | R3 | Position vector from inertial tail frame origin to rigid housing COM |
| $\mathbf{p}_{i,k,rod}$ | CR | Position vector from inertial base frame origin to disk $i$ rod $k$ routing hole |
| $\mathbf{p}_{j,m,SJ}$ | US | Position vector from joint $j$ sensor $m$ base to joint $j$ center |
| $\mathbf{p}_{j,m,sn}$ | US | Position vector from joint $j$ sensor $m$ base to tip |
| $\mathbf{p}_{j,m,sn,B}$ | US | Position vector from link $i=j-1$ disk center to joint $j$ sensor $m$ base |
| $\mathbf{p}_{j,m,sn,T}$ | US | Position vector from link $i=j$ disk center to joint $j$ sensor $m$ tip |
| $\mathbf{q}$ | All | State vector |
| $\mathbf{q}_0$ | R3 | Nominal tail configuration desired when $\kappa=0$ |
| $\mathbf{q}_{des}$ | R3 | Desired state vector |
| $\mathbf{q}_{st}$ | R3 | Stabilizing tail configuration desired when $\kappa=1$ |

Table A.7: Nomenclature, R through U

| Variable | Structure | Description |
|---|---|---|
| $\mathbb{R}$ | All | Set of real numbers |
| $\mathbf{R}_i$ | All | Orientation matrix of frame $i$ with respect to inertial frame |
| $\mathbf{R}_{(i-1)i}$ | C, US | Orientation matrix of frame $i$ with respect to frame $i-1$ |
| $\mathbf{R}_{(LC)T}$ | US | Rotation matrix of inertial tail frame with respect to load cell frame |
| $\mathbf{R}_{(j-1,S)(j,S)}$ | US | Rotation matrix of frame $j,S$ with respect to frame $j-1,S$ |
| $\mathbf{R}_X(\cdot)$ | All | Canonical rotation by the angle $(\cdot)$ about the x-axis |
| $\mathbf{R}_Y(\cdot)$ | All | Canonical rotation by the angle $(\cdot)$ about the y-axis |
| $\mathbf{R}_Z(\cdot)$ | All | Canonical rotation by the angle $(\cdot)$ about the z-axis |
| $\mathbf{r}_{i,k,cbl}$ | CC | Position vector in rigid body $i$ from disk center to cable $k$ routing hole |
| $\mathbf{r}_{i,k,rod}$ | CR | Position vector in rigid body $i$ from disk center to rod $k$ routing hole |
| $r$ | US | Index for matrix or vector row |
| $r_{cbl}$ | R3 | Radius of cable routing cylinder |
| $r_{hl}$ | C | Radius of cable or rod routing hole pattern |
| $r_{sn}$ | US | Radius of sensor mounting pattern |
| $\mathbf{T}$ | S | Actuation transmission matrix for the equations of motion |
| $(\mathbf{T})_{r,c}$ | US | Row $r$, column $c$ term of matrix $\mathbf{T}$ |
| $T_l$ | R3 | Segment $l$ cable tension |
| $T_k$ | US | Cable $k$ tension |
| $T_{0f}$ | US | Sine-wave period from time $t_0$ to time $t_f$ |
| $T_{AE}$ | US | Sine-wave period from time $t_A$ to time $T_E$ |
| $T_{i,k,cbl}$ | CC | Tension in cable $k$ subsegment $i$ |
| $T_{k,cbl,base}$ | CC | Tension in cable $k$ at base |
| $T_{min}$ | US | Minimum cable tension |
| $T_{k,rod,base}$ | CR | Force in rod $k$ at base |
| $T_{k,rod,end}$ | CR | Force in rod $k$ subsegment $N_k$ |
| $t$ | All | Time for trajectory planning |
| $t_{\{0,f\}}$ | S | {Initial, final} trajectory planning time |
| $t_{\{A,\cdots,H\}}$ | S | Time $\{A,\cdots,H\}$ for trajectory planning |
| $\mathbf{u}$ | S | Control input |
| $\mathbf{u}_{\{123,456\}}$ | US | Vector of elements $\{1-3,4-6\}$ of $\mathbf{u}$ |
| $\mathbf{u}_{ABCD}$ | US | Vector of four non-negative cable tensions of $\mathbf{u}_{act}$ |
| $\mathbf{u}_{act}$ | US | Tail actuating control input |
| $\mathbf{u}_{ten}$ | US | Cable tensioning control input |
| $\mathbf{u}_{ten,1}$ | US | Total segment 1 tensioning control input due to cables 1-6 |
| $\mathbf{u}_{\{act,ten\},\{123,456\}}$ | US | Vector of elements $\{1-3,4-6\}$ of $\mathbf{u}_{\{act,ten\}}$ |

Table A.8: Nomenclature, V through $\gamma$

| Variable | Structure | Description |
|---|---|---|
| $\bar{\mathbf{V}}$ | US | Estimated non-actuation loading effects |
| $\mathbf{v}_i$ | C | Linear velocity of rigid body $i$ with respect to the inertial base frame |
| $\hat{\mathbf{x}}_i$ | All | x-axis unit vector of frame $i$ |
| $\hat{\mathbf{x}}_0$ | C | x-axis unit vector of inertial base frame |
| $\hat{\mathbf{x}}_T$ | S | x-axis unit vector of inertial tail frame |
| $\hat{\mathbf{y}}_i$ | All | y-axis unit vector of frame $i$ |
| $\hat{\mathbf{y}}_0$ | C | y-axis unit vector of inertial base frame |
| $\hat{\mathbf{y}}_T$ | S | y-axis unit vector of inertial tail frame |
| $\mathbf{z}$ | US | Reduced state vector |
| $\hat{\mathbf{z}}_{(i-1)i}$ | All | z-axis unit vector of $\mathbf{R}^{i-1}_{(i-1)i}$ |
| $\hat{\mathbf{z}}_i$ | All | z-axis unit vector of frame $i$ |
| $\hat{\mathbf{z}}_0$ | C | z-axis unit vector of inertial base frame |
| $\hat{\mathbf{z}}_{(i-1)i,des}$ | US | Desired z-axis unit vector of $\mathbf{R}_{(i-1)i}$ |
| $\mathbf{z}_{des}$ | US | Desired reduced state vector |
| $\mathbf{z}_{grv,max}$ | US | Reduced state that maximizes gravitational loading |
| $\hat{\mathbf{z}}_T$ | S | z-axis unit vector of inertial tail frame |
| $\alpha_k$ | C | Angle of cable or rod $k$ routing hole position vector |
| $\beta$ | R3 | Joint angle when $\beta_1 = \beta_2$ |
| $\beta_i$ | C | Pitch curvature of subsegment $i$ |
| $\beta_0$ | R3 | $\beta$ at $t_0$ for maneuvering trajectory planning |
| $\beta_l$ | R3 | Joint angle of segment $l$ |
| $(\beta_l)_0$ | R3 | $\beta_l$ of segment $l$ in $\mathbf{q}_0$ |
| $\beta_j$ | US | Angular deflection of universal joint $j$ |
| $\dot{\beta}_B$ | R3 | $\beta$ velocity at $t_B$ for maneuvering trajectory planning |
| $\ddot{\beta}_D$ | R3 | $\beta$ acceleration at $t_D$ for maneuvering trajectory planning |
| $\beta_{des}$ | US | Desired joint deflection for trajectory planning |
| $\beta_H$ | R3 | $\beta$ angle at $t_H$ for maneuvering trajectory planning |
| $\beta_{lim}$ | US | Angular deflection limit of each universal joint |
| $\dot{\beta}_{pk}$ | R3 | Peak $\beta$ acceleration for maneuvering trajectory planning |
| $\boldsymbol{\gamma}_j$ | US | Yaw axis unit vector of universal joint $j$ |
| $\gamma_i$ | C | Yaw curvature of subsegment $i$ |
| $\gamma_j$ | US | Sensor frame yaw angle of universal joint $j$ |

Table A.9: Nomenclature, $\Delta$ through $\tau$

| Variable | Structure | Description |
|---|---|---|
| $\Delta M$ | R3 | Incremental destabilizing moment added to $M_\delta = M_{\delta,0} + M_{\delta,Q}$ to assess tail stabilization limit |
| $\Delta P$ | C | Variation of virtual power |
| $\Delta\dot{\mathbf{q}}$ | C | Variation of virtual power |
| $\delta_{i,k}$ | CR | Radius of curvature offset of rod $k$ subsegment $i$ |
| $\delta_k$ | US | Displacement of cable $k$ from length when tail is straight |
| $\delta_{k,des}$ | US | Desired displacement of cable $k$ from length when tail is straight |
| $\epsilon_i$ | CC | Roll twist angle of subsegment $i$ |
| $\eta_l$ | US | Net yaw angle of segment $l$ |
| $\theta_i$ | C | Bending angle of subsegment $i$ |
| $\theta_j$ | R3 | Angle in joint $j$ between links $i = j-1$ and $i = j$ |
| $\theta_j$ | US | Yaw angle of universal joint $j$ |
| $\theta_{des}$ | US | Desired yaw angle for trajectory planning |
| $\theta_{des,\{0,f\}}$ | US | Desired {initial, final} yaw angle for trajectory planning |
| $\ddot{\theta}_{pk}$ | US | Peak $\theta$ acceleration magnitude for trajectory planning |
| $\kappa$ | R3 | Control action parameter for quadruped disturbance rejection |
| $\kappa_{des}$ | US | Desired bending plane angle for trajectory planning |
| $\kappa_{des,\{0,f\}}$ | US | Desired {initial, final} bending plane angle for trajectory planning |
| $\boldsymbol{\lambda}_i$ | US | Common normal of z-axis unit vectors of frames $i-1$ and $i$ |
| $\boldsymbol{\mu}$ | US | Matrix that maps $\mathbf{q}$ into $\mathbf{z}$ |
| $\left(\boldsymbol{\mu}\bar{\mathbf{T}}\right)_k$ | US | $k$th column of the 4-by-6 $\boldsymbol{\mu}\mathbf{T}$ matrix |
| $\left(\boldsymbol{\mu}\bar{\mathbf{T}}\right)_{r,l}$ | US | 1-by-3 row $r$ vector for the segment $l$ cable coefficients of the 4-by-6 $\boldsymbol{\mu}\mathbf{T}$ matrix |
| $\left(\boldsymbol{\mu}\bar{\mathbf{T}}\right)_{13,12}$ | US | 2-by-3 segment 1 actuation transmission matrix |
| $\left(\boldsymbol{\mu}\bar{\mathbf{T}}\right)_{24,2}$ | US | 2-by-3 segment 2 actuation transmission matrix |
| $\mu$ | C, US | Friction coefficient |
| $\mu_{j,k}$ | US | Friction scaling for cable $k$ subsegment tension affecting joint $j$ |
| $\hat{\boldsymbol{\xi}}_j$ | R3 | Revolute joint $j$ axis unit vector |
| $\xi$ | R3 | Damping ratio for damped harmonic oscillator |
| $\xi$ | US | Bending plane angle |
| $\xi_{\{A,\cdots,E\}}$ | US | $\xi$ angle at $t_{\{A,\cdots,E\}}$ |
| $\ddot{\xi}_{pk}$ | US | Peak $\xi$ acceleration |
| $\boldsymbol{\rho}_j$ | US | Pitch axis unit vector of universal joint $j$ |
| $\rho$ | R3 | Quadruped roll rotation |
| $\rho_j$ | US | Sensor frame pitch angle of universal joint $j$ |
| $\rho_{dz}$ | R3 | Magnitude of maximum acceptable $\rho$ not requiring tail stabilization |
| $\rho_{lim}$ | R3 | Magnitude of $\rho$ at and beyond which $\lvert\kappa\rvert = 1$ |
| $\tau$ | R3 | Roll-DOF torque |

Table A.10: Nomenclature, $\phi$ through Numbers

| **Variable** | **Structure** | **Description** |
|---|---|---|
| $\phi$ | R3 | Roll angle |
| $\phi_0$ | R3 | $\phi$ in $\mathbf{q}_0$ |
| $\phi_i$ | C | Bending plane angle of subsegment $i$ |
| $\phi_j$ | US | Pitch angle of universal joint $j$ |
| $\phi_{des}$ | US | Desired pitch angle for trajectory planning |
| $\phi_{st}$ | R3 | $\phi$ angle in $\mathbf{q}_{st}$ |
| $\chi$ | R3 | Parametrization continuous roll stabilization trajectory |
| $\chi_0$ | R3 | $\chi$ at $t_0$ |
| $\chi_l$ | US | Segment $l$ bending angle |
| $\psi$ | R3 | Interpolation variable for joint angle trajectory planning |
| $\psi_{\{0,f\}}$ | R3 | {Initial, final} joint angle interpolation variable |
| $\psi_l$ | US | Segment $l$ net pitch angle |
| $\psi_{i,k}$ | CC, US | Contact angle of cable $k$ at disk $i$ |
| $\boldsymbol{\omega}_i$ | All | Angular velocity between rigid body $i$ and inertial frame |
| $\boldsymbol{\omega}_{(i-1)i}$ | C, US | Angular velocity between rigid body $i$ and frame $i-1$ |
| $\omega_n$ | R3 | Natural frequency for damped harmonic oscillator |
| $\mathbf{0}_{r\times c}$ | US | $r$-by-$c$ vector/matrix of zeros |
| $\mathbf{1}_{r\times c}$ | US | $r$-by-$c$ vector/matrix of ones |

# Bibliography

[1] Takeshi Aoki, Akiyoshi Ochiai, and Shigeo Hirose. Study on slime robot: Development of the mobile robot prototype model using bridle bellows. In *IEEE International Conference on Robotics and Automation*, pages 2808–2813, New Orleans, LA, 2004.

[2] Andrea Bajo, Roger E. Goldman, and Nabil Simaan. Configuration and joint feedback for enhanced performance of multi-segment continuum robots. In *IEEE International Conference on Robotics and Automation*, pages 2905–2912, Shanghai, China, 2011.

[3] Michael J. Benton. Studying function and behavior in the fossil record. *PLoS Biology*, 8(3):e1000321, 2010.

[4] F. J. Berenguer and F. M. Monasterio-Huelin. Zappa, a quasi-passive biped walking robot with a tail: Modeling , behavior , and kinematic estimation using accelerometers. *IEEE Transactions on Industrial Electronics*, 55(9):3281–3289, 2008.

[5] Michelle Bezanson. The ontogeny of prehensile-tail use in cebus capucinus and alouatta palliata. *American Journal of Primatology*, 74(8):770–782, 2012.

[6] Roger V. Bostelman, James S. Albus, and Ronald E. Graham. Robotcrane and emma applied to waste storage tank remediation. In *American Nuclear Society 7th Topical Meeting on Robotics and Remote Systems*, Augusta, GA, 1997.

[7] Jordan H. Boyle, Sam Johnson, and Abbas A. Dehghani-Sanij. Adaptive undulatory locomotion of a c. elegans inspired robot. *IEEE/ASME Transactions on Mechatronics*, 18(2):439–448, 2013.

[8] David Braganza, Darren M. Dawson, Ian D. Walker, and Nitendra Nath. A neural network controller for continuum robots. *IEEE Transactions on Robotics*, 23(6):1270–1277, 2007.

[9] Randall Briggs, Jongwoo Lee, Matt Haberland, and Sangbae Kim. Tails in biomimetic design: Analysis, simulation, and experiment. In *IEEE/RSJ International Conference on Intelligent Robots and Systems*, pages 1473–1480, Vilamoura, Algarve, Portugal, 2012.

[10] David B. Camarillo, Christopher R. Carlson, and J. Kenneth Salisbury. Configuration tracking for continuum manipulators with coupled tendon drive. *IEEE Transactions on Robotics*, 25(4):798–808, 2009.

[11] Carlos Casarez, Ivan Penskiy, and Sarah Bergbreiter. Using an inertial tail for rapid turns on a miniature legged robot. In *IEEE International Conference on Robotics and Automation*, pages 5469–5474, Karlsruhe, Germany, 2013.

[12] E. Chang-Siu, T. Libby, M. Tomizuka, and R. J. Full. A lizard-inspired active tail enables rapid maneuvers and dynamic stabilization in a terrestrial robot. In *IEEE/RSJ International Conference on Intelligent Robots and Systems*, pages 1887–1894, San Francisco, CA, USA, 2011.

[13] Evan Chang-Siu, Thomas Libby, Matthew Brown, Robert J. Full, and Masayoshi Tomizuka. A nonlinear feedback controller for aerial self-righting by a tailed robot. In *IEEE International Conference on Robotics and Automation*, pages 32–39, Karlsruhe, Germany, 2013.

[14] Gregory S. Chirikjian. Hyper-redundant manipulator dynamics: A continuum approximation. *Advanced Robotics*, 9(3):217–243, 1995.

[15] Gregory S. Chirikjian and J. W. Burdick. A modal approach to hyper-redundant manipulator kinematics. *IEEE Transactions on Robotics and Automation*, 10(3):343–354, 1994.

[16] V. K. Chitrakaran, A. Behal, Darren M. Dawson, and Ian D. Walker. Setpoint regulation of continuum robots using a fixed camera. *Robotica*, 25(05):581–586, 2007.

[17] Radoslaw Cieslak and Adam Morecki. Elephant trunk type elastic manipulator - a tool for bulk and liquid materials transportation. *Robotica*, 17(1):11–16, 1999.

[18] Pierre E. Dupont, Jesse Lock, Brandon Itkowitz, and Evan Butler. Design and control of concentric-tube robots. *IEEE Transactions on Robotics*, 26(2):209–225, 2010.

[19] Martin Eder, Maximilian Karl, Felix Schultheib, Johannes Schurmann, Alois Knoll, and Stefan Riesner. Design of an inherently safe worm-like robot. In *IEEE International Symposium on Safety, Security, and Rescue*, Linkoping, Sweden, 2013.

[20] Louis J. Everett. An extension of kane's method for deriving equations of motion of flexible manipulators. In *IEEE International Conference on Robotics and Automation*, pages 716–721, Scottsdale, AZ, 1989.

[21] Festo. Bionic handling assistant, 2010. URL http://www.festo.com/net/SupportPortal/Files/42050/Brosch{_}FC{_}BHA{_}3{_}0{_}EN{_}lo.pdf.

[22] Frank E. Fish, Sandra A. Bostic, Anthony J. Nicastro, and John T. Beneski. Death roll of the alligator: Mechanics of twist feeding in water. *Journal of Experimental Biology*, 210(16):2811–2818, 2007.

[23] J. Gallardo-Alvarado and J. M. Rico-Martínez. Kinematics of a hyper-redundant manipulator by means of screw theory. *Proceedings of the Institution of Mechanical Engineers, Part K: Journal of Multi-body Dynamics*, 223(4):325–334, 2009.

[24] N. Giri and I. D. Walker. Three module lumped element model of a continuum arm section. In *2011 IEEE/RSJ International Conference on Intelligent Robots and Systems*, pages 4060–4065, San Francisco, CA, 2011.

[25] Isuru S. Godage, David T. Branson, Emanuele Guglielmino, Gustavo A. Medrano-Cerda, and Darwin G. Caldwell. Dynamics for biomimetic continuum arms : A modal approach. In *IEEE International Conference on Robotics and Biomimetics*, pages 104–109, Phuket, Thailand, 2011.

[26] Ian A. Gravagne, Christopher D. Rahn, and Ian D. Walker. Large deflection dynamics and control for planar continuum robots. *IEEE/ASME Transactions on Mechatronics*, 8(2):299–307, 2003.

[27] Mahdi Haghshenas-Jaryani and Gholamreza Vossoughi. Modeling and sliding mode control of a snake-like robot with holonomic constraints. In *IEEE International Conference on Robotics and Biomimetics*, pages 454–461, Bangkok, Thailand, 2009.

[28] Michael W. Hannan and Ian D. Walker. Kinematics and the implementation of an elephant's trunk manipulator and other continuum style robots. *Journal of Robotic Systems*, 20(2):45–63, 2003.

[29] Guangping He and Zhiyong Geng. Exponentially stabilizing an one-legged hopping robot with non-slip model in flight phase. *Mechatronics*, 19(3):364–374, 2009.

[30] Atsushi Horigome, Hiroya Yamada, Gen Endo, Shin Sen, Shigeo Hirose, and Edwardo F.

Fukushima. Development of a coupled tendon-driven 3d multi-joint manipulator. In *IEEE International Conference on Robotics*, pages 5915–5920, Hong Kong, China, 2014.

[31] Fujio Ikeda and Shigehiro Toyama. A proposal of right and left turning mechanism for quasi-passive walking robot. In *IEEE International Conference on Advanced Robotics and Intelligent Systems*, Taipei, Taiwan, 2015.

[32] Guy Immega and Keith Antonelli. The ksi tentacle manipulator. In *IEEE International Conference on Robotics and Automation*, pages 3149–3154, Nagoya, Japan, 1995.

[33] Aaron M. Johnson, Thomas Libby, Evan Chang-Siu, Masayoshi Tomizuka, Robert J. Full, and D. E. Koditschek. Tail assisted dynamic self righting. In *Conference on Climbing and Walking Robots and Support Technologies for Mobile Machines*, pages 611–620, Baltimore, MD, USA, 2012.

[34] Bryan A. Jones, R. L. Gray, and K. Turlapati. Three dimensional statics for continuum robotics. In *IEEE/RSJ International Conference on Intelligent Robotics and Systems*, pages 2659–2664, St. Louis, MO, 2009.

[35] Jinwoo Jung, Ryan S. Penning, Nicola J. Ferrier, and Michael R. Zinn. A modeling approach for continuum robotic manipulators: Effects of nonlinear internal device friction. In *IEEE/RSJ International Conference on Intelligent Robots and Systems*, pages 5139–5146, San Francisco, CA, 2011.

[36] Ardian Jusufi, Daniel I. Goldman, Shai Revzen, and Robert J. Full. Active tails enhance arboreal acrobatics in geckos. *Proceedings of the National Academy of Sciences of the United States of America*, 105(11):4215–4219, 2008.

[37] Byungkyu Kim, Deok-Ho Kim, Jaehoon Jung, and Jong-Oh Park. A biomimetic un-

dulatory tadpole robot using ionic polymermetal composite actuators. *Smart Materials and Structures*, 14(6):1579–1585, 2005.

[38] Yong Jae Kim, Shanbao Cheng, Sangbae Kim, and Karl Iagnemma. A stiffness-adjustable hyperredundant manipulator using a variable neutral-line mechanism for minimally invasive surgery. *IEEE Transactions on Robotics*, 30(2):382–395, 2013.

[39] N. J. Kohut, D. W. Haldane, D. Zarrouk, and R. S. Fearing. Effect of inertial tail on yaw rate of 45 gram legged robot. In *International Conference on Climbing and Walking Robots and the Support Technologies for Mobile Machines*, pages 157–164, Baltimore, MD, USA, 2012.

[40] Vladislav Kopman, Jeffrey Laut, Francesco Acquaviva, Alessandro Rizzo, and Maurizio Porfiri. Dynamic modeling of a robotic fish propelled by a compliant tail. *IEEE Journal of Oceanic Engineering*, 40(1):209–221, 2014.

[41] Holger Lang, Joachim Linn, and Martin Arnold. Multi-body dynamics simulation of geometrically exact cosserat rods. *Multibody System Dynamics*, 25(3):285–312, nov 2010.

[42] Darwin Lau, Denny Oetomo, and Saman K. Halgamuge. Inverse dynamics of multi-link cable-driven manipulators with the consideration of joint interaction forces and moments. *IEEE Transactions on Robotics*, 31(2):479–488, 2015.

[43] Changquing Li and Christopher D. Rahn. Design of continuous backbone, cable-driven robots. *Journal of Mechanical Design*, 124(2):265–271, 2002.

[44] Tao Li, Kohei Nakajima, and Rolf Pfeifer. Online learning for behavior switching in a soft robotic arm. In *IEEE International Conference on Robotics and Automation*, pages 1296–1302, Karlsruhe, Germany, 2013.

[45] Guan-Horng Liu, Hou-Yi Lin, Huai-Yu Lin, Shao-Tuan Chen, and Pei-Chun Lin. A bio-inspired hopping kangaroo robot with an active tail. *Journal of Bionic Engineering*, 11(4):541–555, 2014.

[46] Heinrich Mallison. Cad assessment of the posture and range of motion of kentrosaurus aethiopicus hennig 1915. *Swiss Journal of Geosciences*, 103(2):211–233, 2010.

[47] Andrew D. Marchese, Konrad Komorowski, Cagdas D. Onal, and Daniela Rus. Design and control of a soft and continuously deformable 2d robotic manipulation system. In *IEEE International Conference on Robotics and Automation*, pages 2189–2196, Hong Kong, China, 2014.

[48] James C. McKenna, David J. Anhalt, Frederick M. Bronson, H. Ben Brown, Michael Schwerin, Elie Shammas, and Howie Choset. Toroidal skin drive for snake robot locomotion. In *IEEE International Conference on Robotics and Automation*, pages 1150–1155, Pasadena, CA, 2008.

[49] William McMahan, Bryan A. Jones, and Ian D. Walker. Design and implementation of a multi-section continuum robot: Air-octor. In *IEEE/RSJ International Conference on Intelligent Robots and Systems*, pages 2578–2585, Alberta, Canada, 2005.

[50] William McMahan, V. Chitrakaran, Matthew A. Csencsits, Darren M. Dawson, Ian D. Walker, Bryan A. Jones, M. Pritts, D. Dienno, M. Grissom, and Christopher D. Rahn. Field trials and testing of the octarm continuum manipulator. In *IEEE International Conference on Robotics and Automation*, pages 2336–2341, Orlando, FL, 2006.

[51] Matthew S. Moses, Michael D. M. Kutzer, Hans Ma, and Mehran Armand. A continuum manipulator made of interlocking fibers. In *IEEE International Conference on Robotics and Automation*, pages 4008–4015, Karlsruhe, Germany, 2013.

[52] Alan Mutka, Matko Orsag, and Zdenko Kovacic. Stabilizing a quadruped robot locomotion using a two degree of freedom tail. In *21st Mediterranean Conference on Control and Automation*, pages 1336–1342, Platanias-Chania, Greece, 2013.

[53] OC-Robotics. Snake-arm robots, 2015. URL http://www.ocrobotics.com/technology--innovation/.

[54] Shawn M. O'Connor, Terence J. Dawson, Rodger Kram, and J. Maxwell Donelan. The kangaroo's tail propels and powers pentapedal locomotion. *Biology Letters*, 10:20140381, 2014.

[55] Hidetaka Ohno and Shigeo Hirose. Study on slime robot: Proposal of slime robot and design of slim slime robot. In *IEEE/RSJ International Conference on Intelligent Robots and Systems*, pages 2218–2223, Takamatsu, Japan, 2000.

[56] Amir Patel and M. Braae. Rapid turning at high-speed: Inspirations from the cheetah's tail. In *IEEE/RSJ International Conference on Intelligent Robots and Systems*, pages 5506–5511, Tokyo, Japan, 2013.

[57] Amir Patel and M. Braae. Rapid acceleration and braking: Inspiration from the cheetah's tail. In *IEEE International Conference on Robotics and Automation*, pages 793–799, Hong Kong, China, 2014.

[58] W. Scott Persons and Philip J. Currie. The tail of tyrannosaurus: Reassessing the size and locomotive importance of the m. caudofemoralis in non-avian theropods. *Anatomical Record*, 294(1):119–131, 2011.

[59] Uwe Proske. Energy conservation by elastic storage in kangaroos. *Endeavour*, 4(4): 148–153, 1 1980.

[60] William R. Provancher, Samuel I. Jensen-Segal, and Mark A. Fehlberg. Rocr: An energy-efficient dynamic wall-climbing robot. *IEEE/ASME Transactions on Mechatronics*, 16(5):897–906, 2011.

[61] Wenhuan Qian, Tao Mei, and Jianghai Zhao. Analysis on the configuration and simulation of a new robot composed with hybrid joints. In *IEEE International Conference on Robotics and Biomimetics*, pages 1838–1844, Shenzhen, China, 2013.

[62] F. Renda, M. Cianchetti, M. Giorelli, A. Arienti, and C. Laschi. A 3d steady-state model of a tendon-driven continuum soft manipulator inspired by the octopus arm. *Bioinspiration and Biomimetics*, 7:025006, 2012.

[63] Thomas R.Kan and David A. Levinson. The use of kane's dynamical equations in robotics. *The International Journal of Robotics Research*, 2(3):3–21, sep 1983.

[64] G. Robinson and J. B. C. Davies. Continuum robots - a state of the art. In *IEEE International Conference on Robotics and Automation*, pages 2849–2854, Detroit, MI, USA, 1999.

[65] William S. Rone and Pinhas Ben-Tzvi. Continuum manipulator statics based on the principle of virtual work. In *ASME International Mechanical Engineering Congress and Exposition*, pages 87675: 1–8, Houston, TX, USA, 2012.

[66] William S. Rone and Pinhas Ben-Tzvi. Multi-segment continuum robot shape estimation using passive cable displacements. In *IEEE International Symposium on Robotic and Sensors Environments*, pages 37–42, Washington, DC, USA, 2013.

[67] William S. Rone and Pinhas Ben-Tzvi. Continuum robotic tail loading analysis for mobile robot stabilization and maneuvering. In *ASME International Design Engineering*

*Technical Conference & Computers and Information in Engineering Conference*, pages 34678: 1–8, Buffalo, NY, USA, 2014.

[68] William S. Rone and Pinhas Ben-Tzvi. Static modeling of a multi-segment serpentine robotic tail. In *ASME International Design Engineering Technical Conference & Computers and Information in Engineering Conference*, pages 46655: 1–9, Boston, MA, USA, 2015.

[69] William S. Rone and Pinhas Ben-Tzvi. Dynamic modeling and simulation of a yaw-angle quadruped maneuvering with a robotic tail. *ASME Journal of Dynamic Systems, Measurement and Control*, 138(8):084502: 1–7, 8 2016.

[70] William S. Rone and Pinhas Ben-Tzvi. Maneuvering and stabilizing control of a quadrupedal robot using a serpentine robotic tail. In *IEEE Conference on Control Technology and Applications*, pages 1763–1768, Kohala Coast, Hawai'i, USA, 8 2017.

[71] William S. Rone and Pinhas Ben-Tzvi. Design, modeling and optimization of the universal-spatial robotic tail. In *ASME International Mechanical Engineering Congress and Exposition*, Tampa, FL, USA, 11 2017.

[72] D. Caleb Rucker and Robert J. Webster III. Statics and dynamics of continuum robots with general tendon routing and external loading. *IEEE Transactions on Robotics*, 27 (6):1033–1044, 2011.

[73] D. Caleb Rucker, Robert J. Webster, Gregory S. Chirikjian, and Noah J. Cowan. Equilibrium conformations of concentric-tube continuum robots. *International Journal of Robotics Research*, 29(10):1263–1280, 2010.

[74] Wael Saab, William S. Rone, and Pinhas Ben-Tzvi. Robotic tails: A state of the art review. *Robotica*, 2017. Accepted.

[75] Wael Saab, William S. Rone, and Pinhas Ben-Tzvi. Discrete modular serpentine robotic tail: Design, analysis and experimentation. *Robotica*, 36(7):994–1018, 7 2018.

[76] Wael Saab, William S. Rone, Anil Kumar, and Pinhas Ben-Tzvi. Design and integration of a novel spatial articulated robotic tail. *IEEE Transactions on Mechatronics*, 2018. Under Review.

[77] Daniel Schmitt, Michael D. Rose, Jean E. Turnquist, and Pierre Lemelin. Role of the prehensile tail during ateline locomotion: Experiment and osteological evidence. *American Journal of Physical Anthropology*, 126(4):435–446, 2005.

[78] Michael Sfakiotakis, David M. Lane, and J. Bruce C. Davies. Review of fish swimming modes for aquatic locomotion. *IEEE Journal of Oceanic Engineering*, 24(2):237–252, 1999.

[79] Irving H. Shames. *Engineering Mechanics: Statics*. Prentice Hall, Upper Saddle River, NJ, 4th edition, 1998.

[80] Nabil Simaan, Russell Taylor, and Paul Flint. A dexterous system for laryngeal surgery. In *IEEE International Conference on Robotics and Automation*, pages 351–357, New Orleans, LA, 2004.

[81] Yogo Takada, Yukinobu Nakanishi, Ryosuke Araki, Motohiro Nonogaki, and Tomoyuki Wakisaka. Effect of material and thickness about tail fins on propulsive performance of a small fish robot. *Journal of Aero Aqua Bio-mechanisms*, 1(1):51–56, 2010.

[82] Enver Tatlicioglu, Ian D. Walker, and Darren M. Dawson. Dynamic modelling for planar extensible continuum robot manipulators. In *IEEE International Conference on Robotics and Automation*, pages 1357–1362, Roma, Italy, 2007.

[83] Lorenzo Toscano, Valentin Falkenhahn, Alexander Hildebrandt, Francesco Braghin, and Oliver Sawodny. Configuration space impedance control for continuum manipulators. In *IEEE International Conference on Automation, Robotics and Applications*, pages 597–602, Queenstown, New Zealand, 2015.

[84] Deepak Trivedi, Christopher D. Rahn, William M. Kier, and Ian D. Walker. Soft robotics: Biological inspiration, state of the art, and future research. *Applied Bionics and Biomechanics*, 5(3):99–117, 2008.

[85] Lung-Wen Tsai. *Robot Analysis: The Mechanics of Serial and Parallel Manipulators*. Wiley-Interscience, New York, 1999.

[86] Arthur Munzenmaier Wahl. *Mechanical Springs*. Penton Publishing Company, Cleveland, Ohio, 1st edition, 1944.

[87] Curt Walker, Charles J. Vierck Jr., and Louis A. Ritz. Balance in the cat: Role of the tail and effects of sacrocaudal transection. *Behavioural Brain Research*, 91:41–47, 1998.

[88] Robert J. Webster III and Bryan A. Jones. Design and kinematic modeling of constant curvature continuum robots: A review. *International Journal of Robotics Research*, 29 (13):1661–1683, 2010.

[89] A. M. Wilson, J. C. Lowe, K. Roskilly, P. E. Hudson, K. A. Golabek, and J. W. McNutt. Locomotion dynamics of hunting in wild cheetahs. *Nature*, 498(7453):185–189, 2013.

[90] Cornell Wright, Austin Buchan, Ben Brown, Jason Geist, Michael Schwerin, David Rollinson, Matthew Tesch, and Howie Choset. Design and architecture of the unified modular snake robot. In *IEEE International Conference on Robotics and Automation*, pages 4347–4354, St. Paul, MN, 2012.

[91] Kai Xu and Nabil Simaan. An investigation of the intrinsic force sensing capabilities of continuum robots. *IEEE Transactions on Robotics*, 24(3):576–587, 2008.

[92] Kai Xu and Nabil Simaan. Analytic formulation for kinematics, statics, and shape restoration of multibackbone continuum robots via elliptic integrals. *Journal of Mechanisms and Robotics*, 2(1):011006, 2010.

[93] Jesse W. Young, Gabrielle A. Russo, Connie D. Fellmann, Meena A. Thatikunta, and Brad A. Chadwell. Tail function during arboreal quadrupedalism in squirrel monkeys (saimiri boliviensis) and tamarins (saguinus oedipus). *Journal of Experimental Zoology Part A: Ecological Genetics and Physiology*, 323(8):556–566, 2015.

[94] Jianguo Zhao, Tianyu Zhao, Ning Xi, Fernando J. Cintron, Matt W. Mutka, and Li Xiao. Controlling aerial maneuvering of a miniature jumping robot using its tail. In *IEEE/RSJ International Conference on Intelligent Robots and Systems*, pages 3802–3807, Tokyo, Japan, 2013.

[95] Wei Zhuang, Xiaoping Liu, Chenwei Fang, and Hanxu Sun. Dynamic modeling of a spherical robot with arms by using kane's method. In *International Conference on Natural Computation*, pages 373–377, Jinan, Shandong, China, 2008.